

Lancaster  
Environment Centre

Lancaster  
University



**Tracing fluid dynamics with noble gas and  
stable isotope systematics: examples from  
Krafla, Iceland and Sichuan Basin, China**

Yan Li

Thesis submitted for the degree of Ph.D. at Lancaster University

September 2018

# **Declaration**

Except where reference is made to other sources, I declare that the contents in this thesis are my own work and have not been previously submitted, in part or in full, for the award of a higher degree elsewhere.

Yan Li

Lancaster University

September 2018

# Acknowledgements

There are many people I would like to thank for their help and guidance during my PhD work. First and foremost is my supervisors, Dr Zheng Zhou and Dr Greg Holland. Thank you, Joe, for giving me the opportunity to work in your lab and providing me with endless support, patience and guidance over the years. Greg, thank you so much for all your assistance and great suggestions on my PhD work. I am so grateful to have you both as my supervisors and your continued encouragement and inspiration has been invaluable. Thank you to my master supervisor, Professor Yunpeng Wang for your help and support in my work. I would like to thank NGX engineers Damian Tootell, Chris Varden, Dave Burgess for all their assistance in the laboratory. Thank you, Dave Hughes, Lingling Liao for their assistance in stable isotope analyses. A big thank you to Emily Heath, thanks for offering me the demonstrating work, which has significantly helped me improve my communicational skills.

I have been fortunate enough to find myself surrounded by wonderful people in Lancaster, Lingfei Wang, Wei Chen, Shizhen Zhao, Youliang Zhang, Ruilin Zhu, Runmei Wang, Yanying Li, Wen Zhang, Ben Jackson, Mounir Takriti, Michael Tso. Thank you for the friendship and encouragement. Special thanks to Chun Lin for your guidance and help in the world of R coding, it has been invaluable and eye-opening! I am so grateful to Kirsty Forber, Tim Jacob, Marvin Kopo and Laura deprose, for the sharing and encouragement in PhD life. Thank you so much to my church friends and aikido mates. Thanks for bringing me so much faith and joy in my life. I am sure I cannot do it without your support. To all my 'party' friends, Huanfang Huang, Guozhen Wei, Shichao Zhang, Ying Zhu, Pengjun Xu, Yuqin Shi, Qunming Wang, Ying Chen, thanks for the delicious food and most importantly, the valuable friendship and encouragement.

To all my Goldfish bowl office mates, Lucas Gent, Kirsty Forber, Sarah Donaldson, Joe Acton, Tom Mon-Mon, Aimee Brett, Xiaoqing Li, Ying Wang, Antonio, Alexander Burrows, Noorliana Mohd Zan, Esti Leibar, Rob Kempster, thank you all for the help and support over the years.

Thanks to Chinese Scholarship Council for funding my research work at Lancaster University.

Last but not least, a big thank you to my parents and girlfriend for their endless love and support all the time. I cannot express how grateful I am to have you all. I hope I can make you feel proud of me in future.

# Abstract

The study of noble gases and reactive gases (i.e., CO<sub>2</sub>, N<sub>2</sub> and CH<sub>4</sub>) in crustal reservoirs can help better understand the origin, migration and accumulation processes of crustal fluids in the subsurface environment, which provide further insights into fluid dynamics underground. This PhD thesis develops noble gas isotopes as geochemical tools in crustal fluid studies. Study sites have been selected to cover different types of geofluids, including geothermal fluids in Krafla, Iceland and natural gases in the Sichuan Basin, China.

Following a short introduction to the research background, objectives and thesis layout are presented in Chapter 1 and Chapter 2 gives a literature review on the application of noble gases as powerful geochemical tools in hydrothermal and hydrocarbon systems. Chapter 3 describes a noble gas extraction and purification system, interfaced to a multi-collector NGX noble gas mass spectrometer (Isotopx), which is constructed particularly for this study. The detailed description of each section in sample preparation system, as well as gas sampling, extraction, purification and separation protocols is provided. Temperatures of 50 K and 95 K can be used as the optimal releasing temperatures for He and Ne on the cryotrap in sample preline. The temperature of 210 K is tested to be the optimal temperature for releasing Ar and Kr but keeping Xe being trapped onto the charcoal trap in the preline.

Chapter 4 characterizes noble gas and stable isotope data of hydrothermal fluid system in Krafla, Iceland. Stable isotope results indicate that CO<sub>2</sub> in the samples is considered to be magmatic in origin, with  $\delta^{13}\text{C}$  (CO<sub>2</sub>) ranging between -7.99 and -3.86 ‰. Modelling results show that processes of boiling and steam separation have occurred during the circulation of geothermal fluids in the shallow crust in the Krafla field. Air addition, possibly introduced by groundwater re-injection, has had a significant effect on the geochemical signatures of Krafla geothermal fluids as well.

Chapter 5 focuses on using noble gas isotopes to trace the interaction between hydrocarbon and groundwater systems in the central Sichuan Basin, China. Twenty-six natural gas samples were collected from the Anyue and Weiyuan gas fields in the central Sichuan basin, China for stable isotope and noble gas isotope determination. Noble gases together with stable carbon isotopic parameter ( $\Delta\delta^{13}\text{C}_{1-2}$ ) can be an effective tool to differentiate the occurrence of two distinct genetic groups of natural gases in the central Sichuan basin. Elemental fractionations of noble gases in samples from the western area (coal-derived gas) can be well explained by solubility-controlled Rayleigh fractionation model with relatively less effect of mass-dependent fractionation process. However, noble gas elemental and isotopic compositions in samples from the eastern area can be interpreted as a mixing effect of solubility-controlled and mass-dependent fractionation processes.

This thesis further develops noble gases as a versatile tool in the study of crustal fluids. It is the first-time noble gas isotopes are used in understanding fluid dynamics in natural gas reservoirs in China. This work has demonstrated a huge potential to apply the noble gas tool in basin studies in China and Asian geology in general.

# Contents

Declaration.....	I
Acknowledgements.....	II
Abstract.....	IV
List of Figures.....	IX
List of Tables.....	XIII
Abbreviations.....	XIV
1 Introduction.....	1
1.1 Research background and motivations.....	1
1.2 Objectives and thesis layout.....	2
2 Literature review.....	4
2.1 Noble gases in subsurface fluids.....	4
2.1.1 The three main physical processes that affect noble gas fractionation.....	5
2.1.2 Properties of each noble gas element.....	6
2.2 Three different sources.....	9
2.2.1 Air Saturated Water (ASW).....	10
2.2.2 Crust.....	12
2.2.3 Mantle.....	14
2.3 Physical chemistry of noble gases in fluids.....	16
2.3.1 Henry's law.....	16
2.3.2 Non-ideality in the gas phase.....	16
2.3.3 Non-ideality in the liquid phase.....	19
2.3.4 Noble gas solubility measurements.....	22
2.4 Noble gases as natural tracers in hydrothermal systems.....	24
2.4.1 Introduction.....	24
2.4.2 Noble gas as fluid tracers.....	24
2.5 Noble gases as natural tracers in hydrocarbon systems.....	27
2.5.1 Introduction.....	27
2.5.2 Noble gases exchange between groundwater and hydrocarbon systems.....	28
2.5.3 Noble gas as sensitive tracers for identifying physical processes.....	30
2.5.4 Enrichment of heavier noble gases.....	31
3 Methodology.....	32
3.1 Introduction to noble gas mass spectrometry.....	32
3.2 NGX noble gas mass spectrometer.....	34
3.3 NGX software.....	38

3.4	NGX performance .....	43
3.5	Functions of each part in the prep line system .....	48
3.6	Sampling and experiment (gas extraction, purification and separation).....	56
3.6.1	Sampling in the field.....	56
3.6.2	Gas extraction .....	59
3.6.3	Gas purification .....	61
3.6.4	Gas separation.....	61
3.6.5	The determination of separation temperature .....	63
3.7	Interferences .....	68
3.8	Blank and air standard.....	69
3.9	Noble gas concentration calculation .....	72
3.10	Error propagation .....	74
4	Noble gas and stable isotope characteristics of hydrothermal fluid system, Krafla, Iceland	75
4.1	Introduction .....	75
4.2	The Krafla Geothermal Field .....	76
4.3	Sampling techniques and experimental methods .....	79
4.4	Results .....	82
4.4.1	Major gas species and stable isotopes .....	82
4.4.2	Noble gases.....	86
4.5	Discussion .....	93
4.5.1	Mantle Helium- MORB-type and plume-type He.....	93
4.5.2	Controls on CO <sub>2</sub> / <sup>3</sup> He: elemental fractionation .....	95
4.5.3	Depletion of atmospheric noble gases in Krafla geothermal field .....	96
4.5.4	Boiling and steam separation effects in the Krafla geothermal field .....	98
4.6	Conclusion.....	102
5	Tracing interaction between hydrocarbon and groundwater systems with noble gases in the central Sichuan Basin, China .....	103
5.1	Introduction .....	103
5.2	Geological setting and sample locations .....	105
5.2.1	Geological background of Sichuan basin .....	105
5.2.2	Study area .....	108
5.3	Sample collection and analytical techniques.....	110
5.3.1	Analysis of natural gas composition and stable carbon isotopic composition .....	110
5.3.2	Noble gas sample collection and analyses.....	111
5.4	Results .....	113

5.4.1 Major gas species and stable carbon isotopes .....	113
5.4.2 Noble gases.....	117
5.4.3 Groundwater-derived noble gas components .....	126
5.4.4 Relationship between groundwater-derived and crustal noble gases .....	128
5.5 Discussion .....	129
5.5.1 Determining the genetic fingerprint of natural gas using noble gas geochemistry	129
5.5.2 Solubility controlled fractionation of $^4\text{He}/^{40}\text{Ar}^*$ and $^{20}\text{Ne}+/^{36}\text{Ar}^+$ .....	132
5.5.3 Diffusion process dependent fractionation .....	136
5.5.4 Kr and Xe enrichment.....	138
5.6 Conclusion.....	140
6 Conclusions and Future Work .....	142
References.....	145

# List of Figures

<b>Chapter 2</b>		<b>Page</b>
<b>Figure 2.1</b>	R/R <sub>a</sub> ratio as a function of <sup>4</sup> He/ <sup>20</sup> Ne ratio for collected fluid samples.	<b>7</b>
<b>Figure 2.2</b>	Neon three-isotope plot for selected noble gas studies of petroleum systems.	<b>8</b>
<b>Figure 2.3</b>	A schematic conceptual model showing three distinct sources of noble gas isotopes modified in petroleum systems.	<b>9</b>
<b>Figure 2.4</b>	CO <sub>2</sub> / <sup>3</sup> He vs. fraction of CO <sub>2</sub> .	<b>15</b>
<b>Figure 2.5</b>	Noble gas fugacity coefficients as a function of depth assuming temperature gradient of 0.03 K/m and hydrostatic pressure.	<b>19</b>
<b>Figure 2.6</b>	Noble gas Setchenow coefficients as a function of T.	<b>21</b>
<b>Figure 2.7</b>	Henry's coefficients for noble gases in water as a function of temperature.	<b>23</b>
<b>Figure 2.8</b>	Cartoon illustrating a geothermal reservoir in a deep convective hydrothermal system.	<b>26</b>
<b>Figure 2.9</b>	<sup>3</sup> He/ <sup>4</sup> He(R/R <sub>a</sub> ) vs. <sup>4</sup> He concentration measurements from selected noble gas studies of petroleum systems.	<b>29</b>
<b>Figure 2.10</b>	Schematic of Rayleigh fractionation and dilution processes.	<b>31</b>
 <b>Chapter 3</b>		 <b>Page</b>
<b>Figure 3.1</b>	Mass spectrometer comprising ion source, analyzer (magnet) and collector (Faraday, multiplier).	<b>34</b>
<b>Figure 3.2</b>	NGX noble gas mass spectrometer from above showing geometry.	<b>36</b>
<b>Figure 3.3</b>	Difference in ion beam travel directions between NGX rotated focal plane and conventional focal plane.	<b>37</b>
<b>Figure 3.4</b>	NGX Inlet Prep Bench window.	<b>38</b>
<b>Figure 3.5</b>	NGX Instrument Control used for loading script files, tuning ion source and controlling hardware parameters.	<b>39</b>
<b>Figure 3.6</b>	Iconia software window showing sample lists, selected analysis methods, inlet scripts and tuning files.	<b>41</b>
<b>Figure 3.7</b>	Data acquisition process on Iconia.	<b>43</b>

<b>Figure 3.8</b>	Variation of the $^{21}\text{Ne}/^{20}\text{Ne}$ over a range of $^{20}\text{Ne}$ beams.	<b>44</b>
<b>Figure 3.9</b>	The linearity of $^{40}\text{Ar}/^{36}\text{Ar}$ with changes in $^{40}\text{Ar}$ intensity showing $^{40}\text{Ar}/^{36}\text{Ar}$ remains constant irrespective of $^{40}\text{Ar}$ intensity.	<b>45</b>
<b>Figure 3.10</b>	Simultaneous collection of all 9 Xe isotopes on Faraday cups.	<b>46</b>
<b>Figure 3.11</b>	The performance of different Xe isotopic ratios as a function of $^{132}\text{Xe}$ intensity.	<b>47</b>
<b>Figure 3.12</b>	Schematic diagram of a fully automated noble gas extraction line at Lancaster University.	<b>48</b>
<b>Figure 3.13</b>	PDR2000 Dual Capacitance Manometer (MKS Instruments).	<b>51</b>
<b>Figure 3.14</b>	RC RGA Analyser System.	<b>52</b>
<b>Figure 3.15</b>	Closed Cycle Cryogenic Cold Trap System.	<b>53</b>
<b>Figure 3.16</b>	Devices for field sampling work.	<b>57</b>
<b>Figure 3.17</b>	Collection of natural gas samples using 10mm diameter internally polished refrigeration grade copper tubes sealed by stainless steel pinch-off clamps on both ends in the Sichuan basin, China, in 2015.	<b>58</b>
<b>Figure 3.18</b>	Hidden MASsoft window showing He leak detection operation.	<b>60</b>
<b>Figure 3.19</b>	The partial pressure of $^4\text{He}$ and $^{20}\text{Ne}$ is shown as a function of cryotrap temperature.	<b>65</b>
<b>Figure 3.20</b>	The partial pressures of $^{40}\text{Ar}$ and $^{132}\text{Xe}$ at different separation temperatures for each cycle.	<b>67</b>
<b>Figure 3.21</b>	The $^3\text{He}$ peak is clearly resolved from the HD molecule.	<b>69</b>
<b>Figure 3.22</b>	HESJ standard used by subsurface fluid isotope geochemistry laboratory at Lancaster University.	<b>71</b>
<b>Chapter 4</b>		<b>Page</b>
<b>Figure 4.1</b>	Krafla geological map showing tectonic features, the different wellfields and individual wells.	<b>78</b>
<b>Figure 4.2</b>	NW-SE cross-section showing a geologic lithology in the Krafla geothermal field.	<b>79</b>
<b>Figure 4.3</b>	Mud pot gases flowing through a funnel to avoid any contact with air.	<b>80</b>

<b>Figure 4.4</b>	The negative relationship between CO <sub>2</sub> and N <sub>2</sub> in the Krafla geothermal field.	<b>83</b>
<b>Figure 4.5</b>	The positive relationship between O <sub>2</sub> and N <sub>2</sub> in the Krafla geothermal field.	<b>84</b>
<b>Figure 4.6</b>	Air-normalized <sup>3</sup> He/ <sup>4</sup> He ratios (R/R <sub>a</sub> ) vs. <sup>4</sup> He/ <sup>20</sup> Ne ratio.	<b>90</b>
<b>Figure 4.7</b>	a) Neon isotopic composition with three different component endmembers; and b) <sup>20</sup> Ne / <sup>22</sup> Ne vs. <sup>21</sup> Ne/ <sup>22</sup> Ne in the Krafla geothermal system.	<b>91</b>
<b>Figure 4.8</b>	<sup>38</sup> Ar/ <sup>36</sup> Ar vs. <sup>40</sup> Ar/ <sup>36</sup> Ar in the Krafla geothermal system.	<b>92</b>
<b>Figure 4.9</b>	A plot of CO <sub>2</sub> / <sup>3</sup> He vs. δ <sup>13</sup> C for Krafla gas samples.	<b>96</b>
<b>Figure 4.10</b>	Noble gas concentrations in Krafla geothermal fluids. normalized to noble gas concentrations in Air Saturated Water at 10 °C.	<b>97</b>
<b>Figure 4.11</b>	a) The F( <sup>20</sup> Ne) vs. F( <sup>132</sup> Xe) values, and b) the F( <sup>84</sup> Kr) vs. F( <sup>132</sup> Xe) values measured in Krafla geothermal fluid.	<b>98</b>
<b>Chapter 5</b>		<b>Page</b>
<b>Figure 5.1</b>	Geological features in the Sichuan Basin, China and location of sample collection sites.	<b>106</b>
<b>Figure 5.2</b>	Schematic of the Sichuan Basin stratigraphy.	<b>108</b>
<b>Figure 5.3</b>	The negative relationship between CH <sub>4</sub> and CO <sub>2</sub> concentrations in samples from the western area, Anyue gas field.	<b>114</b>
<b>Figure 5.4</b>	a) CH <sub>4</sub> concentrations vs. N <sub>2</sub> concentrations, and b) N <sub>2</sub> concentrations vs. CO <sub>2</sub> concentrations for gas samples in this study.	<b>115</b>
<b>Figure 5.5</b>	a) CH <sub>4</sub> concentrations vs. δ <sup>13</sup> C (CH <sub>4</sub> ), and b) C <sub>2</sub> H <sub>6</sub> concentrations vs. δ <sup>13</sup> C (C <sub>2</sub> H <sub>6</sub> ) for gas samples in this study.	<b>115</b>
<b>Figure 5.6</b>	a) <sup>20</sup> Ne concentrations vs. <sup>40</sup> Ar/ <sup>36</sup> Ar ratios, and b) <sup>21</sup> Ne/ <sup>22</sup> Ne vs <sup>40</sup> Ar/ <sup>36</sup> Ar ratios for gas samples in this study.	<b>117</b>
<b>Figure 5.7</b>	a) <sup>3</sup> He/ <sup>4</sup> He ratios (R/R <sub>a</sub> ) vs. <sup>4</sup> He concentrations, and b) <sup>3</sup> He/ <sup>4</sup> He ratios (R/R <sub>a</sub> ) vs. <sup>4</sup> He/ <sup>20</sup> Ne ratios.	<b>118</b>
<b>Figure 5.8</b>	<sup>20</sup> Ne/ <sup>22</sup> Ne vs. <sup>21</sup> Ne/ <sup>22</sup> Ne ratios for all samples in this study.	<b>121</b>
<b>Figure 5.9</b>	<sup>40</sup> Ar/ <sup>36</sup> Ar ratios vs. 1/ <sup>36</sup> Ar.	<b>123</b>

<b>Figure 5.10</b>	Atmosphere-derived noble gas abundances in the Anyue gas field normalized to those of ASW (Air Saturated Water) at 10 °C with $^{36}\text{Ar}$ as the reference isotope.	<b>127</b>
<b>Figure 5.11</b>	a) $^4\text{He}/^{40}\text{Ar}^*$ vs. $^{20}\text{Ne}^+ / ^{36}\text{Ar}^+$ ratios, and b) $^{21}\text{Ne}^* / ^{40}\text{Ar}^*$ vs. $^4\text{He} / ^{40}\text{Ar}^*$ .	<b>129</b>
<b>Figure 5.12</b>	a) $^4\text{He} / ^{21}\text{Ne}^*$ vs. $\Delta\delta^{13}\text{C}_{1-2}$ , b) $^4\text{He} / ^{40}\text{Ar}^*$ vs $\Delta\delta^{13}\text{C}_{1-2}$ and c) $^{21}\text{Ne}^* / ^{40}\text{Ar}^*$ vs $\Delta\delta^{13}\text{C}_{1-2}$ .	<b>131</b>
<b>Figure 5.13</b>	$^4\text{He} / ^{36}\text{Ar}$ vs. $^{40}\text{Ar} / ^{36}\text{Ar}$ .	<b>131</b>
<b>Figure 5.14</b>	Crustal radiogenic $^4\text{He} / ^{40}\text{Ar}^*$ vs. water-derived $^{20}\text{Ne} / ^{36}\text{Ar}$ .	<b>135</b>
<b>Figure 5.15</b>	$^{20}\text{Ne} / ^{36}\text{Ar}$ vs. $^{20}\text{Ne}$ concentrations in samples from the Anyue and Weiyuan gas fields, Sichuan basin.	<b>135</b>
<b>Figure 5.16</b>	Crustal radiogenic $^4\text{He} / ^{40}\text{Ar}^*$ vs. water-derived $^{20}\text{Ne} / ^{36}\text{Ar}$ .	<b>138</b>
<b>Figure 5.17</b>	$^{84}\text{Kr} / ^{36}\text{Ar}$ vs. $^{20}\text{Ne} / ^{36}\text{Ar}$ ratios measured in samples.	<b>139</b>
<b>Figure 5.18</b>	$^{132}\text{Xe} / ^{36}\text{Ar}$ vs. $^{20}\text{Ne} / ^{36}\text{Ar}$ ratios measured in samples.	<b>139</b>

# List of Tables

<b>Chapter 2</b>		<b>Page</b>
<b>Table 2.1</b>	The noble gas isotope composition of the atmosphere.	<b>11</b>
<b>Table 2.2</b>	Noble gas virial and fugacity coefficients as a function of depth.	<b>18</b>
<b>Table 2.3</b>	Noble gas Setchenow coefficients, $K_i(T)$ .	<b>21</b>
<b>Table 2.4</b>	Henry's constants for noble gases in water.	<b>22</b>
 <b>Chapter 3</b>		 <b>Page</b>
<b>Table 3.1</b>	Noise comparison between $1e^{11}\Omega$ and $1e^{12}\Omega$ resistor.	<b>37</b>
<b>Table 3.2</b>	The optimal source tuning parameters for each noble gas.	<b>40</b>
<b>Table 3.3</b>	The optimal isotopic analysis parameters for each noble gas using iconia on NGX.	<b>42</b>
<b>Table 3.4</b>	The performance of the NGX for measuring the major isotopes of five noble gases.	<b>70</b>
 <b>Chapter 4</b>		 <b>Page</b>
<b>Table 4.1</b>	Major gas composition and stable isotope measurements.	<b>85</b>
<b>Table 4.2</b>	Gas geochemistry on Krafla samples based on previous researches.	<b>86</b>
<b>Table 4.3</b>	Noble gas elemental abundances and $F(i)$ values for Krafla geothermal fluids.	<b>87</b>
<b>Table 4.4</b>	Noble gas isotopic ratios for Krafla geothermal fluids.	<b>88</b>
<b>Table 4.5</b>	$^3\text{He}/^4\text{He}$ and $^4\text{He}/^{20}\text{Ne}$ ratios in Krafla gas samples together with proportion of He in three different components — MORB, Plume, and Air.	<b>94</b>
 <b>Chapter 5</b>		 <b>Page</b>
<b>Table 5.1</b>	Major gas composition and stable carbon isotopes.	<b>116</b>
<b>Table 5.2</b>	Sample location, strata and noble gas concentrations.	<b>124</b>
<b>Table 5.3</b>	Noble gas isotopic compositions and groundwater-derived and crustal-derived noble gas elemental compositions.	<b>125</b>

# Abbreviations

<b>ASGW</b>	Air Saturated Geothermal Water
<b>ASW</b>	Air Saturated Water
<b>CEH</b>	Center for Ecology & Hydrology
<b>GC</b>	Gas Chromatograph
<b>HD</b>	Hydrogen Deuteride
<b>HESJ</b>	Helium Standard of Japan
<b>IDDP</b>	Iceland Deep Drilling Project
<b>IRMS</b>	Isotope Ratio Mass Spec
<b>MORB</b>	Mid-Ocean Ridge Basalts
<b>NERC</b>	Natural Environment Research Council
<b>OIB</b>	Ocean Island Basalts
<b>QMS</b>	Quadrupole Mass Spectrometer
<b>RGA</b>	Residual Gas Analysis
<b>SEM</b>	Secondary Electron Multipliers
<b>SMOW</b>	Standard Mean Ocean Water
<b>STP</b>	Standard Temperature Pressure
<b>TCD</b>	Thermal Conductivity Detectors
<b>UHV</b>	Ultra High Vacuum
<b>V-PDB</b>	Vienna Peedee belemnite

# 1 Introduction

## 1.1 Research background and motivations

Our planet is a huge source of energy. Large area on the planet is at a temperature greater than 100°C, which suggests that significant amount of geothermal energy is largely untapped in our planet (Özgür, 2002, Magro et al., 2013). The renewable geothermal energy can be used to provide a wide range of heat sources worldwide, which leads to the rising attention on the investigation and exploitation of unlimited resource of magmatic heat in both academic and industrial communities. Geothermal systems are complex, non-isothermal, and dual phase fluid flow systems (Gardner et al., 2010). The investigations on the record preserved in fluids from the areas of geothermal activity can help constrain heat and groundwater flow, advective heat budgets, hydrothermal processes, as well as monitor volcanic hazards (Hurwitz et al., 2003, Lowenstern and Hurwitz, 2008, Wiersberg et al., 2011, Magro et al., 2013). This is critical for assessing the usefulness of geothermal sites as an energy source over timescales. In addition to geothermal energy, the cleanest, least carbon intensive fossil fuel — natural gas has been served as a useful energy source with the rising demand of energy worldwide (Burruss and Laughrey, 2010, Wen et al., 2015). The study of the origin and post-generation history of conventional and unconventional hydrocarbon in sedimentary basins has been recently drawn much intensive attention. Groundwater has been considered significantly important for hydrocarbon generation, migration and accumulation (Torgersen and Kennedy, 1999), as well as bringing microbes into the previously sterilized subsurface environment to generate biogenic hydrocarbons (Zhou et al., 2005, Schlegel et al., 2011). Moreover, groundwater can dissolve the hydrocarbons and carry them to trapping structures. Therefore, systematic investigation on processes involving fluid flow is paramount not only for understanding Earth evolution, but

also for formulating genetic models and exploration strategies for many of most needed commodities, such as geothermal, hydrocarbon and groundwater. However, due to the complexity of subsurface environments in both geothermal and hydrocarbon systems, the role of groundwater in the transfer of hydrocarbon and geothermal fluid, the interactions between fluids from different sources, and the dominant mechanisms controlling subsurface fluid behaviours in different reservoirs remain controversial.

Noble gases have been proved to be a powerful approach in fluid studies due to the properties of chemical inertness and their low abundance. Noble gas production from natural radioactivity significantly modifies their isotopic signature and provides fluid source and age information (Sano and Wakita, 1985, Smith, 1985, Kennedy et al., 1990). Similarly, small amounts of mantle-derived noble gases or atmosphere-derived noble gases in equilibrium with groundwater, are readily distinguished due to their distinct isotopic signature. Overall, noble gases can be served as ideal geochemical tracers of crustal subsurface fluid dynamics (Pinti and Marty, 1995).

## **1.2 Objectives and thesis layout**

In this dissertation, a brief introduction to the research background, objectives and thesis layout is presented in **Chapter 1** and a corresponding literature review on properties of noble gases, as well as the applications of noble gas as natural tracers in hydrothermal and hydrocarbon systems is provided in **Chapter 2**.

In **Chapter 3** “Methodology”, details on the construction and development of noble gas sample extraction system, and the procedures for noble gas elemental and isotopic analysis are described. Using noble gas and stable isotope geochemical techniques, the origin, migration and interaction of subsurface crustal fluids (i.e. groundwater and natural gas) have been investigated in two different geological settings: (1) a geothermal groundwater field in Krafla,

Iceland; and (2) conventional and unconventional natural gas reservoirs in the Sichuan basin, China.

The objectives of **Chapter 4** “Noble gas and stable isotope characteristics of hydrothermal fluid system, Krafla, Iceland” are to: (1) identify the origin of the fluids; (2) calculate the amount of degassing of noble gases; (3) quantify the mantle input in geothermal fluid; and (4) assess how the main physical processes, such as boiling, steam separation, and re-injection, affect the characteristics of geochemical processes in the Krafla geothermal field.

The objectives of **Chapter 5** “Tracing interaction between hydrocarbon and groundwater systems with noble gases in the central Sichuan Basin, China” are to: (1) identify the sources of hydrocarbons and noble gases; (2) characterize the physical processes responsible for noble gas emplacement into hydrocarbon system during geological timescales; and (3) provide new insights into the evolution of petroleum systems, such as natural gas genesis and transportation, subsurface fluid provenance and fluid flow.

**Chapter 6** summarizes and concludes this dissertation and suggests some further work in future.

## 2 Literature review

This chapter consists of five sections. The first section is a brief introduction to noble gases in subsurface fluids. Then, the characteristics of three different sources (atmosphere, crust and mantle) for noble gases and the physical chemistry of noble gases in fluids will be discussed in the following two sections. The last two sections provide an overview of the applications of noble gases as natural tracers in hydrothermal and hydrocarbon systems.

### 2.1 Noble gases in subsurface fluids

Noble gases, namely helium (He), neon (Ne), argon (Ar), krypton (Kr), and xenon (Xe), have proven to be powerful tools to better understand many geological processes due to their properties of low abundance and chemical inertness (Ozima and Podosek, 2002, Porcelli et al., 2002). For example, noble gas studies play an important role in investigating earthquakes and volcanic activity (Tedesco et al., 1998, Italiano et al., 2001), as well as for reconstructing paleoclimate conditions (Mazor, 1972, Andrews and Lee, 1979, Castro and Goblet, 2003) and interpreting ocean circulation histories (Jenkins and Clarke, 1976).

Due to the continuous increase in energy demands during our daily life, more researchers have focused their studies on much needed natural commodities, such as petroleum, natural gas, groundwater and geothermal energy (Lin et al., 2009, Gardner et al., 2010, Dai et al., 2012, Barry et al., 2013, Zhou et al., 2014, Wen et al., 2017, Byrne et al., 2018, Cao et al., 2018, Wen et al., 2018). The fact that noble gases are unaffected by inorganic or organic chemical reactions and only sensitive to physical processes, such as multi-phase interaction (mixing, diffusion, and phase partitioning), makes noble gases ideal tracers for investigating

the origin and evolution of subsurface fluids in oil and gas systems as well as geothermal fields (Pinti and Marty, 1995, Hilton, 1996, Prinzhofer, 2003, Hunt et al., 2012, Roulleau et al., 2016).

### **2.1.1 The three main physical processes that affect noble gas fractionation**

- Exchange of noble gases between phases

Noble gases are mainly present in three phases: (1) gas phase (atmosphere and gas accumulations); (2) liquid phase (water and oil); and (3) solid phase (minerals, surface adsorption, and hydrates). High noble gas concentrations have been found in hydrocarbon reservoirs, indicating the occurrence of exchange between different phases (gas, water, and oil) (Bosch and Mazor, 1988, Ballentine et al., 1991, Hiyagon and Kennedy, 1992, Elliot et al., 1993, Kennedy et al., 2002, Barry et al., 2017). Since noble gases are more soluble in oil than in water, they are preferentially partitioned into the oil phase compared to the water phase. Another possible exchange between fluid phases and hydrates results in the relative enrichment of heavier noble gases in hydrates, which can be explained by the finding that light noble gases are never stable in hydrates at natural conditions (Dyadin et al., 1997, Prinzhofer, 2013).

- Adsorption/desorption of noble gases on the surface of solids

The property of adsorption for noble gases varies on different surfaces. In organic-rich sedimentary rocks (e.g., shales and cherts), the heavier noble gas species (Kr and Xe) have been shown to preferentially adsorb onto minerals (Podosek et al., 1981). This atmosphere-derived Kr, Xe may be released and added into the hydrocarbon systems at high temperatures, which result in the relative enrichment of Kr and Xe in sedimentary samples (Torgersen and Kennedy, 1999, Zhou et al., 2005).

- Diffusion in liquids or in gas phases

The distribution of noble gases can be altered by diffusion process. Helium has the largest diffusion coefficient in water while xenon's is the lowest. When discussing the diffusion coefficient in the oil phase, the oil composition should be considered (Reid et al., 1977, Jähne et al., 1987). In addition, other parameters, such as rock porosity, tortuosity and permeability are also required for the calculation of diffusion coefficients (Rebour et al., 1997).

### 2.1.2 Properties of each noble gas element

- He

Helium has two stable isotopes ( $^3\text{He}$  and  $^4\text{He}$ ):  $^3\text{He}$  is the primordial helium isotope in origin, which is largely associated with tectonic and volcanic activities during geological evolution (O'Nions and Oxburgh, 1988). In contrast,  $^4\text{He}$  is produced from radioactive decay of U and Th. Measured  $^4\text{He}/^{20}\text{Ne}$  ratios in samples relative to the air ratio (0.032) serves as a sensitive tracer of the degree of atmospheric contamination (Sano et al., 1985, Kipfer et al., 2002, Barry et al., 2013, Wen et al., 2018). If the measured  $^4\text{He}/^{20}\text{Ne}$  ratios are significantly higher than the air ratio, we can assume that the air contaminations in samples is negligible (**Figure 2.1**).

Due to several orders of magnitude difference in  $^3\text{He}/^4\text{He}$  ratios in the crust and mantle,  $^3\text{He}/^4\text{He}$  ratios are used to distinguish between various crustal and mantle sources. Samples from mid-ocean ridge basalts (MORB) have uniform  $^3\text{He}/^4\text{He}$  ratios of  $\sim 8R_a$  (where  $R_a$  is the air  $^3\text{He}/^4\text{He}$  ratio of  $1.4 \times 10^{-6}$ ) (Graham, 2002), whereas the  $^3\text{He}/^4\text{He}$  production ratio in the crust is  $\sim 0.02R_a$  (Mamyryn and Tolstikhin, 1984, Ballentine et al., 2002). In addition, some ocean island basalts (OIB) samples from Hawaii and Iceland are characterized by significantly

high abundance in  $^3\text{He}$  with the  $^3\text{He}/^4\text{He}$  ratios as high as  $30R_a$  (Graham, 2002), suggesting the presence of mantle plumes or thermal upwelling from the deep earth.

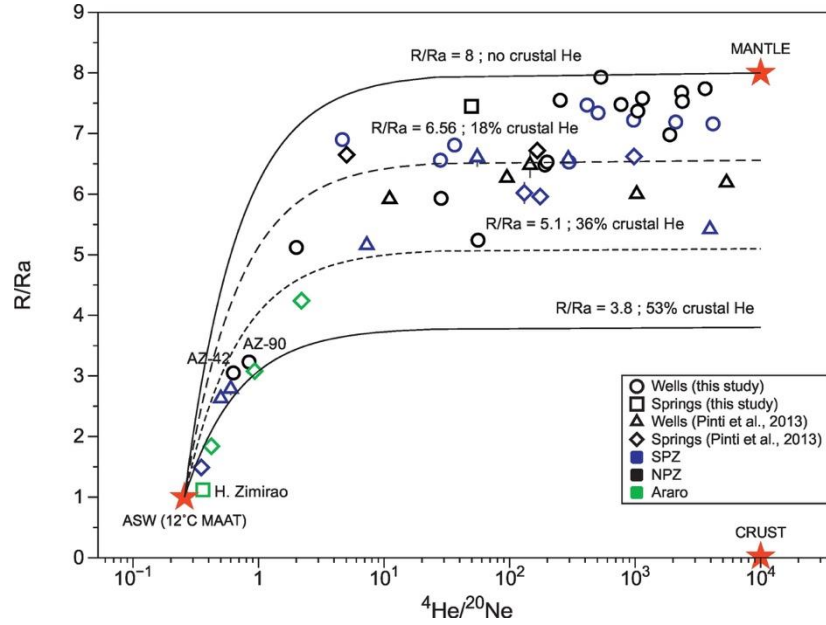


**Fig.2.1.**  $R/R_a$  ratio as a function of  $^4\text{He}/^{20}\text{Ne}$  ratio for collected fluid samples. All data can be explained as a mixing of three components (Air, Crust and Mantle) (from Wen et al. (2018)), where  $R$  is the measured  $^3\text{He}/^4\text{He}$  ratios,  $R_a$  is the air  $^3\text{He}/^4\text{He}$  ratio of  $1.4 \times 10^{-6}$  (Mamyrin et al., 1970, Clarke et al., 1976).

- Ne

Neon has three stable isotopes:  $^{20}\text{Ne}$ ,  $^{21}\text{Ne}$  and  $^{22}\text{Ne}$ .  $^{20}\text{Ne}$  is produced by carbon-burning during stellar nucleosynthesis and was trapped by the Earth during accretion (Clayton, 2007), which resulted in large amounts of  $^{20}\text{Ne}$  in the air. On the contrary, the crust and mantle contribution of  $^{20}\text{Ne}$  can be negligible.  $^{21}\text{Ne}$  and  $^{22}\text{Ne}$  are both nucleogenic, but  $^{22}\text{Ne}$  has a relatively low abundance compared to  $^{21}\text{Ne}$ . Similar to He, air, mantle and crustal Ne component endmember ( $^{20}\text{Ne}/^{22}\text{Ne}_{\text{air}} = 9.80$ ,  $^{21}\text{Ne}/^{22}\text{Ne}_{\text{air}} = 0.029$ ,  $^{20}\text{Ne}/^{22}\text{Ne}_{\text{mntl}} = 12.5$ ,  $^{21}\text{Ne}/^{22}\text{Ne}_{\text{mntl}} = 0.06$ ,  $^{20}\text{Ne}/^{22}\text{Ne}_{\text{crust}} = 0.30$ ,  $^{21}\text{Ne}/^{22}\text{Ne}_{\text{crust}} = 0.52$ ) have been readily defined by

Ballentine (1997) and Ballentine et al. (2002), therefore it is possible to resolve the contribution of atmospheric, mantle and crustal Ne components (**Figure 2.2**).

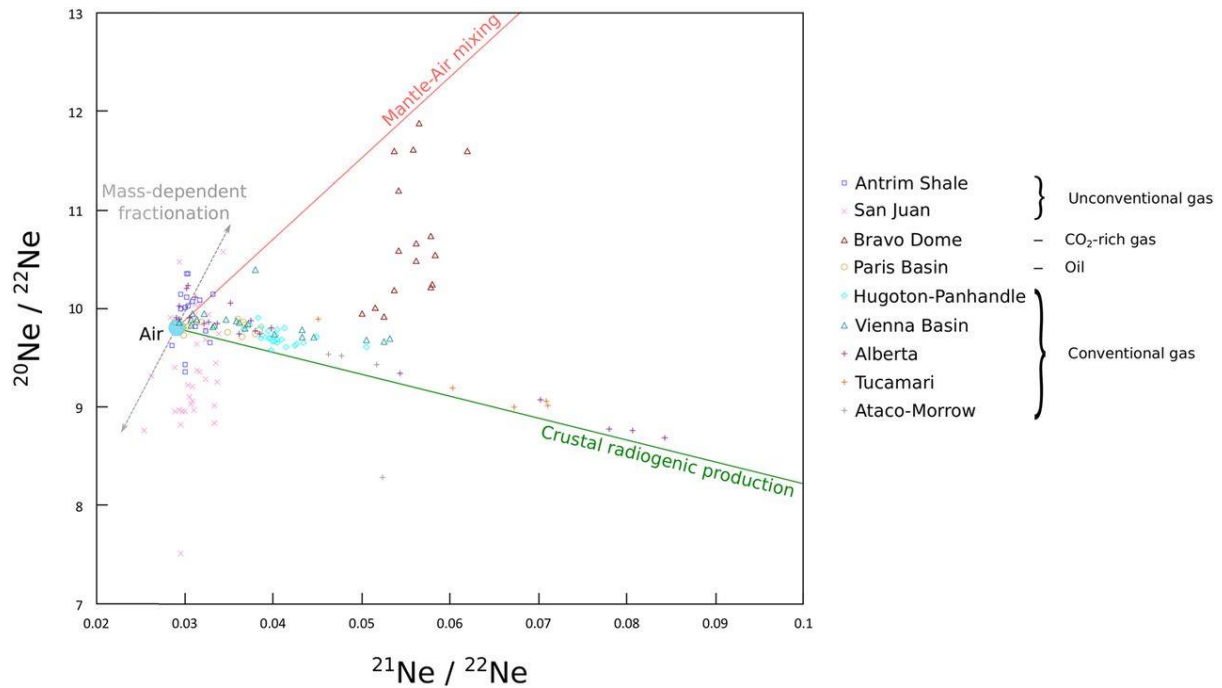


**Fig.2.2.** Neon three-isotope plot for selected noble gas studies of petroleum systems (from Byrne et al. (2018)).

- Ar

Argon has three stable isotopes:  $^{40}\text{Ar}$ ,  $^{38}\text{Ar}$  and  $^{36}\text{Ar}$ .  $^{40}\text{Ar}$  is produced by the radioactive decay of  $^{40}\text{K}$  in the crust while  $^{38}\text{Ar}$  is dominated by the  $\alpha$ -decay of  $^{35}\text{Cl}$  and  $^{37}\text{Cl}$  in the crust.  $^{36}\text{Ar}$  production in the crust is relatively small compared to that of air. Similar to He and Ne, Ar isotopes from different sources can also be calculated by using the three-component end-members.

- Kr/ Xe

Krypton and xenon have six and nine stable isotopes, respectively:  $^{78}\text{Kr}$ ,  $^{80}\text{Kr}$ ,  $^{82}\text{Kr}$ ,  $^{83}\text{Kr}$ ,  $^{84}\text{Kr}$ ,  $^{86}\text{Kr}$ ,  $^{124}\text{Xe}$ ,  $^{126}\text{Xe}$ ,  $^{128}\text{Xe}$ ,  $^{129}\text{Xe}$ ,  $^{130}\text{Xe}$ ,  $^{131}\text{Xe}$ ,  $^{132}\text{Xe}$ ,  $^{134}\text{Xe}$  and  $^{136}\text{Xe}$ . Among them,

$^{84}\text{Kr}$  and  $^{132}\text{Xe}$  are the most abundant isotopes in each group, which accounts for 57 % and 26.89 % of total Kr and Xe abundances in the air, respectively.

## 2.2 Three different sources

Noble gases in crustal fluids are derived from three sources, which are the atmosphere, crust, and mantle (**Figure 2.3**). The distinct isotopic and elemental signatures enable noble gases from various sources to be readily identified (Ozima and Podosek, 2002, Porcelli et al., 2002, Prinzhofer, 2013). Three main terrestrial reservoirs for noble gases are discussed as follows.

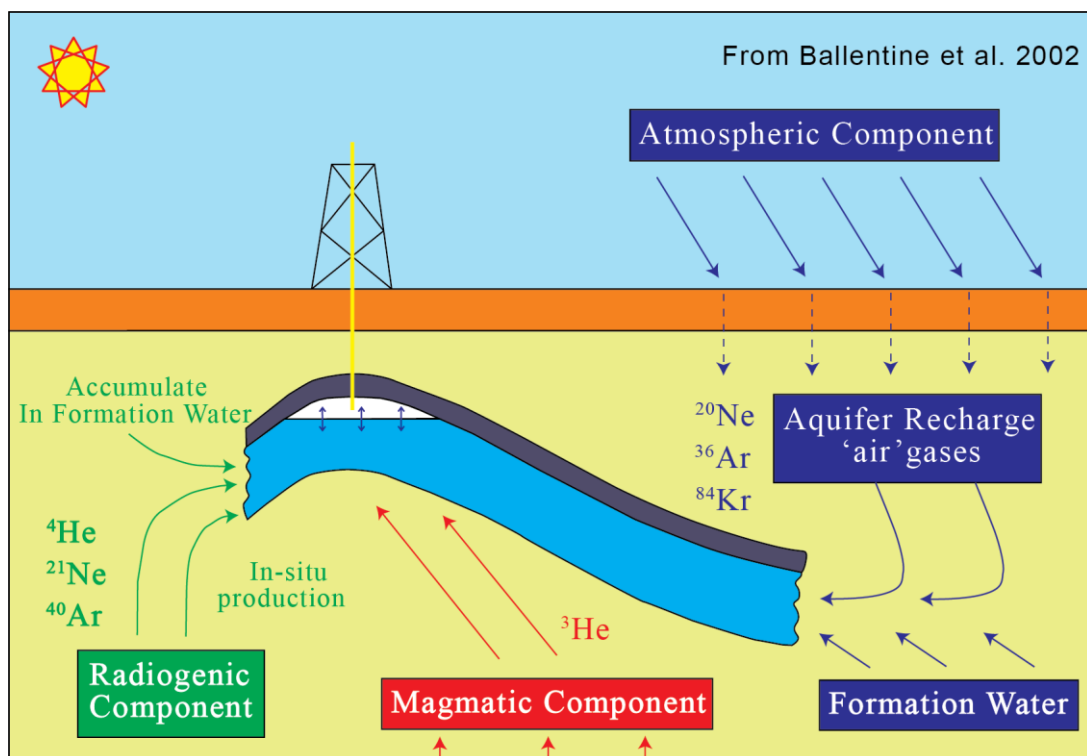


**Fig.2.3.** A schematic conceptual model showing three distinct sources of noble gas isotopes modified in hydrocarbon systems, redrawn from Ballentine et al. (2002).

### 2.2.1 Air Saturated Water (ASW)

Atmosphere derived noble gases (e.g.,  $^{20}\text{Ne}$ ,  $^{36}\text{Ar}$ , and  $^{84}\text{Kr}$ ) are introduced into the subsurface reservoirs by recharge water, which was previously in solubility equilibrium with the atmosphere (Air Saturated Water, ASW).

ASW noble gases are fractionated due to the noble gas solubility differences in water. When the temperature is below 350 K, noble gas solubility in water generally increases with the mass, except that He and Ne have similar solubilities (Crovetto et al., 1982). The concentration of noble gases in the groundwater is associated with several factors including partial pressure of the noble gases in the atmosphere, temperature at which equilibration occurs, groundwater salinity and recharge elevation (Kipfer et al., 2002). Given these quantities, ASW noble gas values can be readily calculated by using Henry's law. However, it should be noted that the values predicted by Henry's law equilibration are commonly lower than empirical measurement data. This phenomenon is referred to gas surplus 'excess air', which most probably results from re-equilibration of entrapped air with water (Heaton and Vogel, 1981, Kipfer et al., 2002). Among these ASW noble gases, neon is found to be most affected by 'excess air' compared to heavier noble gases. In addition, atmospheric noble gas isotopic ratios in water are not significantly affected by the equilibrium partitioning, which means they are the same as those isotopic ratios in air (**Table 2.1**). This is because the isotopes in same noble gas have same properties with respect to solubility.

**Table 2.1.** The noble gas isotope composition of the atmosphere. Data from Porcelli et al. (2002).

Isotope	Relative abundance	Percent Molar Abundance
<sup>3</sup> He	$(1.399 \pm 0.013) \times 10^{-6}$	0.00014
<sup>4</sup> He	$\equiv 1$	100
<sup>20</sup> Ne	$9.80 \pm 0.08$	90.5
<sup>21</sup> Ne	$0.0290 \pm 0.0003$	0.268
<sup>22</sup> Ne	$\equiv 1$	9.23
<sup>36</sup> Ar	$\equiv 1$	0.3364
<sup>38</sup> Ar	$0.1880 \pm 0.0004$	0.0632
<sup>40</sup> Ar	$295.5 \pm 0.5$	99.6
<sup>78</sup> Kr	$0.6087 \pm 0.0020$	0.3469
<sup>80</sup> Kr	$3.9599 \pm 0.0020$	2.2571
<sup>82</sup> Kr	$20.217 \pm 0.004$	11.523
<sup>83</sup> Kr	$20.136 \pm 0.021$	11.477
<sup>84</sup> Kr	$\equiv 100$	57
<sup>86</sup> Kr	$30.524 \pm 0.025$	17.398
<sup>124</sup> Xe	$2.337 \pm 0.008$	0.0951
<sup>126</sup> Xe	$2.180 \pm 0.011$	0.0887
<sup>128</sup> Xe	$47.15 \pm 0.07$	1.919
<sup>129</sup> Xe	$649.6 \pm 0.9$	26.44
<sup>130</sup> Xe	$\equiv 100$	4.07
<sup>131</sup> Xe	$521.3 \pm 0.8$	21.22
<sup>132</sup> Xe	$660.7 \pm 0.5$	26.89
<sup>134</sup> Xe	$256.3 \pm 0.4$	10.43
<sup>136</sup> Xe	$217.6 \pm 0.3$	8.857

The ASW noble gas elemental and isotope compositions in crustal fluids are critical for the understanding of the interactions among various crustal subsurface fluids (groundwater, geothermal fluid, oil and gas). For example, the depletion of atmospheric noble gases caused by subsurface boiling and steam separation processes during fluid ascent has been found in many tectonically active areas, such as Los Humeros Geothermal Field (LHGF), Mexico (Pinti et al., 2017b) and Atlantis II Deep, Red Sea (Winckler et al., 2000). This indicates the occurrence of a thermal event, and it may be possible to reconstruct the thermal histories in those active regions (Ma et al., 2009). In addition, since the hydrocarbon phase is originally free of atmospheric noble gases, the measured atmospheric noble gases in oil and gas reservoirs (Bosch and Mazor, 1988, Hiyagon and Kennedy, 1992, Pinti and Marty, 1995, Zhou et al., 2005, Byrne et al., 2018) resulted from the interactions between groundwater and the hydrocarbon system. This can be used to evaluate the amount of involved aquifer water associated with the hydrocarbon system (Zhou et al., 2005, Barry et al., 2016), as well as to determine the groundwater migration paths and flow rates (Heilweil et al., 2012). Furthermore, atmospheric noble gas ratios (e.g.  $^{20}\text{Ne}/^{36}\text{Ar}$ ) can also be used to identify the extent of air contamination (Barry et al., 2016). If samples have atmospheric noble gas ratios close to those ratios in the air, this may suggest that noble gas compositions are significantly affected by air contributions. This could occur during sampling, delivery or storing procedures. Therefore, these sample data cannot be used to discuss the original system situation (Ballentine et al., 2002, Barry et al., 2016).

### **2.2.2 Crust**

In addition to the atmosphere, the crust, containing approximately 40% of the Earth's radioactive elements (Vinogradov, 1988, Rudnick and Fountain, 1995), serves as an important

reservoir where radiogenic noble gases can be generated. Three most important radiogenic isotopes in the crust are  $^4\text{He}^*$ ,  $^{21}\text{Ne}^*$  and  $^{40}\text{Ar}^*$ , where crustal noble gases are denoted with a “\*” notation. Among these,  $^4\text{He}^*$  is produced by spontaneous  $\alpha$ -decay of  $^{235}\text{U}$ ,  $^{238}\text{U}$  and  $^{232}\text{Th}$ , while  $^{40}\text{Ar}^*$  is generated due to the electronic capture of  $^{40}\text{K}$  (Ballentine and Burnard, 2002, Ozima and Podosek, 2002). On the other hand,  $^{21}\text{Ne}^*$  is mainly produced by reactions between  $\alpha$  particles (derived from U-Th decay) and O, Mg and F nuclei in crustal rocks (Wetherill, 1954).

Crustal noble gases are originally produced within the minerals/rocks, and then subsequently introduced into various subsurface crustal fluid systems. The crustal radiogenic noble gas concentrations and elemental ratios in fluids are dependent on several factors, such as the content of U, Th, and K in the source and/or host rocks, the production rates and release properties of different noble gases as well as the degree of mixing and interaction among various crustal fluids (Zartman et al., 1961, Torgersen et al., 1989, Ballentine et al., 1994, Ballentine and O’Nions, 1994, Pinti and Marty, 1995, Castro et al., 1998). For instance, some researchers have found that  $^4\text{He}^*$  is more easily released than  $^{40}\text{Ar}^*$  at low temperatures (Mamyrin and Tolstikhin, 1984, Elliot et al., 1993, Ballentine and Burnard, 2002), which can result in the higher  $^4\text{He}/^{40}\text{Ar}^*$  ratios in low temperature bacterial gases compared to those in high temperature thermogenic gases. Therefore, the ratios of crustal radiogenic isotopes (e.g.  $^4\text{He}/^{21}\text{Ne}^*$ ,  $^4\text{He}/^{40}\text{Ar}^*$ , and  $^{21}\text{Ne}^*/^{40}\text{Ar}^*$ ) are regarded as powerful tools to trace the release temperatures (Torgersen and Clarke, 1985, Torgersen et al., 1989, Baxter et al., 2002). Furthermore, radiogenic noble gas isotopes in hydrocarbon systems can be used to quantify the concentrations of  $^4\text{He}^*$  in the involved water phase, allowing the estimation of the subsurface fluid residence time (Zhou et al., 2005, Zhou and Ballentine, 2006, Schlegel et al., 2011, Barry et al., 2017). In addition, the studies on the  $^4\text{He}$ /heat flux ratio in the crust reservoirs have been

used to reconstruct the past thermal events and tectonic activities occurred in regions during geological timescale (Stute et al., 1992, Castro and Goblet, 2005, Castro et al., 2007).

### 2.2.3 Mantle

The Earth's mantle serves as another important reservoir for noble gas generation, accumulation and transportation. The primordial mantle-derived noble gases were originally trapped during the early accretion of the Earth (Ozima and Podosek, 2002), which are characterized by distinct isotopic signatures. As described in the He section, helium has been shown to be an ideal tracer of mantle contribution due to its low abundance in the air ( $5.24 \times 10^{-6} \text{ cm}^3\text{STP}({}^4\text{He})/\text{cm}^3$ ) and unambiguous crustal and mantle  ${}^3\text{He}/{}^4\text{He}$  ratios. However, it is difficult to quantify the mantle-derived helium in samples with significantly low  ${}^3\text{He}/{}^4\text{He}$  values ( $0.1\text{Ra} > {}^3\text{He}/{}^4\text{He} > 0.02\text{Ra}$ ). Due to some other possibilities, such as high local Li concentrations (small amounts of  ${}^3\text{He}$  can be produced associated with neutron interactions with Li) or cosmogenic  ${}^3\text{He}$  contributions cannot be ruled out. In these cases, high  ${}^{20}\text{Ne}/{}^{22}\text{Ne}$  ratios,  ${}^{21}\text{Ne}/{}^{22}\text{Ne}$  ratios and  ${}^{40}\text{Ar}/{}^{36}\text{Ar}$  ratios should also be considered to assist in discriminating mantle contributions.

In addition, mantle volatiles (e.g.  ${}^3\text{He}$  and  $\text{CO}_2$ ) can migrate through deep-seated faults and fractures, and are subsequently trapped in shallow crust for substantial geological periods, which can be used to investigate the geological evolution of subsurface fluid systems (Sherwood Lollar et al., 1997, Gilfillan et al., 2009, Zhou et al., 2012). For example, Sherwood Lollar et al. (1997) proposed that magmatic fluids have  $\text{CO}_2/{}^3\text{He}$  ratios ranging between  $10^9$  and  $10^{10}$  (**Figure 2.4**).  $\text{CO}_2/{}^3\text{He}$  ratios higher than this range suggest that mantle contributions

are negligible in those reservoirs. On the other hand, values below this range may be accounted for the partial loss of mantle CO<sub>2</sub>, dilution possibly by CH<sub>4</sub>/N<sub>2</sub> and/or crustal CO<sub>2</sub> contribution.

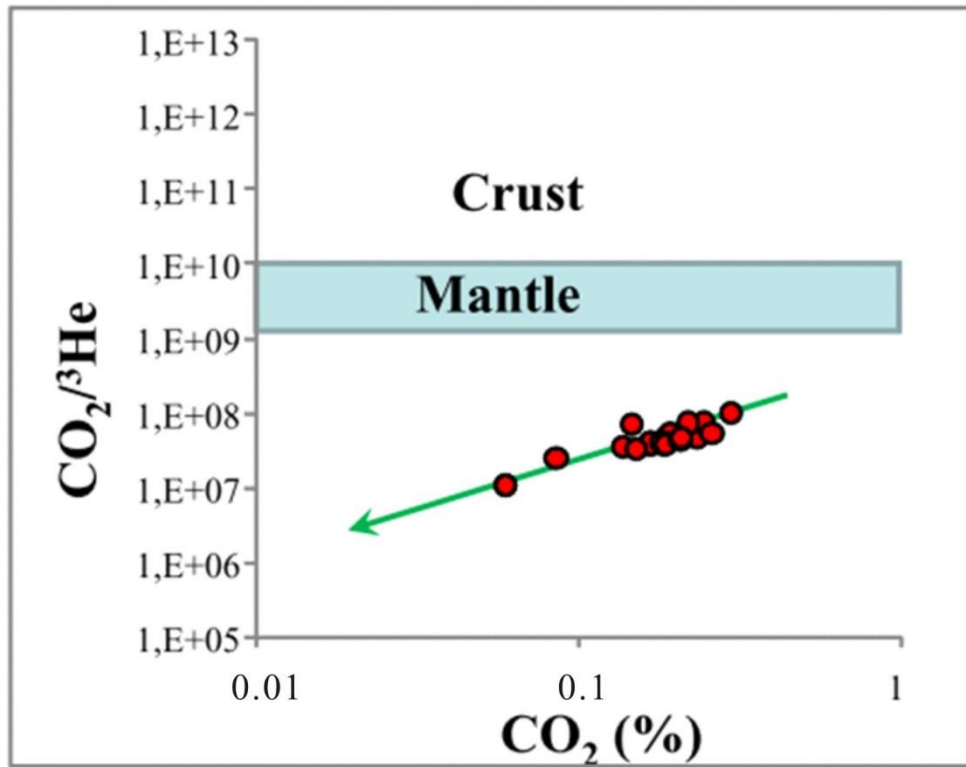


**Fig.2.4.**  $\text{CO}_2/{}^3\text{He}$  vs. fraction of  $\text{CO}_2$  (from Prinzhofer (2013)). Figure shows the range of  $\text{CO}_2/{}^3\text{He}$  values found in magmatic samples. Above this range,  $\text{CO}_2$  is crustal-derived.  $\text{CO}_2/{}^3\text{He}$  values below this range may account for the loss of  $\text{CO}_2$ .

## 2.3 Physical chemistry of noble gases in fluids

### 2.3.1 Henry's law

Assuming ideal gas behaviour in both gas and liquid phases, the concentration of each noble gas in the liquid phase is directly proportional to the partial pressure of that gas in the gas phase, which can be expressed using Henry's law:

$$P_i = K_i x_i \quad 2.1$$

Where  $K_i$  is Henry's constant,  $P_i$  is the partial pressure of gas  $i$ ,  $x_i$  is the mole fraction of  $i$  in solution. Henry's constants are subjected to the composition in each phase and are temperature and salinity dependent. This equation makes it possible to thermodynamically identify the relationships between noble gases in both gas and liquid phases, thereby better understanding the geological evolutions in different systems.

Due to the fact that ideality is not common in most geological systems, Henry's law has to be modified for describing non-ideal behaviour in the gas and fluid phases. Gas-phase fugacity coefficient and the liquid-phase activity coefficient must be considered.

$$\Phi_i P_i = \gamma_i K_i x_i \quad 2.2$$

Where  $\Phi_i$  and  $\gamma_i$  are the gas phase fugacity coefficient and liquid phase activity coefficient respectively.

### 2.3.2 Non-ideality in the gas phase

To calculate gas phase fugacity coefficient  $\Phi_i$ , the real molar volume of the gas ( $V_m$ ) must be taken into consideration, which can be formulated from empirically derived coefficients (Dymond and Smith, 1980, Ballentine et al., 2002) (**Table 2.2**) for the virial equation of state  $V_m$ ,

$$PV_m / RT = 1 + B(T) / V_m + C(T) / V_m^2 \quad 2.3$$

Where P is the total pressure, R is the gas constant, T is the temperature, B(T) and C(T) are the temperature dependent second and third order virial coefficients, respectively. By rearranging equation 2.3 to a third-order polynomial,  $V_m$  can be derived using Newton's iterative method of approximation. Then the molar volume value is used in turn to calculate the fugacity coefficient,

$$\Phi(P, T) = \exp[B(T) / V_m + (C(T) + B(T)^2 / 2V_m^2)] \quad 2.4$$

Coefficients values (B(T), C(T)) with respect to hydrostatic pressures and temperatures with a geothermal gradient of 0.03 K/m are documented in **Table 2.2**, together with the calculated gas phase fugacity coefficient. These data are from Dymond and Smith (1980). **Figure 2.5** shows a plot of the fugacity coefficients for the pure noble gases as a function of depth.

**Table 2.2.** Noble gas virial and fugacity coefficients as a function of depth.

		<b>Helium</b>				<b>Neon</b>			<b>Argon</b>		
Depth	P	T	B(T)	C(T)	$\Phi$	B(T)	C(T)	$\Phi$	B(T)	C(T)	$\Phi$
(m)	(atm)	(K)			(P,T)			(P,T)			(P,T)
300	29	298	11.74	75.1	1.01	11.42	221	1.01	-15.5	991	0.982
1200	116	323	11.58	72.3	1.05	11.86	224	1.05	-11.2	1230	0.964
2000	194	348	11.43	94.8	1.08	12.21	224	1.09	-7.14	959	0.975
2800	271	373	11.35	90.5	1.1	12.52	224	1.12	-3.84	918	1
3700	358	398	11.24	93.8	1.13	12.86	105	1.15	-1.08	877	1.03
4500	436	423	11.07	109.6	1.15	13.1	197	1.18	1.42	833	1.07
		<b>Krypton</b>				<b>Xenon</b>					
Depth	P	T	B(T)	C(T)	$\Phi$	B(T)	C(T)	$\Phi$			
(m)	(atm)	(K)			(P,T)				(P,T)		
300	29	298	-52.36	2612	0.940	-130	6069	0.850			
1200	116	323	-42.78	2260	0.846	-110	5306	0.804			
2000	194	348	-35.21	1076	0.839	-94.5	4635	0.883			
2800	271	373	-28.86	1942	0.861	-81.2	4115	0.888			
3700	358	398	-23.47	1842	0.894	-70.1	3739	0.891			
4500	436	423	-18.82	1759	0.93	-60.7	3469	0.886			

Taken from Ballentine et al. (2002). Original data from Dymond and Smith (1980).

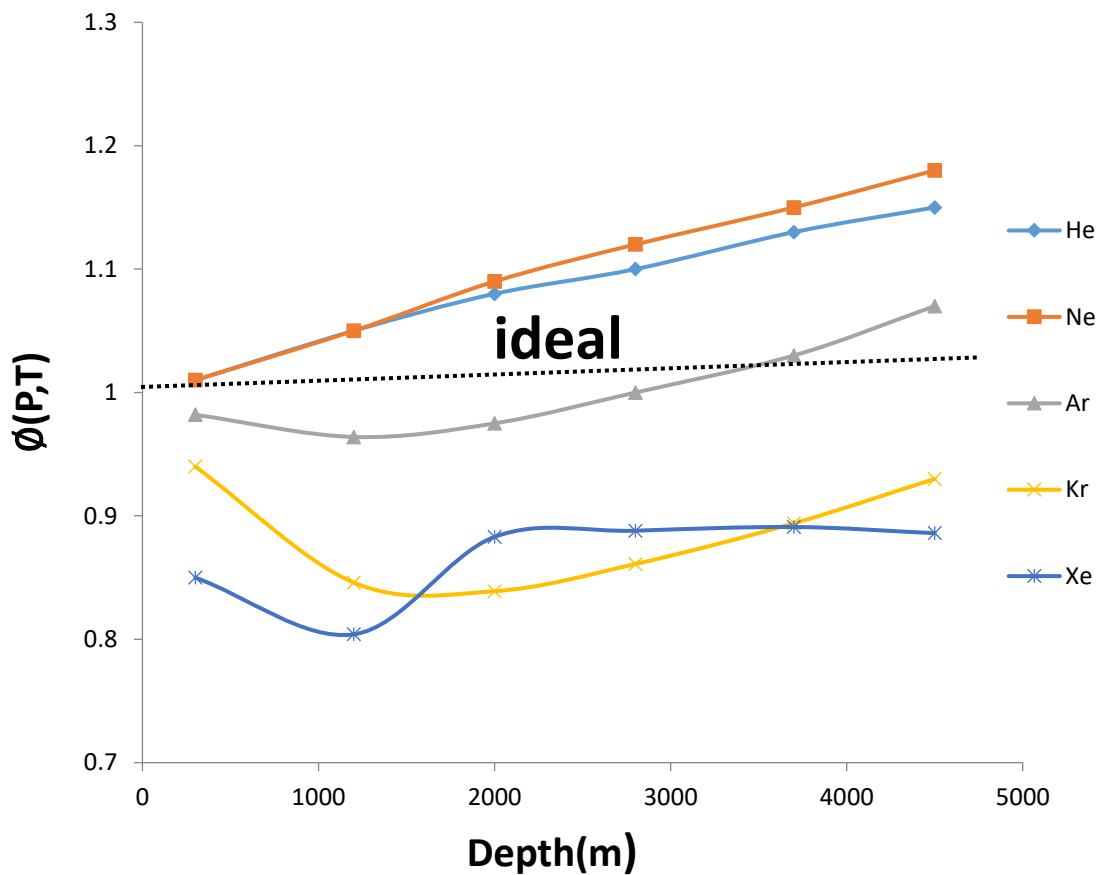


**Fig.2.5.** Noble gas fugacity coefficients as a function of depth assuming temperature gradient of 0.03 K/m and hydrostatic pressure. Redrawn from Ballentine, Burgess & Marty (Ballentine et al., 2002).

### 2.3.3 Non-ideality in the liquid phase

The potential deviation from ideality (i.e. the activity coefficient) for the liquid phase result from additional solute particles in solution. The effect of electrolytes on gas solubility can be identified using the Setschenow equation:

$$\ln\left[\frac{S_i^o(T)}{S_i(T)}\right] = CK_i(T) \tag{2.5}$$

where  $C$  is the molar concentration of the salt in the solution,  $S_i^\circ(T)$  is the solubility of the non-electrolyte  $i$  in pure water at a specified temperature  $T$ ,  $S_i(T)$  is the solubility of non-electrolyte  $i$  in the saline solution at the same temperature  $T$ , and  $k_i(T)$  is the temperature-dependent Setschenow coefficient.

By considering the relationship between Setschenow equation and the Henry's law equation, liquid phase activity coefficient  $\gamma_i$  can be expressed as:

$$\gamma_i = \exp[Ck_i(T)] \quad 2.6$$

This shows that if the concentration  $C$  approaches 0, liquid phase activity coefficient  $\gamma_i$  moves towards 1 (i.e. ideality in the water phase). The negative value of  $k_i(T)$  can result in the increase of solubility while the positive value of  $k_i(T)$  causes the decrease of solubility.

Smith and Kennedy (1983) had measured noble gas solubilities in 0 to 5.2 molar sodium chloride solutions between 273 and 338 K. The coefficients and equation for the experiments are summarized in **Table 2.3**. **Figure 2.6** shows the correlations between noble gas Setchenow coefficients  $k_i$  and temperature  $T$ . Similar thermal trend with respect to noble gas Setchenow coefficients has been observed with the increase of temperature ranging from 273 to 338 K. Among them, only  $k_{\text{He}}$  reaches the lowest value over this temperature range, with the number of 0.2369 at around 315 K.

**Table 2.3.** Noble gas Setchenow coefficients,  $k_i(T)$ .

Species	G1	G2	G3
He	-10.0810	15.1068	4.8127
Ne	-11.9556	18.4062	5.5464
Ar	-10.6951	16.7513	4.9551
Kr	-9.9787	15.7619	4.6181
Xe	-14.5524	22.5255	6.7513

Constants from Smith and Kennedy (1983) to fit  $K_i(T) = G1 + G2/(0.01T) + G3\ln(0.01T)$ , where T is temperature in Kelvin and salinity is in units of mol<sup>-1</sup>

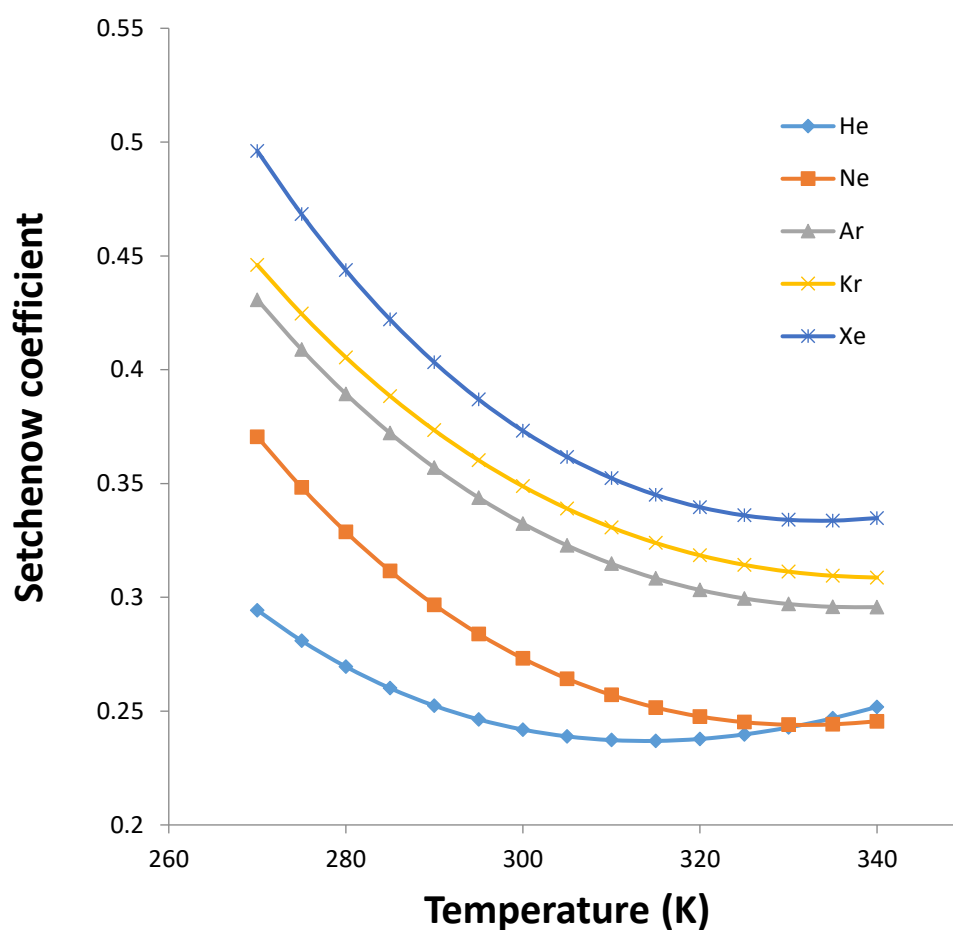


**Fig.2.6.** Noble gas Setchenow coefficients as a function of T. Redrawn from Smith and Kennedy (1983).

### 2.3.4 Noble gas solubility measurements

#### Solubility in pure water

The non-ideality is associated with several parameters, such as pressure, temperature and composition of each phase. Noble gases in a binary phase system will partition in their individual way in order to reach equilibrium. Therefore, the determination of Henry's constants of each noble gas is critical for the characterization of noble gas partition in different phases. Crovetto et al. (1982) measured the noble gas solubility (Ne, Ar, Kr, and Xe) in a pure water system over a range of temperatures and pressures while values for helium were used by Smith (1985). Coefficients and equations for deriving Henry's constants are given in **Table 2.4**. The relationships between Henry's constants and temperature are shown in **Figure 2.7**. Notably, He has the largest Henry's constants at low temperatures than the other noble gases. However, there is a significant decrease in Henry's constants with the increase of temperature.

**Table 2.4.** Henry's constants for noble gases in water.

Species	A <sub>0</sub>	A <sub>1</sub>	A <sub>2</sub>	A <sub>3</sub>
He	-0.00953	0.107722	0.001969	-0.043825
Ne	-7.259	6.95	-1.3826	0.0538
Ar	-9.52	8.83	-1.8959	0.0698
Kr	-6.292	5.612	-0.8881	-0.0458
Xe	-3.902	2.439	0.3863	-0.221

Taken from Ballentine et al. (2002). Coefficients for Ne, Ar, Kr and Xe from Crovetto et al. (1982) to fit the equation:  $\ln(K_i) = A_0 + A_1/(0.001T) + A_2/(0.001T)^2 + A_3/(0.001T)^3$ . Where  $K_i$  is Henry's constant in GPa. Coefficients for He are from Smith (1985) to fit the equation:  $\ln(F_{He}) = A_0 + A_1/(0.001T) + A_2/(0.001T)^2 + A_3/(0.001T)^3$  where  $F_{He} = (X_{He}/X_{Ar})_{liquid}/(X_{He}/X_{Ar})_{gas}$ .  $X$  is the mole fraction.  $T$  is temperature in Kelvin. 1GPa = 9870 atm. For water,  $K_i(atm) = 55.6 K_i^m (atm Kg/mol)$ , Where  $K_i^m$  is Henry's Coefficients expressed in terms of molality.

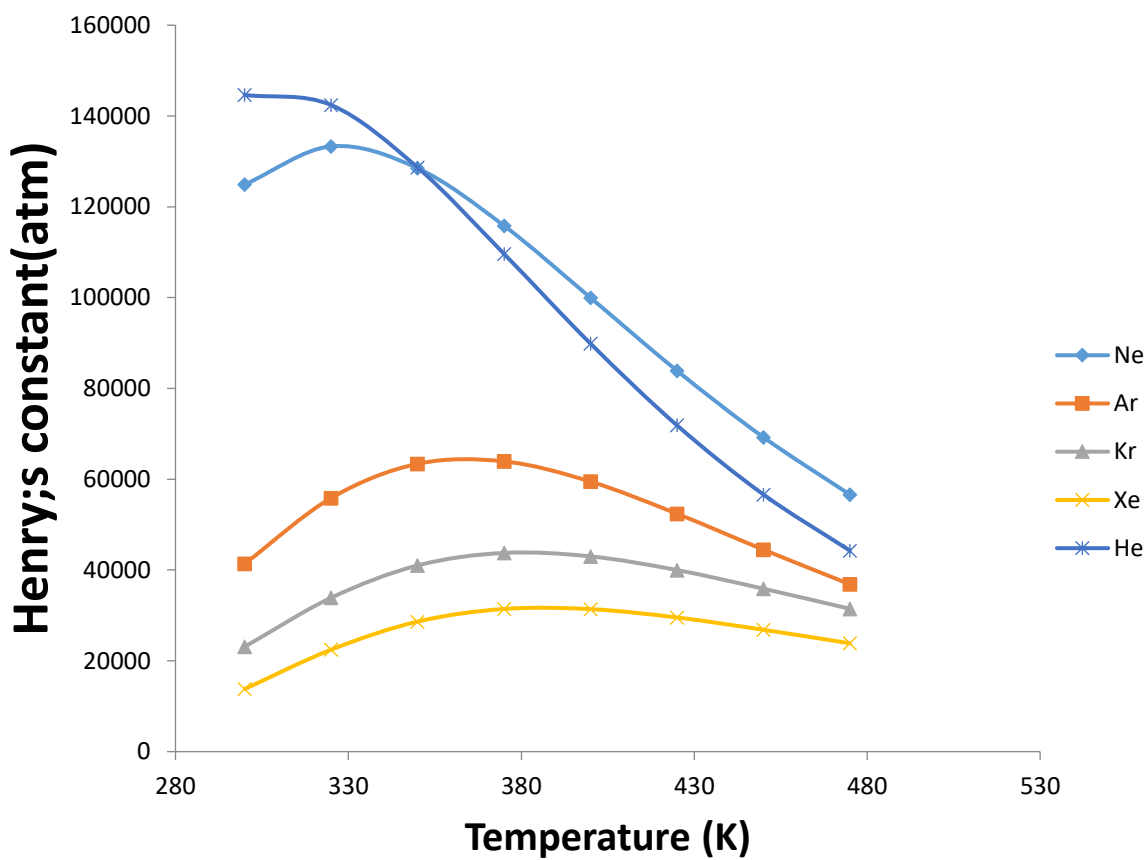


**Fig.2.7.** Henry's coefficients for noble gases in water as a function of temperature. The temperatures range from 273K to the critical point of water. Redrawn from Ballentine et al. (2002).

## 2.4 Noble gases as natural tracers in hydrothermal systems

### 2.4.1 Introduction

Geothermal reservoirs have been found in some tectonically active areas, such as subduction zones (e.g., Turkey (Özgür, 2002)), oceanic ridges (e.g., Iceland (Sano et al., 1985)), and sites of continental rifting (e.g., eastern France (Laplaige et al., 2005) ). Hydrothermal fluids are typically meteoric freshwater containing atmospheric noble gases dissolved during recharge. As the water circulates in the geothermal reservoir, radiogenic derived noble gases  $^4\text{He}$ ,  $^{40}\text{Ar}^*$  are introduced into the water during continuous high-temperature water-rock interactions (Pinti et al., 2013). Furthermore, mantle derived  $^3\text{He}$  which provides heat from magma chamber to geothermal systems (Mazor and Truesdell, 1984, Kennedy et al., 1985) is also observed in geothermal fluids (**Figure 2.8**). The presence of noble gases from three different sources can provide new insights into subsurface fluid evolution (e.g. fluid origins, fluid flow paths, and fluid circulation).

### 2.4.2 Noble gas as fluid tracers

The ascent of super-heated fluid brings it into the relatively low-pressure area, resulting in the occurrence of boiling and steam phase separation. Subsequently, noble gases are continuously lost from the liquid phase into the vapor phase. This can be explained by the fact that noble gases are characterized by low solubilities in freshwater, particularly at high temperature (Crovetto et al., 1982). Eventually, the noble gas compositions in the geothermal fields are fractionated relative to their original composition, as suggested by Mazor and Truesdell (1984), Kennedy et al. (1988) and Winckler et al. (2000).

Noble gas fractionation in the geothermal system can be described by fractionation factors F(i):

$$F(i) = [(i / {}^{36}\text{Ar})_{\text{sample}} / (i / {}^{36}\text{Ar})_{\text{air}}] \quad 2.7$$

Where i represents the abundance of measured atmospheric noble gas isotope (such as  ${}^{20}\text{Ne}$ ,  ${}^{84}\text{Kr}$ , and  ${}^{132}\text{Xe}$ ).

The measured atmospheric noble gas abundances are normalized to the air abundances, with  ${}^{36}\text{Ar}$  as the reference isotope. The F-value is critical to obtain the information on the relative enrichment or depletion with respect to the original ASW values (Mazor and Truesdell, 1984, Pinti et al., 2013, Roulleau et al., 2016). Initial F values are expected to be the same as ASW compositions. Then with the ongoing of the boiling process, lighter noble gases are preferentially partitioned into the vapor phase compared to heavier noble gases, leading to the relative enrichment of heavier noble gases in the residual liquid (Kennedy et al., 1988, Birkle et al., 2016, Roulleau et al., 2016, Wen et al., 2018). This is due to the fact that lighter noble gases are less soluble in water than heavier noble gases (Crovetto et al., 1982, Smith and Kennedy, 1983).

In addition to natural physical processes occurring in geothermal sites, some anthropogenic activities, such as re-injection, are also responsible for the final gas compositions measured in fluids (Pinti et al., 2017b, Wen et al., 2018). In order to maintain the pressure of the reservoir, some colder used brines or even waste water are injected back into geothermal systems. The injectate containing some air bubbles trapped during the re-injection process will significantly affect the noble gas elemental and isotopic signatures in the fluids.

Overall, the applications of noble gas geochemistry in geothermal systems had been proven to be useful tools to identify and quantify the physical processes such as boiling, steam

separation and invasion of re-injected brines, as well as to determine the occurrence of past thermal events.

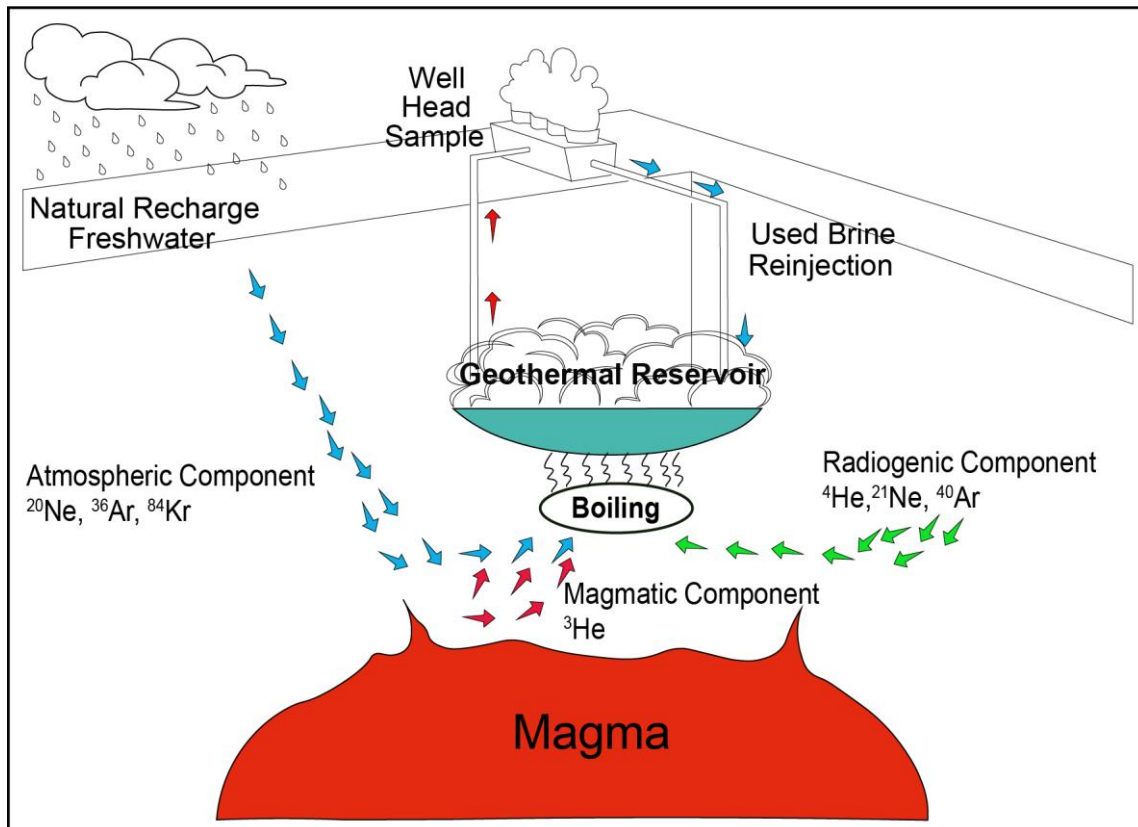


**Fig.2.8.** Cartoon illustrating a geothermal reservoir in a deep convective hydrothermal system (modified from Pinti et al. (2017a)). Three different sources of noble gases are shown in figure. The ascent of fluid will cause the onset of boiling behaviour once hot fluid reaches depth levels of lower hydrostatic pressure.

## **2.5 Noble gases as natural tracers in hydrocarbon systems**

### **2.5.1 Introduction**

The application of geochemical techniques for the study of the generation, migration of hydrocarbon in sedimentary basins has been widely recognized by the academic community over the last several decades (Dow, 1974, Stahl, 1978, Schoell, 1980, Schoell, 1983, Zhu et al., 2007, Dai et al., 2009). For example, the analysis of biomarker and stable isotopes (such as  $^{13}\text{C}$ ) provides the information about the types of source rock, and thermal maturity, allowing further investigations on sedimentary basin burial and thermal histories (Schoell, 1984, Zhu et al., 2007, Dai et al., 2012). However, some other questions, such as secondary migration processes and pathways, and the relationship between groundwater flow and hydrocarbon transport and accumulation, remain elusive. The properties of low abundance and chemical inertness allows noble gases to serve as robust tools for tracing subsurface fluid flow, as well as identifying and quantifying the role of groundwater that interacted with hydrocarbon generation and migration (Ballentine et al., 1991, Pinti and Marty, 1995, Prinzhofer et al., 2010). The investigations of the hydrocarbon generation, migration, as well as subsurface crustal fluid interactions in the hydrocarbon reservoirs can not only provide some useful strategies on the exploration and production of petroleum sources, but also raise the public awareness of associated environmental issues.

### 2.5.2 Noble gases exchange between groundwater and hydrocarbon systems

Demaison and Huizinga (1994) suggested that the secondary migration can take place laterally for up to hundreds of kilometres and vertically through kilometres of groundwater-saturated strata, which has a significant influence on noble gas signatures in the hydrocarbon system. Since noble gases are more soluble in oil and gas than in water (Crovetto et al., 1982), noble gases dissolved in water preferentially partition into the oil and gas phase during the fluid interaction, resulting in strong depletion of noble gases in the groundwater that interacted with a natural gas or oil phase (Ballentine et al., 1996).

Hydrocarbon systems can be divided into conventional hydrocarbon system and unconventional hydrocarbon system. Compared to conventional natural gas reservoirs (e.g., sandstone or carbonate), unconventional systems (e.g. shale) are generated and produced in situ, with little secondary migration taken place, suggesting noble gas signatures are expected to be less affected by basin scale fluid flow regimes (Wen, 2017). Byrne et al. (2018) has documented  $^4\text{He}$  concentrations measured in several cases (conventional and unconventional systems). **Figure 2.9** shows conventional systems have relatively higher  $^4\text{He}$  concentrations compared to unconventional systems, although there is an overlap between these two groups. This can be accounted for by the addition of radiogenic noble gases from large-scale aquifer systems during the secondary migration (Ballentine et al., 1991, Ballentine et al., 1996).

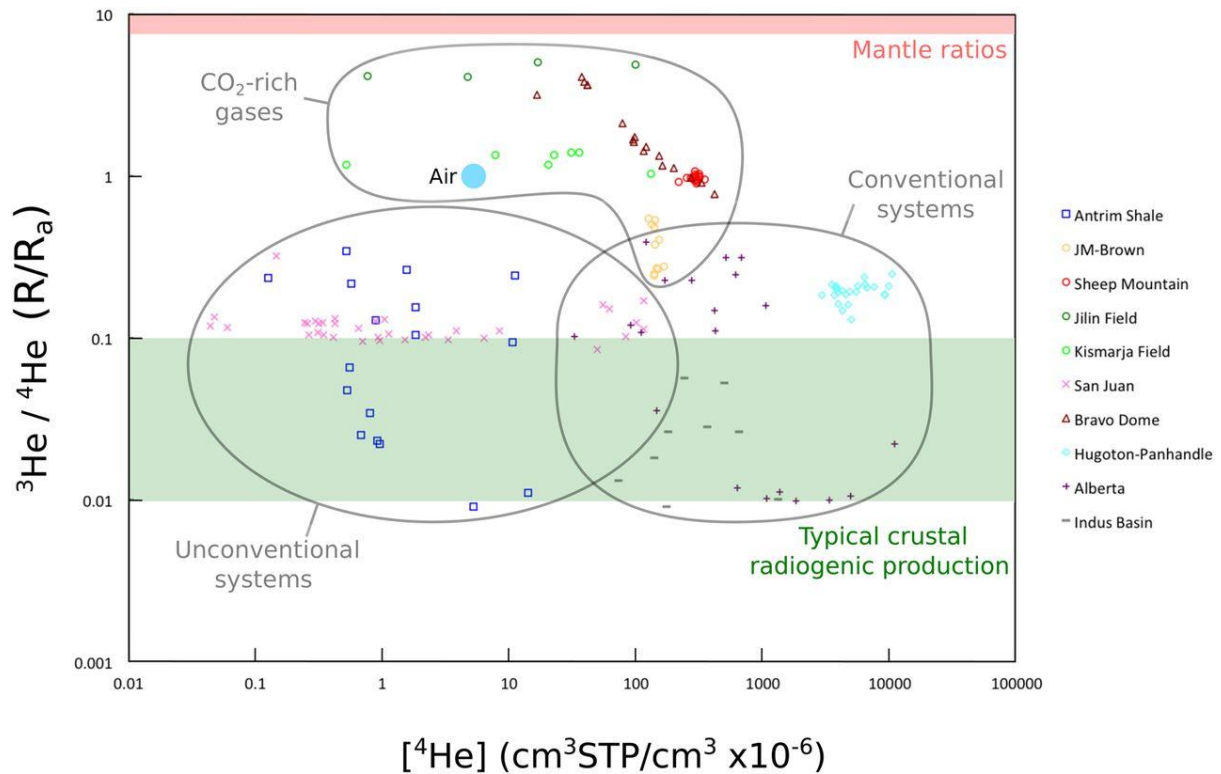


**Fig.2.9.**  $^3\text{He}/^4\text{He}(R/R_a)$  vs.  $^4\text{He}$  concentration measurements from selected noble gas studies of petroleum systems (from Byrne et al. (2018)). Conventional systems have relatively higher  $^4\text{He}$  concentrations compared to unconventional systems.

In addition, based on the fact that the amount of  $^4\text{He}$  in the groundwater system is mainly dependent on in situ  $^4\text{He}$  production and  $^4\text{He}$  from an external crustal flux, the age of groundwater associated with hydrocarbon reservoirs can be possibly estimated. Cases from the San Juan Basin coalbed methane gas field in New Mexico, USA, the Magnus oilfield in the UK North Sea and the Hugoton-Panhandle giant gas field that spans Kansas, Texas and Oklahoma, USA have been selected for using  $^4\text{He}$  to evaluate the age of associated groundwater in Zhou and Ballentine (2006).

### 2.5.3 Noble gas as sensitive tracers for identifying physical processes

Noble gases are sensitive to any physical mechanisms occurred within a hydrocarbon system during geological timescales. For example, isotopic fractionation of  $^{20}\text{Ne}/^{22}\text{Ne}$  and  $^{38}\text{Ar}/^{36}\text{Ar}$  ratios have been observed in the San Juan basin, suggesting the occurrence of diffusion behaviour caused by noble gas concentration gradients created during gas production (Zhou et al., 2005). The relationship between water-derived  $^{20}\text{Ne}/^{36}\text{Ar}$  and crustal  $^4\text{He}/^{40}\text{Ar}^*$  can be interpreted by an open system Rayleigh fractionation degassing model. However, the measured  $^{20}\text{Ne}$  concentrations are significantly lower than predicted values by Rayleigh fractionation-degassing model, suggesting gas that interacted with groundwater has possibly been diluted by desorbed coalbed methane (**Figure 2.10**). Combined with the local gas production histories, the amount of water associated with gas production can be derived at each well (Ballentine et al., 1991, Zhou et al., 2005)

Furthermore, in order to determine the extent of hydrocarbon and groundwater interactions, three possible processes that may take place during hydrocarbon-groundwater exchange have been summarized by Barry et al. (2016): (i) total degassing model, which assumes all noble gases have lost from the water phase;(ii) equilibrium model, which means groundwater and hydrocarbon phase reached an equilibrium at reservoir P, T and salinity; and (iii) open and closed system gas-stripping models. There is no gas loss in the closed system model while noble gases are accumulated in the reservoir due to groundwater gas stripping processes.

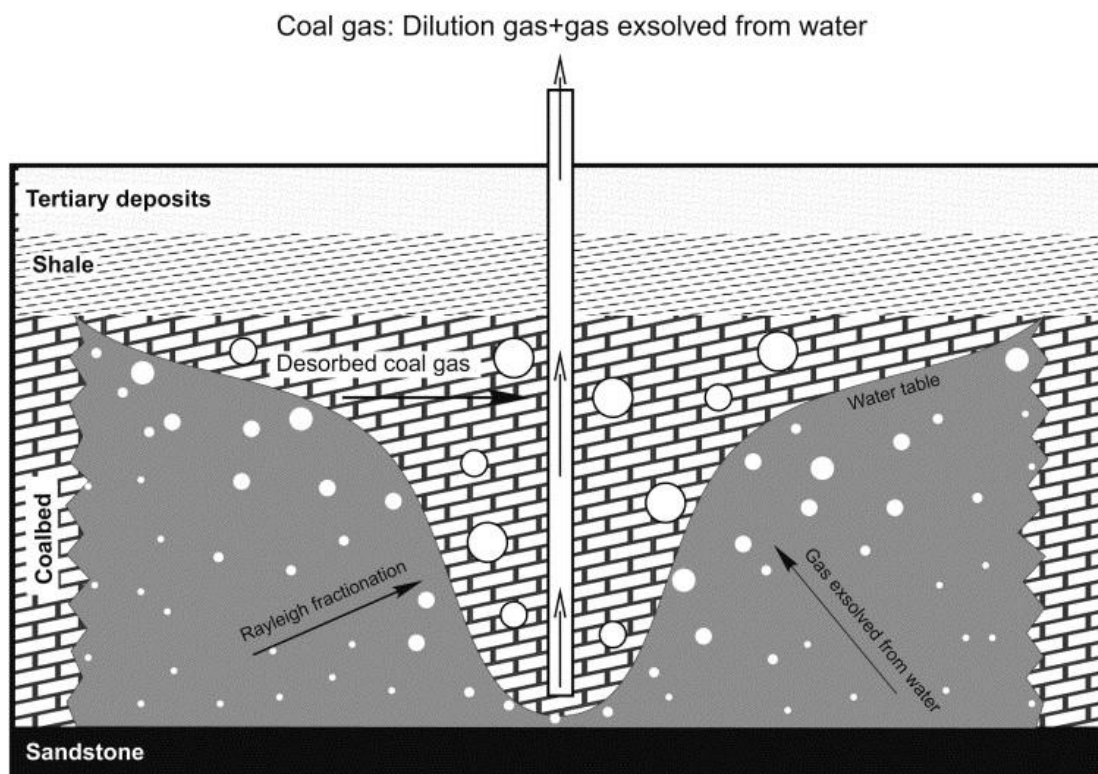


**Fig.2.10.** Schematic of Rayleigh fractionation and dilution processes. Noble gases are continuously lost from the groundwater phase into a gas phase, which is controlled by Rayleigh fractionation. At the same time, these noble gases in the gas phase can be diluted by other gases desorbed from coalbed (from Zhou et al. (2005)).

#### 2.5.4 Enrichment of heavier noble gases

The relative enrichment of Kr/Xe with respect to Ar has been observed in various systems, such as the Michigan basin, Sleipner Vest gas field and Elk Hills oil field (Torgersen and Kennedy, 1999, Zhou et al., 2005, Gilfillan et al., 2008, Barry et al., 2016). Pioneering studies suggested that atmosphere-derived heavy noble gases (Kr and Xe), can be adsorbed and trapped onto organic-rich sediments, which can be released into the fluid system during thermal evolution. This results in the observed ‘excess’ heavier noble gases (Kr/Xe) with an atmospheric isotopic composition (Torgersen and Kennedy, 1999).

## 3 Methodology

This chapter gives a detailed description of the construction and development of noble gas sample preline, the procedures for noble gas elemental and isotopic analysis at the subsurface fluid isotope geochemistry laboratory, Lancaster Environment Centre, Lancaster University, which constitutes a major part of this PhD thesis.

### 3.1 Introduction to noble gas mass spectrometry

A noble gas mass spectrometer is normally composed of three sections: ion source, analyzer and collector (**Figure 3.1**).

- The ion source is where ions are generated, formed into a beam, given a specific energy and directed towards the next part of the mass spectrometer. Currently, the Nier-type sources and Baur-Signer sources are two widely used ion sources on noble gas mass spectrometer. The principle is to use a hot filament to create an electron beam which is capable of ionizing gas molecules in an ionization chamber by electron bombardment interaction.
- The analyser is where the single ion beam is divided into beams based on various  $m/q$  (mass/charge) ratios and the individual beams are brought to a magnetic sector.
- The collector of the mass spectrometer is where the ions of each beam are collected and measured either as individual ions or as an integrated electrical current. This beam intensity can be used to indicate the amount of each isotope in the sample. The collector array is equipped with a combination of Faraday cups and secondary electron multipliers (SEMs). An Electron multiplier is specifically used for low intensity ion

beams because large analytical errors occur when using Faraday detectors with small ion beams, due to the relatively low signal to noise ratio.

There are several specific features for noble gas measurement, which are described as follows.

### **Static mode**

Sample gas is allowed to enter into the mass spectrometer for analyses with the pumping system isolated, which is called “Static” mode (Reynolds, 1956). This increases mass spectrometer sensitivity but has the disadvantage of the signal changing over time when the gas is gradually consumed by ionization (Reynolds, 1956, Reynolds et al., 1978).

### **Mass discrimination effects**

Mass discrimination is relevant to a differential ionization yield as a function of the measured isotope. As a result, an ion beam produced and extracted from the source does not strictly reflect the isotopic composition of the gas present in the source of the mass spectrometer (Marrocchi et al., 2009). Due to the large mass difference between the two He isotopes ( $^3\text{He}$ ,  $^4\text{He}$ ), mass discrimination affects He much more significantly than any other noble gases. Therefore, He requires higher electron beam currents (higher trap currents) than the heavier noble gases in order to increase the He ionization efficiency (Burnard et al., 2013). The trap current used for He analysis in my cases is  $500 \mu\text{A}$ , whereas those for all the rest noble gases are  $200 \mu\text{A}$ .

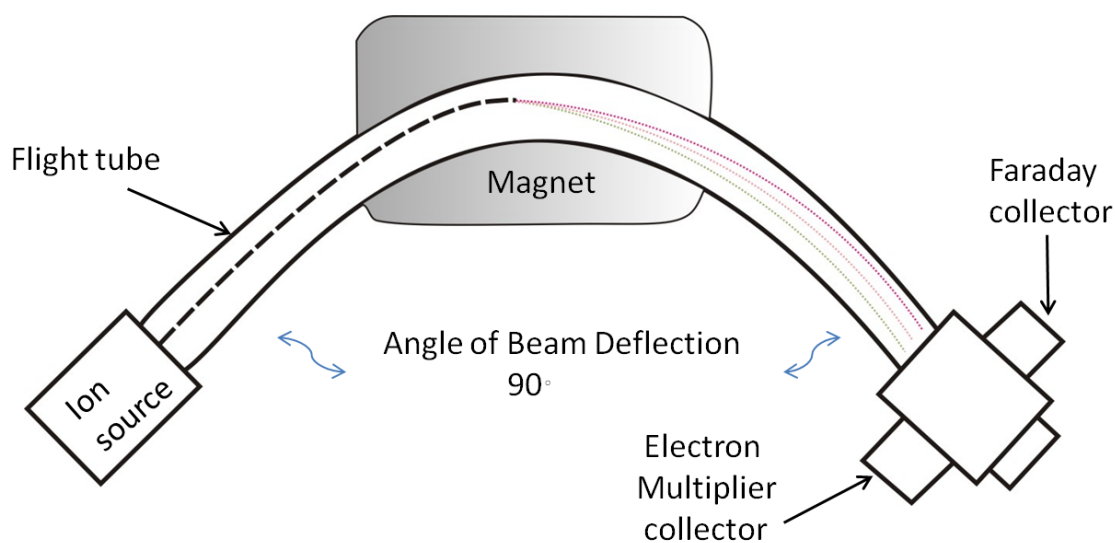


**Fig.3.1.** Mass spectrometer comprising ion source, analyser (Magnet) and collector (Faraday, Multiplier).

### Isobaric interferences

Despite the thorough baking and a good noble gas purification system (getters and furnace) mounted on the noble gas preline and mass spectrometer, it is unavoidable to have some background atoms or molecules (interfering species, such as HD on  $^3\text{He}$ , and  $^{40}\text{Ar}^{++}$  on  $^{20}\text{Ne}$ ) observed in the mass position where noble gas peaks are located. Therefore, these isobaric interferences should be taken into account during measurements. Detailed descriptions of interferences are discussed below in Section 3.7 on interferences.

### 3.2 NGX noble gas mass spectrometer

Noble gas abundances and isotopic ratios were determined using an NGX noble gas mass spectrometer (Isotopx) at the subsurface fluid isotope geochemistry laboratory at the Lancaster University (**Figure 3.2**). NGX noble gas mass spectrometer is a new fully automated

multi-collector mass spectrometer with high precision isotope ratio performance, which is equipped with a high sensitivity ‘Nier’ type gas source and a low volume static vacuum analyser. NGX is characterized by a series of fixed collectors (mix of Faradays and Multiplier) that can be configured during manufacture. The collector array of the NGX at Lancaster University includes nine Faraday cups in fixed positions (H1-H4, AX, and L1-L4) and one ion counting electron multiplier (L6). The Faraday cups are denoted as H1, H2, H3, H4, AX, L1, L2, L3 and L4. H values represent high mass cups, AX represents the axial cup and L values represent low mass cups. L6 denotes electron multiplier. These fixed position Faraday cups are configured to enable a simultaneous measurement of all nine Xe isotopes whilst permitting all other noble gases such as He to be analyzed in peak jumping mode. The NGX operates at an accelerating voltage of 8KV ensuring high sensitivity and enhanced mass resolution (resolution > 600). This resolution is sufficient to resolve hydrocarbons and many other interfering species from the centre of the peaks of interest

### **Low volume and high sensitivity**

Due to the presence of an inverse correlation between instrument volume and measurement sensitivity in a static vacuum mass analyzer, minimizing the overall instrument volume as much as possible is considered before manufacturing. In order to accommodate a multi-collector demand whilst maintaining low instrument volume and high precision performance, NGX uses asymmetrical ion optical geometry where the magnet shortens the image length of the ion beam, allowing a use of significantly smaller flight tube for analysis.

In addition, NGX uses a large, 27cm radius air-cooled electromagnet with an effective radius of 54 cm which routinely operates at up to  $m/q$  270. NGX’s magnet is fitted with an exit lens or ‘pole piece’ capable of rotating the focal plane at the collector, thereby collector focal

plane becoming perpendicular to the ion trajectory (**Figure 3.3**). This design helps lower the collector volume and improve collector efficiency.

### **Straightforward operating procedure**

The feature of a fixed multi-collector has brought many benefits in noble gas analysis, such as simplifying instrument construction, lowering the collector volume and increasing effective sensitivity. Because no zoom lens or movable collectors are required, the operation for noble gas analysis is much more straightforward. In addition, the use of pneumatically operated isolation valve makes it easier to isolate the mechanical pumping line from the system, and to create a static vacuum in the mass spectrometer. These pneumatic valves are mounted on the sample line and controlled by the NGX software, allowing full automation of sample inlet, analysis and pumping.

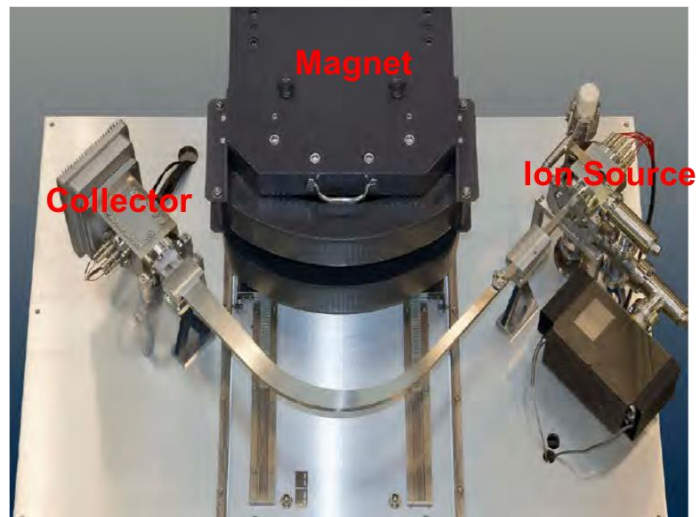


**Fig.3.2.** NGX noble gas mass spectrometer from above showing geometry.

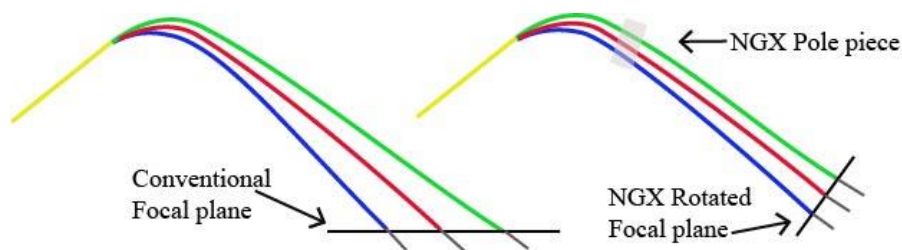


**Fig.3.3.** Difference in ion beam travel directions between NGX rotated focal plane and conventional focal plane.

### **1e<sup>11</sup>Ω and 1e<sup>12</sup>Ω Faraday amplifiers**

NGX’s Faraday’s amplifiers can be fitted with either 1e<sup>11</sup>Ω or 1e<sup>12</sup>Ω gain resistors. The 1e<sup>12</sup>Ω amplifiers are excellent in lowering down the noise level. The noise tests for 1e<sup>11</sup>Ω and 1e<sup>12</sup>Ω gain resistors mounted in a same amplifier over integration periods (1-300 secs) are presented in **Table 3.1**. As shown in **Table 3.1**, the 1e<sup>12</sup>Ω resistors have relatively lower noise level by a factor of 1.5 compared to the 1e<sup>11</sup>Ω resistors over integration periods ranging from one second to 300 seconds. The better performance in lowering down noise level makes the 1e<sup>12</sup>Ω amplifier as an ideal option to use for measuring small amounts of noble gas samples where the ion beam intensity is relatively low.

**Table 3.1.** Noise comparison between 1e<sup>11</sup>Ω and 1e<sup>12</sup>Ω resistor.

Integration time(secs)	Noise (Amps)		
	1e <sup>12</sup> Ω (n = 5)	1e <sup>11</sup> Ω (n = 4)	1e <sup>11</sup> /1e <sup>12</sup>
1	2.3E-16	3.8E-16	1.7
5	1.0E-16	1.7E-16	1.6
10	6.5E-17	1.2E-16	1.8
20	5.1E-17	7.3E-17	1.4
40	3.6E-17	6.3E-17	1.7
60	3.6E-17	5.1E-17	1.4
300	3.5E-17	4.9E-17	1.4

### 3.3 NGX software

A software package consists of NGX-Inlet Prep Bench, NGX Instrument Control and Iconia, which enables the operation of data acquisition, processing and system hardware unit controlling.

#### NGX-Inlet Prep Bench

The NGX-Inlet Prep Bench software (**Figure 3.4**) can be used to manually operate an automated system, record the position of manual valves and to have an instant overview of the Inlet Prep Bench (IPB). In addition, users are allowed to generate their own scripts in the edit script box to control the automatic valves, furnace and cryotrap, providing the basis for fully automated sample measurement.

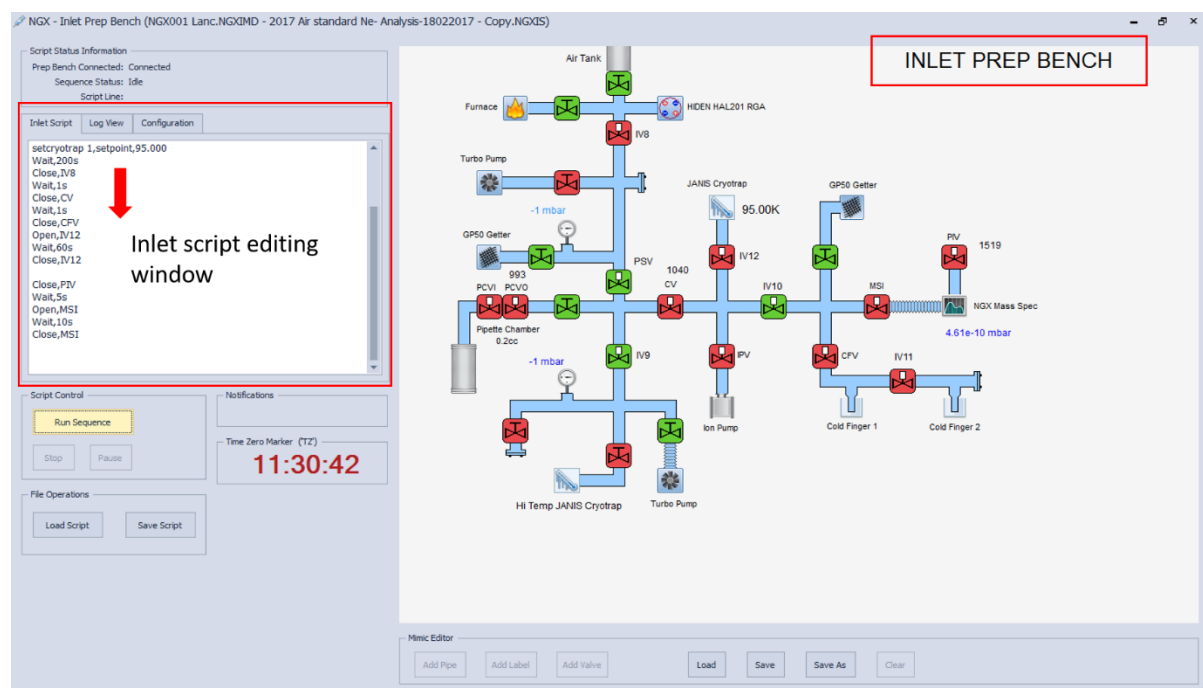


**Fig.3.4.** NGX Inlet Prep Bench window.

## NGX instrument control software

The NGX Instrument Control window displays live feed readings from all gauges and allows control of peripheral equipment such as the turbo pumps and ion gauges (Figure 3.5). Manual analyses can be run from this window. For example, in cases where large amounts of gases are introduced into mass spec to prevent any damage on mass spec system, some required peak scanning tests should be run prior to fully automated measurement using Iconia software. In addition, the NGX Instrument Control window is designed to allow the user to adjust all the parameters of the instrument, such as source tuning (Table 3.2), mass calibration, and collector control, in order to optimize the settings for analyses. The most important role for NGX Instrument Control software is to serve as a diagnostic tool to assess general performance and peak shapes from the NGX Mass Spectrometer (Figure 3.5).

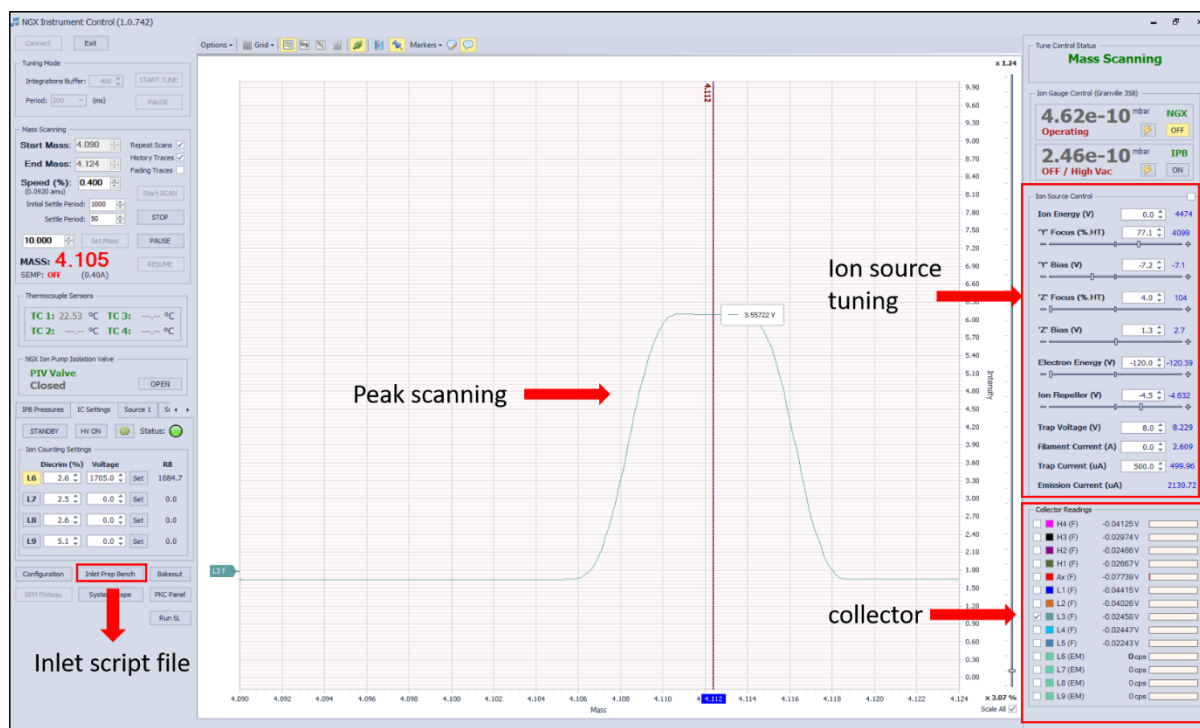


**Fig.3.5.** NGX Instrument Control used for loading script files, tuning ion source and controlling hardware parameters.

Table 3.2 The optimal source tuning parameters for each noble gas

Noble gas	Ion energy	'Y' Focus (%.HT)	'Y' Bias (V)	'Z' Focus (%.HT)	'Z' Bias (V)	Electron Energy(V)	Ion Repeller(V)	Trap Voltage(V)	Filament Current(A)	Trap Current ( $\mu$ A)	Emission Current ( $\mu$ A)
<sup>3</sup> He	4486	4000	-6.9	190	26.3	-113.23	-4.692	8.234	2.354	200.03	847.14
<sup>4</sup> He	4484	3925	-5.7	189	9.6	-120.36	-5.028	8.225	2.360	199.89	901.32
Ne	4456	3962	-2.9	100	17.2	-98.28	-5.155	15.406	2.345	207.21	756.45
Ar	4340	4078	-3.1	101	14.1	-65.66	-3.654	15.411	2.339	205.66	622.69
Kr	4474	4055	-2.5	99	15	-54.04	-4.117	8.229	2.342	199.54	587.7
Xe	4384	4020	-2.3	459	-13.2	-69.18	-4.06	8.225	2.339	200.02	645.07

## Iconia

The fully automated measurements for blank, air and standard samples are achieved by using Iconia software. Each blank, air standard, or sample measurement makes a single line in the sample list of Iconia (**Figure 3.6**). The measurement processes are mainly associated with three files: (i) the source tuning files, containing the ion source settings; (ii) the analysis method files (**Table 3.3**), defining the data acquisition and process details; and (iii) the inlet prep bench script files, showing the whole preparation sequence (purification time, trapping and releasing time, etc.).

The screenshot displays the Iconia software window with a sample list table. The table has the following columns: Run, Filename, Analysis Method, Sample Type, Inlet Script, Tune Filename, and several status columns (ID, No, S, T, C, Lab, M, P, Co, File). The table contains various entries for different sample types and analysis methods, including manual admittance, signal events, and standard analyses. A red box highlights the table area, and a red arrow points to the 'Sample list' label on the left side of the interface.

Run	Filename	Analysis Method	Sample Type	Inlet Script	Tune Filename	ID	No	S	T	C	Lab	M	P	Co	File
50	Test He run 209916	ne 05july	Stam...	<Manual Admittance>	neon_209916	1	0								
51	Test Ar run 210916	Xa 05 july	Stam...	<Manual Admittance>	Xa 110816	1	0								
52	Test He run 210916	ar210916	Stam...	<Manual Admittance>	argon_120816	1	0								
53	Test He run 210916	Helium test 210916	Stam...	<Manual Admittance>	helium_110816	1	0								
54	Test He run 210916	ne 05july	Stam...	<Manual Admittance>	neon_110816	1	0								
55	Test Ar run 230916	Xa 09 july	Stam...	<Manual Admittance>	Xa 110816	1	0								
56	Test He run 230916	Helium test 230916	Stam...	<Manual Admittance>	helium_110816	1	0								
57	Test He run 230916	Zline 230916-n	Stam...	<Manual Admittance>	neon_110816	1	0								
58	Test Ar run 161016	Xa 051016	Stam...	signal event 151016	Xa 110816	1	0								
59	Test Ar run 161016	ar161016	Stam...	signal event 151016	argon_120816	1	0								
60	Test Kr run 161016	kr161016	Stam...	signal event 151016	Kr 230916	1	0								
61	Test He run 161016-HQHD	20CV Helium test 131016	Stam...	signal event 151016	helium_500Trapurement_151016	1	0								
62	Test He run 161016	ne 161016-no21Anel	Stam...	signal event 151016	Neon 110816	1	0								
63	Test ++Ar run 161016	++Ar 161016	Stam...	signal event 151016	argon_120816	2	0								
64	Test ++Ar run 161016	++Ar 161016	Stam...	signal event 151016	argon_120816	1	0								
65	Test Ar run 171116-1	Xa 161016	Stam...	signal event 151016	Xa 110816	1	0								
66	2017 blank	2017 blank_HeHelium test 210717	Blank	signal event 151016	helium_500Trapurement_230617	1	0								
67	Test He-8.607 offset run 040817-3	2017 Helium test 250617	Sample	2017 Furnace-Air standard simplify He Analysis-140...	helium_500Trapurement_230617	1	0								
68	Test He run 040817-2	2017 He test 100417	Sample	2017 Air standard He Analysis-10042017 - Copy	Neon 230617	1	0								
69	Test Ar ++Ar run 040817-2	2017 Ar test 100417	Sample	2017 Air standard 5 expansion-Ar Analysis-10042017 - Copy	argon_120816	1	0								
70	Test Kr run 040817-2	2017 Kr test 100417	Sample	2017 Air standard Kr Analysis-10042017 - Copy	Kr 230916	1	0								
71	Test Ar run 040817-2	2017 Ar test 100417	Sample	2017 Air standard 8-9-Simplify-Xe Analysis-10042017	Xa 110816	1	0								
72	bottle Test He run 230317-4	2017 bottle test Helium test 230317	Stam...	signal event 151016	helium_500Trapurement_151016	1	0								
73	He-15K	2017 bottle test Helium test 230317	Stam...	Temperature 15K-Air standard He Analysis-17042017	helium_500Trapurement_151016	1	0								
74	He-15K	2017 bottle test He test 230317	Stam...	Temperature -Air standard He Analysis-17042017	Neon 110816	1	0								
75	He-20K	2017 bottle test Helium test 230317	Stam...	Temperature 20K-Air standard He Analysis-17042017	helium_500Trapurement_151016	1	0								
76	He-20K	2017 bottle test He test 230317	Stam...	Temperature -Air standard He Analysis-17042017	Neon 110816	1	0								
77	He-25K	2017 bottle test Helium test 230317	Stam...	Temperature 25K-Air standard He Analysis-17042017	helium_500Trapurement_151016	1	0								
78	He-25K	2017 bottle test He test 230317	Stam...	Temperature -Air standard He Analysis-17042017	Neon 110816	1	0								
79	He-30K	2017 bottle test Helium test 230317	Stam...	Temperature 30K-Air standard He Analysis-17042017	helium_500Trapurement_151016	1	0								
80	He-30K	2017 bottle test He test 230317	Stam...	Temperature -Air standard He Analysis-17042017	Neon 110816	1	0								
81	He-35K	2017 bottle test Helium test 230317	Stam...	Temperature 35K-Air standard He Analysis-17042017	helium_500Trapurement_151016	1	0								
82	He-35K	2017 bottle test He test 230317	Stam...	Temperature -Air standard He Analysis-17042017	Neon 110816	1	0								
83	He-40K	2017 bottle test Helium test 230317	Stam...	Temperature 40K-Air standard He Analysis-17042017	helium_500Trapurement_151016	1	0								
84	He-40K	2017 bottle test He test 230317	Stam...	Temperature -Air standard He Analysis-17042017	Neon 110816	1	0								
85	He-45K	2017 bottle test Helium test 230317	Stam...	Temperature 45K-Air standard He Analysis-17042017	helium_500Trapurement_151016	1	0								
86	He-45K	2017 bottle test He test 230317	Stam...	Temperature -Air standard He Analysis-17042017	Neon 110816	1	0								
87	He-50K	2017 bottle test Helium test 230317	Stam...	Temperature 50K-Air standard He Analysis-17042017	helium_500Trapurement_151016	1	0								
88	He-50K	2017 bottle test He test 230317	Stam...	Temperature -Air standard He Analysis-17042017	Neon 110816	1	0								
89	He-55K	2017 bottle test Helium test 230317	Stam...	Temperature 55K-Air standard He Analysis-17042017	helium_500Trapurement_151016	1	0								
90	He-55K	2017 bottle test He test 230317	Stam...	Temperature -Air standard He Analysis-17042017	Neon 110816	1	0								
91	He-60K	2017 bottle test Helium test 230317	Stam...	Temperature 60K-Air standard He Analysis-17042017	helium_500Trapurement_151016	1	0								
92	He-60K	2017 bottle test He test 230317	Stam...	Temperature -Air standard He Analysis-17042017	Neon 110816	1	0								
93	He-65K	2017 bottle test Helium test 230317	Stam...	Temperature 65K-Air standard He Analysis-17042017	helium_500Trapurement_151016	1	0								

**Fig.3.6.** Iconia software window showing sample lists, selected analysis methods, inlet scripts and tuning files.

Table 3.3 The optimal isotopic analysis parameters for each noble gas using iconia on NGX.

Isotope	Collector	Axial Mass	Mass Offset	MST (ms)	Integ Period (ms)	Time (s)
<b>He run</b>						
<sup>4</sup> He	Low3	4.115	0	2000	1000	5
<sup>3</sup> He	Low6	3.244	-0.0076	4000	1000	60
<b>Ne run</b>						
<sup>20</sup> Ne	Axial	19.965	0	5000	1000	5
<sup>22</sup> Ne	Axial	21.985	0	5000	1000	5
<sup>40</sup> Ar	Axial	40.000	0	5000	1000	5
<sup>44</sup> CO <sub>2</sub>	Axial	44.050	0	5000	1000	5
<sup>21</sup> Ne	Low6	22.321	0	5000	1000	5
<sup>22</sup> Ne	Low6	23.392	0	5000	1000	5
<b>Ar run</b>						
<sup>20</sup> Ne	Axial	19.975	0	2000	1000	5
<sup>36</sup> Ar	Low2	36.600	0	2000	1000	5
<sup>40</sup> Ar	Low2	40.662	0	2000	1000	5
<sup>36</sup> Ar	Low6	38.332	0	2000	1000	5
<sup>38</sup> Ar	Low6	40.457	0	2000	1000	5
<b>Kr run</b>						
<sup>78</sup> Kr	Low6	88.834	-6.3570	2000	1000	30
<sup>80</sup> Kr	Low6	88.834	-4.2250	2000	1000	30
<sup>82</sup> Kr	Low6	86.730	0	2000	1000	5
<sup>83</sup> Kr	Low6	87.780	0	2000	1000	5
<sup>84</sup> Kr	Low6	88.834	0	2000	1000	5
<sup>86</sup> Kr	Low6	90.950	0	2000	1000	5
<b>Xe run</b>						
<sup>124</sup> Xe	Low6	137.675	-5.2350	5000	1000	5
<sup>126</sup> Xe	Low6	137.675	-3.3571	2000	1000	5
<sup>128</sup> Xe	Low6	137.675	-1.1230	2000	1000	5
<sup>129</sup> Xe	Low6	137.675	0	2000	1000	5
<sup>130</sup> Xe	Low6	139.926	-1.1265	2000	1000	5
<sup>131</sup> Xe	Low6	139.926	0	2000	1000	5
<sup>132</sup> Xe	Low6	141.054	0	2000	1000	5
<sup>134</sup> Xe	Low6	141.054	2.2676	2000	1000	5
<sup>136</sup> Xe	Low6	141.054	4.5477	2000	1000	5
<sup>84</sup> Kr	Low6	88.885	0	5000	1000	5

Where MST and Integ Period denote mass spec time and integration period in milliseconds, respectively. Time shows the total time for analysis in seconds.

As soon as gas is extracted from the sample holder or air tank, each experiment follows the commands defined in the inlet script file for the gas purification and separation process. Once the noble gases are admitted into mass spec, the method file starts to execute data acquisition (**Figure 3.7**). This analysis process is relevant to several parameter settings such as the method settings previously determined by NGX instrument control software. Once the first measurement is finished, it will automatically run the next experiment following the sample list order until all the ticked sample lists have been completed.



**Fig.3.7.** Data acquisition process on Ionia.

### 3.4 NGX performance

#### Reproducibility of noble gas mass spectrometer

To test the reproducibility and stability of measurement, air aliquots were repeatedly analyzed using NGX fully automated system. **Figure 3.8** shows the variation of  $^{21}\text{Ne}/^{20}\text{Ne}$  as a function of  $^{20}\text{Ne}$  intensity. The reproducibility for the Ne isotopic composition of a set of 73

standards of between  $5.75 \times 10^{-13}$  and  $3.40 \times 10^{-12}$  moles are between 0.2 and 1.2 % for  $^{21}\text{Ne}/^{20}\text{Ne}$  ( $2\sigma$ ). All standards except 6 standards are in good agreement with an average measured  $^{21}\text{Ne}/^{20}\text{Ne}$  ratio of 0.0029323 within the  $2\sigma$ , having  $^{21}\text{Ne}/^{20}\text{Ne}$  ratios from 0.00291 to 0.00296. The reference  $^{21}\text{Ne}/^{20}\text{Ne}$  ratio used is 0.002959 reported by Eberhardt et al. (1965).

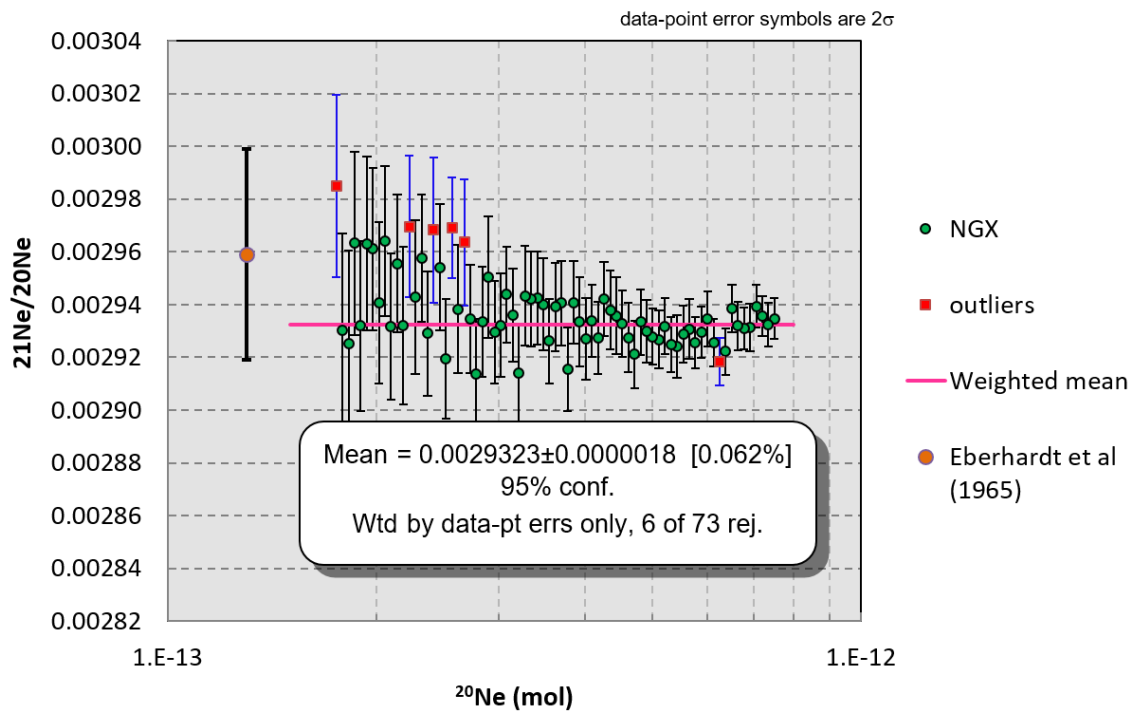


**Fig.3.8.** Variation of the  $^{21}\text{Ne}/^{20}\text{Ne}$  over a range of  $^{20}\text{Ne}$  beams.

### Sensitivity

Similarly, in order to determine the relationship between system sensitivity and partial pressure of noble gas, the performance of Ar results has been monitored by the analysis of different amounts of air. **Figure 3.9** shows the linearity of  $^{40}\text{Ar}/^{36}\text{Ar}$  with changes in  $^{40}\text{Ar}$  intensity. There is no significant difference in  $^{40}\text{Ar}/^{36}\text{Ar}$  ratio with the  $^{40}\text{Ar}$  signal size ranging from 0.03 V to 5.94 V, suggesting the good sensitivity and pressure linearity of the  $^{40}\text{Ar}/^{36}\text{Ar}$  ratios of NGX system.

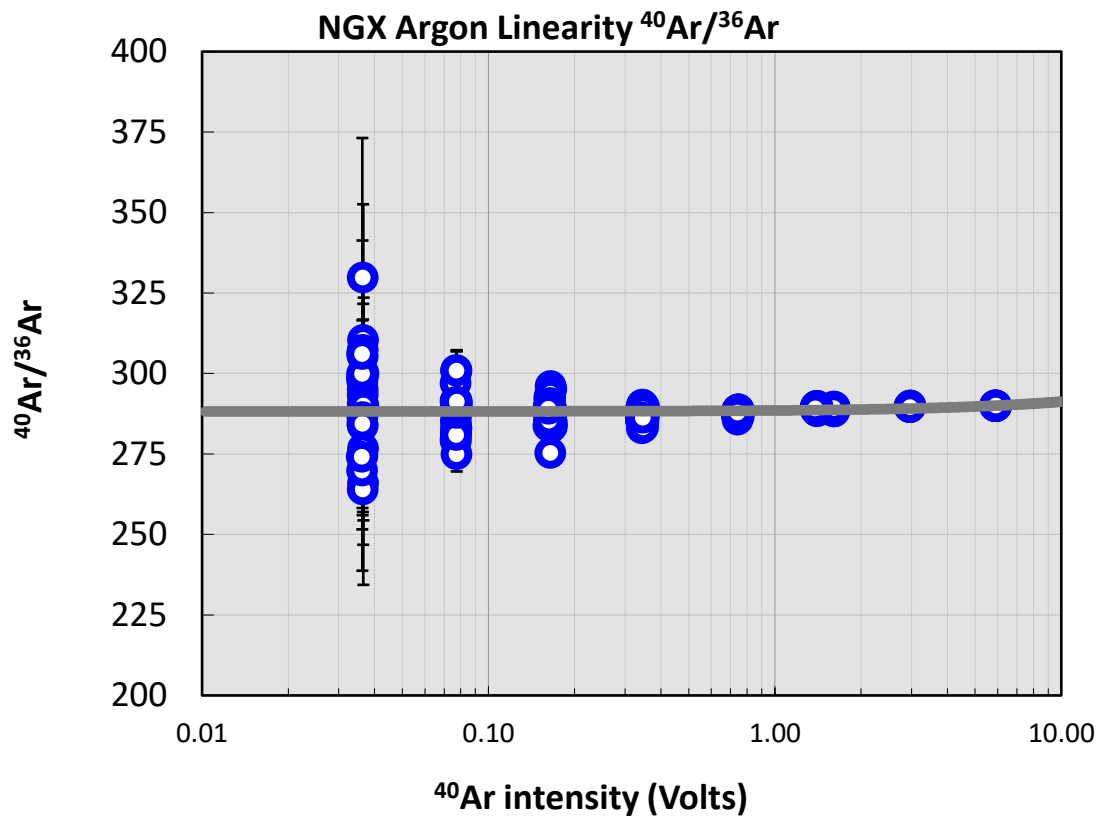


**Fig.3.9.** The linearity of  $^{40}\text{Ar}/^{36}\text{Ar}$  with changes in  $^{40}\text{Ar}$  intensity showing  $^{40}\text{Ar}/^{36}\text{Ar}$  remains constant irrespective of  $^{40}\text{Ar}$  intensity.

### Multi-collection

The large radius magnet provides sufficient mass dispersion to be capable of static multicollection of Xe. In addition, because the collector focal plane is perpendicular to the ion trajectory by using modified magnet exit poles, the peak top can be optimized to be flat irrespective of collector position across the focal plane. The simultaneous collection of 9 isotopes of Xe on different Faraday collectors is shown in **Figure 3.10**. **Figure 3.11** shows the variations of different Xe isotopic ratios with  $^{132}\text{Xe}$  intensity ranging from  $0.5 \times 10^{-12}$  to  $1.4 \times 10^{-12}$  amps, indicating the relatively constant Xe isotopic ratios with the different amounts of  $^{132}\text{Xe}$ .

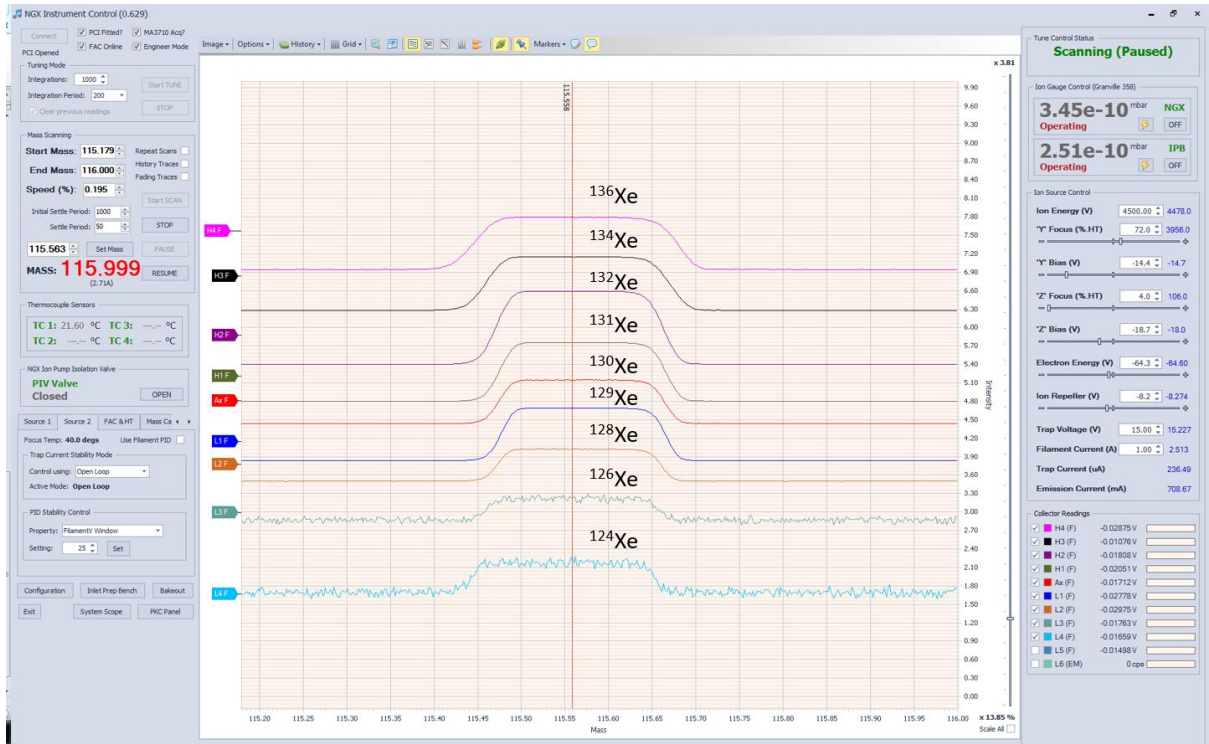
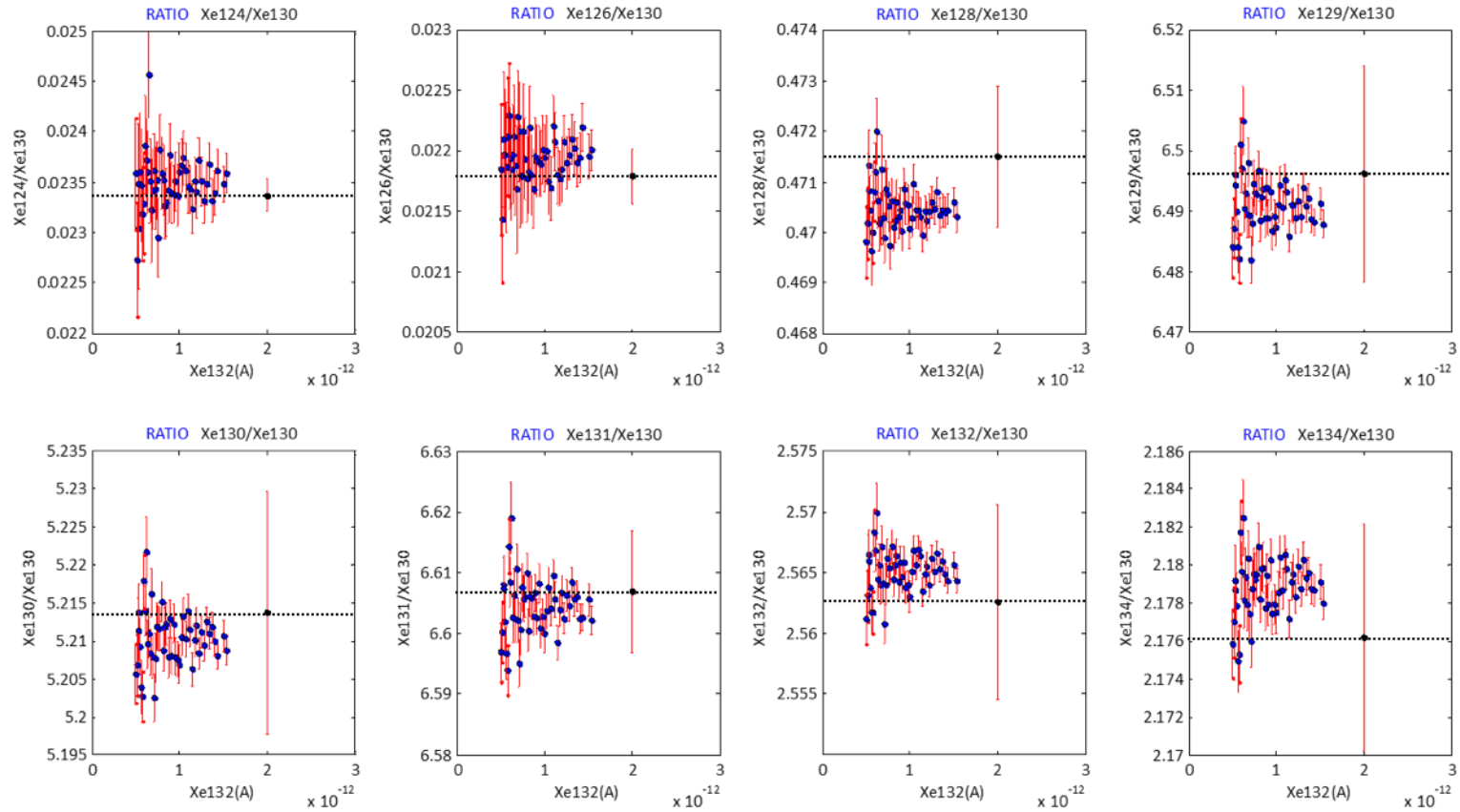
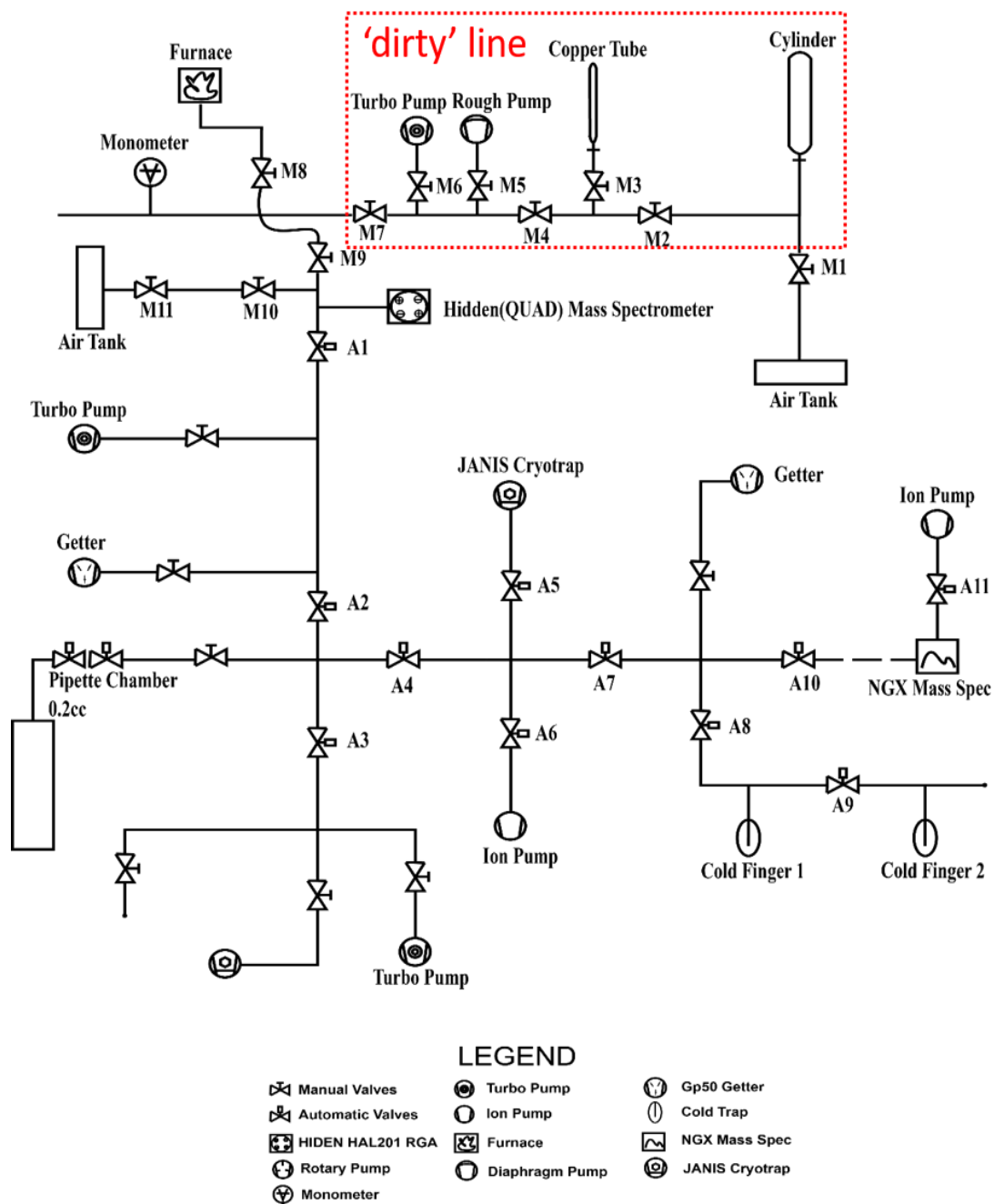


Fig.3.10. Simultaneous collection of all 9 Xe isotopes on Faraday cups.



**Fig.3.11.** The performance of different Xe isotopic ratios as a function of <sup>132</sup>Xe intensity. Dashed line shows Xe isotopic ratio from Porcelli et al. (2002).

### 3.5 Functions of each part in the prep line system



**Fig.3.12.** Schematic diagram of a fully automated noble gas extraction line at Lancaster University.

### Pumping system

The extraction line (**Figure 3.12**) is equipped with a series of pumps (diaphragm pump, turbo pump and ion pump) for maintaining an ultrahigh vacuum environment at different stages.

- A diaphragm pump also called roughing pump, is used to remove air pressure from the system then produce a rough vacuum of  $10^{-3}$  mbar. Because a large amount of air flows into the line during the sample loading process, the roughing pump can ensure a relatively good vacuum to avoid large gases tripping the turbo pump system.
- 80 l/s Pfeiffer turbo molecular pump backed up with a roughing pump mounted on the prep line is used to reduce the vacuum pressure to about  $10^{-7}$  mbar after the vacuum in the line reaches about  $10^{-3}$  mbar.
- 40 l/s ion pump, a closed pumping system, is capable of lowering the pressure down to  $10^{-9}$  mbar under ideal conditions. Two ion pumps are mounted on the prep line and mass spectrometer, respectively, which enables ultra-high vacuum in the prep line and spectrometer. Some possible unexpected incidents, such as power cut may cause the oil in turbo pump flowing back into the prep line/mass spectrometer, which could significantly damage the prep line system and mass spectrometer. Because the ion pump is an oil-free pump, allowing it to be an ideal pump to work during the night with turbo molecular pumps isolated.

### **Vacuum gauges**

Thermal conductivity gauge - Pirani gauge (vacuum level  $\sim 10^{-3}$ ) and Penning gauge (vacuum level  $\sim 10^{-7}$ ) are fitted onto the line for monitoring the pressure in vacuum systems.

In order to avoid any noble gases being consumed by gauges, gauges should be turned off prior to the inlet of pure noble gases into the vacuum line. In addition, one ion gauge (vacuum level  $\sim 10^{-9}$ ), is used to measure the vacuum pressure conditions in the NGX mass spectrometer.

### **Ti-sponge furnace**

Titanium sponge (small grain size with huge surface area) can absorb many active gases (e.g. CH<sub>4</sub>, H<sub>2</sub>S, and CO<sub>2</sub>) into its surface at different temperatures. Titanium sponges are heated at high temperature (T=800°C) using a furnace for 20 mins to absorb some gases, then the furnace is removed, and cooled down to the room temperature for another 20 mins to trap other gases, such as hydrogen.

### **Baratron Manometer**

In order to determine the total gas pressure, a Baratron manometer is fitted onto the line. The MKS Instruments Model PDR 2000 Dual Capacitance Diaphragm Gauge (CDG) Controller displays vacuum pressure as measured from capacitance diaphragm gauges (MKS) (**Figure 3.13**). The sample gas volumes can be calculated by using ideal gas PVT equation with gas pressure measured by the baratron manometer. The manometer is capable of measuring from 20 mTorr to 10000 Torr.

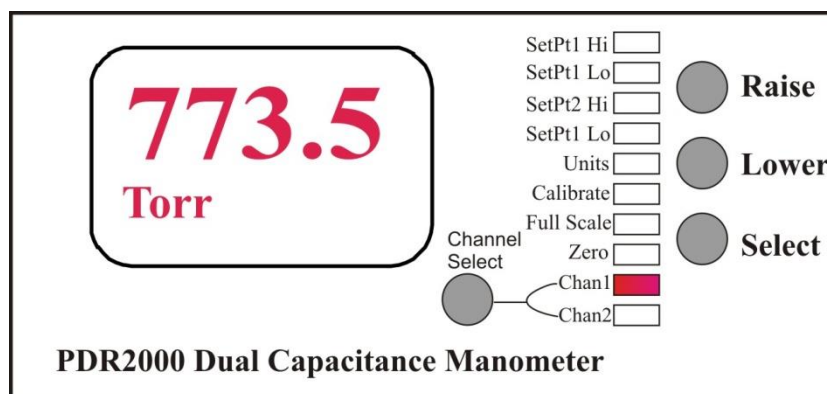


**Fig.3.13.** PDR2000 Dual Capacitance Manometer (MKS Instruments).

### Getter pump

There are two GP50 SAES getters (Ti-Zr alloy) on the prep line, which can target particular gas species at different operating temperatures. Specifically, one getter closer to A2 is held at 350 °C to chemically remove O<sub>2</sub>, N<sub>2</sub>, and CO<sub>2</sub> and to break any remaining CH<sub>4</sub>, while the other getter closer to valve A8 remaining at the room temperature is used to absorb H<sub>2</sub>. Noble gases are unaffected during the entire process.

In case any drastic pressure rise or degassing from the walls of the mass spectrometer itself (Jason C. Poole, 1997), it is necessary to have another getter being fitted directly to the mass spectrometer.

### RC RGA Analyser System (quadrupole mass spectrometer)

The roles of RC RGA Analyser System (Hiden) for our analyses are to pre-analysis the cleanness condition and leak detection of UHV prep line. The quadrupole is kept isolated from the rest of line at UHV.

A standard RC RGA (residual gas analysis) analyzer system constitutes three main units, an RGA Probe, a Radio Frequency (RF) Head, and an RC interface unit (**Figure 3.14**). The

RGA Probe is mounted to a suitable port in the vacuum system and supports the RF Head. The RF Head is connected to the RC Interface via a multi-way cable. The RC Interface is connected to a PC running the MASsoft application via a RS232 serial communications cable, a USB connection or an Ethernet LAN connection. LED on the interface front panel display the state of the analyser and the filaments.

There is a quadruple mass analyser inside in the RGA probe, which consists of an electron impact ion source, an ion extraction system, a quadrupole band-pass mass filter and a detector. The ion source is used to create ions from neutral particles and then the generated ion current can be monitored by a detector which is supported on a ConFlat-type flange.

Sample aliquots are allowed to enter into the analyzer chamber from the gas extraction and separation line, and ion currents are measured by using the secondary electron multiplier (SEM) collector.

Compared with a magnetic deflection mass spectrometer, a quadrupole mass spectrometer (QMS) has several advantages, such as a high scanning rate covering a wider range of mass numbers, simplicity in operation, compactness, the light measuring system, and a lower price.

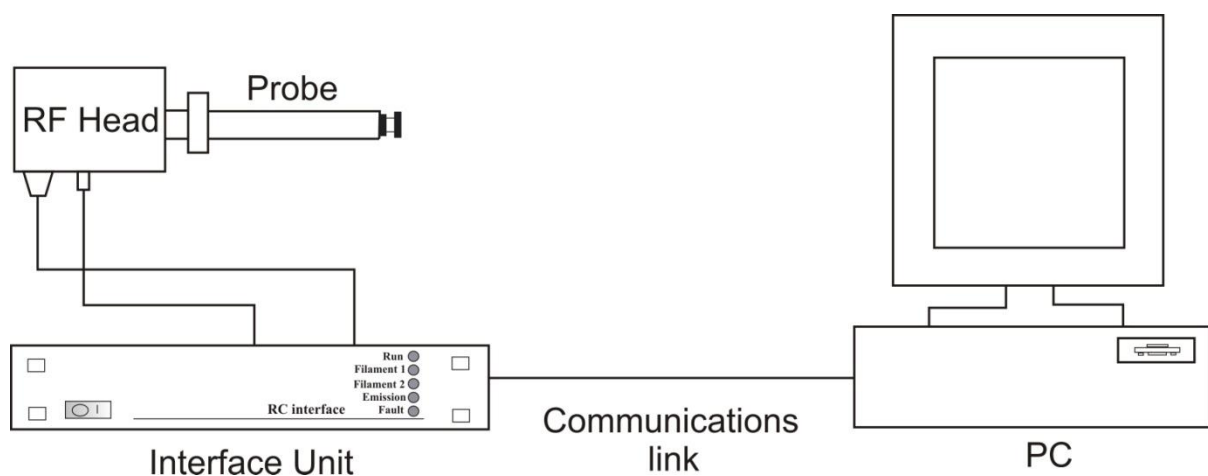


**Fig.3.14.** RC RGA Analyser System.

## Closed Cycle Cryogenic Cold Trap System

The Janis cold trap system (**Figure 3.15**) is a closed cycle refrigerator system designed to operate the temperature from 10K to 350K(Janis). Based on the Gifford-McMahon thermodynamic cycle, a closed loop of helium gas is compressed and circulated through the system via the gas supply and return line. During the expansion phase of each cycle, heat is continuously lost from the cold finger, on which the sample is mounted. A heater and thermometer installed on the cold finger make it possible to precisely control the sample temperature.

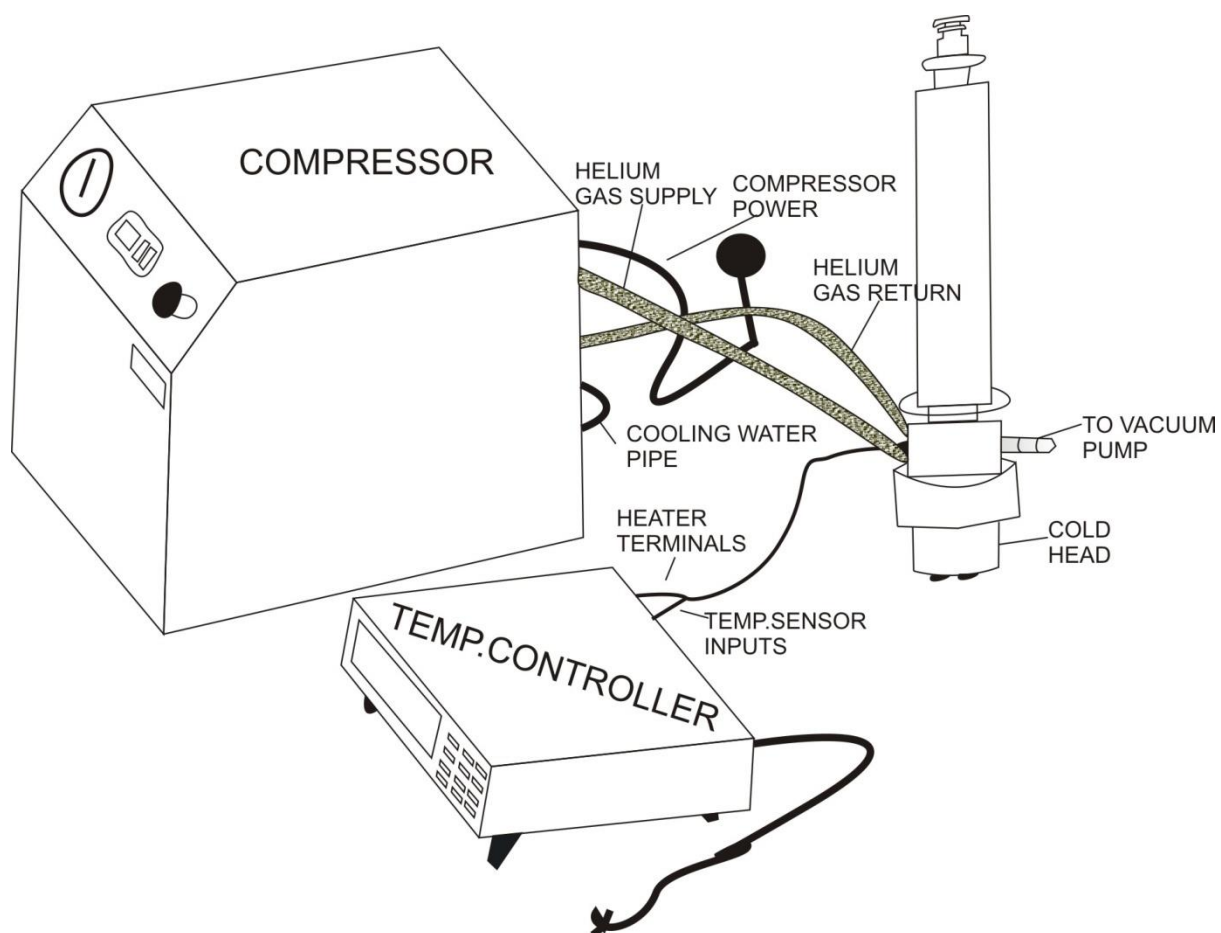


**Fig.3.15.** Closed Cycle Cryogenic Cold Trap System.

Janis CCR systems consist of the following components:

- Compressor: This supplies high-pressure helium gas to the cold head
- Cold Head: This expands the helium gas to cool the sample. It contains two cold stations, the first stage (radiation shield mount) and the second stage (sample mount)
- Gas Lines: These lines are connected between the compressor and cold head supply and return fittings and transport the helium gas between two components. The gas lines are made of stainless steel and have quick disconnect fittings on both ends.
- Vacuum Jacket: This is bolted to the cold head. It includes an evacuation valve, safety pressure relief, electrical feedthroughs, and a clamped vacuum seal for easy access to the sample space.
- Radiation Shield: This bolts to the cold head first stage. It is used to intercept room temperature radiation before it reaches the sample, allowing the lowest possible temperature to be achieved.
- Temperature Controller: This is used to monitor and control the sample temperature.

Operation system access

- Evacuation: Janis CCR systems are equipped with a bellows sealed evacuation valve, which allows evacuation and sealing of the insulating vacuum jacket. Prior to the cooldown operation, a turbomolecular or diffusion pump is connected to the valve and used to evacuate the shroud to a pressure of  $1.0 \times 10^{-4}$  torr or less.

The evacuation valve can remain open during the initial period of the system cooldown stage. However, it should be closed before the temperature reaches 200K to avoid back streaming of oil from the vacuum pump into the cryostat. Outgassing and O-ring permeation may cause the pressure to rise slowly over time, therefore periodic re-

evacuation may be necessary. Re-evacuation is required whenever a new sample is mounted, or when the minimum temperature obtained begins to increase.

- Cryostat cooldown
- Temperature control
- Changing samples: in order to completely release some possible gases trapped onto the inner wall of cryotrap, the cold head should be warmed to room temperature before next sample analyses. This can be accomplished in either of two ways: (1) turn off the refrigerator power, then wait for several hours. Use the control thermometer to monitor whether the system temperature reaches at room temperature or not, or (2) directly set the temperature at 295K by Iconia software/operating the temperature controller box. Once the thermometer reaches 295K, wait until the heater power approaches 0 %. The evacuation valve can now be opened, and the sample can be changed.
- System shutdown: to shut down the system, simply turn off the compressor and temperature controller. If the interconnecting gas lines must be removed for any reason, allowing the system to completely stabilise at room temperature before disconnecting.

### **Reservoir tank**

The sample prep bench is equipped with a 0.2cc pipette together with a 4,000cc reservoir tank, which allows air standards or any spike aliquots to be easily stored into the system. The previously ‘prepared’ gases stored in the tank can be used for analyses by automated operation in the system. Therefore, those ‘stored’ gases make it possible to run overnight measurements automatically, which can be fully manipulated by NGX software Iconia installed in PC.

## **Cold finger charcoal trap**

There are two cold fingers mounted at the end part of the prep line, which are used to separate heavier noble gases (Ar, Kr and Xe). Noble gases can be easily absorbed onto and released from substrates with large surface areas (e.g. activated charcoal) at various temperatures (Reynolds et al., 1978). A cold finger is provided with ~1cc of activated charcoal, which can trap all the heavy noble gases at liquid nitrogen temperature. Similar to the cryotrap system, there is also a heater and thermocouple installed on the cold finger, allowing it to precisely control the heating temperature by temperature-controller panel.

## **Valves**

Automated and manual valves are both used on the prep line. The use of pneumatically actuated Varian valves enables full automation of pre-analysis sample preparation and post-analysis clean up.

## **3.6 Sampling and experiment (gas extraction, purification and separation)**

### **3.6.1 Sampling in the field**

Because the abundances of noble gases are extremely low in the natural environment, any contact with air will significantly affect the measurement results. Therefore, sampling work is fundamental for the subsequent successful analyses. In order to avoid the air contamination, the helium leak-tight and a 50 cm refrigeration grade 10mm outer diameter internally polished copper tubes have been widely used for sample collections in noble gas communities (Kennedy

et al., 1985, Ballentine et al., 1991, Zhou et al., 2005, Gilfillan et al., 2008). Stainless steel clamps are used for holding the copper tube in place during sampling (**Figure 3.16**). The majority of samples for the Sichuan basin study were also collected in dual valved stainless steel cylinders (Swagelok).

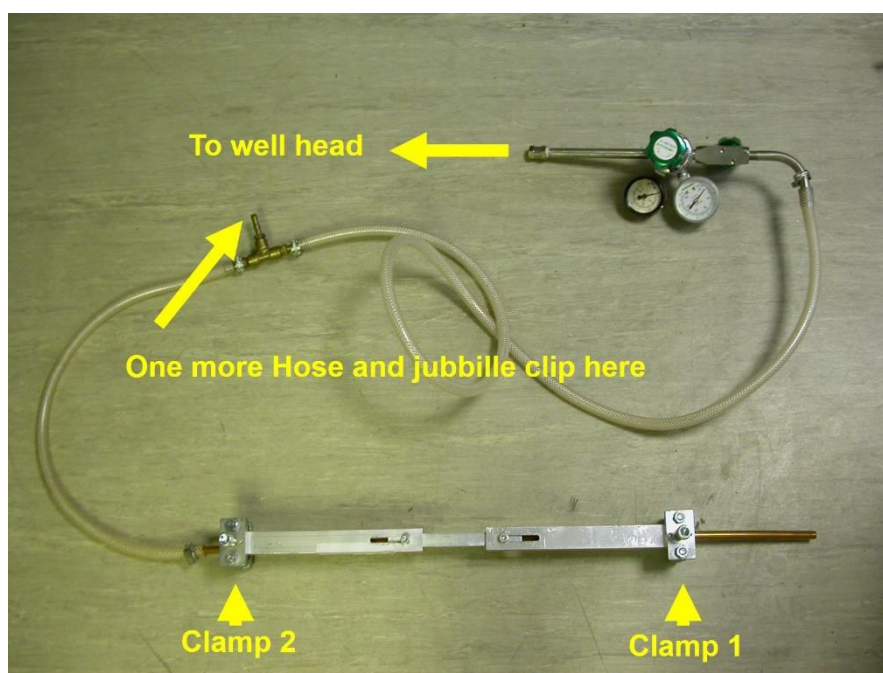


**Fig.3.16.** Devices for field sampling work.

Gas samples are directly taken at well heads in the natural gas reservoir. A stainless-steel pressure regulator is mounted on the well head to effectively adjust the gas flow pressure around 1 ~ 2 bar during sampling. A copper tube is attached to the pressure regulator via a high-pressure hose (withstanding pressure > 2 bars) (**Figure 3.17**). Then, well gases are allowed to flush through copper tubes for 5 mins prior to sampling with the inner pressure of copper tubes around 1 bar. After that, copper tubes are sealed by stainless steel pinch-off clamps starting from the end further away from the well head (clamp 1) then to the end closer to the wellhead (clamp 2). Some important information (e.g. location, well name, date, pressure,

etc.) is marked on each copper tube and written in a notebook before wrapping/packing these samples for transportation and storage.



**Fig.3.17.** Collection of natural gas samples using 10mm diameter internally polished refrigeration grade copper tubes sealed by stainless steel pinch-off clamps on both ends in the Sichuan basin, China, in 2015.

### 3.6.2 Gas extraction

In the laboratory, the sample copper tubes are mounted on an all-metal UHV (Ultra High Vacuum) system designed specifically for the extraction, purification and separation of noble gas via a Swagelok fitting (**Figure 3.12**). Firstly, the clamped copper tube is attached to the inlet port closer to valve M3 with other valves (M2, M3, and M4) closed. Once the sample is successfully attached, gently open M3, M4, and M5, allowing the ‘dirty’ air being pumped by roughing pump. In order to avoid any atmosphere entering into the ‘clean’ line, M6 and M7 are closed prior to opening M4 and M5. After using the rough pump to reach a vacuum of  $1 \times 10^{-3}$  mbar for 15 mins, switch the roughing pump to the turbo molecular pump by closing M5 and opening M6. The system is left to pump down to reach a good background vacuum of  $10^{-7}$  mbar overnight. One important step before leaving the system pumped overnight is to do a leak checking on the prep line, particularly the connecting part in sample inlet area. This can be achieved by spraying helium gas around the sample inlet area, tubes connecting fitting (ConFlat flanges) to see if any obvious  $^4\text{He}$  peak can be observed by using the Hiden MASoft (**Figure 3.18**). The next morning, it is critical to make sure that the background vacuum is in the range of  $10^{-7}$  mbar. This can be achieved by two steps —step 1: quick check. Close all valves in dirty line for 15 mins, then gently open M6, M4, and M3 to see if any significant current values change from the display on the turbo pump. Step 2: After it has been ascertained that no large leak is present in the line, then a helium leak test is again conducted before releasing sample. Once these preparations are finished, close all the valves (M3, M4, and M6) on the dirty line, then sample can be released from the tube to the line. The clamp closest to the system is opened and removed by using devices, such as a pair of pliers, spanners and allen keys. Tightening a v-notched copper tube opener (collar) can help squeeze the previously clamped section of tube then release sample into the system. Gas sample is firstly expanded

into M2-M3-M4 section, then wait one minute for gas equilibration, close M3, open M4, gas in the section M2-M3-M4 is then subsequently introduced into M4-M5-M6-M7 section. Wait another one minute to equilibrate, repeating the same dilution operation, close M4, open M7, gas then flows into M7-M8-M9 section where a Baratron gauge is fitted to measure the gas pressure. M7-M8-M9 section stores the sample gas for subsequent analysis. Because two pumps were mounted in M4-M5-M6-M7 section, M4-M5-M6-M7 section is used for diluting the gas sample if a high amount of gas is monitored in M7-M8-M9. M2-M3-M4 section is served as ‘back up’ part for adding more gas sample to M7-M8-M9 section when required. The measured volumes of M2-M3-M4, M4-M5-M6- M7, and M7-M8-M9 are 33.549, 58.349, 69.392 cm<sup>3</sup>, respectively.

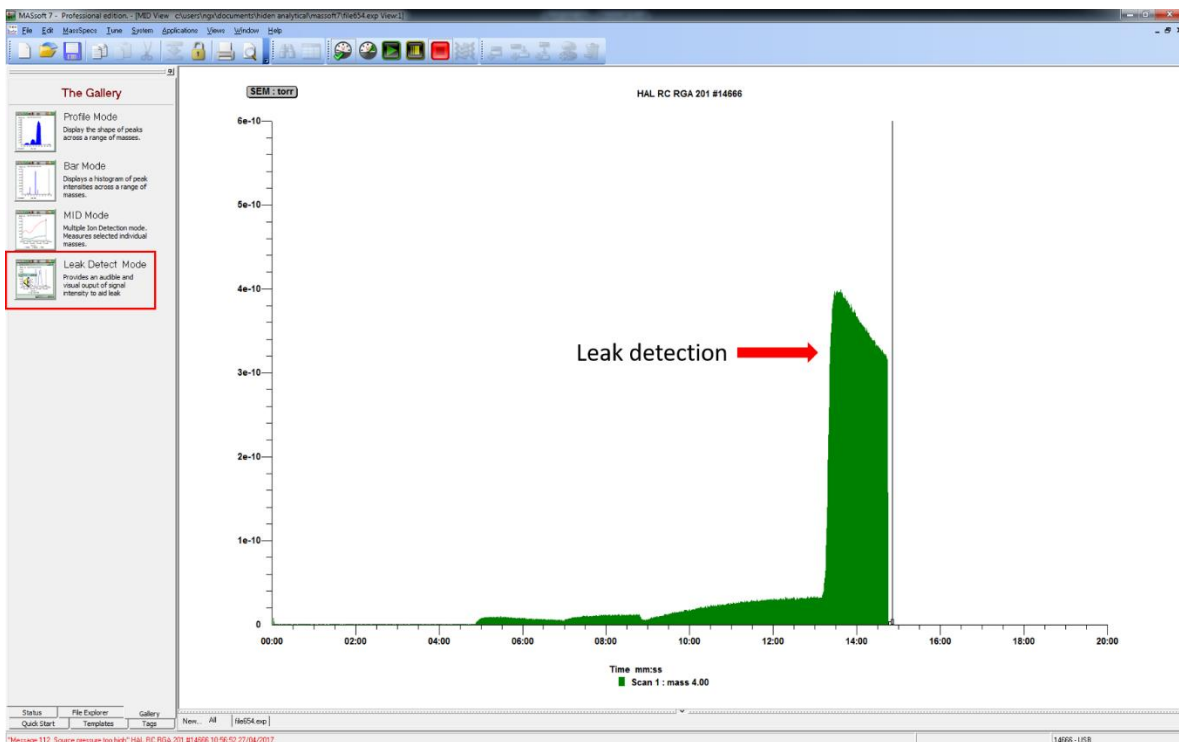


**Fig.3.18.** Hiden MASsoft window showing He leak detection operation.

### **3.6.3 Gas purification**

Once gas sample is isolated in M7-M8-M9 section and the final pressure has been determined using the Baratron monometer on prep line, aliquots of sample are ready for the next step of gas purification, in order to allow pure noble gases into the mass spectrometer for determination. Generally, purification takes advantage of the property of the non-reactivity of the noble gases, chemically removing active species from the extracted gas sample. The purification process can be achieved by two steps described below by using Furnace and two getters (hot getter and room temperature getter), respectively.

A mixture of gas sample is firstly introduced to a pre-heated Ti-sponge furnace at 800°C for 20 mins by opening M8. The observed gas pressure is dropped immediately as soon as valve M8 is opened, indicating the high efficiency of titanium sponge. Then, the furnace is removed to leave Ti-sponge cooling down to room temperature for 20 mins. The external water bath can help cool down the Ti-sponge when needed. Once it is finished, the next step is to open valves M9, A1, A2, A4, and A7, close valve A3, A5, A6, and A8. The sample is subsequently expanded into the prep line fitted with two GP-50 Ti-Zr alloy gas getters at different temperatures for 15 mins. One getter close to A2 is held at 350°C while the other one close to A7 remains at room temperature. Finally, by using a combination of titanium sponge and two getters, the majority of reactive gases (hydrocarbons, H<sub>2</sub>S, CO<sub>2</sub> and CO, etc.) in the sample can be broken down and removed from the system with no effect on noble gases.

### **3.6.4 Gas separation**

Due to several orders of magnitude difference in noble gas concentrations in air standards and samples, it is difficult to measure noble gas concentrations and isotopic ratios simultaneously as a mixture. Therefore, after the removal of reactive gases, the mixture of “pure” noble gases (He, Ne, Ar, Kr and Xe) needs to be separated into single noble gas species before measurement, which can be obtained by using a series of cryogenic traps.

In the first place, heavy noble gases (Ar, Kr and Xe) are trapped onto an activated charcoal cold finger immersed into an external liquid nitrogen bath by opening valves A8 and A9 for 15 mins. Then ‘trapped’ heavier noble gases are isolated from the line by closing valve A9. Open valve A5, the remaining gases (He and Ne) are absorbed onto a cryogenic cold trap which was pre-cooled at 10K for 15 mins.

After all gases are trapped in the vacuum line, the temperature on the cryogenic trap is raised to 50K for 15 minutes to release He into the line. Then close valves A7 and A8, open valve A3 for 10 mins, the released He in the line except A7-A8- A10 section will be pumped out, close valve A3, open valve A7, wait for 5 mins, repeat the first cycle twice, close valves A7 and A11, open valve A10 for one minute then close it, ‘single’ He, is then admitted into the NGX noble gas mass spectrometer for He abundance and isotope determination. After He measurement, cryogenic trap was then warmed to 95 K for 15 minutes to release Ne into the line. Then following the exact same operation as He, Ne isotopes can be measured on NGX. Notably, during noble gas measurement in the mass spectrometer, the sample prep-line is kept being pumped by turbo-molecular pump backed up with a rotary pump (at a vacuum of  $10^{-7}$  mbar) in order to avoid any residual gases in the line to affect the following analyses.

Once Ne isotope measurement is finished, close valves A1, A3 and A5, and open valve A9, the charcoal trap is then warmed to 210K for 15 mins. The previous ‘absorbed’ Ar and Kr are subsequently released and expanded into the line. After several expansion and dilution cycles similar to He and Ne, a small aliquot of Ar and Kr was isolated and simultaneously inlet

into the mass spectrometer for abundance and isotopic analyses. Again, the line is being pumped to remove residual Ar and Kr gases in line during Ar and Kr analyses. After 15 minutes, close valve A9, the heater on the cold finger needs to be turned off and cold finger is then cooled down to the liquid nitrogen temperature ( $T=77\text{K}$ ).

In order to minimise the significant effect of large amounts of Ar onto the release of Xe from activated charcoal, three separation cycles as follows are required to effectively separate Xe from Ar and Kr. Firstly, close valve A3, and open A9, the temperature on the charcoal trap is raised to 210K for 15 minutes in order to desorb Ar and Kr remaining on the charcoal into the prep-line. Then, open A3, and close A9, these released gases are pumped off for another 15 minutes, at the same time, temperature on the charcoal is warmed to 450K for releasing Xe. Once the pumping step is finished, close valve A3, and open valve A9, the released Xe in cold finger is then expanded into the line for another 5 mins. After that, the gases in the line are re-absorbed onto the charcoaled trap at 210K. The second and third cycles are following exactly the same procedures to ensure the complete separation of Xe from Ar and Kr prior to Xe isotope determination.

### **3.6.5 The determination of separation temperature**

In order to determine the optimal releasing temperature for He and Ne on the cryotrap and Ar, Kr and Xe on the cold finger, several necessary tests for noble gas separation are required as described below.

#### **He and Ne separation**

A small aliquot of air is firstly introduced into the prep-line for clean-up step by using Ti-sponge furnace and two getters. Then lighter noble gases (He and Ne) and heavier noble gases (Ar, Kr and Xe) are trapped into the cryotrap at 10 K and cold finger at liquid nitrogen (LN) temperature (77K), respectively. Once He and Ne are trapped on cryotrap held at 10K for 15 mins, the cryotrap temperature is raised from 10K to 110K by an increment of 5K. Each increment interval takes for around 3 mins to allow 'free'  $^4\text{He}$  and  $^{20}\text{Ne}$  to be expanded into the line by opening A5, closing A3, M9, and M10. Then open A1, the partial pressure of 'free'  $^4\text{He}$  and  $^{20}\text{Ne}$  are measured by Quadrupole Mass Spectrometer (QMS). Once the test is finished, Quadrupole system is isolated from the line. **Figure 3.19** describes the partial pressure of  $^4\text{He}$ ,  $^{20}\text{Ne}$  over the temperature range from 10K to 110K. As shown in the **Figure 3.19**,  $^4\text{He}$  has been initially released at around 30K, reaching a peak at 50K with an observed gas pressure of  $9.37 \times 10^{-7}$  torr. In contrast, most  $^{20}\text{Ne}$  is still largely being trapped on cryotrap with the fact that only  $3.98 \times 10^{-8}$  torr  $^{20}\text{Ne}$  has been measured at 50K. Therefore, T=50K can be used for releasing He but remaining Ne on a cryotrap. For Ne, some  $^{20}\text{Ne}$  ( $5.33 \times 10^{-8}$  torr) was firstly detected on quadrupole with the temperature starting at around 55K at which He has been completely released from cryotrap. The maximum releasing pressure of  $^{20}\text{Ne}$  ( $1.47 \times 10^{-6}$  torr) occurred at 95K, which can be determined as the optimal releasing temperature for Ne on a cryotrap.

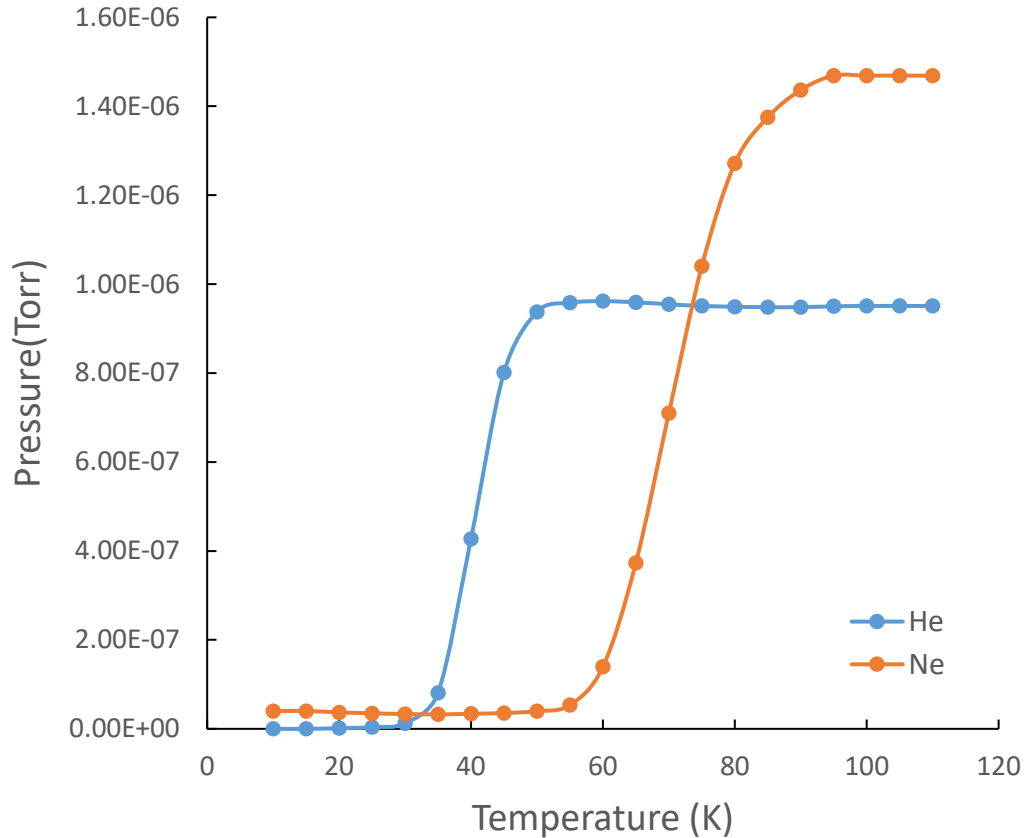


**Fig.3.19.** The partial pressures of  $^4\text{He}$  and  $^{20}\text{Ne}$  are shown as a function of cryotrap temperature.

### Separation of Ar and Kr from Xe

The fact that Kr atoms can be occluded in sorption layers formed by Ar atom at low temperature on the trap results in significant amount of Kr is desorbed together with Ar at same releasing temperature (Stanley et al., 2009), therefore the same temperature was used for releasing both Ar and Kr and the gases were measured simultaneously on the NGX mass spec. To determine the temperature for releasing Ar and Kr but keeping Xe absorbed on the charcoal trap, the charcoal was heated to different temperatures (195K, 200K, 205K, 210K, 215K, 220K). Similar to He and Ne experiments, the partial pressure of released Ar and Xe at different temperatures was measured by Quadrupole Mass Spectrometer (QMS). Below is the detailed description for the determination of the releasing temperature (T=195K for example).

Once the prep line reaches a good vacuum of  $10^{-7}$  mbar, the charcoal trap is warmed to 195K for 15 minutes. After the released gases are expanded into the prep line, the turbo pump is used to evacuate the prep line for 15 minutes by closing A2, opening A9 and A3. Then isolating the pump by closing valve A3, and heating the charcoal trap to 450 K, all gases now can be completely desorbed at this temperature based on previous studies (Porcelli et al., 2002). Open valve A2 and quadrupole manual valve, and then gases are admitted into Quadrupole Mass Spectrometer for gas determination.

Given the fact that the concentration of Ar in the air standard is five orders of magnitude greater than that of Xe (Porcelli et al., 2002), there must be still quite large amount of Ar measured on quadrupole relative to Xe despite the Ar/Kr release and pumping steps described above. Therefore, in order to further reduce the remaining Ar, charcoal is cooled back down to the previous temperature ( $T=195$  K) for 15 minutes once gas measurement is finished in quadrupole. This step can re-trap Xe onto the charcoal but leave Ar/Kr remaining in the line. Then repeat the first cycle, pump away all the gases in the line, and heat the charcoal to release ‘trapped’ gases, then these gases are allowed to enter into the quadrupole for analyses. The third cycle is again running the same procedures as the first two cycles. **Figure 3.20** illustrates the measured partial pressure values of  $^{40}\text{Ar}$  and  $^{132}\text{Xe}$  in each cycle at different temperatures.

After the first cycle separation, the partial pressures of  $^{40}\text{Ar}$  range from  $6.45 \times 10^{-6}$  torr to  $1.98 \times 10^{-5}$  torr, which are several orders of magnitude greater than those for  $^{132}\text{Xe}$ . The less the  $^{40}\text{Ar}$  is measured, the more efficient the release temperature is. The lowest  $^{40}\text{Ar}$  value is observed when the release temperature is 210 K (**Figure 3.20**). Then significant decreases in  $^{40}\text{Ar}$  values have been found after the second cycle separation procedure. In particular, the partial pressure of  $^{40}\text{Ar}$  is down to  $2.85 \times 10^{-8}$  torr at release temperature= 210K, which is slightly higher than the measured  $^{132}\text{Xe}$  pressure of  $1.84 \times 10^{-8}$  torr. It should be noted that there is no significant measurable loss in Xe values during 3 separation cycles for all tests with

different release temperatures. This suggests that most Xe can be trapped on the charcoal at different Ar/Kr release temperatures, although the efficiency for releasing Ar/Kr at different temperatures are various. Therefore, T=210 K is tested to be the optimal temperature for releasing Ar/Kr but keeping Xe being trapped onto the charcoal.

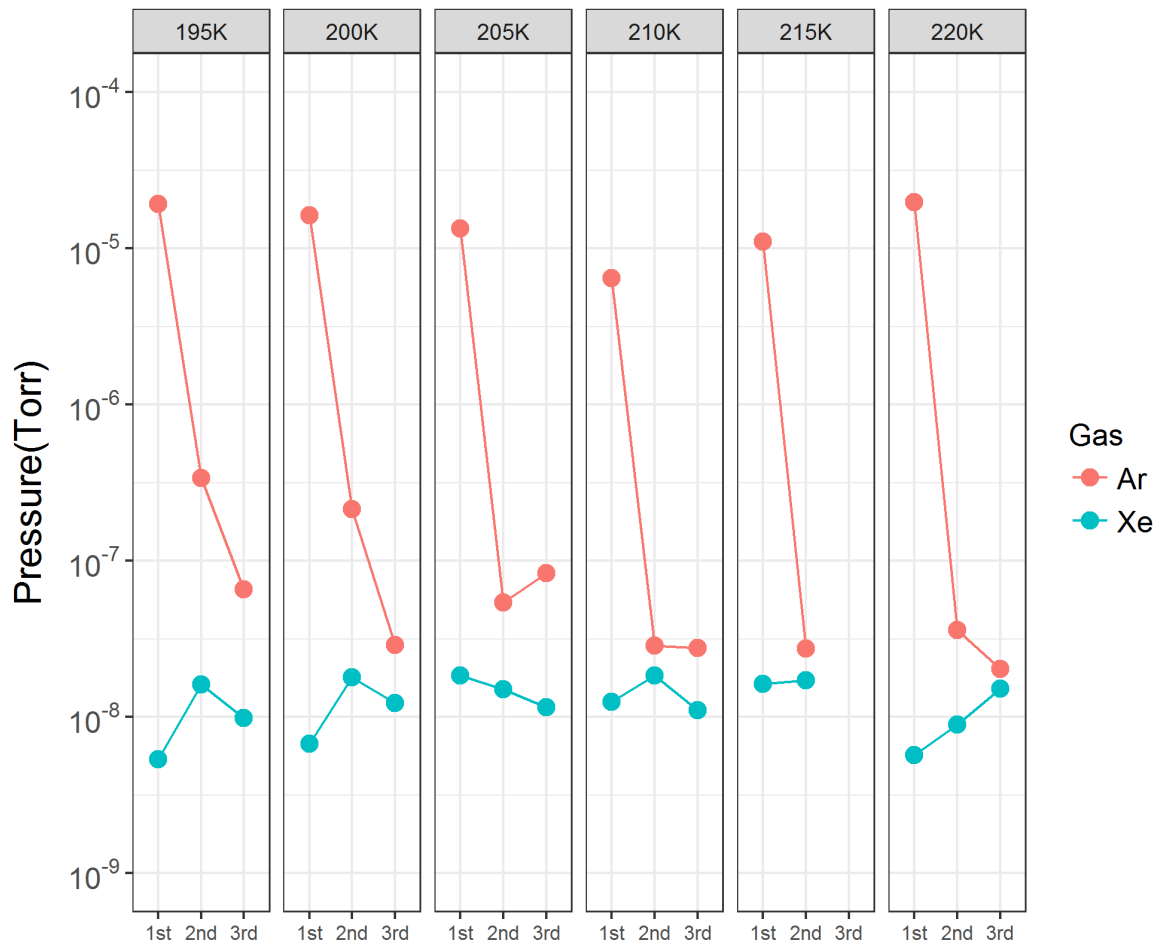


**Fig.3.20.** The partial pressures of  $^{40}\text{Ar}$  and  $^{132}\text{Xe}$  at different separation temperatures for each cycle.

### 3.7 Interferences

The HD peak and  $^3\text{He}^+$  can be completely separated under the mass spectrometer resolution of 600 (**Figure 3.21**). However, the major interferences of  $^{40}\text{Ar}^{++}$  on  $^{20}\text{Ne}$  and  $^{44}\text{CO}_2^{++}$  on  $^{22}\text{Ne}$  are unresolved under our instrument resolution. Therefore, during noble gas isotope and abundance determination, appropriate mass peaks are monitored in order to correct for interferences caused by the doubly charged ions of  $^{40}\text{Ar}^{++}$  and  $^{44}\text{CO}_2^{++}$ .

The interference corrections are found negligible for  $^{44}\text{CO}_2^{++}$  because  $\text{CO}_2$  backgrounds are observed to be lower than the detection limit. However, it is necessary to apply  $^{40}\text{Ar}^{++}$  interference corrections to  $^{20}\text{Ne}$ , particularly for samples with very low neon abundances. The correction of  $^{40}\text{Ar}^{++}$  for relative  $^{20}\text{Ne}$  elemental abundance analysis accounts for approximately 10% of the sample signal size. The  $^{40}\text{Ar}^{++}/^{40}\text{Ar}$  can be given by the concentration of  $^{20}\text{Ne}$  measured in Ar run against that of  $^{40}\text{Ar}$ .

$$\text{Ar run: } ^{40}\text{Ar}^{++} / ^{40}\text{Ar} = (^{20}\text{Ne})_{\text{Ar}} / (^{40}\text{Ar})_{\text{Ar}} \quad 3.1$$

Where  $(^{20}\text{Ne})_{\text{Ar}}$  and  $(^{40}\text{Ar})_{\text{Ar}}$  denote the measured  $^{20}\text{Ne}$  and  $^{40}\text{Ar}$  abundance in the Ar run, respectively.

The corrected  $^{20}\text{Ne}$  abundance can be calculated by:

$$\text{Ne run: } (^{20}\text{Ne})_{\text{c}} = (^{20}\text{Ne})_{\text{ne}} - (^{40}\text{Ar})_{\text{ne}} \times ^{40}\text{Ar}^{++} / ^{40}\text{Ar} \quad 3.2$$

Where  $(^{20}\text{Ne})_{\text{c}}$  represent the corrected  $^{20}\text{Ne}$  abundance,  $(^{20}\text{Ne})_{\text{ne}}$  and  $(^{40}\text{Ar})_{\text{ne}}$  denote the measured  $^{20}\text{Ne}$  and  $^{40}\text{Ar}$  abundance in the Ne run, respectively.

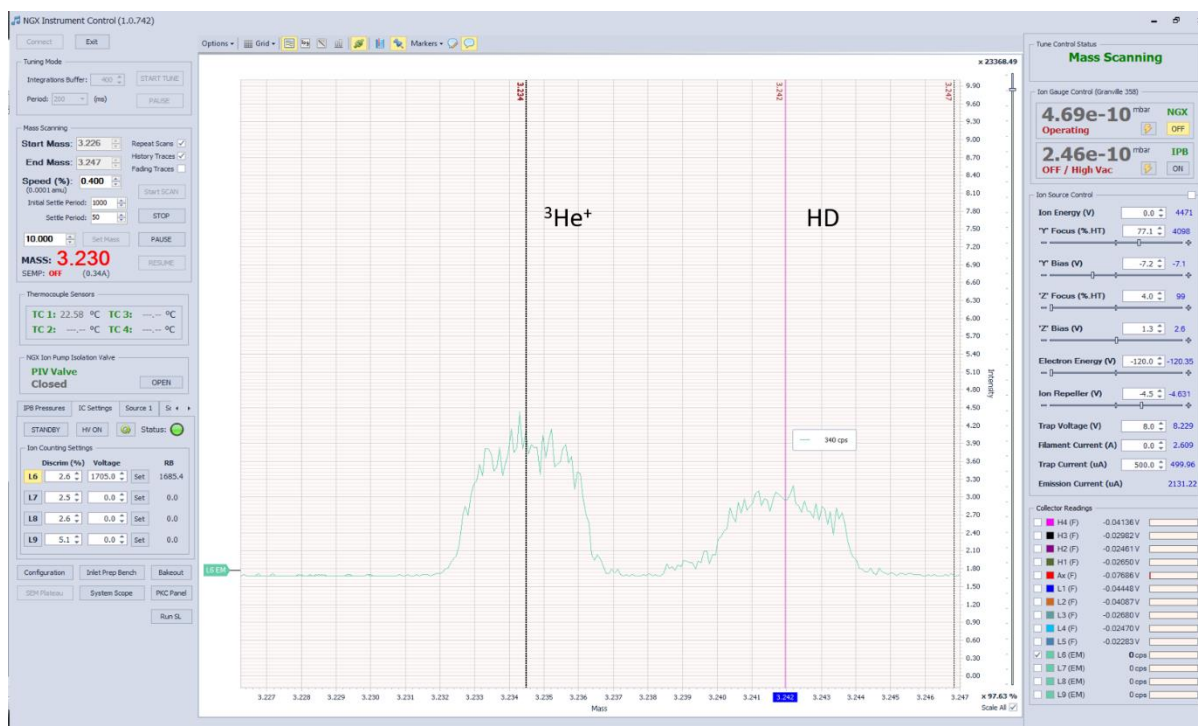


**Fig.3.21.** The  $^3\text{He}$  peak is clearly resolved from the HD molecule.

### 3.8 Blank and air standard

Because changes in instrument sensitivity (e.g. electronics) over time may potentially affect the noble gas analyses, it is necessary to run procedural blanks and standards to check system sensitivity and stability each day. A pipetted volume of  $0.91 \pm 0.02 \text{ cm}^3$  of air standard and a procedural blank are conducted following exactly the same procedure of the sample measurement prior to each sample run, giving a view of overall changes of the mass spec system.

Besides the role on checking system sensitivity and stability, blank and air standard runs can also provide useful information on whether there is any possible leak or background leftover from previous measurements in either prep line or mass spectrometer system.

#### Blank

The average procedural blank data measured on NGX mass spec between July 6<sup>th</sup>, 2017-October 1<sup>st</sup>, 2017 is shown in **Table 3.4**. The procedural blanks of major isotopes (<sup>4</sup>He, <sup>20</sup>Ne, <sup>40</sup>Ar, <sup>84</sup>Kr, and <sup>132</sup>Xe) account for 0.10 %, 0.11 %, 1.59 %, 2.51 %, 1.62 % of air standard signals, respectively (Table 3.4).

Table 3.4 The performance of the NGX for measuring the major isotopes of five noble gases.

Intensity	<sup>4</sup> He (V)	<sup>20</sup> Ne (V)	<sup>40</sup> Ar (V)	<sup>84</sup> Kr (cps)	<sup>132</sup> Xe (cps)
Air standard	1.98	5.23×10 <sup>-2</sup>	3.74	1.24×10 <sup>3</sup>	1.63×10 <sup>3</sup>
Blank	1.97×10 <sup>-3</sup>	5.76×10 <sup>-5</sup>	5.93×10 <sup>-2</sup>	31.1	26.4
Blank (as % of standard)	0.10	0.11	1.59	2.51	1.62

Where air standard values and blank values are the mean intensities of 16 air standard runs and 16 procedural blank runs measured on NGX mass spec between July 6<sup>th</sup>, 2017-October 1<sup>st</sup>, 2017, respectively.

### Air standard

Due to the low abundance of He in the atmosphere, the air standard for noble gas measurement at Lancaster University is taken from a bottle which is filled with a mixture of He spike and Air. He spike is HESJ-standard (**Figure 3.22**) (J. MATSUDA, 2002) with the estimated air normalizing <sup>3</sup>He/<sup>4</sup>He ratio of 20.63 ± 0.10. The calculated pressure of air in He spike + Air bottle (P<sub>standard</sub>) are 0.0274 torr while the partial pressure of He in this bottle (P<sub>He spike</sub>) is approximately 0.000273 torr.



**Fig.3.22.** HESJ standard used by subsurface fluid isotope geochemistry laboratory at Lancaster University.

The total volume of air at STP ( $V_{\text{air}}$ ) in the bottle is calculated by:

$$\frac{P_{\text{air}} \times V_{\text{air}}}{T_{\text{air}}} = \frac{P_{\text{standard}} \times (V_{\text{bottle}} + V_{\text{pipette}})}{T_{\text{lab}}} \quad 3.3$$

Where  $V_{\text{bottle}}$ ,  $V_{\text{pipette}}$  denote the bottle, pipette volumes, which are  $3025 \pm 37$  cc,  $0.91 \pm 0.02$  cc, respectively.  $P_{\text{standard}}$ ,  $P_{\text{air}}$  refer to pressure of air in standard bottle (0.0274 torr), the pressure of one atmosphere (760 torr), respectively.  $T_{\text{lab}}$ ,  $T_{\text{air}}$  denote the temperature in lab ( $T=294\text{K}$ ), the temperature at STP ( $T=273\text{K}$ ), respectively.

The volumes of each noble gas ( $V_{\text{ng}}$ ) in HESJ+ air standard bottle for Ne, Ar, Kr, and Xe are derived from typical atmospheric partial pressures (Ozima and Podosek, 2002, Porcelli et al., 2002) and the calculated the total volume of air at STP ( $V_{\text{air}}$ ) in the bottle. The volume of  $^4\text{He}$  in HESJ+ air standard bottle is associated with typical atmospheric partial pressure of He, the measured partial pressure of He in this bottle, and the amount of  $^4\text{He}$  at STP in the air

with same amount of the bottle volume. Then the volume of  $^3\text{He}$  is calculated using the calculated  $^3\text{He}/^4\text{He}$  ratio ( $20.63 \pm 0.10$ ) together with the  $^4\text{He}$  volume in the HESJ+ air standard bottle.

The calculation for the volume of gas in each pipetted air standard ( $V_{\text{standard}}$ ) can be expressed as:

1<sup>st</sup> pipette:

$$V_{\text{standard}}^1 = V_{\text{ng}} - V_{\text{ng}} \times \frac{V_{\text{bottle}}}{V_{\text{bottle}} + V_{\text{pipette}}} \quad 3.4$$

2<sup>nd</sup> pipette:

$$V_{\text{standard}}^2 = V_{\text{ng}} \times \frac{V_{\text{bottle}}}{V_{\text{bottle}} + V_{\text{pipette}}} - V_{\text{ng}} \times \left( \frac{V_{\text{bottle}}}{V_{\text{bottle}} + V_{\text{pipette}}} \right)^2 \quad 3.5$$

3<sup>rd</sup> pipette:

$$V_{\text{standard}}^3 = V_{\text{ng}} \times \left( \frac{V_{\text{bottle}}}{V_{\text{bottle}} + V_{\text{pipette}}} \right)^2 - V_{\text{ng}} \times \left( \frac{V_{\text{bottle}}}{V_{\text{bottle}} + V_{\text{pipette}}} \right)^3 \quad 3.6$$

For n<sup>th</sup> pipette:

$$V_{\text{standard}}^n = V_{\text{ng}} \times \left[ \left( \frac{V_{\text{bottle}}}{V_{\text{bottle}} + V_{\text{pipette}}} \right)^{n-1} - \left( \frac{V_{\text{bottle}}}{V_{\text{bottle}} + V_{\text{pipette}}} \right)^n \right] \quad 3.7$$

### 3.9 Noble gas concentration calculation

The noble gas elemental abundance for each sample is calculated by comparison with pipetted volumes of air standards after blank correction. The volume of gas in samples can be derived by the observed standard, sample and blank intensity – voltage (with the unit of volt

on Faraday collector) and ion count rate (with the unit of cps on multiplier collector), as well as the volume of standard.

$$V_{\text{isotope}} = V_{\text{standard}} \times \frac{I_{\text{isotope}} - I_{\text{blank}}}{I_{\text{standard}} - I_{\text{blank}}} \quad 3.8$$

Where  $V_{\text{isotope}}$ ,  $V_{\text{standard}}$  denote the volume of isotope in the sample, the air standard, respectively,  $I_{\text{isotope}}$ ,  $I_{\text{standard}}$ , and  $I_{\text{blank}}$  refer to the voltage and ion count rate measured for the isotope, air standard and procedural blank, respectively.

Isotope concentration is given by the calculated isotope volume ( $V_{\text{isotope}}$ ) normalising to the total volume of sample ( $V_{\text{sample}}$ ). The total volume of sample can be calculated by using the ideal gas PVT equation with the pressure of gas sample measured by Baratron Manometer. As mentioned in Section 3.5.2, gas sample enters M7-M8-M9 section where a Baratron gauge is fitted to measure the gas pressure.

$$\frac{P_{\text{air}} \times V_{\text{sample}}}{T_{\text{air}}} = \frac{P_{\text{M7-8-9}} \times V_{\text{M7-8-9}}}{T_{\text{lab}}} \quad 3.9$$

Where  $V_{\text{M7-8-9}}$  denotes the measured volume of M7-M8-M9 section (69 cc).  $P_{\text{M7-8-9}}$ ,  $P_{\text{air}}$  refer to measured sample pressure in M7-M8-M9 section (**Figure 3.12**), the pressure of one atmosphere (760 torr), respectively.  $T_{\text{lab}}$  and  $T_{\text{air}}$  denote the temperature in lab ( $T = 294 \text{ K}$ ) and the temperature at STP ( $T = 273 \text{ K}$ ), respectively.

Finally, isotope concentration ( $C_{\text{isotope}}$ ) can be expressed as follows:

$$C_{\text{isotope}} = \frac{V_{\text{isotope}}}{V_{\text{sample}}} \quad 3.10$$

### 3.10 Error propagation

Each value derived from experimental measurement has a degree of uncertainty. Therefore, in order to calculate the error for noble gas concentrations and isotopic ratios, error for each part of process should be considered. Based on the error propagation rules with the detail described below, the error of final result can be derived.

Example:

The final result R is calculated by three measured quantities of X, Y and Z. Each quantity of X, Y and Z has uncertainties of  $\delta X$ ,  $\delta Y$ , and  $\delta Z$ , respectively.

Addition/subtraction of measured quantities:

$$R = X + Y - Z \quad 3.11$$

$$\delta R = \sqrt{(\delta X)^2 + (\delta Y)^2 + (\delta Z)^2} \quad 3.12$$

Multiplication and division of measured quantities:

$$R = \frac{X + Y}{Z} \quad 3.13$$

$$\delta R = |R| \sqrt{\left(\frac{\delta X}{X}\right)^2 + \left(\frac{\delta Y}{Y}\right)^2 + \left(\frac{\delta Z}{Z}\right)^2} \quad 3.14$$

# 4 Noble gas and stable isotope characteristics of hydrothermal fluid system, Krafla, Iceland

## 4.1 Introduction

The Krafla high-temperature geothermal system in northern Iceland has drawn much attention since a shallow magma reservoir was accidentally discovered during IDDP (Iceland Deep Drilling Project), which aimed at improving the economics of geothermal energy production by exploring for supercritical hydrothermal fluids as a possible energy source in 2009. The usefulness of geothermal systems as an energy source is dominated by their complicated inner hydraulic conditions, which can be well understood by investigating the record preserved in fluids from the geothermal reservoir. Studies on characteristics of hydrothermal systems by using  $\delta D$  and  $\delta^{18}O$  in Krafla geothermal fluids have been described by Elders et al. (2011), Ármannsson et al. (2013), Pope et al. (2016). However, it is still unclear about the possible geothermal evolution history in the Krafla field, such as the source of fluid, fluid circulation, subsurface mixing of different fluid sources, water-rock interactions and water flow paths.

Noble gases provide one of the best tools to study the geothermal fluid due to the properties of low abundance and chemical inertness. They are mainly from three different sources: mantle, crust and atmosphere. Geothermal fluids are characterized by meteoric freshwater containing atmospheric noble gases dissolved during recharge. As the water flows through faults/fractures in the geothermal system, radiogenic  $^4He$  and possibly  $^{40}Ar$  produced by the decay of U, Th and K during prolonged high-temperature water–rock interactions will geochemically change the fluid compositions (Kennedy and van Soest, 2006). Due to three orders of magnitude difference in  $^3He/^4He$  ratios between the mantle and crustal origins (Hilton

et al., 2002, Sano and Fischer, 2013), mantle  $^3\text{He}$  component derived from the magma chamber that provides heat to the geothermal field can be distinguished. Therefore, the identification of these three components in the geothermal system plays an important role in understanding the origin of the geothermal fluids, their pathways and subsurface interactions between fluids and rocks.

Lighter noble gases are less soluble in water than heavier noble gases at high temperatures (Crovetto et al., 1982). Some physical processes such as boiling may occur as pressure decreases during fluid ascent, resulting in strong depletion of noble gases in the residual liquid (Mazor and Truesdell, 1984, Winckler et al., 2000, Pinti et al., 2013, Roulleau et al., 2016). Thus, noble gas elemental compositions can be greatly fractionated relative to initial compositions in the subsurface liquid, suggesting the occurrence of some thermal activities during fluid circulation.

In this study, we present noble gas, major volatile compositions and stable isotope data obtained in eight production wells and two gas-discharging pools in the Krafla geothermal field. By combining reactive ( $\text{CO}_2$ ,  $\text{N}_2$ ) and noble gas data, we are able to : (1) determine the origin and mixing processes of the fluids, i.e. magmatic fluids and fluids in equilibrium with air; (2) investigate the subsurface fluid flow paths, fluid circulation and the role of various fluid sources, as well as quantify fluid-rock interaction; and (3) assess how the main physical processes, such as boiling, steam separation and re-injection, affect the characteristics of geochemical processes in the Krafla geothermal field.

## **4.2 The Krafla geothermal field**

The Krafla geothermal field lies in the northeastern part of the neovolcanic zone in Iceland (**Figure 4.1**). It is located in a large collapse caldera ( $8 \times 10$  km) of the Krafla central

volcano dominated by NE trending fissure swarms (Sæmundsson, 1978). The presence of a magma chamber at a depth of 3 – 7km beneath the caldera has been detected seismically during the 1975–1984 eruptions by S-wave attenuation (Einarsson, 1978).

The geothermal area (**Figure 4.1**) can be divided into several subfields- Leirbotnar (Lower Leirbotnar, Vítismóar), Sudurhlídar, Vesturhlídar, Sandabotnar, Hvíthólar, Vestursvædi, and Leirhnúkur. Leirbotnar and Sudurhlídar, the two largest and most central well fields in the northwest and southeast of the Krafla area, are separated by the Hveragil fracture system. The Hvíthólar wellfield lies approximately 2 km south of the Leirbotnar field.

Drilling data from geothermal wells indicates a complex geothermal system with various subsurface temperature characteristics (Ármansson et al., 1987, Arnórsson, 1995, Ármannsson, 2016). For example, in the Leirbotnar field the system consists of a relatively cool (190 – 220 °C) upper zone down to 1000 – 1400 m depth and a hot (300 – 350 °C) lower zone, whereas the Sudurhlídar system follows a boiling temperature-pressure curve at all depths. The Hvíthólar field is characterised by a relatively hot (boiling) upper part to about 1000m depth with a much cooler lower part.

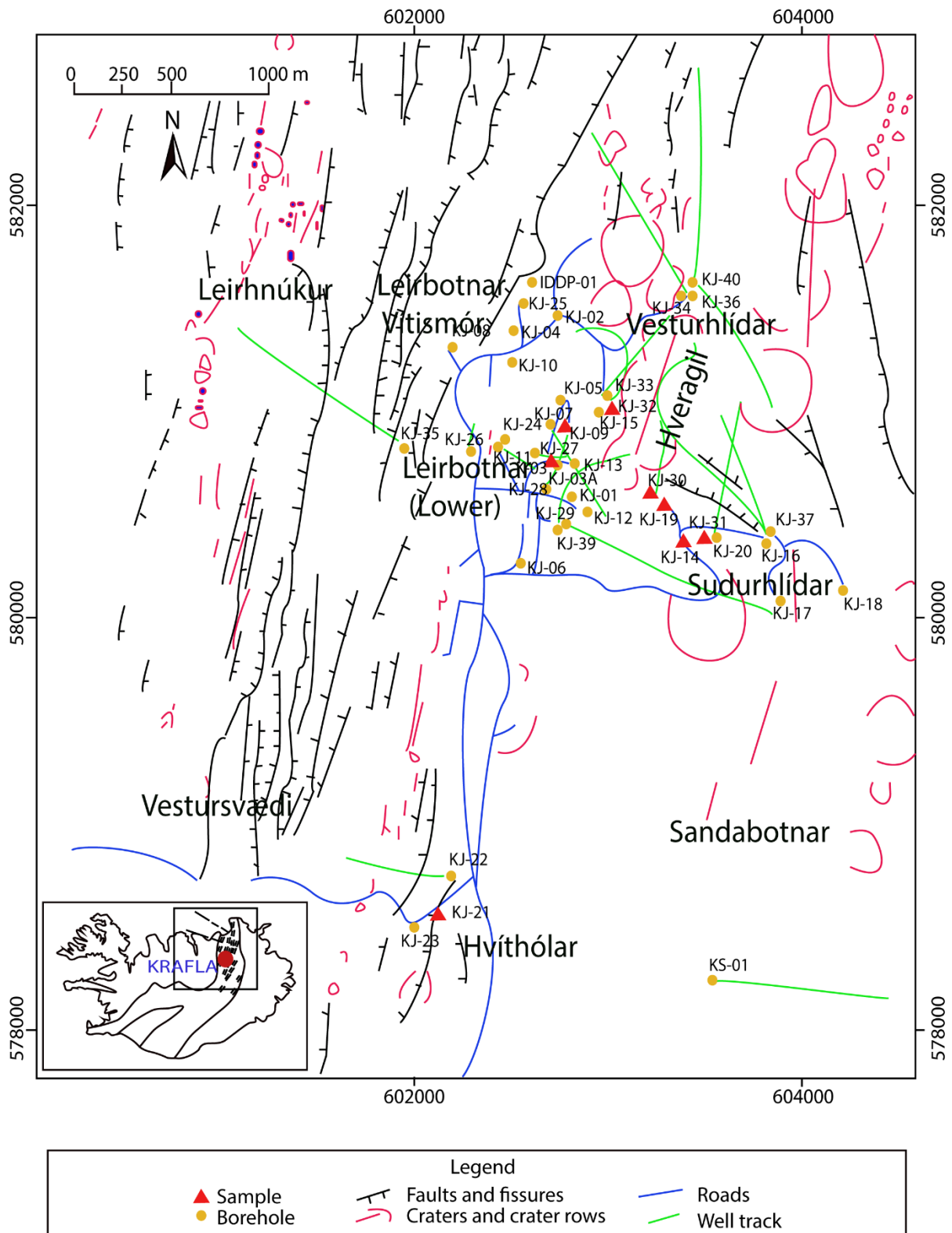


**Fig.4.1.** Krafla geological map showing tectonic features, the different wellfields and individual wells (modified from Ármannsson et al. (2013), (2014)).

Three main lithological units (**Figure 4.2**) have been observed in the Krafla geothermal system (Stefa´nsson, 1981, Ármannsson et al., 1987): (1) the hyaloclastic formation; (2) the lava formation; and (3) the basalt, dolerite and gabbro intrusion (Stefa´nsson, 1981). Hyaloclastite erupted during the last glacial stage is the dominant subsurface lithology to 800m depth. The interglacial lavas at depths of between 800 – 1200 m underlies the hyaloclastic formation in the system. The hyaloclastites and lavas are primarily formed of saturated tholeiitic basalt. Below 1200 m, intrusive rocks begin to dominate. Doleritic intrusions are pervasive in the deeper parts of the reservoir, but felsic intrusions have been encountered in several drill holes. Coarser grained intrusions, e.g. gabbros, become more abundant at greater depth, especially in the Sudurhlídar well field.

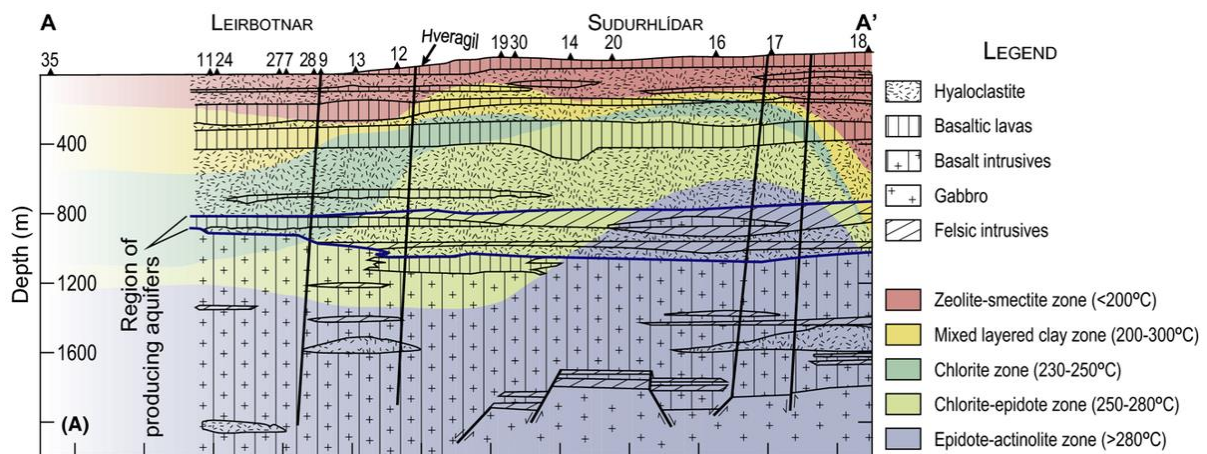


**Fig.4.2.** NW-SE cross-section showing a geologic lithology in the Krafla geothermal field (from Pope et al. (2016).

### 4.3 Sampling techniques and experimental methods

A total of 12 gas samples (**Fig.4.1**) were collected in the Krafla geothermal field for major volatiles, stable isotope and noble gas analysis. Among these, 2 samples were from mud pot bubbling regions (Krisuvic-1, Hverir-31) and 10 samples were from commercial boreholes

(KJ-9-1, KJ-9-2, KJ-14, KJ-19, KJ-20, KJ-21-1, KJ-21-2, KJ-27, KJ-30 and KJ-32). At Krisuvic, Hverir area, a funnel was placed in the mud pot bubbling water to avoid interaction between the released gas and the water column (**Fig.4.3**). From the funnel, the gas flowed through a silicon tube to 10mm diameter internally polished copper tubes sealed by stainless steel pinch-off clamps on both sides of the sampler. Well KJ-9, KJ-27, KJ-32 and Well KJ-14, KJ-19, KJ-20, KJ-30 were located in the Leirbotnar and Sudurhlídar well fields, respectively. Well KJ-21 is in the south of central Krafla region called Hvíthólar. These gas samples were directly collected at the wellheads, with a steam/water separator that separates the water from the gas phase. Gas samples were also collected using copper tubes. In order to minimize air contamination during the sampling procedure, gases were allowed to flush through copper tubes for 10 mins prior to sampling.



**Fig.4.3** Mud pot gases flowing through a funnel to avoid any contact with air.

Noble gas abundances and isotopic ratios were determined using an Isotopx NGX noble gas mass spectrometer at subsurface fluid isotope geochemistry laboratory at Lancaster University (see details in Chapter 3). In the laboratory, the sample copper tubes were mounted on an all-metal UHV (Ultra High Vacuum) system designed specifically for the extraction, purification and separation of noble gases. A mixture of gas samples was firstly transferred into a calibrated volume of 69.392 cm<sup>3</sup> containing a Baratron manometer at lab temperature. After expansion and dilution, approximately 1cc STP sample gas was isolated and pre-purified by consecutive exposure to a Ti-sponge furnace (heated to 800°C for 20 mins, and then cooled down to room temperature for 20 mins). Subsequently, the sample was expanded into the extraction line fitted with two GP-50 Ti-Zr alloy gas getters (one held at 350°C, the other at room temperature). The majority of reactive gases (hydrocarbons, H<sub>2</sub>S, CO<sub>2</sub> and CO, etc.) in the samples are decomposed and removed from the system using a combination of the titanium sponge and two getters with no effect on the noble gases. After the removal of reactive gases, the mixture of noble gases (He, Ne, Ar, Kr and Xe) was separated using a series of cryogenic traps prior to inlet into the NGX mass spec for analysis (see details in Chapter 3).

The <sup>4</sup>He, <sup>20</sup>Ne and <sup>40</sup>Ar were measured using a Faraday detector while the remaining isotopes were counted on an electron multiplier. A known amount of air standard and a procedural blank were conducted following the same procedures of the sample measurement prior to each sample run. The noble gas elemental abundances for each sample were calculated by normalising to those of air standards after blank correction. During Ne abundance and isotope analysis, appropriate mass peaks were monitored to correct for interferences caused by doubly charged ions of <sup>40</sup>Ar<sup>2+</sup> and <sup>44</sup>CO<sub>2</sub><sup>2++</sup> on <sup>20</sup>Ne and <sup>22</sup>Ne. <sup>4</sup>He, <sup>20</sup>Ne, <sup>36</sup>Ar, <sup>84</sup>Kr, and <sup>132</sup>Xe abundances had typical uncertainties of 1.5, 1.8, 1.7, 3.5 and 2.5 %, respectively. All uncertainties are at ±1σ level of confidence. Errors include statistical analytical error, blank

error, air standard reproducibility, the expansion volume uncertainty and mass spectrometer sensitivity stability.

Gas compositions in samples were measured using an Agilent 7890A gas chromatograph (GC), and  $\delta^{15}\text{N}(\text{N}_2)$  were determined on GC-IRMS, at State Key Laboratory of Organic Geochemistry, Guangzhou Institute of Geochemistry, Chinese Academy of Sciences (Tian et al., 2009, Tian et al., 2012). Analytical results were obtained using the mean value of two measurements performed for each gas sample.

The GC-MS conditions for measuring nitrogen isotope were injection temperature 30°C (held for 10.5 min) and maintained constant at 30°C during the whole process. Measurement uncertainty for  $\delta^{15}\text{N}$  is  $\pm 0.2\%$ .

$\delta^{13}\text{C}$  ( $\text{CO}_2$ ) and  $\delta^{18}\text{O}$  ( $\text{CO}_2$ ) were analysed at the NERC Life Sciences Mass Spectrometry Facility, Lancaster node, CEH Lancaster, using a GV Instruments Tracegas Preconcentrator coupled to an Isoprime IRMS. Pulses of known reference  $\text{CO}_2$  and blanks were run prior to sample analysis. The isotopic data are reported in per mil (‰) relative to international standard Vienna Peedee belemnite (V-PDB) standard for carbon and relative to Standard Mean Ocean Water (SMOW) for oxygen. The precision of sample analysis was  $\pm 0.2\%$  at one standard deviation (Smith et al., 2016, Webb et al., 2016).

## 4.4 Results

### 4.4.1 Major gas species and stable isotopes

Gas compositions and stable isotope results ( $\delta^{13}\text{C}$  ( $\text{CO}_2$ ),  $\delta^{18}\text{O}$  ( $\text{CO}_2$ ) and  $\delta^{15}\text{N}$  ( $\text{N}_2$ )) are listed in **Table 4.1** together with sample types, well depths and reservoir temperatures.

As shown in **Table 4.1**, the major gases in samples from the Krafla geothermal field contain CH<sub>4</sub>, CO<sub>2</sub>, N<sub>2</sub>, O<sub>2</sub> and H<sub>2</sub>, with the concentrations ranging from 0 to 2.49 % (CH<sub>4</sub>), 0.79 to 99.23 % (CO<sub>2</sub>), 0.71 to 83.02 % (N<sub>2</sub>), 0.03 to 11.81 % (O<sub>2</sub>), 0 to 6.79 % (H<sub>2</sub>), respectively. There is a negative relationship observed between CO<sub>2</sub> and N<sub>2</sub> in the Krafla geothermal field, showing that CO<sub>2</sub> concentrations in samples increase with the decrease of N<sub>2</sub> (**Figure 4.4**). In contrast, **Figure 4.5** shows a positive correlation between N<sub>2</sub> and O<sub>2</sub>.

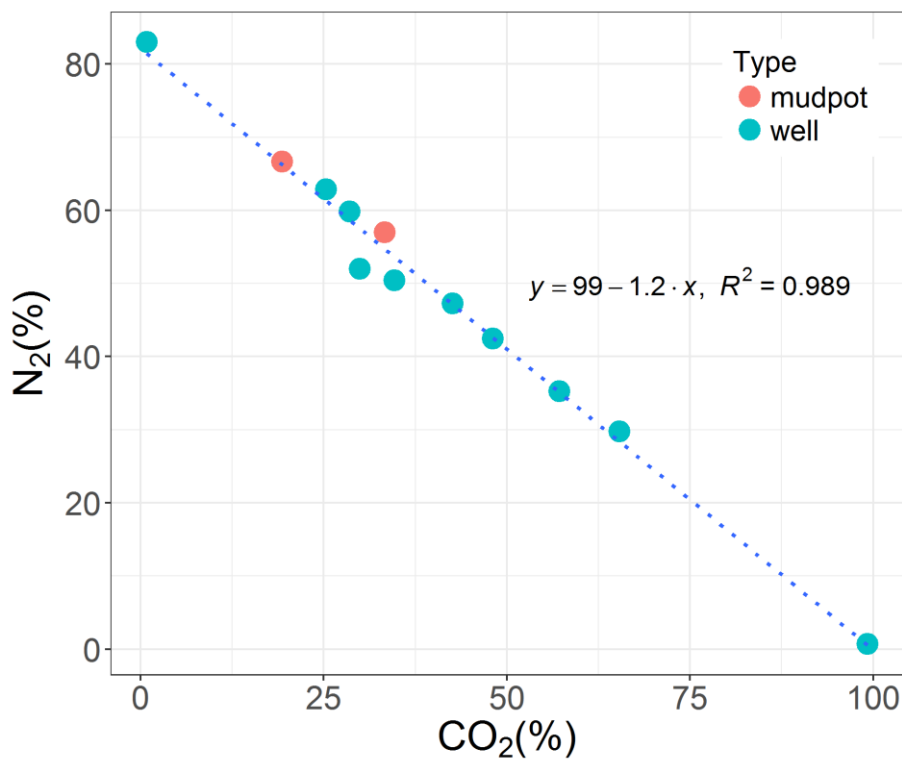


**Fig.4.4.** The negative relationship between CO<sub>2</sub> and N<sub>2</sub> in the Krafla geothermal field.

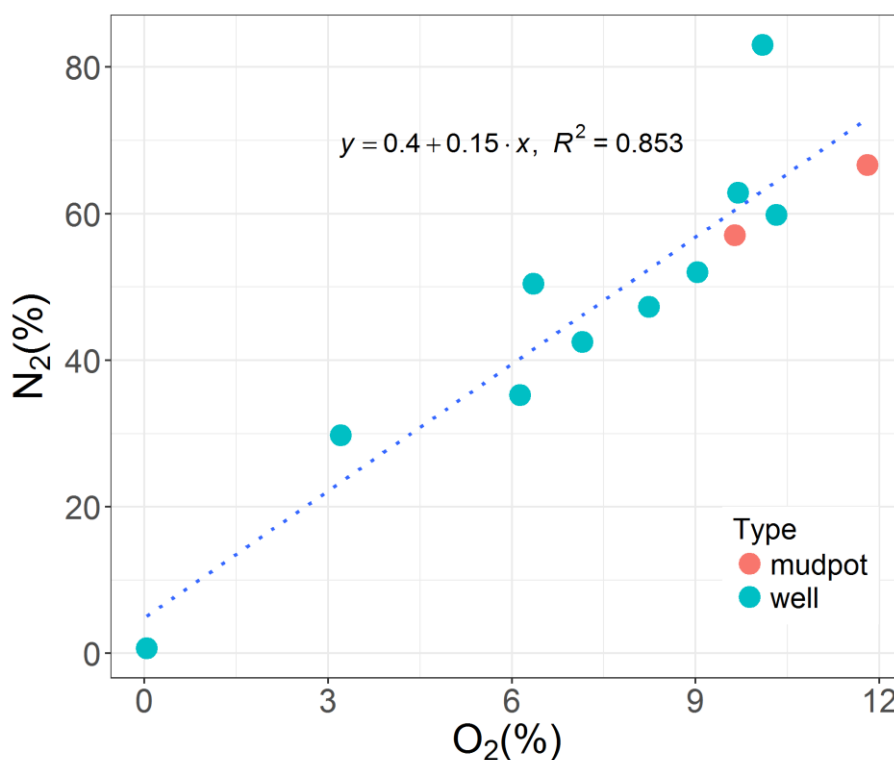


**Fig.4.5.** The positive relationship between O<sub>2</sub> and N<sub>2</sub> in the Krafla geothermal field.

Samples in Krafla have relatively constant  $\delta^{13}\text{C}$  (CO<sub>2</sub>) values, ranging from -7.99 to -3.86 ‰ while  $\delta^{18}\text{O}$  (CO<sub>2</sub>) and  $\delta^{15}\text{N}$  (N<sub>2</sub>) vary from -23.81 to -2.58 ‰ and from -1.26 to -0.94 ‰ (**Table 4.1**), respectively.

By comparing with previous gas geochemistry data in Krafla, Iceland (Table 3.2), Sano et al. (1985) and Poreda et al. (1992) suggested that CO<sub>2</sub> was the dominant gas in gas samples with relatively low abundance of N<sub>2</sub>. This is in distinct contrast with the gas composition results in **Table 4.1**, showing significant amount of N<sub>2</sub> is found in Krafla gas samples. This could be possibly resulted from the ongoing of re-injection in this area since 2002, which is described in Section 3.5.4 boiling and steam separation effects below. However,  $\delta^{13}\text{C}$  (CO<sub>2</sub>) is in good agreement with previous studies (**Table 4.2**). Combined with the tectonic setting in Iceland, CO<sub>2</sub> in the gas phase derived from geothermal water is considered to be magmatic in origin.

**Table 4.1** Major gas composition and stable isotope measurements of Krafla gas samples.

Sample	Type	T (°C)	Depth (m)	Compositions					Stable isotopes			
				CH <sub>4</sub> (±2 %)	CO <sub>2</sub> (%) (±2 %)	N <sub>2</sub> (%) (±2 %)	O <sub>2</sub> (%) (±2 %)	H <sub>2</sub> (%) (±2 %)	δ <sup>13</sup> C (CO <sub>2</sub> ) (±0.2 ‰)	δ <sup>18</sup> O (CO <sub>2</sub> ) (±0.2 ‰)	δ <sup>15</sup> N (N <sub>2</sub> ) (±0.2 ‰)	
<i>Leirbotnar</i>												
KJ-9-1	Well	189.3	1312	2.49	34.65	50.45	6.35	6.06	–	–	–	
KJ-9-2	Well	189.3	1312	2.24	29.92	52.02	9.03	6.79	-5.87	-6.66	-1.117	
KJ-27	Well	184.1	1771	0.43	57.15	35.26	6.13	1.02	-3.86	-23.8	-1.083	
KJ-32	Well	181.2	1875	0.54	48.06	42.52	7.15	1.73	-5.62	-7.22	-1.255	
<i>Sudurhlíðar</i>												
KJ-14	Well	186.4	2107	0.03	99.23	0.7100	0.03	0.00	-7.99	-8.64	-1.205	
KJ-19	Well	201.0	2150	0.00	42.55	47.32	8.24	1.89	-5.56	-21.6	-1.264	
KJ-20	Well	190.0	–	0.00	28.50	59.84	10.3	1.34	-7.55	-6.62	-0.999	
KJ-30	Well	204.4	2054	0.00	65.33	29.79	3.20	1.68	-6.48	-18.7	-1.147	
<i>Hvíthólar</i>												
KJ-21-1	Well	185.1	1200	0.00	0.800	83.02	10.1	6.09	–	–	–	
KJ-21-2	Well	185.1	1200	0.38	25.28	62.88	9.70	1.76	–	–	–	
<i>Hverir</i>												
Hverir-31	Muddy spring	79.60	–	0.19	19.28	66.68	11.8	2.04	-4.87	-2.58	-0.942	
<i>Krisuvic</i>												
Krisuvic-1	Muddy spring	96.00	–	0.00	33.31	57.05	9.64	0.00	-6.16	-5.03	-1.075	

Horizontal line in the table denotes that data not measured.

**Table 4.2** Gas geochemistry on Krafla samples based on previous researches.

Results from	Number of samples	Year	$\delta^{13}\text{C}$ (CO <sub>2</sub> )	$\delta^{18}\text{O}$ (CO <sub>2</sub> )	$\delta^{15}\text{N}$ (N <sub>2</sub> )	CO <sub>2</sub> (%)	N <sub>2</sub> (%)
Sano et al. (1985)	2	1982	-4.0~-2.7		+0.2~+3 .0	49.9~93 .2	4.53~37. 1
Armannsson et al. (1989)	6	1978	-6.9~-3.4				
Armannsson et al. (1989)	3	1984	-3.5~-2.4	-18.5~- 14.8	+0.2~+4 .0		
Poreda et al. (1992)	5		-3.5 (1 sample)			82.7~98 .5	0.135~9. 04
Barry et al. (2014)	4	2006	-5.26~-1.39				
Barry et al. (2014)	3	2007/20 08	-4.78~-2.44				

#### 4.4.2 Noble gases

**Table 4.3** reports the noble gas abundances (<sup>3</sup>He, <sup>4</sup>He, <sup>20</sup>Ne, <sup>40</sup>Ar, <sup>36</sup>Ar, <sup>84</sup>Kr, and <sup>132</sup>Xe) expressed as cm<sup>3</sup> STP/cm<sup>3</sup> total gas. In this section, we use fractionation factors ( $F(i) = (i/^{36}\text{Ar})_{\text{sample}}/(i/^{36}\text{Ar})_{\text{air}}$ ) to describe the relative enrichment or depletion of noble gases with respect to those of atmosphere (Mazor and Bosch, 1992, Pinti et al., 2013), which are presented in **Table 4.3**. **Table 4.4** shows the measured air-normalized He ratio ( $R/R_a$ ,  $R_a = 1.4 \times 10^{-6}$ ) (Ozima and Podosek, 2002) together with the neon, argon, krypton and xenon isotopic ratios.

**Table 4.3** Noble gas elemental abundances and F(i) values for Krafla geothermal fluids.

Sample	<sup>3</sup> He	<sup>4</sup> He	<sup>20</sup> Ne	<sup>40</sup> Ar	<sup>36</sup> Ar	<sup>84</sup> Kr	<sup>132</sup> Xe	F( <sup>20</sup> Ne)	F( <sup>84</sup> Kr)	F( <sup>132</sup> Xe)	CO <sub>2</sub> / <sup>3</sup> He (×10 <sup>9</sup> )
	cm <sup>3</sup> STP/cm <sup>3</sup> gas										
	×10 <sup>-11</sup>	×10 <sup>-6</sup>	×10 <sup>-9</sup>	×10 <sup>-5</sup>	×10 <sup>-8</sup>	×10 <sup>-9</sup>	×10 <sup>-10</sup>				
<i>Leirbotnar</i>											
KJ-9-1	11±0.189	8.47±0.122	381±7.04	49.7±0.704	170±2.87	57±2.14	74.9±2.24	0.428±0.012	1.620±0.069	5.914±0.212	3.150±0.083
KJ-9-2	10.7±0.175	8.05±0.117	333±6.79	46.8±0.662	164±2.81	63.2±2.24	72.1±1.95	0.387±0.011	1.862±0.076	5.901±0.198	2.796±0.072
KJ-27	46.9±0.746	36±0.525	305±5.57	43.3±0.612	151±2.92	41.6±1.48	50.7±1.04	0.385±0.011	1.331±0.056	4.507±0.135	1.219±0.031
KJ-32	10.8±0.17	8.43±0.122	59.3±1.02	8.9±0.126	29.5±0.463	12.8±0.388	14.1±0.398	0.384±0.010	2.096±0.075	6.416±0.217	4.450±0.113
<i>Sudurhlíðar</i>											
KJ-14	3.85±0.0684	2.8±0.0401	27.5±0.462	3.43±0.0486	11.6±0.196	4.45±0.138	6.58±0.183	0.452±0.012	1.853±0.068	7.614±0.259	25.775±0.690
KJ-19	2.9±0.0542	2.15±0.0345	9.7±0.191	1.11±0.0157	3.83±0.0725	1.33±0.0655	1.2±0.0339	0.483±0.014	1.678±0.090	4.206±0.149	14.674±0.402
KJ-20	9.66±0.19	7.41±0.127	11.1±0.202	1.47±0.0208	4.86±0.0874	1.78±0.0759	1.42±0.0361	0.436±0.012	1.769±0.084	3.922±0.128	2.950±0.083
KJ-30	15±0.235	11.5±0.163	25.2±0.428	4.01±0.0568	13±0.216	7.3±0.31	5.83±0.155	0.370±0.010	2.713±0.127	6.020±0.198	4.355±0.111
<i>Hvíthólar</i>											
KJ-21-1	24.9±0.513	18.4±0.288	309±5.43	50.3±0.711	173±2.81	85.7±2.85	62.6±1.52	0.341±0.009	2.393±0.092	4.857±0.150	0.032±0.001
KJ-21-2	17.8±0.352	13.1±0.195	255±4.43	40.2±0.569	138±2.27	56.9±2.03	49.7±1.24	0.353±0.009	1.992±0.081	4.834±0.152	1.420±0.040
<i>Hverir</i>											
Hverir-31	9±0.376	5.77±0.0907	672±11.8	65±0.919	229±3.89	79±2.95	42.8±1.04	0.560±0.015	1.667±0.070	2.509±0.078	2.142±0.099
<i>Krisuvic</i>											
Krisuvic-1	13.4±0.257	6.93±0.0987	142±2.57	16±0.226	53.1±0.819	23.7±0.851	16.3±0.426	0.510±0.013	2.156±0.087	4.120±0.132	2.486±0.069

**Table 4.4** Noble gas isotopic ratios for Krafla geothermal fluids.

Sample	R/Ra	(R/Ra) <sub>c</sub>	<sup>20</sup> Ne/ <sup>22</sup> Ne	<sup>21</sup> Ne/ <sup>22</sup> Ne	<sup>40</sup> Ar/ <sup>36</sup> Ar	<sup>38</sup> Ar/ <sup>36</sup> Ar	<sup>86</sup> Kr/ <sup>84</sup> Kr	<sup>136</sup> Xe/ <sup>132</sup> Xe
<i>Leirbotnar</i>								
KJ-9-1	9.276±0.208	9.397±0.233	9.225±0.223	0.0291±0.0013	292.35±6.443	0.1929±0.0060	0.2947±0.0233	0.3044±0.0165
KJ-9-2	9.494±0.208	9.607±0.234	9.597±0.243	0.0291±0.0012	285.37±6.340	0.1829±0.0062	0.3054±0.0219	0.3273±0.0164
KJ-27	9.306±0.201	9.328±0.222	9.807±0.233	0.0264±0.0011	286.75±6.868	0.1861±0.0061	0.2692±0.0916	0.3432±0.0130
KJ-32	9.151±0.196	9.169±0.217	9.737±0.224	0.0292±0.0012	301.69±6.377	0.1895±0.0050	0.3070±0.0189	0.3319±0.0153
<i>Sudurhlíðar</i>								
KJ-14	9.821±0.224	9.849±0.246	9.649±0.221	0.0288±0.0012	295.69±6.520	0.1914±0.0057	0.3146±0.0206	0.3207±0.0166
KJ-19	9.635±0.237	9.647±0.257	10.157±0.256	0.0285±0.0013	289.82±6.848	0.1914±0.0077	0.3038±0.0309	0.3408±0.0164
KJ-20	9.312±0.243	9.316±0.260	9.737±0.234	0.0290±0.0013	302.47±6.921	0.1922±0.0070	0.2792±0.0216	0.3092±0.0133
KJ-30	9.317±0.197	9.323±0.218	9.844±0.224	0.0305±0.0013	308.46±6.735	0.1854±0.0053	0.2685±0.0231	0.3310±0.0169
<i>Hvíthólar</i>								
KJ-21-1	9.666±0.250	9.713±0.270	9.088±0.212	0.0294±0.0012	290.75±6.260	0.1879±0.0051	0.3291±0.0234	0.3211±0.0157
KJ-21-2	9.706±0.240	9.760±0.262	9.586±0.223	0.0295±0.0012	291.30±6.322	0.1862±0.0056	0.3005±0.0220	0.3058±0.0132
<i>Hverir</i>								
Hverir-31	11.141±0.497	11.531±0.534	9.081±0.211	0.0295±0.0012	283.84±6.273	0.1930±0.0057	0.3241±0.0261	0.3224±0.0158
<i>Krisuvic</i>								
Krisuvic-1	13.812±0.330	13.896±0.361	10.000±0.238	0.0299±0.0011	301.32±6.302	0.1849±0.0048	0.2785±0.0174	0.3368±0.0157
<i>Air ratios</i>								
	1	1	9.80	0.0290	295.5	0.1880	0.30524	0.3293

#### 4.4.2.1 Helium

$^3\text{He}$  and  $^4\text{He}$  concentrations in the Krafla samples vary from  $2.9 \times 10^{-11}$  to  $4.69 \times 10^{-10}$   $\text{cm}^3\text{STP}/\text{cm}^3$  and from  $2.15 \times 10^{-6}$  to  $3.60 \times 10^{-5}$   $\text{cm}^3\text{STP}/\text{cm}^3$ , respectively. In order to minimize the air contamination caused by either the sampling processes or fluid circulation with the addition of recharged meteoric water, air-normalized  $^3\text{He}/^4\text{He}$  ratios ( $R/R_a$ ) were corrected as follows (Craig, 1978, Sano et al., 2006, Pinti et al., 2013)

$$(R/R_a)_c = [(R/R_a)_{\text{meas}} - r] / (1 - r) \quad 4.1$$

$$r = (^4\text{He}/^{20}\text{Ne})_{\text{air}} / (^4\text{He}/^{20}\text{Ne})_{\text{meas}} \quad 4.2$$

where  $(R/R_a)_{\text{meas}}$  is the measured helium isotopic ratio normalised to air ratio ( $R_a = 1.4 \times 10^{-6}$ ) (Ozima and Podosek, 2002),  $(R/R_a)_c$  is  $(R/R_a)_{\text{meas}}$  corrected for air contamination;  $(^4\text{He}/^{20}\text{Ne})_{\text{air}}$  is the atmospheric ratio of 0.318 (Ozima and Podosek, 2002), while  $(^4\text{He}/^{20}\text{Ne})_{\text{meas}}$  is the ratio measured in the gas sample.

**Figure 4.6** illustrates the  $(R/R_a)_c$  ratios in the gas samples from Krafla against  $^4\text{He}/^{20}\text{Ne}$ .  $(R/R_a)_c$  ratios in samples range from 9.17 to 13.90, suggesting significantly contribution from the mantle source. Notably, gas samples collected from boreholes have relatively constant  $^3\text{He}/^4\text{He}$  ratios with the increase of  $^4\text{He}/^{20}\text{Ne}$ , giving an average value of 9.47 Ra. However, the mudpot bubbling gases sampled from Hverir and Krisuvic region, which are geographically distinct from Krafla geothermal wells, have the highest  $(R/R_a)_c$  values of 11.5 Ra and 13.9Ra, respectively. The highest  $(R/R_a)_c$  value has also been found in mud volcanoes and fumarole samples from the Los Azufres geothermal field (Pinti et al, 2013) , which may due to the direct ascent of geothermal fluid to the shallow crust. Overall, these constantly high  $^3\text{He}/^4\text{He}$  ratios

suggest that the reservoir receives deep-seated volatiles and heat from a very active magmatic system at depth (Sano et al., 1985, Pinti et al., 2017b).

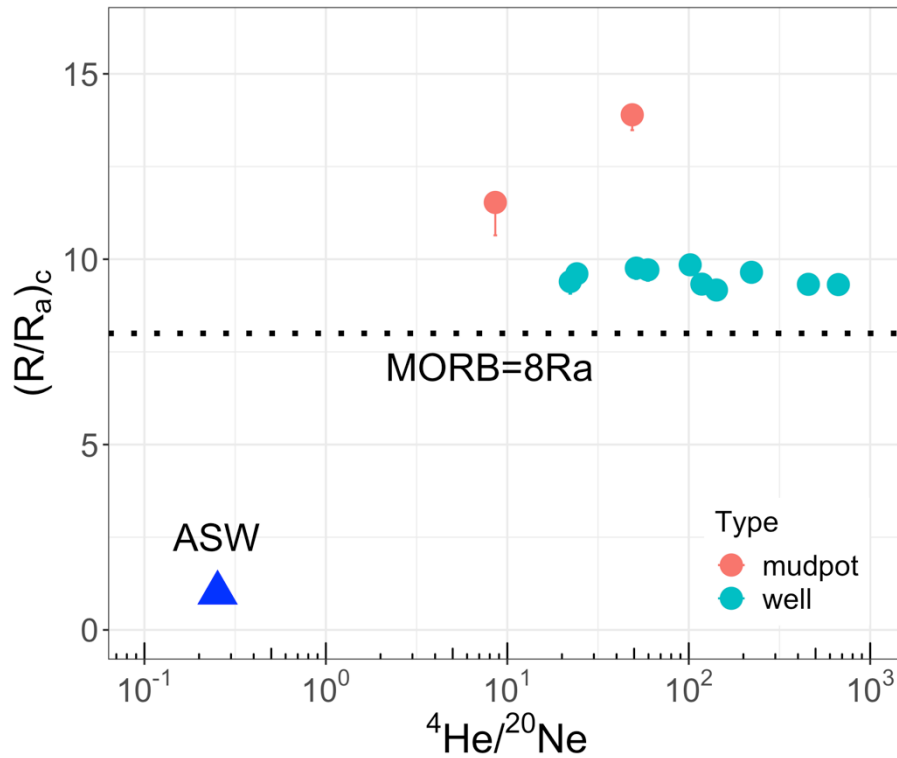


**Fig.4.6.** Air-normalized  $^3\text{He}/^4\text{He}$  ratios ( $R/R_a$ ) vs.  $^4\text{He}/^{20}\text{Ne}$  ratio. MORB  $^3\text{He}/^4\text{He}$  endmember is  $8R_a$  from Ozima and Podosek (2002). ASW component has a  $^4\text{He}/^{20}\text{Ne}$  ratio of 0.253, which was calculated with solubility equations of Crovetto et al. (1982) and used for average annual local recharge temperature of  $10\text{ }^\circ\text{C}$ .

#### 4.4.2.2 Ne, Ar, Kr, Xe

Measured  $^{20}\text{Ne}$  concentrations in samples from the Krafla area range between  $9.7 \times 10^{-9}$  and  $6.72 \times 10^{-7} \text{ cm}^3\text{STP}/\text{cm}^3$ .  $^{20}\text{Ne}/^{22}\text{Ne}$  and  $^{21}\text{Ne}/^{22}\text{Ne}$  isotopic ratios vary from 9.08 to 10.2 and from 0.0264 to 0.0305, respectively (**Figure 4.7**). A plot of three components endmembers shows that these values are similar to the atmospheric values ( $^{20}\text{Ne}/^{22}\text{Ne} = 9.80$  and  $^{21}\text{Ne}/^{22}\text{Ne} = 0.0290$ ) (Ozima and Podosek, 2002).

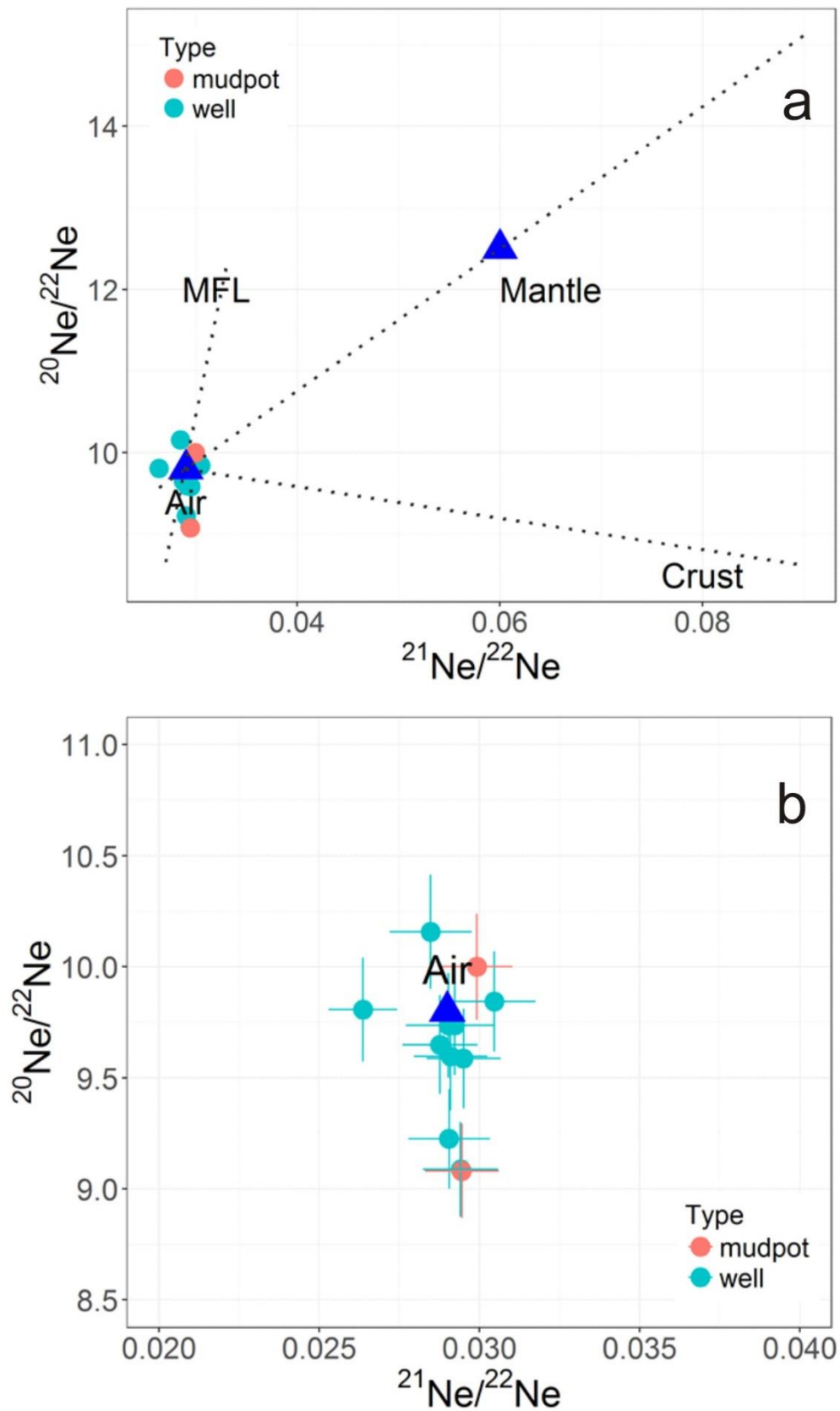


**Fig.4.7.** a). Neon isotopic composition with three different component endmembers. b).  $^{20}\text{Ne}/^{22}\text{Ne}$  vs.  $^{21}\text{Ne}/^{22}\text{Ne}$  in the Krafla geothermal system.

$^{40}\text{Ar}$  and  $^{36}\text{Ar}$  concentrations in samples from the Krafla area range from  $1.11 \times 10^{-5}$  to  $6.5 \times 10^{-4}$  and  $3.83 \times 10^{-8}$  to  $2.29 \times 10^{-6}$   $\text{cm}^3\text{STP}/\text{cm}^3$ , respectively. Similarly, there is no significant deviation observed between Ar isotopic results ( $^{40}\text{Ar}/^{36}\text{Ar}$ ,  $^{38}\text{Ar}/^{36}\text{Ar}$ ) and those of atmosphere, with  $^{40}\text{Ar}/^{36}\text{Ar}$  and  $^{38}\text{Ar}/^{36}\text{Ar}$  ratios ranging between 283.8 and 308.5, 0.183 and 0.193, respectively (**Figure 4.8**).

Measured samples in the Krafla geothermal field have  $^{84}\text{Kr}$  and  $^{132}\text{Xe}$  concentrations varying from  $1.33 \times 10^{-9}$  to  $8.57 \times 10^{-8}$  and  $1.2 \times 10^{-10}$  to  $7.49 \times 10^{-9}$   $\text{cm}^3\text{STP}/\text{cm}^3$ , respectively.  $^{86}\text{Kr}/^{84}\text{Kr}$  and  $^{136}\text{Xe}/^{132}\text{Xe}$  values are air-like, which are from 0.269 to 0.329 and from 0.304 to 0.343, respectively.

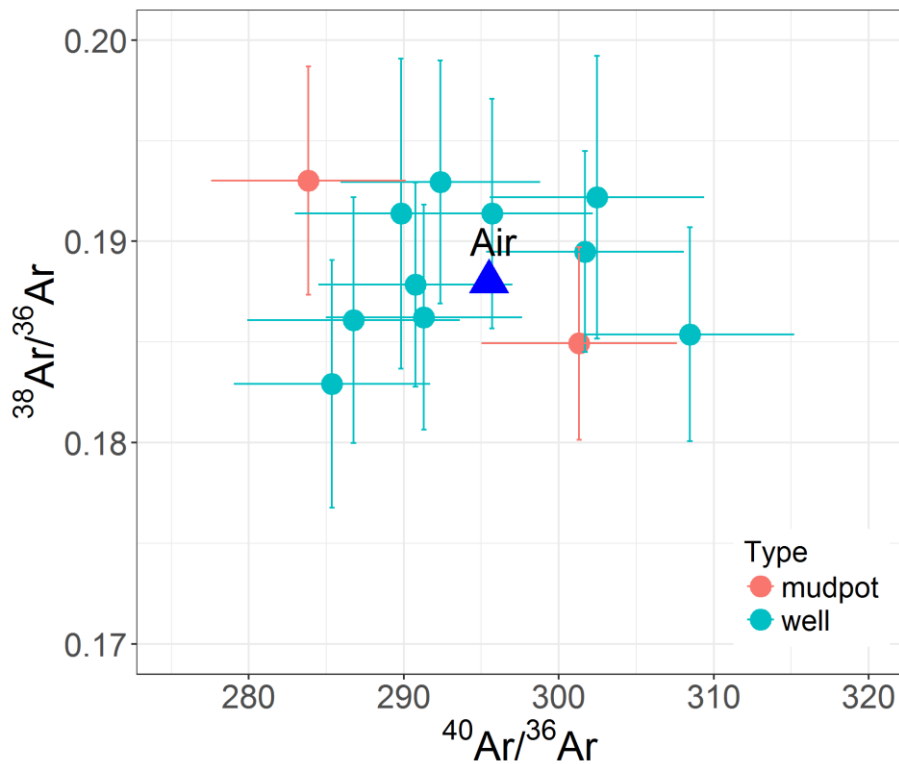


**Fig.4.8.**  $^{38}\text{Ar}/^{36}\text{Ar}$  vs.  $^{40}\text{Ar}/^{36}\text{Ar}$  in the Krafla geothermal system.

## 4.5 Discussion

### 4.5.1 Mantle Helium-MORB-type and plume-type He

$^3\text{He}/^4\text{He}$  in terrestrial samples are mainly from three sources: atmosphere, crust (0.02Ra), and mantle (8 Ra) (Ozima and Podosek, 2002). In terms of mantle-derived He, it can be divided into three groups: (1) MORB-type He with a  $^3\text{He}/^4\text{He}$  ratio of about  $1.1 \times 10^{-5}$  (Lupton and Craig, 1975, Ozima and Podosek, 1983); (2) plume-type He of up to  $5 \times 10^{-5}$ , higher values than MORB-type (Kaneoka and Takaoka, 1980, Kurz et al., 1982, Rison and Craig, 1983); (3) subduction-type He of around  $8 \times 10^{-6}$  (Craig, 1978, Nagao et al., 1981, Torgersen and Jenkins, 1982). As discussed in the 4.4.2.1 Helium section, measured He ratios in Krafla samples are mainly mantle-derived. In order to determine the contributions of MORB-type and plume-type He, the following equations can be used (Sano et al., 1985):

$$(^3\text{He}/^4\text{He})_s = (^3\text{He}/^4\text{He})_a \times A + (^3\text{He}/^4\text{He})_m \times M + (^3\text{He}/^4\text{He})_p \times P \quad 4.3$$

$$1/(^4\text{He}/^{20}\text{Ne})_s = A/(^4\text{He}/^{20}\text{Ne})_a + M/(^4\text{He}/^{20}\text{Ne})_m + P/(^4\text{He}/^{20}\text{Ne})_p \quad 4.4$$

$$A + M + P = 1 \quad 4.5$$

Where subscripts s, a, m, and p illustrate sample, atmospheric, MORB-type, and plume-type, respectively. A, M and P represent the fractions of atmospheric, MORB-type and plume-type He, respectively.

Taking values  $(^3\text{He}/^4\text{He})_a = 1.4 \times 10^{-6}$ ,  $(^3\text{He}/^4\text{He})_m = 1.1 \times 10^{-5}$ ,  $(^3\text{He}/^4\text{He})_p = 5.0 \times 10^{-5}$ ,  $(^4\text{He}/^{20}\text{Ne})_a = 0.318$ ,  $(^4\text{He}/^{20}\text{Ne})_m = 1000$ , and  $(^4\text{He}/^{20}\text{Ne})_p = 1000$  (Sano and Wakita, 1985), the proportion of those three components (MORB, Plume and Air) in Krafla samples can be calculated below (Sano et al., 1985) (**Table 4.5**).

**Table 4.5**  $^3\text{He}/^4\text{He}$  and  $^4\text{He}/^{20}\text{Ne}$  ratios in Krafla gas samples together with proportion of He in three different components — MORB, Plume and Air.

Sample	$^3\text{He}/^4\text{He}$	$^4\text{He}/^{20}\text{Ne}$	MORB (%)	Plume (%)	Air (%)
<i>Leirbotnar</i>					
KJ-9-1	1.30E-05	2.22E+01	93.11	5.49	1.40
KJ-9-2	1.33E-05	2.42E+01	92.53	6.19	1.28
KJ-27	1.31E-05	1.18E+02	94.45	5.32	0.24
KJ-32	1.28E-05	1.42E+02	95.26	4.55	0.19
<i>Sudurhlíðar</i>					
KJ-14	1.38E-05	1.02E+02	92.53	7.19	0.28
KJ-19	1.35E-05	2.21E+02	93.47	6.42	0.11
KJ-20	1.30E-05	6.66E+02	94.77	5.22	0.02
KJ-30	1.30E-05	4.57E+02	94.71	5.25	0.04
<i>Hvítthólar</i>					
KJ-21-1	1.35E-05	5.96E+01	92.93	6.57	0.50
KJ-21-2	1.35E-05	5.15E+01	92.74	6.68	0.59
<i>Hverir</i>					
Hverir-31	1.56E-05	8.59E+00	83.68	12.65	3.67
<i>Krisuvic</i>					
Krisuvic-1	1.93E-05	4.88E+01	77.98	21.40	0.62

Samples collected from the Krafla geothermal field show large MORB-type He contributions, accounting for up to 95.26 % in sample KJ-32. Plume-type He only represents below 8 % of the total He concentration in all samples, except for those two bubbling gas samples, each of which having plume-type He of 12.65 % and 21.40 % in total, respectively. Based on these values and geological histories in Iceland, the Krafla area is considered to be an extension of the normal oceanic ridge with the dominated rock of tholeiitic basalt (ÓSkarsson et al., 1982). These results are in good agreement with  $^3\text{He}/^4\text{He}$  data given by Sano et al. (1985), showing a significant contribution of MORB-type He. This suggests there is no significant variation in  $^3\text{He}/^4\text{He}$  ratios over decades.

#### 4.5.2 Controls on CO<sub>2</sub>/<sup>3</sup>He: elemental fractionation

**Figure 4.9** shows a plot of CO<sub>2</sub>/<sup>3</sup>He and δ<sup>13</sup>C (CO<sub>2</sub>) values for Krafla gas samples. There is no significant change in δ<sup>13</sup>C (CO<sub>2</sub>) with the increase of CO<sub>2</sub>/<sup>3</sup>He ratios. The elemental CO<sub>2</sub>/<sup>3</sup>He ratios range from 1.2 × 10<sup>9</sup> to 4.4 × 10<sup>9</sup> in all samples except for KJ-19 and KJ-14 from Krafla geothermal sites, which are reasonably consistent with the MORB value of 1.5 × 10<sup>9</sup> (Marty et al., 1989). KJ-19 and KJ-14 have relatively larger CO<sub>2</sub>/<sup>3</sup>He ratios of 1.4 × 10<sup>10</sup> and 2.5 × 10<sup>10</sup>, respectively. This can be accounted for the solubility difference between CO<sub>2</sub> and He (Marty et al., 1989, Sano et al., 1998). Due to the relatively lower solubility of He compared to CO<sub>2</sub>, He is more easily lost from the liquid phase than CO<sub>2</sub> during boiling and steam separation processes (as discussed in Section 3.5.4 boiling and steam separation effects below) or during gas exsolution from supersaturated water. Because there is no correlation observed between CO<sub>2</sub>/<sup>3</sup>He and the sample locations, we suggest that these solubility-controlled fractionation processes potentially result in the relatively higher CO<sub>2</sub>/<sup>3</sup>He ratios in these two samples.

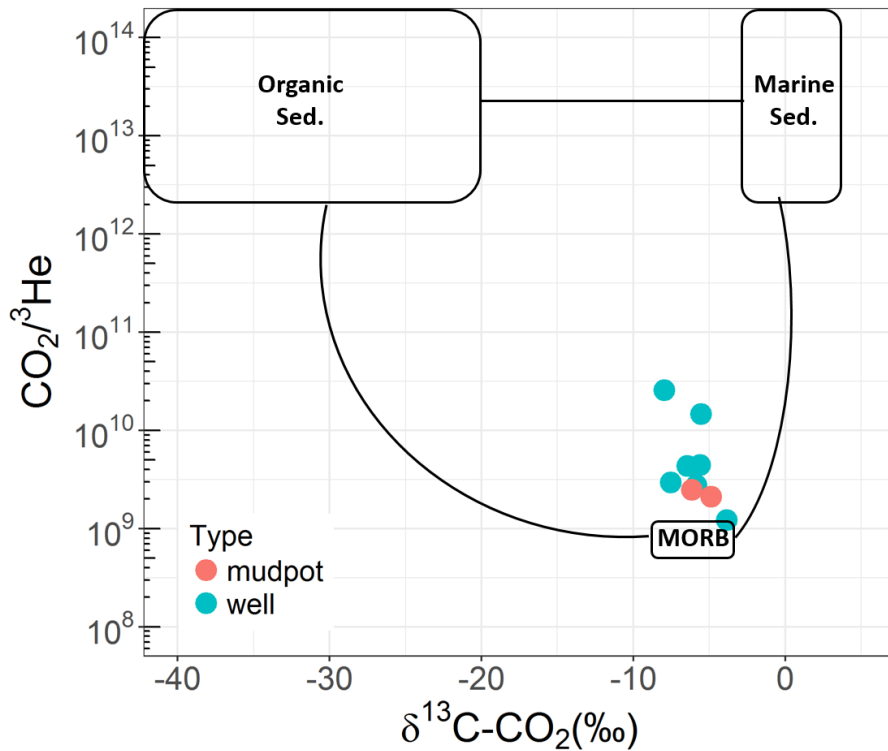


**Fig.4.9.** A plot of  $\text{CO}_2/{}^3\text{He}$  vs.  $\delta^{13}\text{C}$  for Krafla gas samples. The endmember compositions for sedimentary organic sediments, MORB and marine sediments are  $\delta^{13}\text{C} = -30, -6.5$  and  $0 \text{ ‰}$ ; and  $\text{CO}_2/{}^3\text{He} = 1 \times 10^{13}, 2 \times 10^9$  and  $1 \times 10^{13}$ , respectively (Sano and Marty, 1995).

#### 4.5.3 Depletion of atmospheric noble gases in the Krafla geothermal field

Noble gas concentrations ( ${}^4\text{He}$ ,  ${}^{20}\text{Ne}$ ,  ${}^{36}\text{Ar}$ ,  ${}^{84}\text{Kr}$ , and  ${}^{132}\text{Xe}$ ) in Krafla geothermal fluid normalized to noble gas concentrations in Air Saturated Water (ASW) at  $10 \text{ }^\circ\text{C}$  are shown in **Figure 4.10**. The noble gas concentrations in Air Saturated Water (ASW) were calculated with solubility equations of Crovetto et al. (1982) and used for average annual local recharge temperature of  $10 \text{ }^\circ\text{C}$  and an average altitude of 818m in Iceland.

${}^4\text{He}$  concentrations for all samples are found in excess of those expected for ASW at  $10 \text{ }^\circ\text{C}$ , with the values of up to three orders of magnitude higher than that of ASW at  $10 \text{ }^\circ\text{C}$  for sample KJ-27, suggesting significant contributions of crustal and mantle origins. The

atmospheric contribution to  $^4\text{He}$  is negligible in these samples, which will not be further discussed in this work.

However,  $^{20}\text{Ne}$ ,  $^{36}\text{Ar}$ ,  $^{84}\text{Kr}$ , and  $^{132}\text{Xe}$ , in the subsurface fluids are almost entirely derived from the atmosphere dissolved in groundwater at recharge (Ballentine et al., 2002).

Bubbling gas sample Hverir-31 has the highest  $^{20}\text{Ne}$ ,  $^{36}\text{Ar}$  concentrations than the rest of the samples, showing increases in noble gas concentrations by a factor of 3.56 and 1.72 relative to ASW values at 10 °C, respectively. Ne-Ar-Kr-Xe concentrations in samples (KJ-9-1, KJ-9-2, KJ-27, KJ-21-1, and KJ-21-2) are similar to or moderately higher compared to those of ASW at 10 °C. However, apparent atmospheric noble gas depletions with respect to ASW values at 10 °C are observed for the rest of samples (Krisuovic-1, KJ-32, KJ-30, KJ-14, KJ-20, and KJ-19).

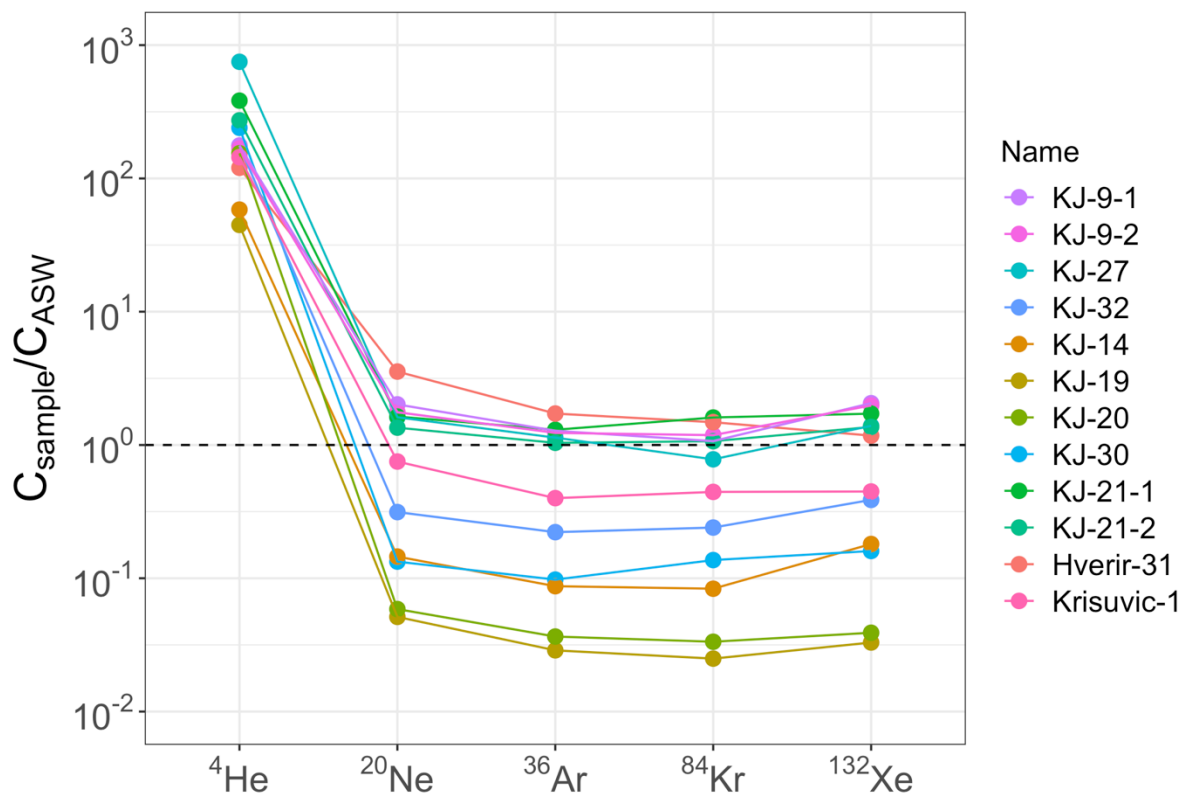


**Fig.4.10.** Noble gas concentrations in Krafla geothermal fluids normalized to noble gas concentrations in Air Saturated Water at 10 °C.

### **Possible reasons for depletion**

Because atmospheric noble gases are derived from water in equilibrium with the atmosphere (Mazor and Bosch, 1987), the initial concentrations of atmospheric noble gases are expected to be close to those expected for ASW at 10 °C. The variation of air-derived noble gas geochemical signatures could be impacted by several mechanisms, such as diffusion and degassing during sampling. For the former mechanism, as there is no obvious isotopic fractionation observed in our samples, a diffusion process is unlikely to be responsible for the depletion (Winckler et al., 2000, Ma et al., 2009). Degassing during sampling can also be ruled out as the sample holders (copper tubes) were pinched off under closed conditions preventing any contact with the atmosphere.

As the above-mentioned potential processes cannot explain what is observed in Krafla, alternative processes, in particular, boiling and steam separation, may be responsible for the observed gas loss relative to those in the initial geothermal fluid.

But for those samples having air-derived noble gas concentrations similar to ASW values, we hypothesize that the addition of air during re-injection (see details in the next section) can potentially increase the concentrations of noble gases which was previously depleted during boiling and steam separation processes in geothermal fluids.

#### **4.5.4 Boiling and steam separation effects in the Krafla geothermal field**

The observed depletion of atmospheric (air-derived) noble gases were potentially caused by the boiling and steam separation processes between liquid and gas phases during

evolution of the geothermal fluid. Once the hot fluid ascends above the water table where the initial dissolved atmospheric noble gases are kept in closed-system conditions by hydrostatic pressure, boiling and steam separation starts, which leads to continuous loss of noble gases from the geothermal reservoir. Because noble gases preferentially partition into the lower density phase, a significant depletion in absolute gas concentrations is found in the residual liquid phase (Winckler et al., 2000, Ma et al., 2009).

Noble gas elemental compositions can be useful tracers of physical changes in the reservoir caused by boiling and steam separation (Mazor and Truesdell, 1984, Mazor and Bosch, 1992, Pinti et al., 2013). Fractionation Factors ( $F(i) = (i^{36}\text{Ar})_{\text{sample}} / (i^{36}\text{Ar})_{\text{air}}$ ) have been described in the 3.4.2 Results section. **Figure 4.11** shows  $F(^{20}\text{Ne})$  vs.  $F(^{132}\text{Xe})$  values and  $F(^{84}\text{Kr})$  vs.  $F(^{132}\text{Xe})$  values measured in Krafla geothermal fluids. Air saturated water (ASW) at 10 °C (the annual temperature of local meteoric recharge in Iceland) and air saturated geothermal water (ASGW) at reservoir temperatures of 180 °C and at 205 °C (the lowest and highest measured geothermal reservoir temperatures in Krafla) are also indicated.

Lighter noble gases (Ne, Ar) are less soluble compared to heavier noble gases (Kr, Xe) in the water (Crovetto et al., 1982, Kennedy et al., 1988, Birkle et al., 2016, Wen et al., 2018). During the boiling and steam separation processes, lighter noble gases would more easily escape into the gas phase, leaving the relative enrichment of Kr, Xe in the residual liquid. In order to reconstruct the subsurface's fluid history, boiling models are required for describing the partitioning of gases between the liquid and vapour phases, which can be given by Rayleigh distillation. Assuming the gas phase is continuously lost from the initial liquid, this process can be expressed by the following equation (Ma et al., 2009):

$$4.6$$

where  $f^{36}\text{Ar}$  is the fraction of  $^{36}\text{Ar}$  remaining in the residual liquid following boiling and steam separation and  $K$  is Henry's constant (Crovetto et al., 1982, Ballentine et al., 2002). Solubility data from Crovetto et al. (1982) were used to simulate boiling and steam phase

separation processes. In **Figure 4.11**, boiling curves for the residual liquid after steam separation were simulated for an ASGW at 180 °C and boiling occurred at lower temperatures of 150 °C and 100 °C, and for an ASGW at 205 °C and boiling occurred at lower temperatures of 180 °C and 150 °C. A simulated curve of an initial ASW of 10 °C followed by boiling and steam separation at temperature of 180 °C is also indicated.

In **Figure 4.11(a)**, F values measured for Krafla samples plot away from all the simulated boiling curves for the residual liquid, after steam separation. Despite this deviation from boiling and steam separation model, it is still worth noting that the sample distribution trend is similar to those simulated boiling curves at different boiling temperatures, showing that  $F(^{20}\text{Ne})$  values decrease with the increase of  $F(^{132}\text{Xe})$  in the residual liquid after boiling. Sample Hvetir-31 collected from gas discharging pool in Hvetir has the highest  $F(^{20}\text{Ne})$  and lowest  $F(^{132}\text{Xe})$  values of 0.56, 2.51 compared to those of other samples.

Measured  $F(^{84}\text{Kr})$  and  $F(^{132}\text{Xe})$  results for samples collected in Krafla are scattered in **Figure 4.11(b)**. All the data plot close to different modelling curves with different boiling temperatures, which might suggest the occurrence of boiling and steam separation processes.

In order to maintain the pressure of the reservoir, some colder used brines or even waste water have been injected back into Krafla geothermal systems since 2002 (Egill Juliusson, 2015). Pinti et al. (2017b) has pointed out that the injectate containing some air bubbles trapped during the re-injection process has significantly affected the noble gas elemental and isotopic signatures in Los Humeros Geothermal fluids.

Therefore, the observed noble gas elemental fractionation in the Krafla geothermal field can be possibly explained by a mixing of: 1) boiling and steam separation processes at hydrothermal reservoir depth; and 2) air addition during re-injection procedure.

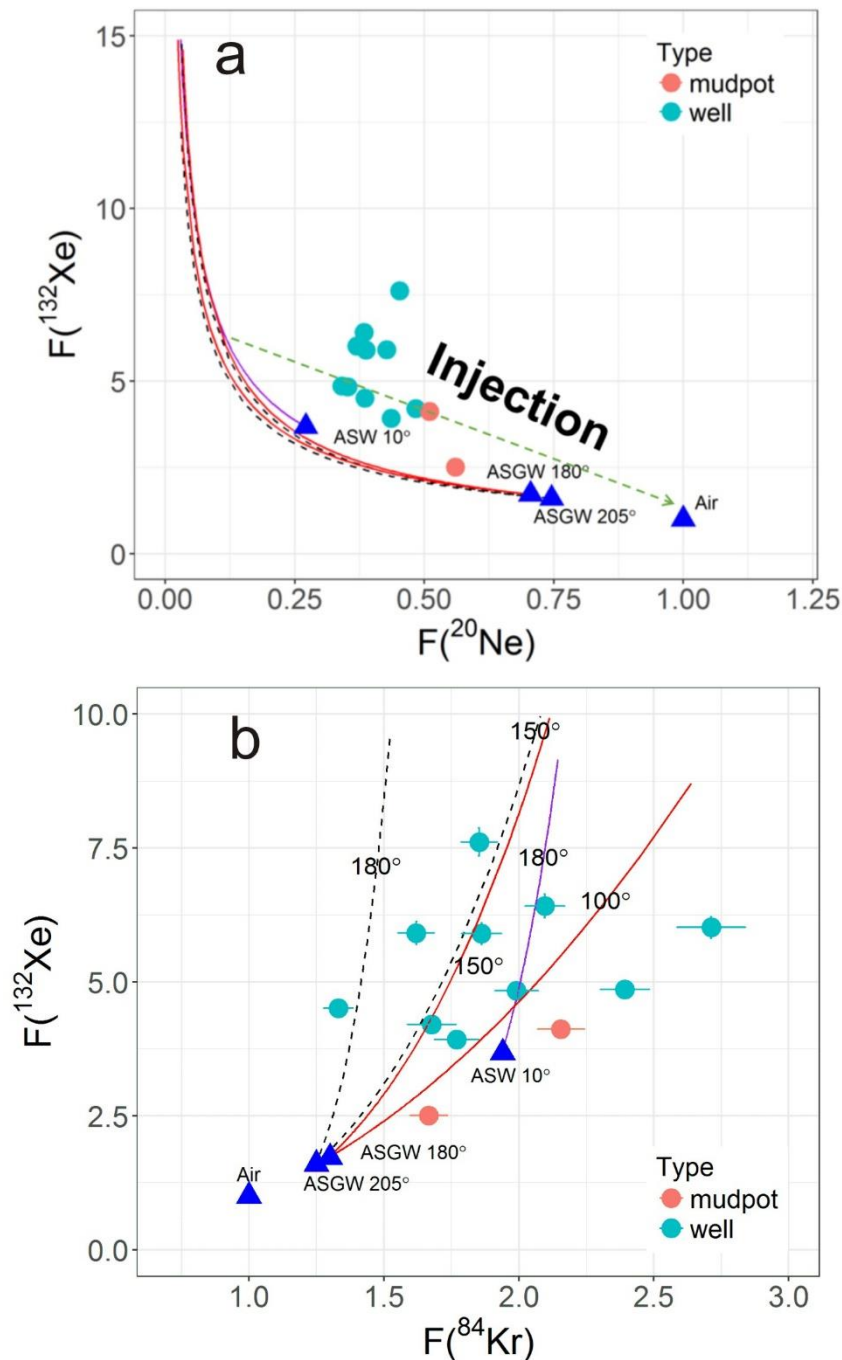


**Fig.4.11.** (a) The  $F(^{20}\text{Ne})$  vs.  $F(^{132}\text{Xe})$  values and (b) the  $F(^{84}\text{Kr})$  vs.  $F(^{132}\text{Xe})$  values measured in Krafla geothermal fluids. Blue triangles represent Air and ASW (Air Saturated Water) at 10 °C and ASGW (Air Saturated Geothermal Water) at 180 °C and 205 °C. The solid red curves are Rayleigh fractionation trends considering an initial ASGW of 180 °C followed by boiling and steam separation at lower temperatures of 150 °C and 100 °C. The dashed black curves are simulated considering an initial ASGW of 205 °C followed by boiling and steam separation at lower temperatures of 180 °C and 150 °C. The solid purple curve represents a simulated modelling with an initial ASW of 10 °C followed by boiling and steam separation at temperature of 180 °C.

## 4.6 Conclusion

Noble gas and stable isotope ( $\delta^{13}\text{C}$  ( $\text{CO}_2$ ),  $\delta^{18}\text{O}$  ( $\text{CO}_2$ ), and  $\delta^{15}\text{N}$  ( $\text{N}_2$ )) data were analysed for eight geothermal boreholes and two gas discharging pools in the Krafla geothermal field. According to tectonic settings in Iceland,  $\text{CO}_2$  in the gas phase derived from geothermal water is considered to be magmatic in origin, with  $\delta^{13}\text{C}$  ( $\text{CO}_2$ ) ranging between -7.99 and -3.86 ‰. Gas samples collected from boreholes have relatively constant mantle-dominated  $^3\text{He}/^4\text{He}$  ratios, giving an average value of 9.47 Ra. Two higher ratios (11.1 Ra and 13.8 Ra) are found in mudpot bubbling gas samples. The high  $^3\text{He}/^4\text{He}$  ratios suggest that the geothermal water reservoir receives deep-seated volatiles and heat from an active magmatic system at depth. Ne, Ar, Kr and Xe isotopic ratios are mainly Air-like.

Solubility driven elemental fractionations (Ne/Ar, Kr/Ar, and Xe/Ar) confirm the hypothesis that the processes of boiling and steam separation have occurred during the circulation of geothermal fluids in the shallow crust in the Krafla field. However, some samples show elemental ratios which cannot be explained by modelled boiling curves for residual liquid after steam separation. This can be accounted for by the addition of air, possibly introduced by re-injection, which have a significant effect on the geochemical signatures of Krafla geothermal fluid.

# 5 Tracing interaction between hydrocarbon and groundwater systems with noble gases in the central Sichuan Basin, China

## 5.1 Introduction

Pioneering work has shown that conventional geochemical tools, such as biomarkers, stable isotopes and vitrinite reflectance analysis, etc., can provide important information about hydrocarbon generation, accumulation and migration processes (Dow, 1974, Stahl, 1978, Philp, 1993, Hughes et al., 1995, Li et al., 2005, Dai et al., 2012), as well as to determine kerogen types, ages and thermal maturity of source rocks in hydrocarbon reservoirs (Dow, 1977, Schoell, 1980, Whiticar et al., 1986, Schoell, 1988, Dai et al., 2014, Li et al., 2015). Groundwater plays a significant role in hydrocarbon formation, transportation and preservation through the hydrocarbon system from source rocks to the reservoirs (Kennedy et al., 1985, Ballentine et al., 1991, Pinti and Marty, 1995, Zhou et al., 2005). However, questions with respect to subsurface fluids dynamics, in particular, the relationship between groundwater flow and hydrocarbon migration, remain enigmatic.

Noble gas systematics have been shown to be effective tracers for subsurface fluid interactions because they are relatively low in abundance and chemically inert (Kennedy et al., 2002, Kipfer et al., 2002, Ozima and Podosek, 2002, Holland and Ballentine, 2006, Byrne et al., 2018). Noble gases associated with subsurface fluids can be derived from three main terrestrial sources, the atmosphere, the crust and the mantle. Firstly, atmosphere-derived noble gases (e.g.  $^{20}\text{Ne}$ ,  $^{36}\text{Ar}$ ,  $^{84}\text{Kr}$  and  $^{132}\text{Xe}$ ) are introduced into the crustal fluid systems dissolved in groundwater during recharge (Torgersen and Kennedy, 1999). Secondly, radiogenic noble gases (e.g.  $^4\text{He}$ ,  $^{40}\text{Ar}$ , and  $^{21}\text{Ne}$ ) are generated within the crust, which are associated with the

radioactive decay of K, U and Th. Thirdly, the partial melting in the mantle related to crustal extension results in the occurrence of mantle-derived noble gases (Battani et al., 2000). Among all three major sources of noble gases, radiogenic and atmosphere-derived noble gases are dominating in hydrocarbon systems proposed by previous studies (Ballentine et al., 1991, Ballentine, 2002, Kennedy et al., 2002, Barry et al., 2016). These differently sourced noble gases have their distinct isotopic compositions and relative abundance patterns, allowing the contributions of each source for noble gases to be resolved. In addition, noble gas elemental abundances are significantly modified by physical processes such as mixing, diffusion, and partitioning between different fluids, e.g., groundwater, oil, gas and igneous melt, etc., which can then be used to identify the mechanisms that control the transport and emplacement of fluids from these sources into the accumulating reservoirs (Kennedy et al., 1985, Ballentine et al., 1991, Lollar et al., 1994, Kennedy et al., 2002, Zhou et al., 2005, Zhou et al., 2012).

In this chapter, both stable and noble gas isotopic data of natural gas samples from the Anyue and Weiyuan gas fields in the central Sichuan basin, China are presented. Sichuan basin is one of the most important on-shore gas producing areas with several different sets of hydrocarbon reservoirs in China. The geological studies regarding hydrocarbon systems such as source rocks, reservoirs and tectonic activity in the Sichuan basin have been documented in many publications (Wei et al., 2008, Dai et al., 2012, Wang et al., 2013, Dai et al., 2014). However, the role of groundwater in the gas generation, migration and accumulation processes remains unclear. The purposes of this study are to: 1) identify and quantify the involvement of crustal, mantle and atmosphere-derived noble gases associated with hydrocarbon generation, migration and accumulation processes; 2) characterize the physical processes responsible for noble gas emplacement into hydrocarbon system during geological timescales, thereby better understanding the role that groundwater plays in transfer of hydrocarbons within sedimentary

basins; and 3) provide new insights into the evolution of petroleum systems, such as natural gas genesis and transportation, subsurface fluid provenance and fluid flow.

## **5.2 Geological setting and sample locations**

### **5.2.1 Geological background of the Sichuan Basin**

The Sichuan Basin, with an area of 190,000 km<sup>2</sup>, is a large and ancient hydrocarbon-bearing superimposed basin located in the western region of the Yangtze craton. It is surrounded by the Micang and Daba mountains in the north, the Daliang mountains in the south, the Longmen and Qionglai mountains in the west and Qiyao mountains in the east (Zhai, 1989a, Zou, 2013, Dai et al., 2014) (**Figure 5.1**). Tectonically, the Sichuan Basin can be divided into East, South (including South and Southwest), West and Central Sichuan gas-oil accumulation zones, separated by the Longquanshan fracture in the west and the Huayingshan fracture in the east (Ma et al., 2008, Wang et al., 2013, Ni et al., 2014).

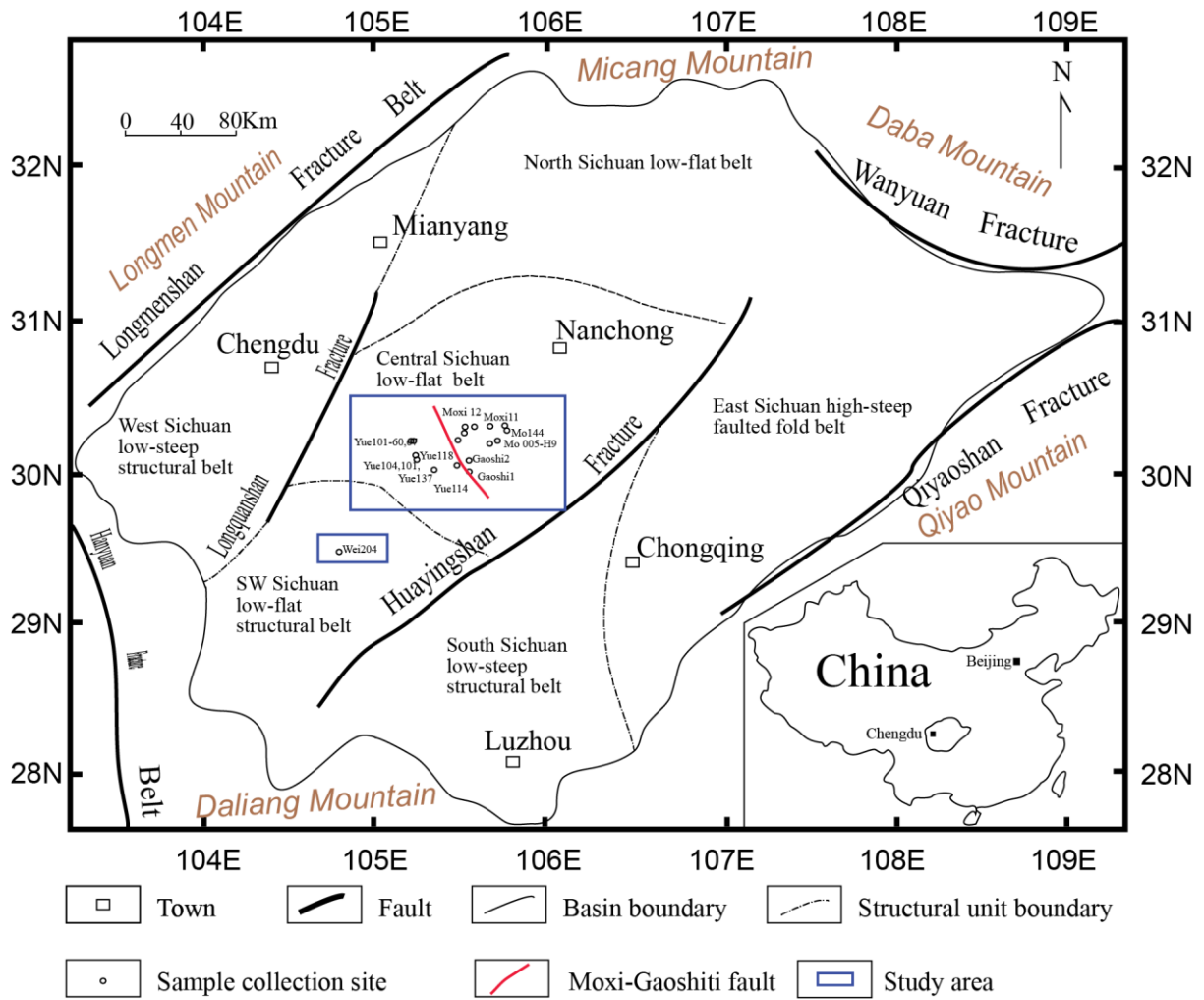


**Fig.5.1.** Geological features in the Sichuan Basin, China and location of sample collection sites (modified from Yuan et al. (2012)).

The basin is a late Triassic foreland basin overlying a Sinian-Middle Triassic (Z1-T2) passive continental margin (Li et al., 2013, Liang et al., 2014, Li et al., 2015). Several stages of tectonic episodes occurred during geological timescales -- Jinning (~ 850 Ma), Chengjiang (~ 700 Ma), Tongwan (~ 570 Ma), Caledonian (~ 320 Ma), Yunnan (~ 270 Ma), Dongwu (~ 256 Ma), Indosinian (205 ~ 195 Ma), Yanshanian (180 ~ 140 Ma) and Himalayan (80 ~ 3Ma) movements (Zhai, 1989b, Tong, 1992, Ni et al., 2014), which played an important role in the formation of Sichuan.

Yangtze Paraplatform is the basement of the Sichuan basin and was formed and developed during Jinning and Chengjiang orogenies. The occurrence of Tongwan movement at the end of Sinian caused elevations and subsidence in the Sichuan basin, resulting in an unconformity between the Upper Sinian and Lower Cambrian. Caledonian movement produced some tensional fault depressions along cratonic margins, which then extended into the platform. Leshan-Longnysi uplift was formed in the central Sichuan Basin at the end of the Silurian (Zhai, 1989b). The Sichuan basin has experienced several volcanic episodes during Yunnan and Dongwu movements, with large-scale basalt eruption in the Permian. In the Early and Middle Triassic, the cratonic margins were uplifted because of the compression from the Paleo-Tethys and the Pacific oceanic crust. As a result, algal banks and oolitic shoals were produced during this process, which caused the retreat of the seawater and then turned the central part of the Sichuan basin into a saline basin (Ma et al., 2008). This is the critical period for transition from marine sediment to fluvial, lacustrine sediment in the Sichuan basin. The western basin boundaries were rapidly uplifted several times by late Indosinian and early Yanshanian movement, with strong depression in the mountain front. A continental basin being characterized by an uplifted centre surrounded by a depression began to form. The late Yanshanian movement caused several strong episodes of folding in some parts of the basin. Then large lateral compression occurred at the end of Cretaceous during the Himalayan movement, which caused the average uplifting amplitude of 3000 m in the central Sichuan Basin (Qin et al., 2017a). Following this, the rhombic-shaped tectonic Sichuan basin has finally formed.

Six main source rocks have been found in the Sichuan basin (**Figure 5.2**), including Lower Cambrian marine shales and mudstones, Lower Silurian marine shales, Lower Permian marine carbonates, Upper Permian marine-lacustrine coal measures, Upper Triassic lacustrine

coal measures and Lower Jurassic lacustrine mudstones (Zhu et al., 2007, Dai et al., 2009, Dai et al., 2012, Ni et al., 2014)

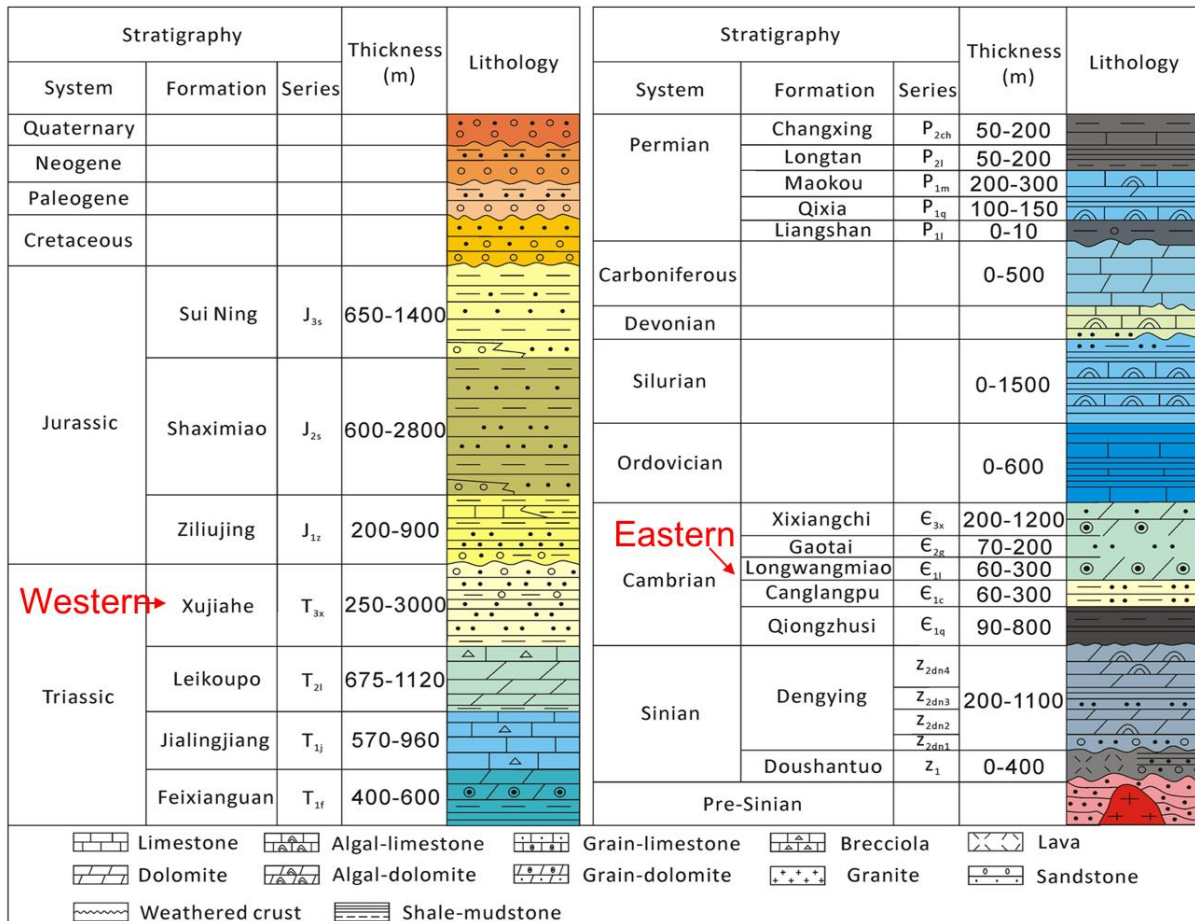


**Fig.5.2.** Schematic of the Sichuan Basin stratigraphy; major formations and lithologies in the basin are indicated (from Yang et al. (2018)).

### 5.2.2 Study area

The gas samples collected for this study are located in the Anyue and Weiyuan gas fields in the central and south of the Sichuan Basin, respectively. Twenty-six samples were taken directly from producing wells in these fields, all of which were subdivided into three

groups by locations, i.e. west and east of Anyue gas field and Weiyuan gas field. Among all samples, 10 samples (e.g. Yue) were collected from the western area of the Anyue gas field while 15 samples (e.g. Moxi) being taken from the eastern part in Gaoshiti-Moxi paleo-uplift (a N-S trending syndepositional paleo-uplift developed during Tongwan movement from late Sinian to early Cambrian (Wei et al., 2014)), Anyue gas field. These two areas in the Anyue gas field, central Sichuan basin are separated by a NW-SE fault system. Wells in the western region have an average depth of 2800m while wells in the eastern area are considerably deeper with an average depth of 4800m. One sample (Wei 204) were collected in the Weiyuan gas field located in the south of the Sichuan basin.

Gas bearing formations in the western and eastern areas of the Anyue gas field and Weiyuan gas field are the Upper Triassic Xujiahe Formation ( $T_{3x}$ ), Lower Cambrian Longwangmiao Formation( $C_{1l}$ ), and Silurian Longmaxi Formation( $S_{1l}$ ), respectively (Dai et al., 2012, Dai et al., 2014, Qin et al., 2017a, Qin et al., 2017b).

Although the natural gas exploration in the Sichuan basin began since 1950, the Xujiahe Formation ( $T_{3x}$ ) gas pools in the central basin have drawn much attention in recent years. Several prospective gas fields, e.g. Guang'an, Hechuan, and Anyue have been explored in the central basin, with the proven reserves of more than  $100 \times 10^8 \text{ m}^3$  (Dai et al., 1997). The Xujiahe Formation in the Upper Triassic is composed of six members ( $T_{3x}^1 \sim T_{3x}^6$ ). Among these,  $T_{3x}^1$ ,  $T_{3x}^3$  and  $T_{3x}^5$  are mainly source rocks with coal seal and dark mudstone, while the other three are mainly sandstone reservoirs (Xiao et al., 2008, Dai et al., 2012). In central Sichuan basin, the total thicknesses of sandstone, mudstone or coal are 200 ~ 340m and 100 ~ 300m, respectively (Yang et al., 2010).

The Longwangmiao Formation gas field was discovered in the central Gaoshiti-Moxi paleo-uplift in 2013, with proven gas reserves of  $4403 \times 10^8 \text{ m}^3$  (Zhou et al., 2015). The

Longwangmiao Formation is mainly dominated by crystalline dolomite, and grain dolomite, forming a regional high quality dolomite reservoir (Chen et al., 2017). The Longwangmiao Formation gas reservoir has the high temperature (up to 140 °C) and ultrahigh pressure with pressure coefficient of 1.5 ~ 1.7 (Qin et al., 2017b). The predominant source rocks in this field are black mudstone and shale of Lower Cambrian Qiongzhusui Formation (Qin et al., 2017b).

Longmaxi shale, one of the most important target layers for shale gas exploration and development in the Sichuan basin, is expected to have gas reserves of  $10 \times 10^{12} \text{m}^3$  in the entire Sichuan basin (Huang, 2009, Zheng et al., 2013). It is characterized by its large thickness, high TOC (TOC > 2%) and vitrinite reflectance (Ro) (Zou, 2013, Dai et al., 2014). The vitrinite reflectance (Ro) in the Longmaxi shale range from 1.6% to 2.28% (Liang et al., 2014), suggesting that the Longmaxi shale has reached the gas generation window.

### **5.3 Sample collection and analytical techniques**

#### **5.3.1 Analysis of natural gas composition and stable carbon isotopic composition**

Samples for gas composition and stable isotope analyses were collected at the well head using stainless steel cylinders with doubled high-pressure valves at both ends. In the process of sampling, the gauge at wellhead was removed, and the steel cylinder was connected to the producing pipeline. Natural gases were flushed through the steel cylinder for 5 minutes prior to sampling in order to remove contamination. Then the valves at the far end of the sample cylinder were closed first, followed by the closure of the valves at the near end of the steel cylinder. Sample cylinders were filled with wellhead natural gas up to the wellhead pressure (70 bar). Gas composition and carbon isotope analyses were carried out at Key Laboratory of

the Research Institute of Petroleum Exploration and Development of PetroChina following procedures described in Qin et al. (2017a), Qin et al. (2017b).

Gas compositions in samples were performed using an Agilent 6890N Gas Chromatograph (GC) fitted with double thermal conductivity detectors (TCD) and a quartz capillary column (30 m × 0.25 mm × 0.25 μm). The inlet temperature and TCD temperature were 150 °C and 200 °C, respectively. The initial oven temperature was held at 40 °C for 7.5 mins isothermally, then heated from 40 °C to 90 °C at a rate of 15 °C /min, then raised from the current temperature of 90 °C to 180 °C at a rate of 6 °C/min. He and N<sub>2</sub> were used as the carrier gases (Qin et al., 2017a, Qin et al., 2017b).

Carbon isotopic compositions were obtained using a MAT 253 gas isotopic mass spectrometer. To separate gas components for individual isotopic analysis (from methane to butane), natural gas samples were firstly introduced into the chromatography column of an SRI 8610C gas chromatograph, and then transferred into combustion furnace by a carrier gas (He) and oxidized into CO<sub>2</sub> by CuO at 850 °C. All of the converted species were then being carried into the mass spectrometer by He for isotopic determination. Carbon isotopic compositions were reported as δ values in per mil (‰) relative to the international standard Vienna Pee Dee belemnite (VPDB). Precision of sample analysis was 0.2‰ one standard deviation (Qin et al., 2017a, Qin et al., 2017b).

### **5.3.2 Noble gas sample collection and analyses**

Samples for noble gas analyses were taken at well heads using 10 mm diameter internally polished refrigeration grade copper tubes sealed by stainless steel pinch-off clamps

on both ends. In order to minimize the air contamination during sampling procedure, well gases were allowed to flush through copper tubes for 10 mins prior to sampling.

Noble gas abundances and isotopic ratios were determined using an Isotopx NGX noble gas mass spectrometer at subsurface fluid isotope geochemistry laboratory at the Lancaster University (see details in chapter 3). In the laboratory, the sample copper tubes were mounted on an all-metal UHV (Ultra High Vacuum) system designed specifically for the extraction, purification and separation of noble gases. A mixture of gas samples were firstly transferred into a calibrated volume of 69.392 cm<sup>3</sup> containing a Baratron monometer at lab temperature. After expansion and dilution, approximately 1cc STP sample gas was isolated and pre-purified by consecutive exposure to a Ti-sponge furnace (heated to 800°C for 20 mins, and then cooled down to room temperature for 20 mins). Subsequently, the sample was expanded into the extraction line fitted with two GP-50 Ti-Zr alloy gas getters (one held at 350°C, the other at room temperature). Majority of reactive gases (hydrocarbons, H<sub>2</sub>S, CO<sub>2</sub> and CO, etc.) in samples are decomposed and removed from the system using a combination of titanium sponge and two getters with no effect on the noble gases. After the removal of reactive gases, mixture of noble gases (He, Ne, Ar, Kr and Xe) were then separated using a series of cryogenic traps prior to inlet into the NGX mass spec for analysis (See details in chapter 3).

The <sup>4</sup>He, <sup>20</sup>Ne and <sup>40</sup>Ar were measured using a Faraday detector while the remaining isotopes were counted on an electron multiplier. A known amount of air standard and a procedural blank were conducted following the same procedure of the sample measurement prior to each sample run. The noble gas elemental abundances for each sample were calculated by normalising to those of air standards after the blank correction. During Ne abundance and isotope analysis, appropriate mass peaks were monitored to correct for interferences caused by doubly charged ions of <sup>40</sup>Ar<sup>2+</sup> and <sup>44</sup>CO<sub>2</sub><sup>2++</sup> on <sup>20</sup>Ne and <sup>22</sup>Ne, respectively. <sup>4</sup>He, <sup>20</sup>Ne, <sup>36</sup>Ar, <sup>84</sup>Kr, and <sup>132</sup>Xe abundances had typical uncertainties of 1.6, 1.7, 1.7, 3.6 and 2.5%, respectively.

All uncertainties are at  $\pm 1\sigma$  level of confidence. Errors include statistical analytical error, blank error, air standard reproducibility, the expansion volume uncertainty and mass spectrometer sensitivity stability.

## 5.4 Results

All gas samples collected from Anyue and Weiyuan gas fields were analyzed for their noble gas abundance and isotopic composition, as well as their major composition abundance and stable carbon isotopes.

### 5.4.1 Major gas species and stable carbon isotopes

The major gases in the western area of the Anyue gas field are comprised of hydrocarbons ( $\text{CH}_4$ ,  $\text{C}_2\text{H}_6$  and  $\text{C}_3\text{H}_8$ ),  $\text{CO}_2$ ,  $\text{N}_2$  and  $\text{O}_2$ , with the concentrations ranging from 85.22 to 93.64 % ( $\text{CH}_4$ ), 3.80 to 8.57 % ( $\text{C}_2\text{H}_6$ ), 0 to 2.54 % ( $\text{C}_3\text{H}_8$ ), 0.12 to 3.05 % ( $\text{CO}_2$ ), 0.05 to 0.71 % ( $\text{N}_2$ ) and 0.01 to 0.16 % ( $\text{O}_2$ ), respectively (**Table 5.1**). In the eastern area,  $\text{CH}_4$  is much more abundant, varying between 98.73 and 99.87 %. The remaining gases observed in the eastern samples are  $\text{C}_2\text{H}_6$  (0.04 ~ 0.21 %),  $\text{CO}_2$  (0 ~ 0.38 %) and  $\text{N}_2$  (0.33 ~ 0.95 %). Dryness coefficient ( $C_1/C_{1-C_5}$ ) represents the percentage of methane relative to the sum of all hydrocarbons measured in samples, which are widely used to identify the origin of natural gases. Generally, the dry coefficient of pyrolysis-originated gas will increase as thermal evolution proceeds. Samples from the eastern area are significantly more enriched in  $\text{CH}_4$  relative to samples from the western area, with the values up to 0.9997. In contrast, dryness coefficients ( $C_1/C_{1-C_5}$ ) in the western samples range from 0.8792 to 0.9551, indicating that natural gases in the western area are characterized by wet gases.

In **Figure 5.3**, a negative correlation between  $\text{CH}_4$  and  $\text{CO}_2$  is observed in samples from the western region of the Anyue gas field. However,  $\text{CH}_4$  remains constant with the increase

of CO<sub>2</sub> for eastern samples in the Anyue gas field. Furthermore, there is no clear trend of the correlation between CH<sub>4</sub> and N<sub>2</sub>, N<sub>2</sub> and CO<sub>2</sub> for all the samples (**Figure 5.4**).

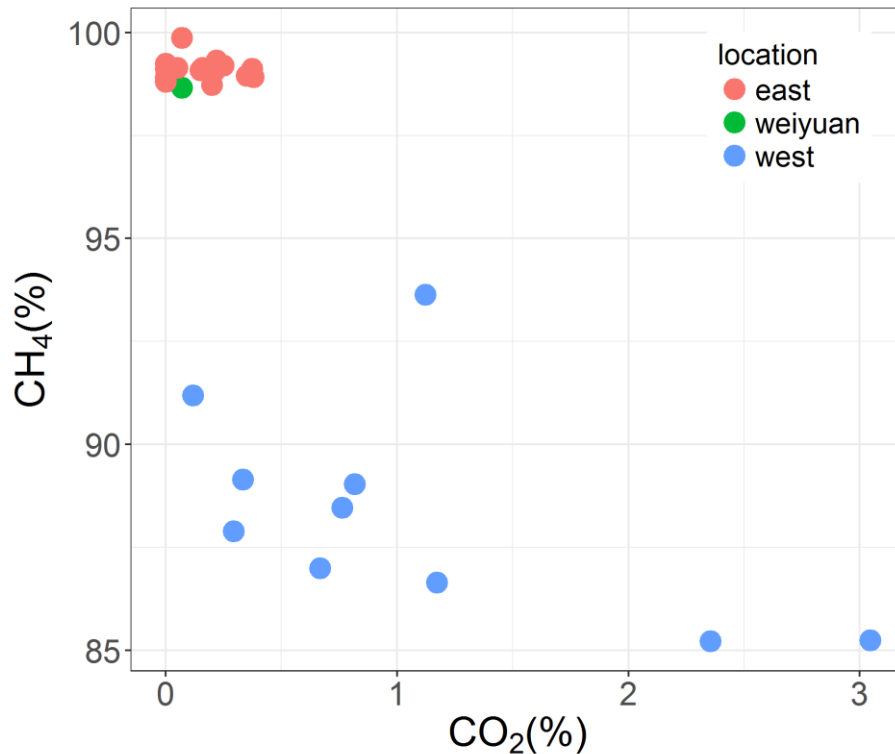


**Fig.5.3.** CH<sub>4</sub> and CO<sub>2</sub> concentrations for samples in study area.

Samples in the western area have much more negative  $\delta^{13}\text{C}$  (CH<sub>4</sub>) values than those in the eastern area, with the  $\delta^{13}\text{C}$  (CH<sub>4</sub>) ranging from -44.3 to -41.3 ‰ and -35.0 to -32.6 ‰ in the western and eastern regions of the Anyue gas field, respectively (**Table 5.1**).  $\delta^{13}\text{C}$  (C<sub>2</sub>H<sub>6</sub>) changes from -27.7 to -25.6 ‰ and -34.6 to -30.5 ‰ in the western and eastern regions, respectively.  $\delta^{13}\text{C}$  (C<sub>3</sub>H<sub>8</sub>) varies from -24.7 to -22.9 ‰ in the western area while there is no  $\delta^{13}\text{C}$  (C<sub>3</sub>H<sub>8</sub>) data obtained for samples from the eastern area. Notably,  $\delta^{13}\text{C}$  (CH<sub>4</sub>) increases with the increase of CH<sub>4</sub> content while  $\delta^{13}\text{C}$  (C<sub>2</sub>H<sub>6</sub>) decreases with the increase of C<sub>2</sub>H<sub>6</sub> content in the western area (**Figure 5.5**). According to the major gas compositions and carbon isotope data described above, the natural gas in the Anyue and Weiyuan gas fields is most likely thermogenic in origin, which is consistent with previous studies (Dai et al., 2012, Chen et al.,

2017, Qin et al., 2017a, Qin et al., 2017b). However, natural gases in different regions have experienced different stages of thermal evolution. Natural gas in the eastern region ( $R_o = 2.0 \sim 3.5 \%$ ) (Zou et al., 2014) has much greater thermal maturity than natural gas in the western region ( $R_o = 1.0 \sim 1.3\%$ ) (Qin et al., 2017a), which demonstrated heavier  $\delta^{13}\text{C}$  ( $\text{CH}_4$ ) and lower amounts of heavy hydrocarbons ( $\text{C}_2^+$ ) compared to those in the western area, Anyue gas field.

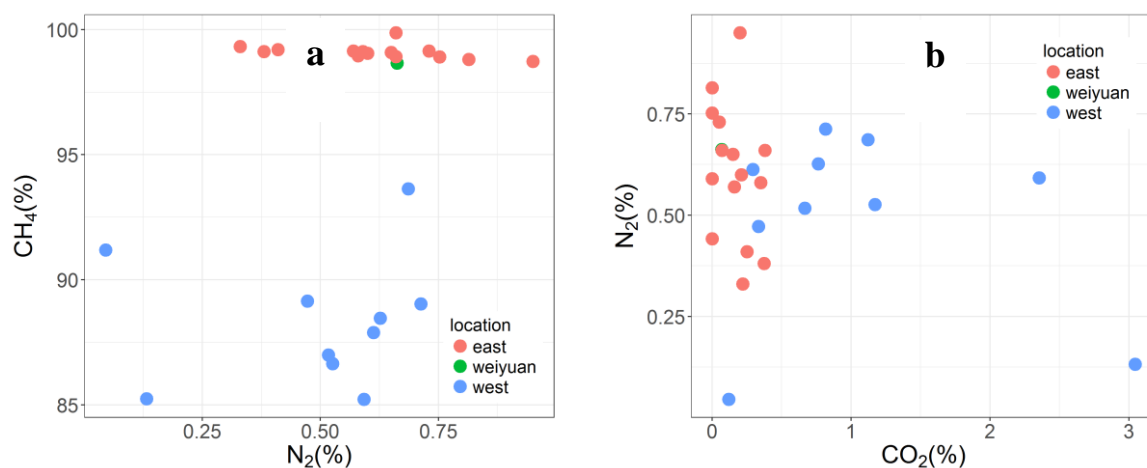


**Fig.5.4.** a)  $\text{CH}_4$  concentrations vs.  $\text{N}_2$  concentrations. b)  $\text{N}_2$  concentrations vs.  $\text{CO}_2$  concentrations for gas samples in this study. There is no clear trend of the correlation between  $\text{CH}_4$  and  $\text{N}_2$ ,  $\text{N}_2$  and  $\text{CO}_2$  for all the samples.

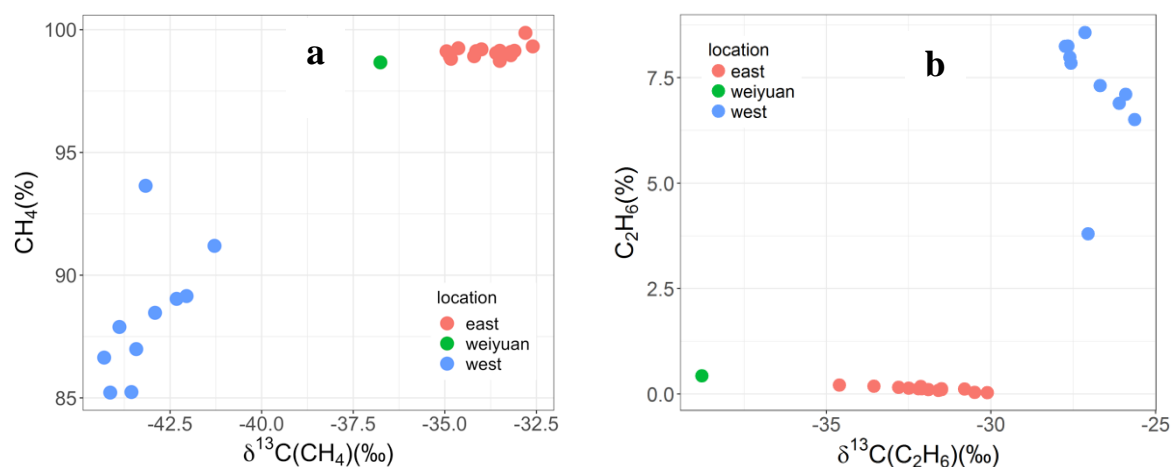


**Fig.5.5.** a)  $\text{CH}_4$  concentrations vs.  $\delta^{13}\text{C}(\text{CH}_4)$ . b)  $\text{C}_2\text{H}_6$  concentrations vs.  $\delta^{13}\text{C}(\text{C}_2\text{H}_6)$  for gas samples in this study.  $\delta^{13}\text{C}(\text{CH}_4)$  increases with the increase of  $\text{CH}_4$  content while  $\delta^{13}\text{C}(\text{C}_2\text{H}_6)$  decreases with the increase of  $\text{C}_2\text{H}_6$  content in the western area.

**Table 5.1** Major gas composition and stable carbon isotopes.

Well	Location	Gas composition (%)										C1/C1-C5	Stable isotopes		
		CH <sub>4</sub> (±2%)	C <sub>2</sub> H <sub>6</sub> (±2%)	C <sub>3</sub> H <sub>8</sub> (±2%)	IC <sub>4</sub> (±2%)	NC <sub>4</sub> (±2%)	IC <sub>5</sub> (±2%)	NC <sub>5</sub> (±2%)	CO <sub>2</sub> (±2%)	O <sub>2</sub> (±2%)	N <sub>2</sub> (±2%)		δ <sup>13</sup> C (CH <sub>4</sub> ) (±0.2‰)	δ <sup>13</sup> C (C <sub>2</sub> ) (±0.2‰)	δ <sup>13</sup> C (C <sub>3</sub> ) (±0.2‰)
Yue 101-11	west	88.47	7.31	1.80	0.34	0.28	0.20	0.06	0.76	0.14	0.63	0.8984	-42.9	-26.7	-23.2
Yue 101	west	93.64	3.80	0.00	0.47	0.00	0.12	0.00	1.12	0.15	0.69	0.9551	-43.2	-27.0	-23.9
Yue 104	west	85.24	8.25	2.46	0.39	0.33	0.10	0.03	3.05	0.02	0.13	0.8806	-43.6	-27.7	-24.7
Yue 137	west	85.22	8.24	2.52	0.42	0.41	0.12	0.00	2.36	0.13	0.59	0.8792	-44.1	-27.7	-24.6
Yue 118	west	87.89	7.85	2.31	0.38	0.37	0.12	0.03	0.29	0.14	0.61	0.8882	-43.9	-27.6	-24.7
Yue 103	west	89.15	7.11	1.80	0.45	0.38	0.17	0.04	0.33	0.11	0.47	0.8997	-42.1	-25.9	-23.0
Yue 101-60	west	89.04	6.89	1.68	0.33	0.26	0.12	0.04	0.82	0.16	0.71	0.9053	-42.3	-26.1	-23.3
Yue 101-67	west	91.19	6.51	1.46	0.33	0.27	0.07	0.00	0.12	0.01	0.05	0.9135	-41.3	-25.6	-22.9
Yue 101-93-H1	west	86.64	7.98	2.54	0.47	0.45	0.10	0.00	1.17	0.12	0.53	0.8825	-44.3	-27.6	-24.4
Yue 101-76-X2	west	86.99	8.57	2.53	0.51	0.00	0.10	0.00	0.67	0.12	0.52	0.8814	-43.4	-27.1	-23.9
Wei 204	weiyuan	98.67	0.44	0.01	0.00	0.00	0.00	0.00	0.07	0.15	0.66	0.9955	-36.8	-38.8	-41.2
Moxi 13	east	99.09	0.11	0.00	0.00	0.00	0.00	0.00	0.15	0.00	0.65	0.9989	-33.2	-31.5	NA
Moxi 9	east	99.14	0.09	0.00	0.00	0.00	0.00	0.00	0.05	0.00	0.73	0.9991	-33.1	-31.6	-25.9
Moxi 009-3-X1	east	99.14	0.12	0.00	0.00	0.00	0.00	0.00	0.16	0.00	0.57	0.9988	-33.5	-30.8	-25.9
Moxi 12	east	98.96	0.11	0.00	0.00	0.00	0.00	0.00	0.35	0.00	0.58	0.9989	-33.2	-31.9	NA
Gaoshi 2	east	98.92	0.04	0.00	0.00	0.00	0.00	0.00	0.38	0.00	0.66	0.9996	-34.2	-30.5	-25.4
Moxi 204	east	99.87	0.13	0.00	0.00	0.00	0.00	0.00	0.07	0.00	0.66	0.9987	-32.8	-31.5	-26.0
Moxi 11	east	98.73	0.12	0.00	0.00	0.00	0.00	0.00	0.20	0.00	0.95	0.9988	-33.5	-31.5	NA
Mo 005-H10	east	99.24	0.21	0.00	0.00	0.00	0.00	0.00	0.00	0.10	0.44	0.9979	-34.6	-34.6	NA
Mo 004-H9	east	99.12	0.16	0.00	0.00	0.00	0.00	0.00	0.00	0.13	0.59	0.9984	-35.0	-32.8	NA
Moxi 8	east	99.05	0.14	0.00	0.00	0.00	0.00	0.00	0.21	0.00	0.60	0.9986	-33.6	-32.5	NA
Mo144	east	98.90	0.18	0.00	0.00	0.00	0.00	0.00	0.00	0.16	0.75	0.9982	-34.9	-32.1	NA
Mo 005-H9	east	98.81	0.19	0.00	0.00	0.00	0.00	0.00	0.00	0.18	0.81	0.9981	-34.8	-33.6	NA
Moxi 008-H1	east	99.32	0.13	0.00	0.00	0.00	0.00	0.00	0.22	0.00	0.33	0.9987	-32.6	-32.2	-29.3
Moxi 008-7-H1	east	99.20	0.13	0.00	0.00	0.00	0.00	0.00	0.25	0.00	0.41	0.9987	-34.0	-32.1	NA

## 5.4.2 Noble gases

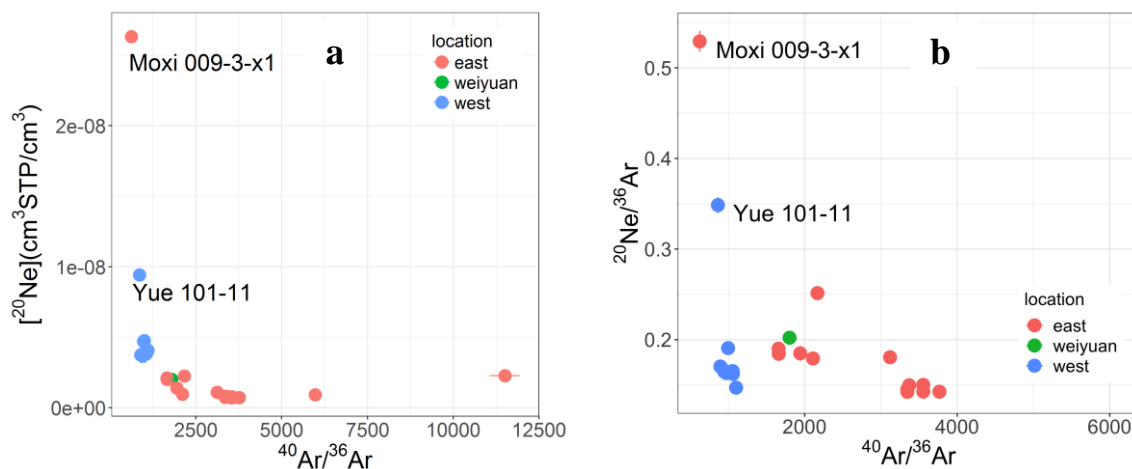


**Fig.5.6.** a)  $^{20}\text{Ne}$  concentrations vs.  $^{40}\text{Ar}/^{36}\text{Ar}$  ratios, and b)  $^{20}\text{Ne}/^{36}\text{Ar}$  vs.  $^{40}\text{Ar}/^{36}\text{Ar}$  ratios for gas samples in this study. Two outlier samples (Yue 101-11 and Moxi 009-3-x1) are indicated.

Noble gas abundances and isotopic compositions are summarized in **Tables 5.2 and 5.3**. It is clear that Yue 101-11 in the western area and Moxi 009-3-x1 in the eastern area have distinct noble gas signatures from other samples in the same sampling areas. In **Figure 5.6 (a)**,  $^{20}\text{Ne}$  concentrations in gas samples are relatively constant in both the western and eastern areas, except for Yue 101-11, Moxi 009-3-x1, which have the highest values of up to  $9.41 \times 10^{-9}$  and  $2.63 \times 10^{-8} \text{ cm}^3\text{STP}/\text{cm}^3$ , respectively. In addition, measured  $^{20}\text{Ne}/^{36}\text{Ar}$  ratios of 0.3485 and 0.5292 for Yue 101-11(west) and Moxi 009-3-x1(east) are much greater than other samples in their fields (**Figure 5.6 (b)**), similar to atmospheric  $^{20}\text{Ne}/^{36}\text{Ar}$  ratio of 0.52, indicating large contribution from air. Therefore, these two samples (Yue 101-11, Moxi 009-3-x1) are considered to be outlier samples which are significantly contaminated by air, that most likely occurred during sample collection process.

### 5.4.2.1 Helium

$^4\text{He}$  concentrations in the western and eastern samples vary from  $1.72 \times 10^{-4}$  to  $2.84 \times 10^{-4} \text{ cm}^3\text{STP/cm}^3$  and from  $9.01 \times 10^{-5}$  to  $1.59 \times 10^{-4} \text{ cm}^3\text{STP/cm}^3$ , respectively (**Figure 5.7 (a)**). Measured  $^3\text{He}/^4\text{He}$  ratios  $R$ , are normalised to the atmospheric  $^3\text{He}/^4\text{He}$  ratio  $R_a$  of  $1.4 \times 10^{-6}$  (Ozima and Podosek, 2002).  $R/R_a$  values measured in samples from the western and eastern areas range from 0.0096 to 0.0196 and 0.0115 to 0.0256, respectively, suggesting a strong crustal signature.  $^4\text{He}/^{20}\text{Ne}$  ratios in samples are much higher than the atmosphere value of  $^4\text{He}/^{20}\text{Ne}=0.288$ , indicating that the atmospheric He contributions are negligible (**Figure 5.7 (b)**). Assuming  $R/R_a = 8.0$  and  $0.02$  are endmembers for mantle and crustal-radiogenic sources, respectively (Ballentine and Burnard, 2002, Dunai and Porcelli, 2002), then  $^4\text{He}$  in all the samples are almost entirely crustal derived ( $>99\%$ ). The crustal derived helium in samples indicates tectonically stable conditions during the formation of the Sichuan basin, which prevented significant volatile contributions from mantle (Ni et al., 2014, Wei et al., 2014).

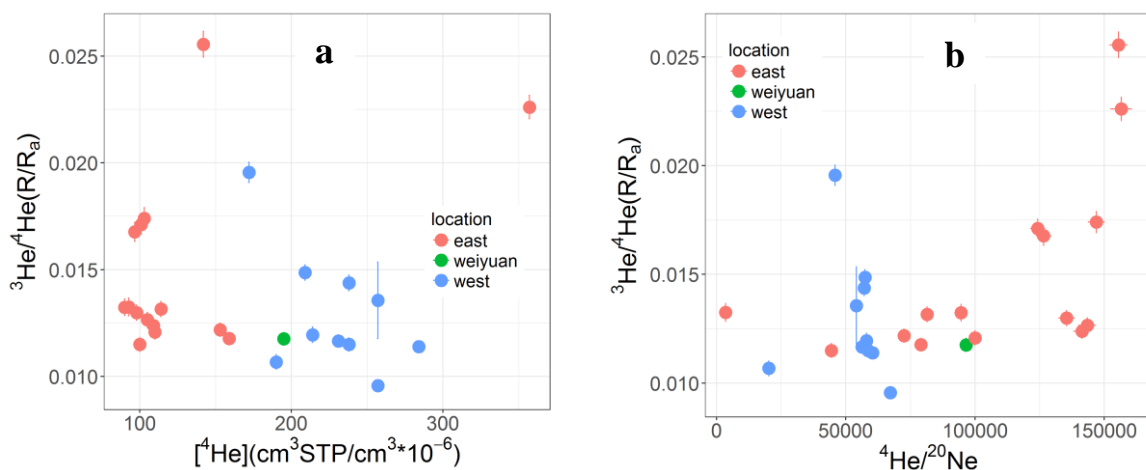


**Fig.5.7.** a)  $^3\text{He}/^4\text{He}$  ratios ( $R/R_a$ ) vs.  $^4\text{He}$  concentrations; and b)  $^3\text{He}/^4\text{He}$  ratios ( $R/R_a$ ) versus  $^4\text{He}/^{20}\text{Ne}$  ratios.  $R/R_a$  values measured in samples from western and eastern areas range from 0.0096 to 0.0196 and 0.0115 to 0.0256, respectively, suggesting strong crustal contributions.

#### 5.4.2.2 Neon

Measured  $^{20}\text{Ne}$  concentrations in samples from the western and eastern areas range between  $3.64 \times 10^{-9}$  to  $4.75 \times 10^{-9} \text{ cm}^3\text{STP/cm}^3$  and  $7.01 \times 10^{-10}$  to  $2.25 \times 10^{-9} \text{ cm}^3\text{STP/cm}^3$ , respectively.  $^{20}\text{Ne}$  is predominantly derived from groundwater previously equilibrated with atmosphere, then incorporated into the subsurface fluid systems via phase interaction.  $^{20}\text{Ne}/^{22}\text{Ne}$  and  $^{21}\text{Ne}/^{22}\text{Ne}$  ratios in samples from the western area vary between 9.51 to 10.44 and 0.0415 to 0.0497, respectively, while ratios for samples from the eastern area are between 8.96 to 10.14 and 0.0442 to 0.0799, respectively. **Figure 5.8** illustrates the measured  $^{20}\text{Ne}/^{22}\text{Ne}$  and  $^{21}\text{Ne}/^{22}\text{Ne}$  ratios from all samples in the study. Neon isotope ratios in samples from both the eastern area and western area suggest that a two-component mixing process between the air and crust endmembers is the major process happening in the gas reservoirs. There is also minor addition from mantle component in the samples (Zhou et al., 2005, Zhou et al., 2012, Byrne et al., 2018, Warr et al., 2018). By taking air, mantle and crustal Ne component endmembers as  $^{20}\text{Ne}/^{22}\text{Ne}_{\text{air}} = 9.80$ ,  $^{21}\text{Ne}/^{22}\text{Ne}_{\text{air}} = 0.029$ ,  $^{20}\text{Ne}/^{22}\text{Ne}_{\text{mntl}} = 12.5$ ,  $^{21}\text{Ne}/^{22}\text{Ne}_{\text{mntl}} = 0.06$ ,  $^{20}\text{Ne}/^{22}\text{Ne}_{\text{crust}} = 0.30$  and  $^{21}\text{Ne}/^{22}\text{Ne}_{\text{crust}} = 0.52$  (Ballentine and Burnard, 2002), it is possible to resolve the contribution of atmospheric, mantle and crustal Ne components.

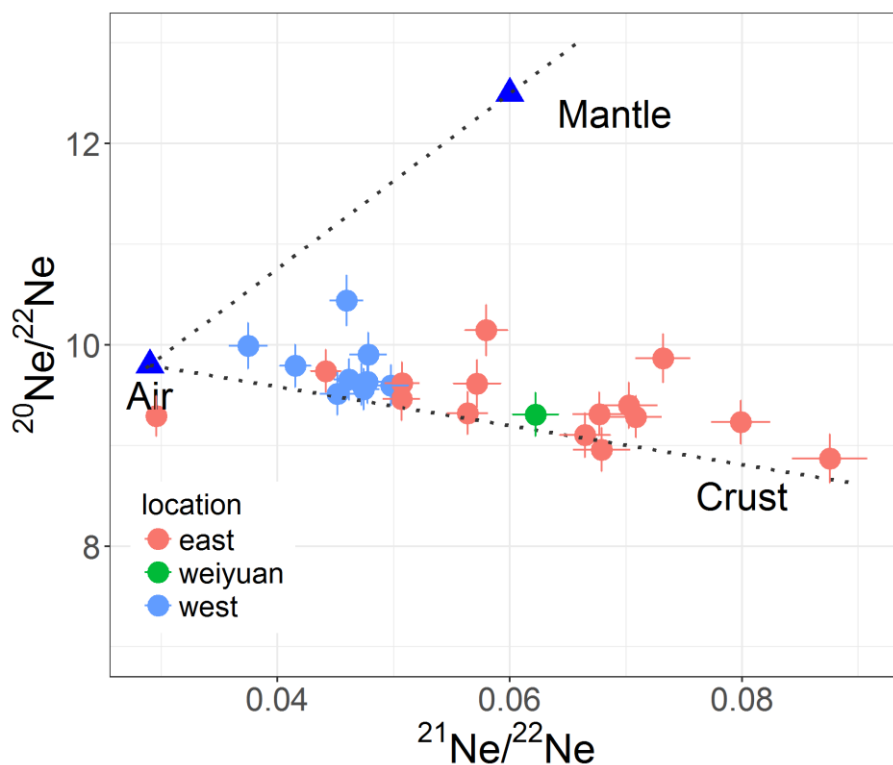
$$(20)_{\text{air}} = (20)_{\text{meas}} \times \frac{\left\{ \left( \frac{21}{22} \right)_{\text{mntl}} - \left( \frac{21}{22} \right)_{\text{rad}} + \left( \frac{22}{20} \right)_{\text{meas}} \times \left( \left( \frac{21}{22} \right)_{\text{rad}} \times \left( \frac{20}{22} \right)_{\text{mntl}} - \left( \frac{21}{22} \right)_{\text{mntl}} \times \left( \frac{20}{22} \right)_{\text{rad}} \right) + \left( \frac{21}{20} \right)_{\text{meas}} \times \left( \left( \frac{20}{22} \right)_{\text{rad}} - \left( \frac{20}{22} \right)_{\text{mntl}} \right) \right\}}{\left\{ \left( \frac{21}{22} \right)_{\text{mntl}} - \left( \frac{21}{22} \right)_{\text{rad}} + \left( \frac{22}{20} \right)_{\text{air}} \times \left( \left( \frac{21}{22} \right)_{\text{rad}} \times \left( \frac{20}{22} \right)_{\text{mntl}} - \left( \frac{21}{22} \right)_{\text{mntl}} \times \left( \frac{20}{22} \right)_{\text{rad}} \right) + \left( \frac{21}{20} \right)_{\text{air}} \times \left( \left( \frac{20}{22} \right)_{\text{rad}} - \left( \frac{20}{22} \right)_{\text{mntl}} \right) \right\}} \quad 5.1$$

$$(21)_{\text{mntl}} = (21)_{\text{meas}} \times \frac{\left\{ \left( \frac{20}{22} \right)_{\text{air}} - \left( \frac{20}{22} \right)_{\text{rad}} + \left( \frac{22}{20} \right)_{\text{meas}} \times \left( \left( \frac{21}{22} \right)_{\text{air}} \times \left( \frac{20}{22} \right)_{\text{rad}} - \left( \frac{20}{22} \right)_{\text{air}} \times \left( \frac{21}{22} \right)_{\text{rad}} \right) + \left( \frac{20}{21} \right)_{\text{meas}} \times \left( \left( \frac{21}{22} \right)_{\text{rad}} - \left( \frac{21}{22} \right)_{\text{air}} \right) \right\}}{\left\{ \left( \frac{20}{22} \right)_{\text{air}} - \left( \frac{20}{22} \right)_{\text{rad}} + \left( \frac{22}{21} \right)_{\text{mntl}} \times \left( \left( \frac{21}{22} \right)_{\text{air}} \times \left( \frac{20}{22} \right)_{\text{rad}} - \left( \frac{20}{22} \right)_{\text{air}} \times \left( \frac{21}{22} \right)_{\text{rad}} \right) + \left( \frac{20}{21} \right)_{\text{mntl}} \times \left( \left( \frac{21}{22} \right)_{\text{rad}} - \left( \frac{21}{22} \right)_{\text{air}} \right) \right\}} \quad 5.2$$

$$(22)_{\text{rad}} = (22)_{\text{meas}} \times \frac{\left\{ \left( \frac{20}{22} \right)_{\text{air}} \times \left( \frac{21}{22} \right)_{\text{mntl}} - \left( \frac{20}{22} \right)_{\text{mntl}} \times \left( \frac{21}{22} \right)_{\text{air}} + \left( \frac{21}{22} \right)_{\text{meas}} \times \left( \left( \frac{20}{22} \right)_{\text{mntl}} - \left( \frac{20}{22} \right)_{\text{air}} \right) + \left( \frac{20}{22} \right)_{\text{meas}} \times \left( \left( \frac{21}{22} \right)_{\text{air}} - \left( \frac{21}{22} \right)_{\text{mntl}} \right) \right\}}{\left\{ \left( \frac{20}{22} \right)_{\text{air}} \times \left( \frac{21}{22} \right)_{\text{mntl}} - \left( \frac{20}{22} \right)_{\text{mntl}} \times \left( \frac{21}{22} \right)_{\text{air}} + \left( \frac{21}{22} \right)_{\text{rad}} \times \left( \left( \frac{20}{22} \right)_{\text{mntl}} - \left( \frac{20}{22} \right)_{\text{air}} \right) + \left( \frac{20}{22} \right)_{\text{rad}} \times \left( \left( \frac{21}{22} \right)_{\text{air}} - \left( \frac{21}{22} \right)_{\text{mntl}} \right) \right\}} \quad 5.3$$

Where parentheses subscripts rad, air, mntl and meas denote crust, air, mantle and measured values, respectively.

Resolved excess  $^{21}\text{Ne}^*$  ( $^{21}\text{Ne}_{\text{rad}} + ^{21}\text{Ne}_{\text{mntl}}$ ) accounts for 36.6 % to 56.4 % and 40.7 % to 74.3 % of  $^{21}\text{Ne}$  concentrations in the western and eastern samples, respectively. Except for Yue 101, which has 67.9% mantle-derived  $^{21}\text{Ne}$ ,  $^{21}\text{Ne}^*$  is mainly crustal-dominated with average magmatic contribution of 17.5 %, 15.6 % of  $^{21}\text{Ne}^*$  in the western and eastern area, respectively. Samples in the western and eastern area have  $^4\text{He}/^{21}\text{Ne}^*$  ratios between  $2.18 \times 10^7$  to  $3.09 \times 10^7$  and  $2.17 \times 10^7$  to  $3.22 \times 10^7$ , respectively. These are significantly higher than the measured average crustal value of  $^4\text{He}/^{21}\text{Ne}^* = 1.5 \times 10^7$  (Kennedy et al., 1990), which is associated with the shallow, low temperature geological settings in the study (Gilfillan et al., 2008).



### 5.4.2.3 Argon

Similar to  $^{20}\text{Ne}$ , atmosphere-derived  $^{36}\text{Ar}$  concentrations in samples range from  $2.20 \times 10^{-8}$  to  $2.88 \times 10^{-8}$  and  $4.52 \times 10^{-9}$  to  $1.11 \times 10^{-8} \text{ cm}^3\text{STP/cm}^3$  in the western and eastern areas of the Anyue gas field, respectively. Samples from the eastern area have considerably higher  $^{40}\text{Ar}/^{36}\text{Ar}$  ratios (3043 on average) than those from the western area which has an average  $^{40}\text{Ar}/^{36}\text{Ar}$  ratio of 1003 (**Figure 5.9**), showing significant deviation from atmospheric  $^{40}\text{Ar}/^{36}\text{Ar}$  value of 295.5 (Ballentine and Burnard, 2002, Ozima and Podosek, 2002). Resolved non-atmosphere derived excess  $^{40}\text{Ar}$  ( $^{40}\text{Ar}^*$ ) was calculated as follows:

$$^{40}\text{Ar}^* = ^{40}\text{Ar}_{\text{meas}} \times [1 - (^{40}\text{Ar} / ^{36}\text{Ar})_{\text{air}} / (^{40}\text{Ar} / ^{36}\text{Ar})_{\text{meas}}] \quad 5.4$$

where  $(^{40}\text{Ar}/^{36}\text{Ar})_{\text{air}}=295.5$  (Ballentine and Burnard, 2002, Ozima and Podosek, 2002).

Resolved non-atmosphere derived excess  $^{40}\text{Ar}$  ( $^{40}\text{Ar}^*$ ) contributes from 67 to 73.17 % and 82.17 to 95.05 % of measured  $^{40}\text{Ar}$  concentrations in the western and eastern samples, respectively. The resolved  $^4\text{He}/^{40}\text{Ar}^*$  ratios of western and eastern gases vary between 10.7 to 14.73 and 5.53 to 10.69, respectively. The Measured average  $^4\text{He}/^{40}\text{Ar}^*$  ratio is 13.4 and 7.27 for samples from the western and eastern area, respectively, both of which are higher than average crustal production value of  $^4\text{He}/^{40}\text{Ar}^*=4.9$  (Ballentine et al., 1991). This is consistent with resolved  $^4\text{He}/^{21}\text{Ne}^*$  ratios described above.

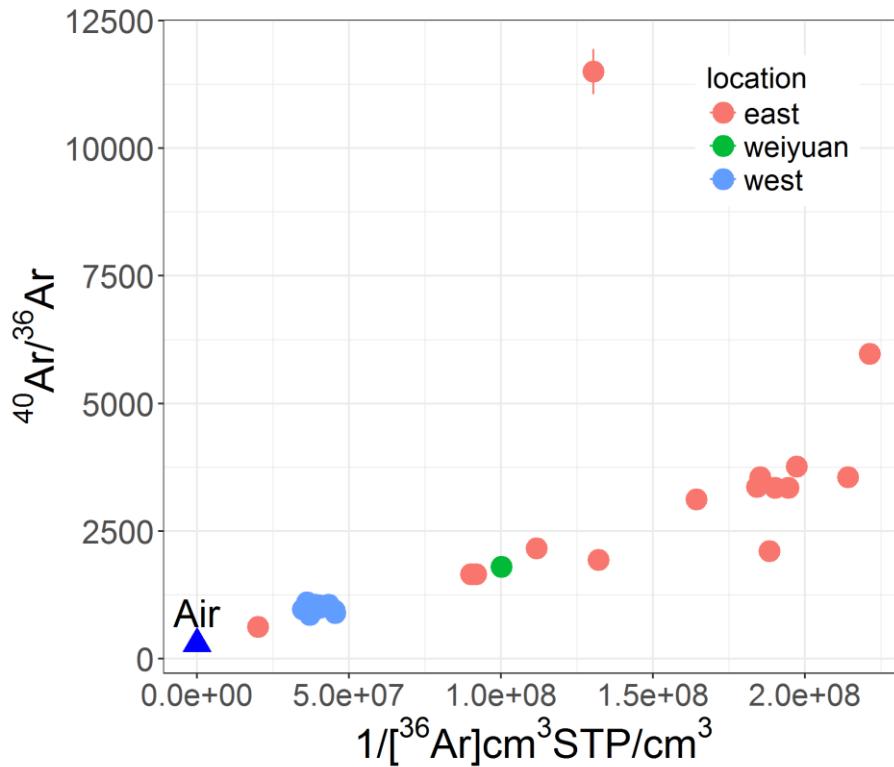


**Fig.5.9.**  $^{40}\text{Ar}/^{36}\text{Ar}$  ratios vs  $1/^{36}\text{Ar}$ .  $^{40}\text{Ar}/^{36}\text{Ar}$  ratios in all samples are significantly higher than air value of 295.5 (Ozima and Podosek, 2002).

#### 5.4.2.4 Krypton and Xenon

$^{84}\text{Kr}$  concentrations in gas samples from the western and eastern areas vary between  $9.14 \times 10^{-10}$  to  $1.62 \times 10^{-9}$  and  $4.11 \times 10^{-10}$  to  $6.96 \times 10^{-10} \text{ cm}^3\text{STP}/\text{cm}^3$ , respectively. Taking an atmospheric  $^{86}\text{Kr}/^{84}\text{Kr} = 0.302$ , they are predominantly air-like, having an average  $^{86}\text{Kr}/^{84}\text{Kr}$  values of 0.309 and 0.317 in the western and eastern area, respectively.  $^{132}\text{Xe}$  concentrations in all samples range between  $5.12 \times 10^{-11}$  to  $2.13 \times 10^{-10}$  and  $3.53 \times 10^{-11}$  to  $7.28 \times 10^{-11} \text{ cm}^3\text{STP}/\text{cm}^3$  in the western and eastern samples, respectively.  $^{136}\text{Xe}/^{132}\text{Xe}$  ratios in samples are indistinguishable from the air value of  $^{136}\text{Xe}/^{132}\text{Xe} = 0.3293$ , varying in the western and eastern region between 0.3198 to 0.3322 and 0.3213 to 0.3399, respectively.

**Table 5.2** Sample location, strata and noble gas concentrations.

Well	Latitude (°N)	Longitude (°E)	Strata	<sup>4</sup> He ( $\times 10^{-5}$ ) cm <sup>3</sup> STP/cm <sup>3</sup>	<sup>20</sup> Ne ( $\times 10^{-10}$ ) cm <sup>3</sup> STP/cm <sup>3</sup>	<sup>20</sup> Ne <sup>+</sup> ( $\times 10^{-10}$ ) cm <sup>3</sup> STP/cm <sup>3</sup>	<sup>40</sup> Ar ( $\times 10^{-5}$ ) cm <sup>3</sup> STP/cm <sup>3</sup>	<sup>36</sup> Ar ( $\times 10^{-9}$ ) cm <sup>3</sup> STP/cm <sup>3</sup>	<sup>36</sup> Ar <sup>+</sup> ( $\times 10^{-9}$ ) cm <sup>3</sup> STP/cm <sup>3</sup>	<sup>84</sup> Kr ( $\times 10^{-10}$ ) cm <sup>3</sup> STP/cm <sup>3</sup>	<sup>132</sup> Xe ( $\times 10^{-11}$ ) cm <sup>3</sup> STP/cm <sup>3</sup>
<i>West area in Anyue</i>											
Yue 101	30-6-40	105-16-14	T <sub>3</sub> x <sup>2</sup>	25.7±0.363	47.5±0.882	30.8±0.938	2.48±0.035	24.9±0.42	24.5±0.679	12.6±0.381	15.8±0.297
Yue 104	30-6-40	105-16-14	T <sub>3</sub> x <sup>2</sup>	23.8±0.337	40.6±0.665	33.3±0.925	3.04±0.0429	27.6±0.469	27.1±0.754	16.2±0.479	21.3±0.422
Yue 137	30-3-11	105-21-34	T <sub>3</sub> x <sup>2</sup>	25.7±0.364	38.2±0.583	35.1±0.919	2.44±0.0346	23.1±0.361	22.7±0.596	11.7±0.274	17.4±0.342
Yue 118	30-9-21	105-15-37	T <sub>3</sub> x <sup>2</sup>	23.8±0.338	41.7±0.671	39.0±1.057	2.72±0.0384	25.7±0.406	25.2±0.667	15.9±0.345	18.3±0.306
Yue 103	30-14-24	105-15-8	T <sub>3</sub> x <sup>2</sup>	21.4±0.303	36.9±0.582	35.2±0.939	2.12±0.03	22.3±0.341	21.9±0.567	13.9±0.294	15.9±0.266
Yue 101-60	30-14-52	105-13-47	T <sub>3</sub> x <sup>2</sup>	20.9±0.295	36.4±0.571	33.7±0.897	2.09±0.0296	22.1±0.341	21.8±0.566	9.55±0.214	17±0.334
Yue 101-67	30-14-52	105-13-47	T <sub>3</sub> x <sup>2</sup>	17.2±0.244	37.5±0.589	34.1±0.915	1.97±0.0279	22±0.367	21.7±0.597	9.14±0.276	5.12±0.104
Yue 101-93-H1	30-5-39	105-29-42	T <sub>3</sub> x <sup>2</sup>	28.4±0.402	47±0.769	43.4±1.191	2.8±0.0396	28.8±0.45	28.3±0.743	12.8±0.322	19.7±0.437
Yue 101-76-X2	30-14-24	105-15-8	T <sub>3</sub> x <sup>2</sup>	23.1±0.327	41.1±0.691	40.6±1.139	2.64±0.0374	25±0.415	24.5±0.673	10±0.313	18.2±0.412
<i>Weiyuan</i>											
Wei 204	29-32-56	104-48-45	S <sub>1</sub> l	19.5±0.276	20.2±0.353	18.9±0.550	1.8±0.0255	9.99±0.2	9.6±0.305	5.53±0.199	4.96±0.113
<i>East area in Anyue gas field</i>											
Moxi 13	30-15-59	105-32-16	C <sub>1</sub> l	10.3±0.148	7.01±0.117	6.1±0.172	1.66±0.0235	4.67±0.0813	4.3±0.122	4.53±0.107	4.18±0.0717
Moxi 9	30-16-8	105-29-10	C <sub>1</sub> l	10±0.142	22.5±0.361	20.4±0.554	1.94±0.0275	8.95±0.146	8.5±0.231	6.17±0.161	7.28±0.124
Moxi 12	30-20-40	105-31-46	C <sub>1</sub> l	9.79±0.139	7.23±0.135	7.5±0.230	1.91±0.027	5.07±0.0971	4.6±0.142	4.79±0.135	4.97±0.0889
Gaoshi 2	30-6-14	105-32-59	C <sub>1</sub> l	14.2±0.201	9.13±0.161	7.5±0.221	2.7±0.0382	4.52±0.095	3.9±0.129	6.42±0.175	3.53±0.0675
Moxi 204	30-21-17	105-41-26	C <sub>1</sub> l	11±0.156	11±0.189	10.8±0.308	1.9±0.0269	6.09±0.113	5.7±0.169	5.97±0.177	4.77±0.0907
Moxi 11	30-21-35	105-45-52	C <sub>1</sub> l	10.9±0.154	7.71±0.144	7.6±0.233	1.92±0.0272	5.4±0.106	5.0±0.155	5.3±0.151	4.63±0.0839
Mo 005-H10	30-15-49	105-42-1	C <sub>1</sub> l	9.01±0.128	9.52±0.183	8.2±0.256	1.12±0.0158	5.31±0.0987	5.1±0.152	4.11±0.133	4.17±0.0761
Mo 004-H9	30-14-58	105-40-44	C <sub>1</sub> l	15.9±0.225	20.1±0.337	18.2±0.508	1.81±0.0255	10.9±0.183	10.5±0.291	5.99±0.147	6.21±0.123
Moxi 8	30-15-30	105-39-9	C <sub>1</sub> l	10.5±0.149	7.32±0.141	4.7±0.148	1.72±0.0243	5.14±0.0985	4.8±0.146	4.47±0.129	4.52±0.09
Mo144	30-13-48	105-40-48	C <sub>1</sub> l	15.3±0.217	21.1±0.354	20.4±0.572	1.84±0.026	11.1±0.178	10.7±0.287	6.96±0.194	6.14±0.111
Mo 005-H9	30-15-49	105-43-9	C <sub>1</sub> l	11.4±0.162	14±0.281	9.2±0.298	1.47±0.0208	7.57±0.306	7.3±0.428	5.31±0.171	5.33±0.0979
Moxi 008-H1	30-18-9	105-40-29	C <sub>1</sub> l	10.1±0.143	8.13±0.142	7.2±0.211	1.83±0.0259	5.43±0.106	5.0±0.156	4.48±0.126	4.73±0.0911
Moxi 008-7-H1	30-16-44	105-39-1	C <sub>1</sub> l	9.67±0.137	7.64±0.143	6.4±0.197	1.76±0.0249	5.26±0.109	4.9±0.159	4.36±0.136	4.47±0.0867
<i>Outlier samples</i>											
Yue 101-11	30-6-40	105-16-14	T <sub>3</sub> x <sup>2</sup>	1.9±0.299	94.1±1.61	81.5±2.336	2.33±0.033	27±0.527	26.6±0.826	12.3±0.51	14.1±0.373
Moxi 009-3-x1	30-18-4	105-30-55	C <sub>1</sub> l	0.927±0.131	263±4.15	316.0±8.445	3.1±0.0439	49.7±0.758	49.3±1.272	14.4±0.378	8.95±0.162

**Table 5.3** Noble gas isotopic compositions and groundwater-derived and crustal-derived noble gas elemental compositions.

well	$^3\text{He}/^4\text{He}$ (R/R <sub>a</sub> )	$^{20}\text{Ne}/^{22}\text{Ne}$	$^{21}\text{Ne}/^{22}\text{Ne}$	$^{40}\text{Ar}/^{36}\text{Ar}$	$^{38}\text{Ar}/^{36}\text{Ar}$	$^{86}\text{Kr}/^{84}\text{Kr}$	$^{136}\text{Xe}/^{132}\text{Xe}$	$^4\text{He}/^{21}\text{Ne}^*$ ( $\times 10^7$ )	$^{20}\text{Ne}^+ / ^{36}\text{Ar}^+$	$^4\text{He}/^{40}\text{Ar}^*$	$^{21}\text{Ne}^*/^{40}\text{Ar}^*$ ( $\times 10^{-7}$ )
<i>West area in Anyue</i>											
Yue 101	0.0136±0.00179	10.44±0.252	0.0459±0.00145	996±21.90	0.188±0.0060	0.329±0.0204	0.3278±0.00993	2.18±0.096	0.1258±0.0052	14.73±0.438	6.76±0.333
Yue 104	0.0115±0.00031	9.90±0.222	0.0478±0.00161	1101±24.33	0.192±0.0059	0.278±0.0376	0.3254±0.00993	2.44±0.115	0.1231±0.0048	10.70±0.319	4.38±0.228
Yue 137	0.0096±0.00028	9.60±0.204	0.0497±0.00152	1056±22.29	0.193±0.0050	0.295±0.0129	0.3264±0.00989	2.73±0.118	0.1550±0.0057	14.62±0.426	5.35±0.257
Yue 118	0.0144±0.00037	9.61±0.209	0.0472±0.00134	1058±22.42	0.184±0.0048	0.321±0.0130	0.3322±0.00915	2.66±0.106	0.1546±0.0059	12.14±0.354	4.57±0.207
Yue 103	0.0119±0.00036	9.56±0.206	0.0474±0.00134	951±19.81	0.187±0.0049	0.310±0.0126	0.3314±0.00916	2.71±0.108	0.1602±0.0060	14.65±0.423	5.40±0.243
Yue 101-60	0.0149±0.00036	9.66±0.208	0.0462±0.00132	946±19.81	0.187±0.0046	0.318±0.0134	0.3253±0.01047	2.81±0.113	0.1549±0.0058	14.54±0.421	5.17±0.235
Yue 101-67	0.0196±0.00047	9.79±0.213	0.0415±0.00135	895±19.60	0.187±0.0056	0.303±0.0170	0.3242±0.01081	2.96±0.136	0.1572±0.0060	13.03±0.387	4.40±0.224
Yue 101-93-H1	0.0114±0.00027	9.63±0.212	0.0477±0.00134	972±20.49	0.195±0.0051	0.315±0.0152	0.3269±0.01166	2.71±0.107	0.1531±0.0058	14.57±0.423	5.37±0.241
Yue 101-76-X2	0.0117±0.00029	9.51±0.213	0.0451±0.00150	1056±23.05	0.186±0.0051	0.312±0.0178	0.3198±0.01130	3.09±0.145	0.1655±0.0065	12.15±0.360	3.93±0.203
<i>Weiyuan</i>											
Wei 204	0.0118±0.00030	9.31±0.216	0.0622±0.00200	1802±44.19	0.187±0.0079	0.316±0.0232	0.3226±0.01158	2.47±0.111	0.1964±0.0084	12.96±0.410	5.25±0.269
<i>East area in Anyue gas field</i>											
Moxi 13	0.0174±0.00049	9.28±0.209	0.0709±0.00222	3555±79.76	0.190±0.0060	0.313±0.0151	0.3301±0.00914	2.92±0.129	0.1428±0.0057	6.77±0.204	2.32±0.115
Moxi 9	0.0115±0.00032	9.74±0.213	0.0442±0.00131	2168±46.84	0.187±0.0056	0.327±0.0166	0.3297±0.00912	2.41±0.101	0.2391±0.0092	5.97±0.176	2.48±0.117
Moxi 12	0.0130±0.00036	8.96±0.219	0.0679±0.00248	3767±89.68	0.185±0.0071	0.311±0.0166	0.3300±0.00995	3.00±0.154	0.1609±0.0070	5.56±0.173	1.86±0.105
Gaoshi 2	0.0256±0.00060	9.23±0.217	0.0799±0.00254	5973±151.34	0.193±0.0086	0.304±0.0162	0.3399±0.01090	2.51±0.112	0.1932±0.0085	5.53±0.179	2.21±0.113
Moxi 204	0.0121±0.00033	9.32±0.214	0.0564±0.00177	3120±72.82	0.186±0.0071	0.295±0.0173	0.3333±0.01068	3.17±0.140	0.1894±0.0078	6.40±0.197	2.02±0.101
Moxi 11	0.0124±0.00033	9.10±0.221	0.0665±0.00220	3556±86.07	0.181±0.0072	0.296±0.0165	0.3218±0.01032	3.22±0.150	0.1527±0.0067	6.19±0.194	1.92±0.101
Mo 005-H10	0.0132±0.00039	9.62±0.239	0.0572±0.00205	2109±49.22	0.198±0.0075	0.353±0.0216	0.3213±0.01036	2.77±0.139	0.1605±0.0070	9.36±0.288	3.37±0.187
Mo 004-H9	0.0118±0.00030	9.62±0.215	0.0507±0.00151	1661±36.39	0.189±0.0057	0.332±0.0151	0.3349±0.01041	3.05±0.128	0.1726±0.0068	10.69±0.317	3.51±0.166
Moxi 8	0.0127±0.00035	9.87±0.243	0.0732±0.00237	3346±79.67	0.182±0.0075	0.315±0.0180	0.3341±0.01045	2.60±0.118	0.0990±0.0043	6.70±0.208	2.57±0.132
Mo144	0.0122±0.00031	9.46±0.213	0.0507±0.00161	1658±35.43	0.188±0.0056	0.320±0.0170	0.3257±0.01008	2.90±0.130	0.1899±0.0074	10.12±0.296	3.48±0.172
Mo 005-H9	0.0132±0.00035	10.14±0.256	0.0580±0.00186	1942±83.17	0.176±0.0084	0.347±0.0194	0.3265±0.01017	2.17±0.098	0.1272±0.0085	9.15±0.433	4.22±0.262
Moxi 008-H1	0.0171±0.00043	9.31±0.217	0.0677±0.00229	3370±81.26	0.190±0.0073	0.308±0.0176	0.3277±0.00994	2.68±0.127	0.1441±0.0061	6.05±0.190	2.26±0.120
Moxi 008-7-H1	0.0168±0.00044	9.40±0.229	0.0702±0.00249	3346±83.96	0.198±0.0076	0.298±0.0172	0.3266±0.00992	2.53±0.126	0.1314±0.0059	6.03±0.193	2.38±0.132
<i>Outlier samples</i>											
Yue 101-11	0.0107±0.00035	9.99±0.230	0.0375±0.00168	863±20.81	0.189±0.0074	0.339±0.0252	0.3248±0.01658	1.70±0.108	0.3059±0.0129	12.40±0.398	7.31±0.495
Moxi 009-3-x1	0.0133±0.00041	9.29±0.200	0.0296±0.00092	624±12.98	0.188±0.0048	0.310±0.0159	0.3296±0.01003	--	0.6409±0.0238	5.68±0.164	--

### 5.4.3 Groundwater-derived noble gas components

$^{20}\text{Ne}$ ,  $^{36}\text{Ar}$ ,  $^{84}\text{Kr}$  and  $^{132}\text{Xe}$  are dominantly derived from the atmosphere dissolved in groundwater at recharge (Ballentine et al., 2002). By resolving Ne and Ar isotopes from different components, air derived  $^{20}\text{Ne}$  ( $^{20}\text{Ne}^+$ ) represents 64.86 to 98.86 % and 64.45 to 98.60 % of the total  $^{20}\text{Ne}$  concentrations for the western and eastern samples, respectively, while air derived  $^{36}\text{Ar}$  ( $^{36}\text{Ar}^+$ ) accounts for on average 95.5% of  $^{36}\text{Ar}$  for all samples in the study. Samples from the western and eastern areas have  $^{20}\text{Ne}^+ / ^{36}\text{Ar}^+$  ratios ranging between 0.1231 to 0.1655 and 0.099 to 0.2391, respectively. Groundwater-derived noble gas concentrations in this study are assumed to originate from ASW (Air saturated water) at 10 °C at an altitude of 400m, i.e., the mean annual air temperature and average altitude in the central Sichuan basin, respectively. In addition, a 10% Ne excess air component is also taken into account for calculation (Stute et al., 1992, Stute et al., 1995, Kipfer et al., 2002).  $^{20}\text{Ne}^+ / ^{36}\text{Ar}^+$  ratios in all the western samples and most eastern samples are similar to or lower than the  $^{20}\text{Ne} / ^{36}\text{Ar}$  ratio = 0.156 expected for ASW at 10 °C. However, higher values of  $^{20}\text{Ne}^+ / ^{36}\text{Ar}^+$  ratios with respect to ASW at 10 °C have been observed in some samples from the eastern area (**Figure 5.10b**).  $^{84}\text{Kr} / ^{36}\text{Ar}$  ratios vary from 0.04 to 0.0623 and 0.055 to 0.142 for the samples in the western and eastern area, respectively. Measured  $^{132}\text{Xe} / ^{36}\text{Ar}$  ratios for samples in two regions range between 0.0023 to 0.0077 and 0.0055 to 0.0098, respectively. Measured  $^{84}\text{Kr} / ^{36}\text{Ar}$  and  $^{132}\text{Xe} / ^{36}\text{Ar}$  ratios in samples are generally higher than those predicted ASW values of 0.0393 and 0.00267, respectively (**Figure 5.10**). The mechanisms that can explain these groundwater-derived noble gas elemental fractionations are discussed in next Section 5.5 discussion.

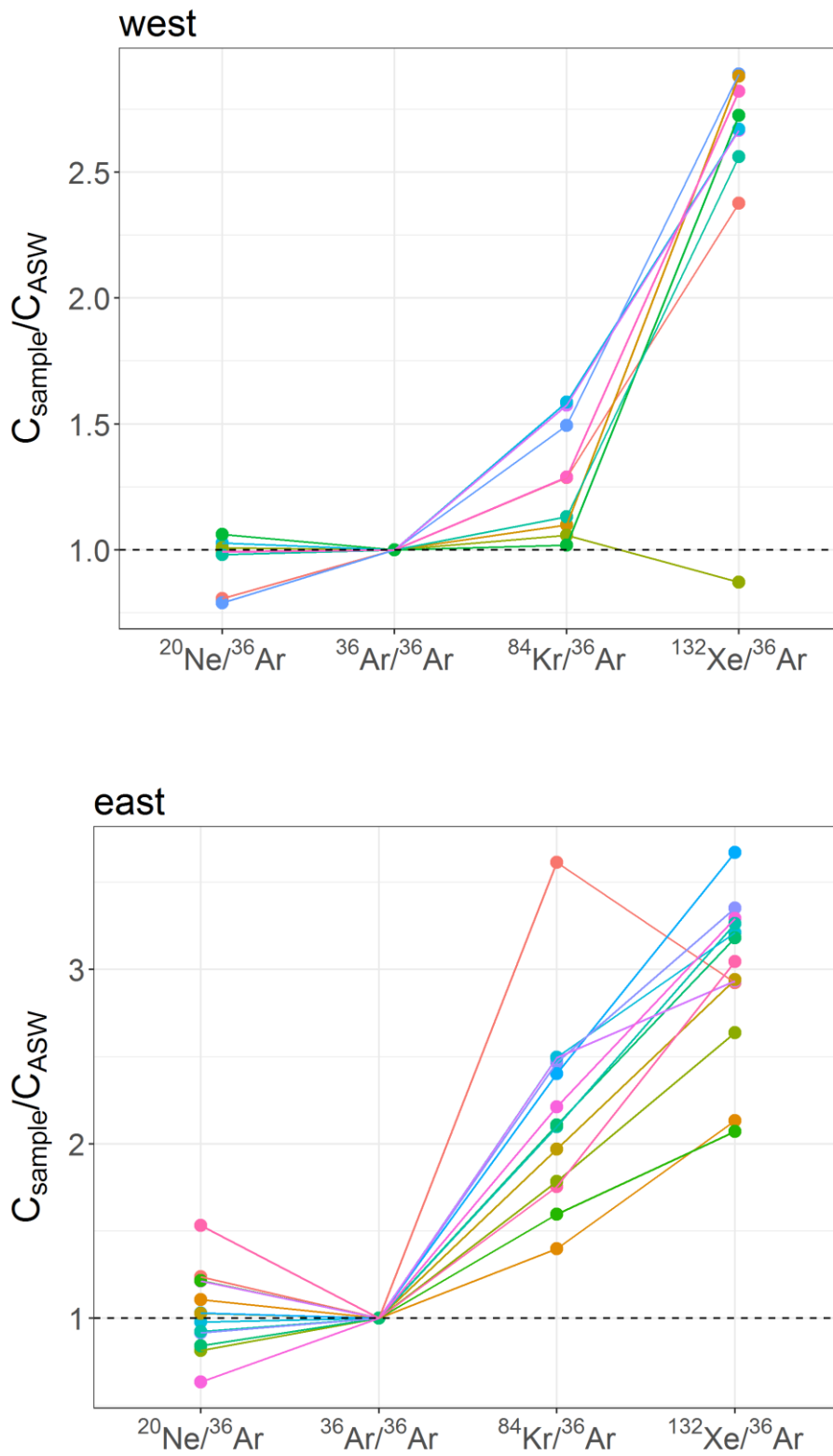


**Fig.5.10.** Atmosphere-derived noble gas abundances in Anyue gas field normalized to those of ASW (Air Saturated Water) at 10 °C with  $^{36}\text{Ar}$  as the reference isotope.

#### 5.4.4 Relationship between groundwater-derived and crustal noble gases

Crustal radiogenic  $^{21}\text{Ne}^*/^{40}\text{Ar}^*$  ratios in samples from the western and eastern region, Anyue gas field range between  $3.93 \times 10^{-7}$  to  $6.76 \times 10^{-7}$  and  $1.86 \times 10^{-7}$  to  $4.22 \times 10^{-7}$ , respectively. While crustal radiogenic noble gases are produced and accumulated in situ in a fluid system, atmosphere-derived  $^{20}\text{Ne}^+/^{36}\text{Ar}^+$  ratio serves as an ideal tracer for gas migration in such system. Therefore, crustal and groundwater-derived noble gases can be used together to identify the relationship of noble gases from different sources. **Figure 5.11** shows the relationships between  $^4\text{He}/^{40}\text{Ar}^*$  against  $^{20}\text{Ne}^+/^{36}\text{Ar}^+$  and  $^{21}\text{Ne}^*/^{40}\text{Ar}^*$  against  $^4\text{He}/^{40}\text{Ar}^*$ . There is no obvious correlation observed between  $^4\text{He}/^{40}\text{Ar}^*$  and  $^{20}\text{Ne}^+/^{36}\text{Ar}^+$  in all samples. However, it should be noted that  $^4\text{He}/^{40}\text{Ar}^*$  values in the eastern samples are significantly lower than those in the west, probably due to their individual geological setting. This may be accounted for by higher formation temperature in the eastern area which can cause more radiogenic  $^{40}\text{Ar}$  release from the host mineral grains (Hunt et al., 2012). This hypothesis is compatible with the characteristics of the carbon isotopic compositions in samples from the eastern area, which have heavier  $\delta^{13}\text{C}$  and higher  $\text{C}_1/\text{C}_{2+}$ , resulting from greater burial depth and higher thermal maturity than samples in the western area. There is a positive correlation between  $^{21}\text{Ne}^*/^{40}\text{Ar}^*$  and  $^4\text{He}/^{40}\text{Ar}^*$  in all samples shown in **Figure 5.11 (b)**. This trend suggests that they may have been mixed well in the groundwater and consequently, follow the same mechanisms in the migration process. Similar to  $^4\text{He}/^{40}\text{Ar}^*$ , the fact that observed low  $^{21}\text{Ne}^*/^{40}\text{Ar}^*$  ratios in eastern samples approach the crustal production  $^{21}\text{Ne}^*/^{40}\text{Ar}^*$  ratio of  $4.94 \times 10^{-7}$ , is also consistent with the high temperature thermal history in this area.

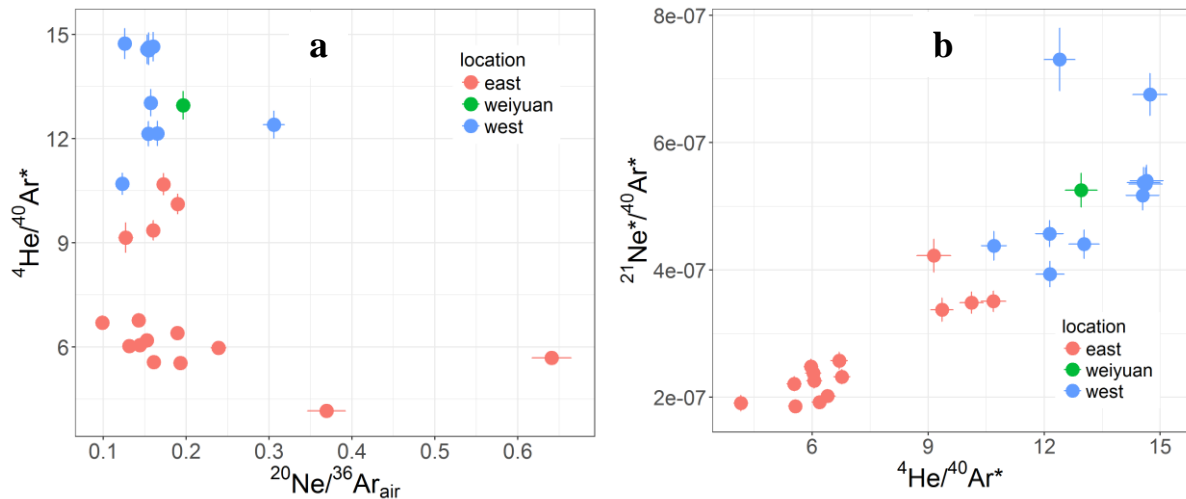


**Fig.5.11.** a)  ${}^4\text{He}/{}^{40}\text{Ar}^*$  vs  ${}^{20}\text{Ne}^+ / {}^{36}\text{Ar}^+$  ratios, and b)  ${}^{21}\text{Ne}^* / {}^{40}\text{Ar}^*$  vs.  ${}^4\text{He}/{}^{40}\text{Ar}^*$ . A positive correlation between  ${}^{21}\text{Ne}^* / {}^{40}\text{Ar}^*$  and  ${}^4\text{He}/{}^{40}\text{Ar}^*$  in all samples, suggesting they may have been mixed well in the groundwater and consequently, then followed the same mechanisms in the migration process.

## 5.5 Discussion

### 5.5.1 Determining the genetic fingerprint of natural gas using noble gas geochemistry

Four parameters, such as  $\text{C}_2^+$  concentration, carbon and hydrogen isotope variations in methane ( $\delta^{13}\text{C}(\text{CH}_4)$ ,  $\delta\text{D}(\text{CH}_4)$ ) and carbon isotope variation in ethane  $\delta^{13}\text{C}(\text{C}_2\text{H}_6)$ , are generally used for assessing the characteristics of natural gases from different sources (Schoell, 1983, Schoell, 1988). Natural gases in a gas reservoir can be classified as biogenic gas with a  $\delta^{13}\text{C}(\text{C}_1)$  less than  $-60\text{‰}$  and thermogenic gas with a  $\delta^{13}\text{C}(\text{C}_1)$  greater than  $-50\text{‰}$  (Schoell, 1983, Schoell, 1988). As thermal evolution proceeds, natural gases become more enriched in  $\delta^{13}\text{C}$  and low heavier hydrocarbon ( $\text{C}_2^+$ ) (Schoell, 1983, Jenden et al., 1993, Hunt et al., 2012). When organic matter reaches high-over mature stage, the natural gas is characterized by almost entirely methane ( $\text{C}_1$ ), with less than 1% heavier hydrocarbons ( $\text{C}_2^+$ ) (Schoell, 1980, Schoell, 1983, Tissot and Welte, 1984). Therefore, based on their major species and carbon isotopic

ratios, samples in the western and eastern areas in this study are typical thermogenic gas, but at different stage of thermal maturity. As described above, samples in eastern area have much heavier  $\delta^{13}\text{C}$  ( $\text{CH}_4$ ) and lower content of heavy hydrocarbon ( $\text{C}_2^+$ ) relative to those western samples, suggesting natural gas in eastern region is at higher thermal maturity level than those in the western region. Noble gas results together with carbon isotopic data ( $\Delta\delta^{13}\text{C}_{1-2}$ , representing carbon isotopic difference between ethane and methane) can be used to differentiate the occurrence of two distinct genetic groups of natural gases in the central Sichuan basin.

**Figure 5.12** shows crustal radiogenic noble gases  $^4\text{He}/^{21}\text{Ne}^*$ ,  $^4\text{He}/^{40}\text{Ar}^*$  and  $^{21}\text{Ne}^*/^{40}\text{Ar}^*$  vs.  $\Delta\delta^{13}\text{C}_{1-2}$  (carbon isotopic difference between ethane and methane). The noble gas elemental compositions ( $^4\text{He}/^{40}\text{Ar}^*$  and  $^{21}\text{Ne}^*/^{40}\text{Ar}^*$ ) together with  $\Delta\delta^{13}\text{C}_{1-2}$  can clearly distinguish these two different groups. Samples from the western area have significantly higher  $^4\text{He}/^{40}\text{Ar}^*$  and  $^{21}\text{Ne}^*/^{40}\text{Ar}^*$  ratios than samples from the eastern area. In addition, the carbon isotopic difference between  $\text{CH}_4$  and  $\text{C}_2\text{H}_6$  is considerably larger in the western samples than that in the eastern samples, which is consistent with the source rock geothermal history, as this can be explained by relatively higher thermal maturity in the eastern area which allows more  $^{40}\text{Ar}$  being released from the host mineral grains. However, it is impossible to differentiate the two types of gases only by  $^4\text{He}/^{21}\text{Ne}^*$  values, because stratigraphic sequences may experience sufficient temperatures beyond which Ne is preferentially retained as compared to He (i.e., above Ne closure temperature of  $\sim 80^\circ\text{C}$ ) (Hunt et al., 2012).

Previous studies (Pinti et al., 1997, Prinzhofer et al., 2010) have proposed that atmospheric gas components are useful for distinguishing different natural gas types, which are also observed in this study. The western samples are relatively more enriched in atmospheric noble gas isotopes ( $^{20}\text{Ne}$ ,  $^{36}\text{Ar}$ ,  $^{84}\text{Kr}$ , and  $^{132}\text{Xe}$ ) than those in the eastern samples (**Table 5.2**).

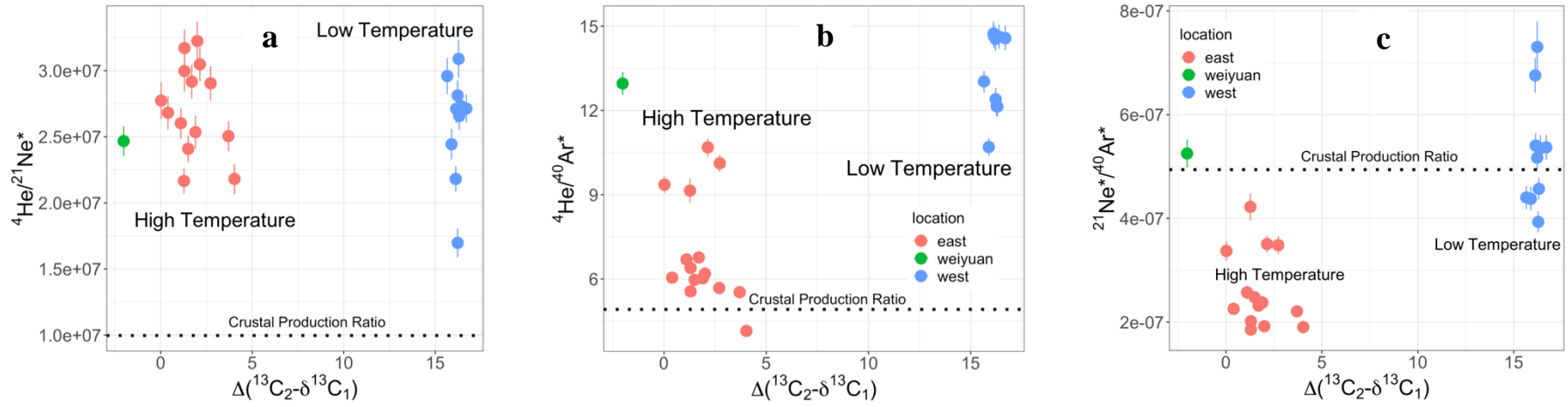


**Fig.5.12.** a)  ${}^4\text{He}/{}^{21}\text{Ne}^*$  vs.  $\Delta\delta^{13}\text{C}_{1-2}$ ; b)  ${}^4\text{He}/{}^{40}\text{Ar}^*$  vs.  $\Delta\delta^{13}\text{C}_{1-2}$ ; and c)  ${}^{21}\text{Ne}^*/{}^{40}\text{Ar}^*$  vs.  $\Delta\delta^{13}\text{C}_{1-2}$ .

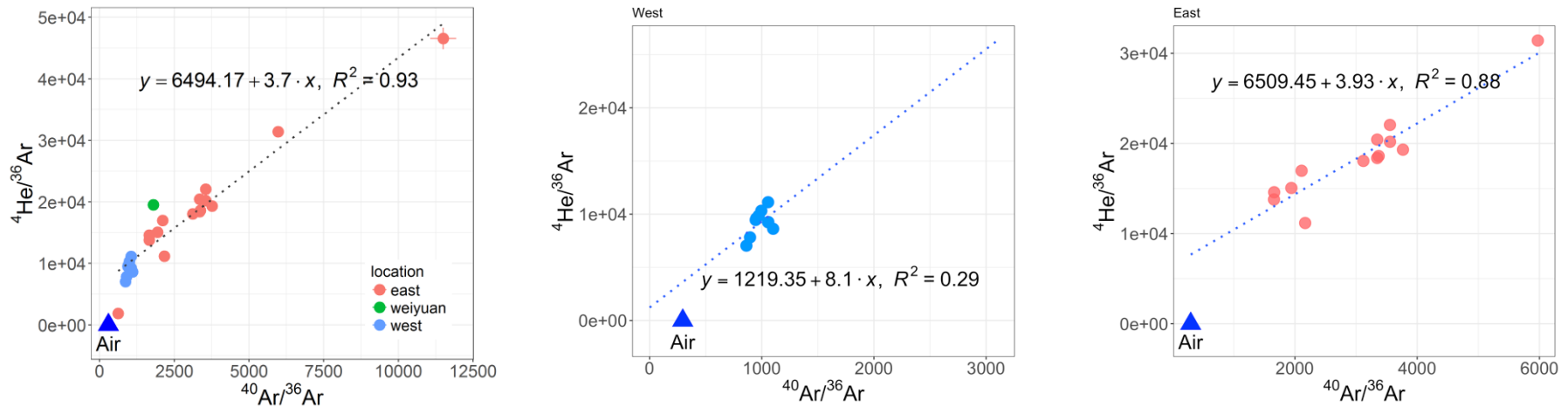


**Fig. 5.13.**  ${}^4\text{He}/{}^{36}\text{Ar}$  vs.  ${}^{40}\text{Ar}/{}^{36}\text{Ar}$ .

### 5.5.2 Solubility controlled fractionation of $^4\text{He}/^{40}\text{Ar}^*$ and $^{20}\text{Ne}^+ / ^{36}\text{Ar}^+$

Groundwater plays a significant role in establishing the noble gas systematics of hydrocarbon systems. When the temperature is lower than 350K, the noble gas solubility in water is positively correlated with the increase of noble gas masses (Crovetto et al., 1982). Barry et al. (2016) showed that in a closed gas-stripping system,  $(^{20}\text{Ne}/^{36}\text{Ar})_{\text{Sample}} / (^{20}\text{Ne}/^{36}\text{Ar})_{\text{ASW}}$  values in the gas phase would start from above the ASW line and then keep going down towards the line until reaching the line  $(^{20}\text{Ne}/^{36}\text{Ar})_{\text{Sample}} = (^{20}\text{Ne}/^{36}\text{Ar})_{\text{ASW}}$ . In contrast, heavier noble gases (Kr, Xe) would start from below the ASW line then keep going up towards the line until reaching the line  $((i/^{36}\text{Ar})_{\text{Sample}} = (i/^{36}\text{Ar})_{\text{ASW}})$ . However, in an open gas-stripping system, noble gas partitioning processes would still continue after noble gas ratios in gas phase are equal to their ASW values. As a result, gases are characterized by relatively lower  $^{20}\text{Ne}/^{36}\text{Ar}$  ratios and higher  $^{84}\text{Kr}/^{36}\text{Ar}$ ,  $^{132}\text{Xe}/^{36}\text{Ar}$  with respect to their ASW ratios at 10 °C.

**Figure 5.10** exhibits that most samples in the Anyue field have the relative depletion of  $^{20}\text{Ne}/^{36}\text{Ar}$  and enrichment of  $^{84}\text{Kr}/^{36}\text{Ar}$  and  $^{132}\text{Xe}/^{36}\text{Ar}$  compared to those ratios in ASW at 10 °C, suggesting the closed gas-stripping system is unlikely applicable to this study. In order to determine possible processes responsible for the water-gas partition, an open system Rayleigh fractionation model is discussed below to interpret the noble gas data in samples, based on the geological conditions of the Anyue gas field, including reservoir temperature, salinity and recharge elevation. Rayleigh fractionation can be formulated by

$$([A]/[B])_{\text{water}} = ([A]/[B])_o \times P^{(\alpha-1)} \quad 5.5$$

Where  $([A]/[B])_{\text{water}}$  is the noble gas elemental ratios in the water phase,  $([A]/[B])_o$  is the initial A/B ratio in the liquid(water) phase, P is the fraction of B remaining in the water

phase, and  $\alpha$  is the solubility-controlled fractionation coefficient given for a gas/liquid system.

$\alpha$  is defined as:

$$\alpha = \frac{\frac{\gamma_A}{\Phi_A} K_A^d}{\frac{\gamma_B}{\Phi_B} K_B^d} \quad 5.6$$

Dimensionless Henry's constants  $K^d$  were derived from empiric equations (Crovetto et al., 1982). Fugacity coefficients  $\Phi$  and liquid activity coefficients  $\gamma$  were calculated following Smith and Kennedy (1983) and Ballentine et al. (2002).

According to the gas-liquid fractionation equation given by Bosch and Mazor (1988), when the gas water volume ratio ( $V_{\text{gas}}/V_{\text{water}}$ ) becomes small, the noble gas elemental compositions in the gas phase are fractionated proportionally to their relative solubilities in the water phase:

$$\text{As } \frac{V_{\text{gas}}}{V_{\text{water}}} \rightarrow 0, \quad \frac{\left(\frac{[A]}{[B]}\right)_{\text{gas}}}{\left(\frac{[A]}{[B]}\right)_{\text{water}}} \rightarrow \frac{\frac{\gamma_A}{\Phi_A} K_A^d}{\frac{\gamma_B}{\Phi_B} K_B^d} = \alpha \quad 5.7$$

The Rayleigh fractionation of noble gases exsolving from the groundwater phase into the gas phase can be modelled using an average well depth of 2800 m at the hydrostatic pressure of 270atm and a temperature of 90°C for the western area of the Anyue field, and, an average well depth of 4800m at the hydrostatic pressure of 464atm, and a temperature of 150°C for the eastern area, respectively. The salinity used is 2M NaCl in this study. The calculated ASW (Air saturated water)  $^{20}\text{Ne}/^{36}\text{Ar}$  ratio for the study is 0.156. **Figure 5.13** shows  $^4\text{He}/^{36}\text{Ar}$  and  $^{40}\text{Ar}/^{36}\text{Ar}$  ratios in all samples. The correlation between the  $^4\text{He}/^{36}\text{Ar}$  and  $^{40}\text{Ar}/^{36}\text{Ar}$  ratios provides information on the local radiogenic  $^4\text{He}/^{40}\text{Ar}^*$  production endmember ratio. The slope of the correlation line provides an estimate of the local crustal radiogenic  $^4\text{He}/^{40}\text{Ar}^*$  ratio of

8.1 and 3.7 in the western and eastern region, respectively. By taking some local geological condition into account,  ${}^4\text{He}/{}^{40}\text{Ar}^* = 12$  for the western area and  ${}^4\text{He}/{}^{40}\text{Ar}^* = 8$  for the eastern area were chosen as the initial crustal radiogenic  ${}^4\text{He}/{}^{40}\text{Ar}^*$  ratios in the groundwater for the Rayleigh fractionation model between  ${}^4\text{He}/{}^{40}\text{Ar}^*$  and  ${}^{20}\text{Ne}/{}^{36}\text{Ar}$  (**Figure 5.14**).  ${}^4\text{He}/{}^{40}\text{Ar}^*$  and  ${}^{20}\text{Ne}/{}^{36}\text{Ar}$  in samples from the western area show a good fit to the Rayleigh fractionation model line, suggesting the presence of an open system degassing of gases from the groundwater, resulting in significant noble gas elemental fractionation. However, the apparent deviation of the  ${}^4\text{He}/{}^{40}\text{Ar}^*$  and  ${}^{20}\text{Ne}/{}^{36}\text{Ar}$  ratios from the modelled fractionation trend in the eastern area reveals that additional processes (i.e. diffusion) also contributes to the gas migration and accumulation, which is discussed in the following sections 5.5.3 Mass-dependent fractionation.

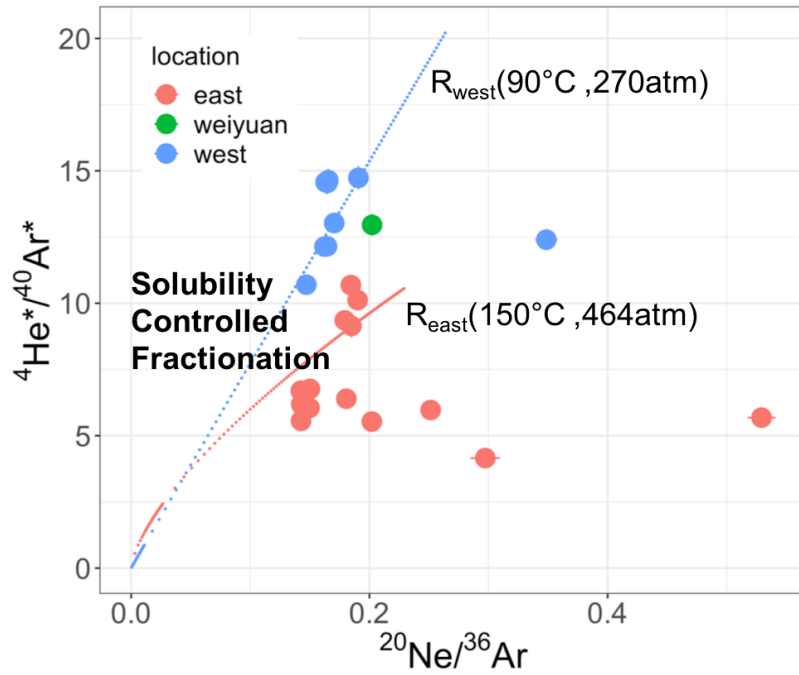


**Fig.5.14.** Crustal radiogenic  $^{4}He/^{40}Ar^{*}$  vs. water-derived  $^{20}Ne/^{36}Ar$ .  $^{20}Ne/^{36}Ar$  and  $^{4}He/^{40}Ar^{*}$  ratios in western samples can be interpreted by an open system Rayleigh fractionation gas-stripping process.

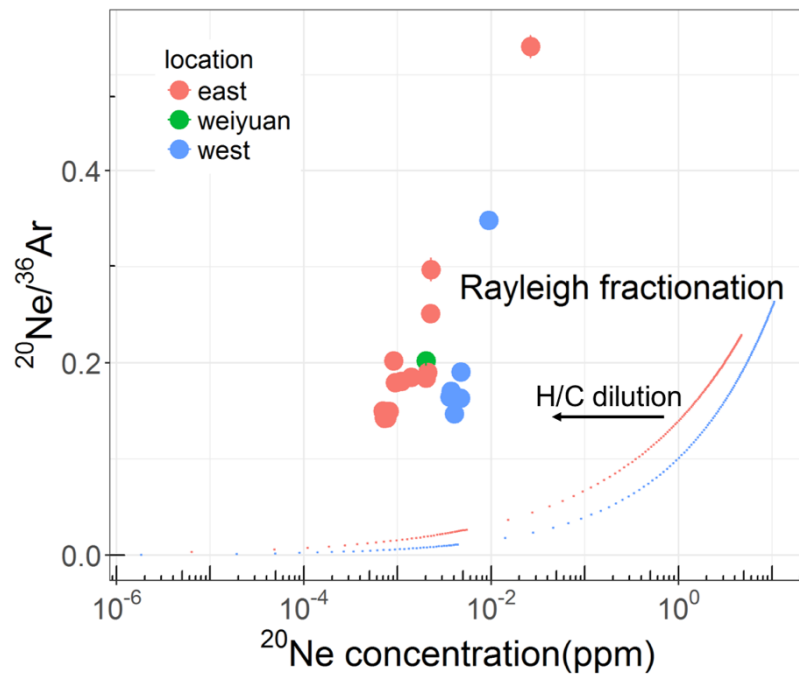


**Fig. 5.15.**  $^{20}Ne/^{36}Ar$  vs.  $^{20}Ne$  concentrations in samples from the Anyue and Weiyuan gas field, Sichuan basin.  $^{20}Ne$  concentrations in all samples are much lower than predicted values by Rayleigh fractionation model.

The Rayleigh fractionation model can be used to evaluate the discrepancy between observed noble gas concentrations and the model predicted noble gas values. Under equilibrium conditions, the distribution of noble gases between gas and liquid phases is controlled by Henry's Law. When  $V_{\text{gas}}/V_{\text{water}}$  moves towards zero, the concentration of gas  $i$  in the gas phase  $C_g^i$  is related to the concentration in the water phase  $C_{\text{water}}^i$  by

$$C_g^i = K_i^d C_{\text{water}}^i \quad 5.8$$

where  $K_i^d$  is dimensionless Henry's constant (Ballentine et al., 2002).

In **Figure 5.15**, measured  $^{20}\text{Ne}$  concentrations in all samples are several orders of magnitude lower than Rayleigh fractionation model predicted values. This can be explained by the dilution of the noble gases in samples by hydrocarbon gases (e.g.  $\text{CH}_4$ ), in particular,  $\text{CH}_4$  desorbed from source coals in the western area of the Anyue gas field. The same mechanism has been suggested by Zhou et al. (2005) for the San Juan basin coalbed methane system in the USA.

### 5.5.3 Diffusion process dependent fractionation

As a Rayleigh fractionation process cannot explain the noble gas elemental fractionation patterns in samples from the eastern area, other processes may have been involved in the formation of the Anyue gas field. As the difference in diffusion properties in noble gases can cause preferential partitioning of noble gases from groundwater into gas phase as documented in Zhou et al. (2005). The mass dependent noble gas fractionation process has the potential to generate the observed kinetic isotopic fractionation.

Assuming a gas  $i$  with mass  $M_i$  diffuses through a gas with an average molecular mass  $M_g$ , the reduced mass  $M_i^*$  is then expressed as follows (Marty, 1984, Jähne et al., 1987, Ballentine et al., 2002)

$$M_i^* = \frac{M_i \times M_g}{M_i + M_g} \quad 5.9$$

Where  $M_i$  and  $M_g$  denote mass of isotope  $i$  and  $g$ , the average mass of the medium of the boundary layer where diffusion occurs. Because of the large hydrogen bonds in the water phase (Zhou et al., 2005), this means the value of  $M_g$  approaches infinity, therefore the reduced mass  $M_i^*$  can be equal to  $M_i$  (Jähne et al., 1987, Lippmann et al., 2003). As the diffusion coefficients are proportional to the inverse of the square root of their reduced mass, the diffusion coefficient  $\alpha$  is defined by:

$$\alpha_{A/B} = \sqrt{\frac{M_B}{M_A}} \quad 5.10$$

Where: A, B denotes noble gas isotopes, and  $M_A$ ,  $M_B$  denotes their respective mass

With the calculated diffusion coefficient  $\alpha$ , we modelled the possible mass-dependent Rayleigh fractionation behaviour in this study. **Figure 5.16** displays a plot of  $^4\text{He}/^{40}\text{Ar}^*$  ratios against  $^{20}\text{Ne}/^{36}\text{Ar}$  ratios for all samples together with the modelled mass dependent kinetic fractionation curve.  $^4\text{He}/^{40}\text{Ar}^*$  and  $^{20}\text{Ne}/^{36}\text{Ar}$  ratios in most samples in the study are compatible with the kinetically controlled mass fractionation. These results indicate that kinetic fractionation process plays an important role in the noble gas evolution in the Anyue and Weiyuan gas fields.

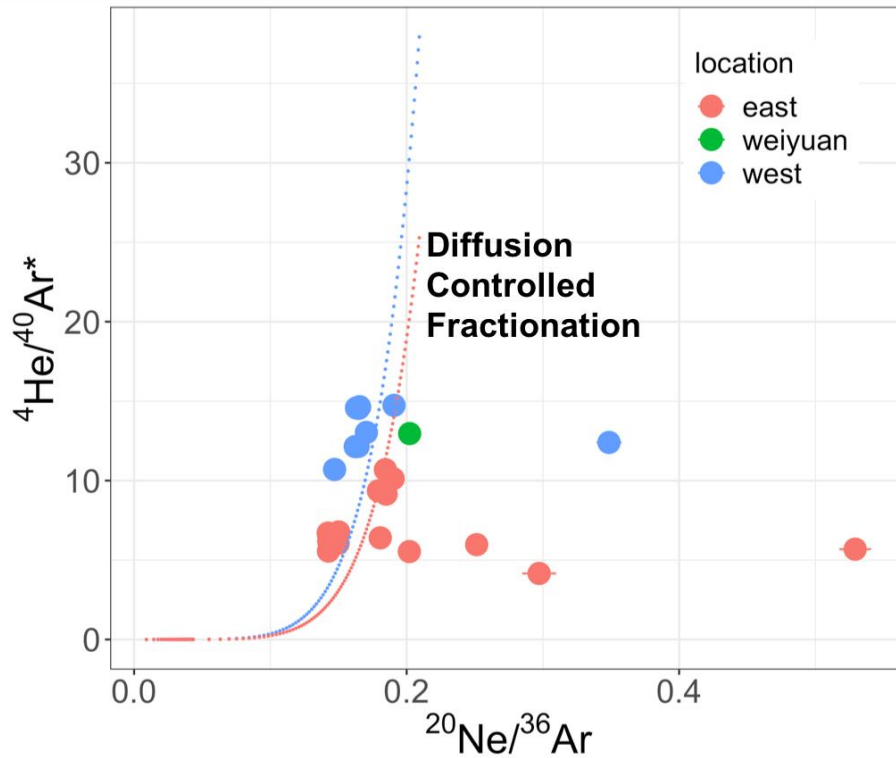


**Fig.5.16.** Crustal radiogenic  ${}^4\text{He}/{}^{40}\text{Ar}^*$  vs. water-derived  ${}^{20}\text{Ne}/{}^{36}\text{Ar}$ .  ${}^4\text{He}/{}^{40}\text{Ar}^*$  and  ${}^{20}\text{Ne}/{}^{36}\text{Ar}$  ratios in most samples in the study are compatible with the simulated kinetically mass-dependent fractionation model.

#### 5.5.4 Kr and Xe enrichment

In **Figure 5.17** and **Figure 5.18**, almost all the measured  ${}^{84}\text{Kr}/{}^{36}\text{Ar}$  and  ${}^{132}\text{Xe}/{}^{36}\text{Ar}$  ratios in gas samples are significantly above the predicted values from the solubility-controlled Rayleigh fractionation model. Two possible mechanisms may be responsible for these observed heavy noble gas enrichments. The first is gas-oil interaction and the second is the release of heavy noble gases initially trapped on source rocks.

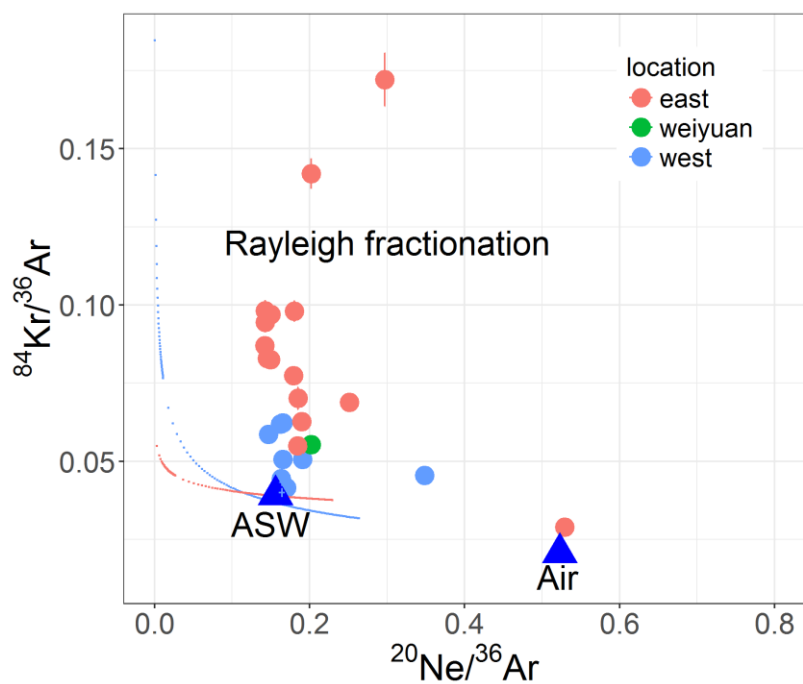


**Fig.5.17.**  $^{84}\text{Kr}/^{36}\text{Ar}$  vs.  $^{20}\text{Ne}/^{36}\text{Ar}$  ratios measured in samples. Almost all the measured  $^{84}\text{Kr}/^{36}\text{Ar}$  values in gas samples are significantly above the predicted solubility-controlled Rayleigh fractionation values.

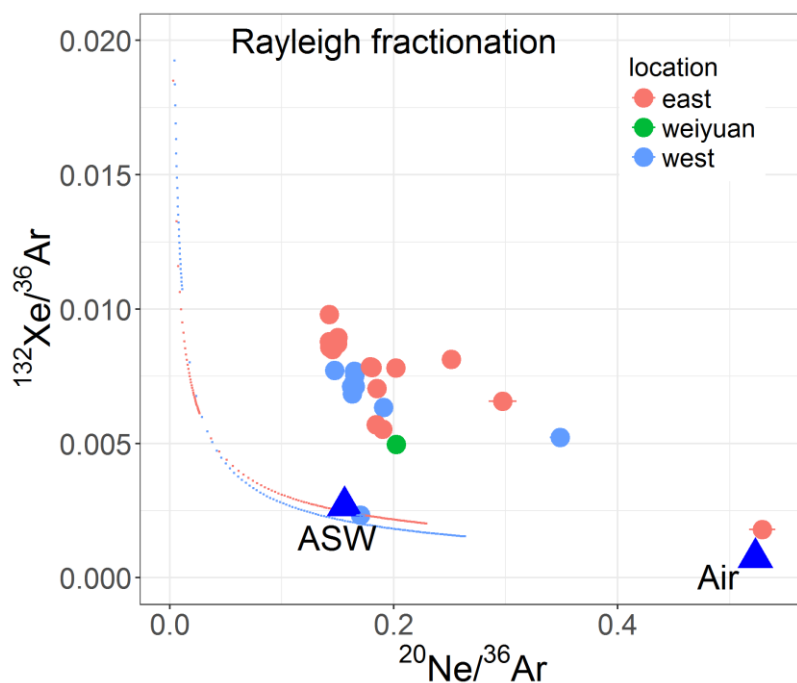


**Fig.5.18.**  $^{132}\text{Xe}/^{36}\text{Ar}$  vs.  $^{20}\text{Ne}/^{36}\text{Ar}$  ratios measured in samples. Similar to  $^{84}\text{Kr}/^{36}\text{Ar}$ , samples are much more enriched in  $^{132}\text{Xe}/^{36}\text{Ar}$  ratios than the predicted solubility controlled Rayleigh fractionation values.

Bosch and Mazor (1988), Kharaka and Specht (1988) and Barry et al. (2016) have shown that the interactions between oil and gas can possibly result in the relative enrichment of heavy noble gases, which follows in the same manner as open system degassing mechanism. However, there is no evidence of significant oil components observed in the Anyue gas field (Qin et al., 2017a, Qin et al., 2017b), and it is also difficult to quantify the involvement of oil on heavy noble gas enrichments. Therefore, the discrepancy in relative Kr and Xe abundance patterns with respect to the Rayleigh fractionation model can be potentially attributed to the addition of sedimentary component from the source rock during geological evolution. It is not uncommon to observe excess heavy noble gases in natural gas samples. Similar Kr-Xe enrichments have been observed in gas reservoirs in the North Sea (van Soest et al., 2000), natural gas samples from the Sleipner Vest gas field (Barry et al., 2016), coalbed gases from San Juan Basin (Zhou et al., 2005). suggested that atmosphere-derived heavy noble gases (Kr and Xe), can be initially adsorbed and trapped in organic-rich sediments, which then escaped into the fluid system, mixed with the hydrocarbon phases, provides an additional source of these noble gases. These ‘additional’ components have an isotopic composition indistinguishable from air but lead to relative gas abundance pattern that is highly enriched in the heavy noble gases (Kr and Xe) (Torgersen and Kennedy, 1999, Kennedy et al., 2002).

## **5.6 Conclusion**

Noble gas and stable isotope data were analysed for 26 natural gas samples from the Anyue and Weiyuan gas fields in the central Sichuan basin, China. Natural gas in the eastern region (Lower Cambrian Longwangmiao Formation with average depth of 4800m) has much greater thermal maturity than natural gas in the western region (upper Triassic Xujiahe Formation with average depth of 2800m), which is demonstrated by heavier  $\delta^{13}\text{C}$  ( $\text{CH}_4$ ) and

lower amount of heavy hydrocarbons ( $C_2^+$ ) compared to those in the western area, Anyue gas field. Noble gases are predominantly crustal and ASW-derived, with negligible mantle contributions. Noble gases together with stable carbon isotopic parameter ( $\Delta\delta^{13}C_{1-2}$ ) can be an effective tool to differentiate the occurrence of two distinct genetic groups of natural gases in the central Sichuan basin. Several models have been established in this work to understand the physical processes responsible for gas emplacement into hydrocarbon reservoirs. The noble gas elemental fractionations in samples from the western area (coal-derived gas) can be well explained by a solubility-controlled Rayleigh fractionation model with relatively less effect of mass-dependent fractionation process. However, noble gas elemental and isotopic compositions in samples from the eastern area can be interpreted as a mixing effect of solubility-controlled and mass-dependent fractionation processes.

## 6 Conclusions and future work

This thesis has discussed in detail the construction and development of a sample preparation line and the analytical procedures for noble gas elemental and isotopic determination. Various samples have been measured on the analytical system set up during this thesis work. Combining noble gas and stable isotope geochemical techniques, the origin, migration and interaction of subsurface crustal fluids (i.e. groundwater and natural gas) have been investigated in two different geological settings: (1) geothermal field in Krafla, Iceland; and (2) conventional and unconventional natural gas reservoirs in the Sichuan Basin, China.

One major objective of this thesis was to construct a noble gas extraction and purification system, interfaced to a multi-collector NGX noble gas mass spectrometer (Isotopx). A sample preparation line was built, and gas sampling, extraction, purification and separation protocols were established successfully as part of this thesis work. Temperatures of 50 K and 95 K can be used as the optimal releasing temperatures for He and Ne respectively on a cryotrap. Temperature of 210 K is tested to be the optimal temperature for releasing Ar and Kr but keeping Xe being trapped onto charcoal. During noble gas isotope and abundance determinations, appropriate mass peaks are monitored in order to correct for interferences caused by doubly charged ions, such as  $^{40}\text{Ar}^{++}$  and  $^{44}\text{CO}_2^{++}$ . In addition, procedural blanks and standards have been run on a daily basis in order to check the system sensitivity and stability.

Noble gas and stable isotope characteristics of the hydrothermal fluid system in Krafla, Iceland were studied in this thesis. Noble gas and stable isotope ( $\delta^{13}\text{C}$  ( $\text{CO}_2$ ),  $\delta^{18}\text{O}$  ( $\text{CO}_2$ ), and  $\delta^{15}\text{N}$  ( $\text{N}_2$ )) data were analysed for eight geothermal boreholes and two gas discharging pools in the Krafla geothermal field. According to tectonic settings in Iceland,  $\text{CO}_2$  in the gas phase is derived from geothermal water and considered to be magmatic in origin, with  $\delta^{13}\text{C}$  ( $\text{CO}_2$ ) ranging between -7.99 and -3.86 ‰. High  $^3\text{He}/^4\text{He}$  ratios in samples suggest that the geothermal water reservoir receives deep-seated volatiles and heat from an active magmatic system at

depth. Modelling shows that processes of boiling and steam separation have occurred during the circulation of geothermal fluids in the shallow crust in the Krafla field. However, some samples show elemental ratios which cannot be explained by the modelled boiling curves for residual liquid after steam separation. This can be explained by the addition of air, possibly introduced by groundwater re-injection, which has had a significant effect on the geochemical signatures of the Krafla geothermal fluid.

It is the first time in this thesis that noble gases have been used in tracing interaction between hydrocarbon and groundwater systems in the central Sichuan Basin, China. Twenty-six natural gas samples were collected from the Anyue and Weiyuan gas fields in the central Sichuan basin, China for stable isotope and noble gas isotope determination. Natural gas in the eastern region (Lower Cambrian Longwangmiao Formation with average depth of 4800 m) has much greater thermal maturity than natural gas in the western region (upper Triassic Xujiahe Formation with average depth of 2800 m), which is demonstrated by heavier  $\delta^{13}\text{C}$  ( $\text{CH}_4$ ) and lower amounts of heavy hydrocarbons ( $\text{C}_2^+$ ) compared to those in the western area, Anyue gas field. Noble gases are predominantly crustal and derived from air saturated water, with negligible mantle contributions. Several models have been established in this work to understand the physical processes responsible for gas emplacement into hydrocarbon reservoirs. The noble gas elemental fractionations in samples from the western area (coal-derived gas) can be well explained by a solubility-controlled Rayleigh fractionation model with relatively less effect of mass-dependent fractionation processes. However, noble gas elemental and isotopic compositions in samples from the eastern area can be interpreted as a mixing effect of solubility-controlled and mass-dependent fractionation processes.

## **Future work**

Some possible directions of future work are outlined below.

As discussed in Chapter 3, the NGX mass spectrometer is specifically designed for collecting nine Xe isotopes simultaneously on Faraday cups. However, due to relatively low amount of Xe in samples, it is difficult to measure Xe isotopes on Faraday cups due to large errors. Instead, all the Xe measurements were carried out using the multiplier collector. More gas samples could be put into mass spectrometer specifically for Xe measurement on Faraday cups in order to obtain higher precision of Xe isotopes in samples.

Furthermore, although major modelling work has been made to interpret the stable isotope and noble gas data in samples from different geological systems, there are still supplementary work in progress. In Krafla geothermal system, the effects of re-injection on altering the noble gas signatures in geothermal fields could be quantified. In addition, development of noble gas tools to calculate total amount of geothermal water is required in order to better understand the crustal fluid interactions.

There is still possibility to further develop noble gas models in the Sichuan Basin study. For example,  $^4\text{He}$  dating of groundwater, calculation of gas-groundwater volume ratio and quantifying the extent of excess Kr and Xe in the Anyue gas field. These works will help further investigate the role of groundwater associated with the hydrocarbon system in study.

## References

- ANDREWS, J. N. & LEE, D. J. 1979. Inert gases in groundwater from the Bunter Sandstone of England as indicators of age and palaeoclimatic trends. *Journal of Hydrology*, 41, 233-252.
- ARMANNSSON, H. 2016. The fluid geochemistry of Icelandic high temperature geothermal areas. *Applied Geochemistry*, 66, 14-64.
- ÁRMANNSSON, H., FRIDRIKSSON, T., BENJAMÍNSSON, J. & HAUKSSON, T. 2013. History of Gas in Geothermal Fluids, Krafla, Northeast Iceland. *Procedia Earth and Planetary Science*, 7, 23-26.
- ÁRMANNSSON, H., FRIDRIKSSON, T., GUDFINNSSON, G. H., ÓLAFSSON, M., ÓSKARSSON, F. & THORBJÖRNSSON, D. 2014. IDDP—The chemistry of the IDDP-01 well fluids in relation to the geochemistry of the Krafla geothermal system. *Geothermics*, 49, 66-75.
- ÁRMANNSSON, H., GUDMUNDSSON, Á. & STEINGRÍMSSON, B. S. 1987. Exploration and development of the Krafla geothermal area. *Jökull*, 37, 13-30.
- ARNÓRSSON, S. 1995. Geothermal systems in Iceland: Structure and conceptual models—II. Low-temperature areas. *Geothermics*, 24, 603-629.
- BALLENTINE, C. J. 1997. Resolving the mantle He/Ne and crustal  $^{21}\text{Ne}/^{22}\text{Ne}$  in well gases. *Earth and Planetary Science Letters*, 152, 233-249.
- BALLENTINE, C. J. 2002. Regional-groundwater-focusing-of-nitrogen-and-noble-gases-into-the-Hugoton-Panhandle-giant-gas-field-USA\_2002\_Geochemica-et-Cosmochimica-Acta. *Geochemica Et Cosmochimica Acta*, 66, 2483-2497.
- BALLENTINE, C. J. & BURNARD, P. G. 2002. Production, Release and Transport of Noble Gases in the Continental Crust. *Reviews in Mineralogy and Geochemistry*, 47, 481-538.
- BALLENTINE, C. J., MARTY, B. & BURGESS, R. 2002. Tracing Fluid Origin, Transport and Interaction in the Crust. *Reviews in Mineralogy and Geochemistry*, 47, 539-614.
- BALLENTINE, C. J., MAZUREK, M. & GAUTSCHI, A. 1994. Thermal constraints on crustal rare gas release and migration: Evidence from Alpine fluid inclusions. *Geochemica et Cosmochimica Acta*, 58, 4333-4348.
- BALLENTINE, C. J., O'NIONS, R. K. & COLEMAN, M. L. 1996. A Magnus opus: Helium, neon, and argon isotopes in a North Sea oilfield. *Geochemica et Cosmochimica Acta*, 60, 831-849.
- BALLENTINE, C. J. & O'NIONS, R. K. 1994. The use of natural He, Ne and Ar isotopes to study hydrocarbon-related fluid provenance, migration and mass balance in sedimentary basins. *Geological Society, London, Special Publications*, 78, 347-361.
- BALLENTINE, C. J., ONIONS, R. K., OXBURGH, E. R., HORVATH, F. & DEAK, J. 1991. Rare-Gas Constraints on Hydrocarbon Accumulation, Crustal Degassing and Groundwater-Flow in the Pannonian Basin. *Earth and Planetary Science Letters*, 105, 229-246.
- BARRY, P. H., HILTON, D. R., FISCHER, T. P., DE MOOR, J. M., MANGASINI, F. & RAMIREZ, C. 2013. Helium and carbon isotope systematics of cold “mazuku” CO<sub>2</sub> vents and hydrothermal gases and fluids from Rungwe Volcanic Province, southern Tanzania. *Chemical Geology*, 339, 141-156.
- BARRY, P. H., LAWSON, M., MEURER, W. P., DANABALAN, D., BYRNE, D. J., MABRY, J. C. & BALLENTINE, C. J. 2017. Determining fluid migration and isolation times in multiphase crustal domains using noble gases. *Geology*, 45, 775-778.
- BARRY, P. H., LAWSON, M., MEURER, W. P., WARR, O., MABRY, J. C., BYRNE, D. J. & BALLENTINE, C. J. 2016. Noble gases solubility models of hydrocarbon charge mechanism in the Sleipner Vest Gas Field. *Geochemica et Cosmochimica Acta*.
- BATTANI, A., SARDA, P. & PRINZHOFER, A. 2000. Basin scale natural gas source, migration and trapping traced by noble gases and major elements: the Pakistan Indus basin. *Earth and Planetary Science Letters*, 181, 229-249.

- BAXTER, E. F., DEPAOLO, D. J. & RENNE, P. R. 2002. Spatially correlated anomalous  $^{40}\text{Ar}/^{39}\text{Ar}$  “age” variations in biotites about a lithologic contact near Simplon Pass, Switzerland: a mechanistic explanation for excess Ar. *Geochimica et Cosmochimica Acta*, 66, 1067-1083.
- BIRKLE, P., MARIN, E. P., PINTI, D. L. & CASTRO, M. C. 2016. Origin and evolution of geothermal fluids from Las Tres Virgenes and Cerro Prieto fields, Mexico - Co-genetic volcanic activity and paleoclimatic constraints. *Applied Geochemistry*, 65, 36-53.
- BOSCH, A. & MAZOR, E. 1988. Natural gas association with water and oil as depicted by atmospheric noble gases: case studies from the southeastern Mediterranean Coastal Plain. *Earth and Planetary Science Letters*, 87, 338-346.
- BURNARD, P., ZIMMERMANN, L. & SANO, Y. 2013. The noble gases as geochemical tracers: history and background. *Springer*, Heidelberg, 1-15.
- BURRUSS, R. C. & LAUGHREY, C. D. 2010. Carbon and hydrogen isotopic reversals in deep basin gas: Evidence for limits to the stability of hydrocarbons. *Organic Geochemistry*, 41, 1285-1296.
- BYRNE, D. J., BARRY, P. H., LAWSON, M. & BALLENTINE, C. J. 2018. Noble gases in conventional and unconventional petroleum systems. *Geological Society, London, Special Publications*, 468, 127-149.
- CAO, C., ZHANG, M., TANG, Q., YANG, Y., LV, Z., ZHANG, T., CHEN, C., YANG, H. & LI, L. 2018. Noble gas isotopic variations and geological implication of Longmaxi shale gas in Sichuan Basin, China. *Marine and Petroleum Geology*, 89, 38-46.
- CASTRO, M. C. & GOBLET, P. 2003. Calibration of regional groundwater flow models: Working toward a better understanding of site-specific systems. *Water Resources Research*, 39.
- CASTRO, M. C. & GOBLET, P. 2005. Calculation of ground water ages—A comparative analysis. *Groundwater*, 43, 368-380.
- CASTRO, M. C., HALL, C. M., PATRIARCHE, D., GOBLET, P. & ELLIS, B. R. 2007. A new noble gas paleoclimate record in Texas — Basic assumptions revisited. *Earth and Planetary Science Letters*, 257, 170-187.
- CASTRO, M. C., JAMBON, A., MARSILY, G. & SCHLOSSER, P. 1998. Noble gases as natural tracers of water circulation in the Paris Basin: 1. Measurements and discussion of their origin and mechanisms of vertical transport in the basin. *Water Resources Research*, 34, 2443-2466.
- CHEN, Z., YANG, Y., WANG, T. G., CHENG, B., LI, M., LUO, B., CHEN, Y., NI, Z., YANG, C., CHEN, T., FANG, R. & WANG, M. 2017. Dibenzothiophenes in solid bitumens: Use of molecular markers to trace paleo-oil filling orientations in the Lower Cambrian reservoir of the Moxi–Gaoshiti Bulge, Sichuan Basin, southern China. *Organic Geochemistry*, 108, 94-112.
- CLARKE, W. B., JENKINS, W. J. & TOP, Z. 1976. Determination of tritium by mass spectrometric measurement of  $^3\text{He}$ . *The International Journal of Applied Radiation and Isotopes*, 27, 515-522.
- CLAYTON, R. N. 2007. Isotopes: From Earth to the Solar System. *Annual Review of Earth and Planetary Sciences*, 35, 1-19.
- CRAIG, H. 1978. A mantle helium component in circum-Pacific volcanic gases: Hakone, the Marianas and Mt. Lassen. *Terrestrial Rare Gases*, 3-16.
- CROVETTO, R., FERNÁNDEZ-PRINI, R. & JAPAS, M. L. 1982. Solubilities of inert gases and methane in H<sub>2</sub>O and in D<sub>2</sub>O in the temperature range of 300 to 600 K. *The Journal of Chemical Physics*, 76, 1077-1086.
- DAI, J., WANG, T., SONG, Y., ZHANG, H., XU, Y. & ZHANG, Q. 1997. Formation and Distribution of Medium-large-sized Gas Field in China. *Geological Publishing House, Beijing (in Chinese)*.
- DAI, J., ZOU, C., LIAO, S., DONG, D., NI, Y., HUANG, J., WU, W., GONG, D., HUANG, S. & HU, G. 2014. Geochemistry of the extremely high thermal maturity Longmaxi shale gas, southern Sichuan Basin. *Organic Geochemistry*, 74, 3-12.
- DAI, J. X., NI, Y. Y., TAO, S. Z. & XIA, Y. H. 2009. Gas-source correlation of marine source rocks in the Sichuan Basin. *Geochimica Et Cosmochimica Acta*, 73, A257-A257.

- DAI, J. X., NI, Y. Y. & ZOU, C. N. 2012. Stable carbon and hydrogen isotopes of natural gases sourced from the Xujiache Formation in the Sichuan Basin, China. *Organic Geochemistry*, 43, 103-111.
- DEMAISON, G. & HUIZINGA, B. J. 1994. Genetic Classification of Petroleum Systems Using Three Factors: Charge, Migration, and Entrapment. In: MAGOON, L. B. & DOW, W. G. (eds.) *The Petroleum System—From Source to Trap*. American Association of Petroleum Geologists.
- DOW, W. G. 1974. Application of oil-correlation and source-rock data to exploration in Williston Basin. *AAPG Bulletin*, 58, 1253-1262.
- DOW, W. G. 1977. Kerogen studies and geological interpretations. *Journal of Geochemical Exploration*, 7, 79-99.
- DUNAI, T. J. & PORCELLI, D. 2002. Storage and Transport of Noble Gases in the Subcontinental Lithosphere. *Reviews in Mineralogy and Geochemistry*, 47, 371-409.
- DYADIN, Y. A., LARIONOV, E. G., MIKINA, T. V. & STAROSTINA, L. I. 1997. Clathrate formation in Kr-H<sub>2</sub>O and Xe-H<sub>2</sub>O systems under pressures up to 15 kbar. *Mendeleev Communications*, 7, 74-75.
- DYMOND, J. & SMITH, E. 1980. The virial coefficients of gases and mixtures. *Clarendon Press, Oxford, UK*.
- EBERHARDT, P., GEISS, J. & GRÖGLER, N. 1965. Further evidence on the origin of trapped gases in the meteorite Khor Temiki. *Journal of Geophysical Research*, 70, 4375-4378.
- EGILL JULIUSSON, S. M., AND ASGERDUR SIGURDARDOTTIR 2015. Phase-Specific and Phase-Partitioning Tracer Experiment in the Krafla Reservoir, Iceland. *Proceeding World Geothermal Congress*.
- EINARSSON, P. 1978. S-wave shadows in the Krafla Caldera in NE-Iceland, evidence for a magma chamber in the crust. *Bulletin Volcanologique*, 41, 187-195.
- ELDERS, W. A., FRÍÐLEIFSSON, G. Ó., ZIERENBERG, R. A., POPE, E. C., MORTENSEN, A. K., GUÐMUNDSSON, Á., LOWENSTERN, J. B., MARKS, N. E., OWENS, L., BIRD, D. K., REED, M., OLSEN, N. J. & SCHIFFMAN, P. 2011. Origin of a rhyolite that intruded a geothermal well while drilling at the Krafla volcano, Iceland. *Geology*, 39, 231-234.
- ELLIOT, T., BALLENTINE, C. J., O'NIONS, R. K. & RICCHIUTO, T. 1993. Carbon, helium, neon and argon isotopes in a Po basin (northern Italy) natural gas field. *Chemical Geology*, 106, 429-440.
- GARDNER, W. P., SUSONG, D. D., SOLOMON, D. K. & HEASLER, H. P. 2010. Using noble gases measured in spring discharge to trace hydrothermal processes in the Norris Geyser Basin, Yellowstone National Park, U.S.A. *Journal of Volcanology and Geothermal Research*, 198, 394-404.
- GILFILLAN, S. M., LOLLAR, B. S., HOLLAND, G., BLAGBURN, D., STEVENS, S., SCHOELL, M., CASSIDY, M., DING, Z., ZHOU, Z., LACRAMPE-COULOUME, G. & BALLENTINE, C. J. 2009. Solubility trapping in formation water as dominant CO<sub>2</sub> sink in natural gas fields. *Nature*, 458, 614-8.
- GILFILLAN, S. M. V., BALLENTINE, C. J., HOLLAND, G., BLAGBURN, D., LOLLAR, B. S., STEVENS, S., SCHOELL, M. & CASSIDY, M. 2008. The noble gas geochemistry of natural CO<sub>2</sub> gas reservoirs from the Colorado Plateau and Rocky Mountain provinces, USA. *Geochimica et Cosmochimica Acta*, 72, 1174-1198.
- GRAHAM, D. W. 2002. Noble Gas Isotope Geochemistry of Mid-Ocean Ridge and Ocean Island Basalts: Characterization of Mantle Source Reservoirs. *Reviews in Mineralogy and Geochemistry*, 47, 247-317.
- HEATON, T. H. E. & VOGEL, J. C. 1981. "Excess air" in groundwater. *Journal of Hydrology*, 50, 201-216.
- HEILWEIL, V. M., HEALY, R. W. & HARRIS, R. N. 2012. Noble gases and coupled heat/fluid flow modeling for evaluating hydrogeologic conditions of volcanic island aquifers. *Journal of Hydrology*, 464-465, 309-327.
- HILTON, D. R. 1996. The helium and carbon isotope systematics of a continental geothermal system: results from monitoring studies at Long Valley caldera (California, U.S.A.). *Chemical Geology*, 127, 269-295.

- HILTON, D. R., FISCHER, T. P. & MARTY, B. 2002. 09 Noble Gases and Volatile Recycling at Subduction Zones. *Reviews in Mineralogy and Geochemistry*, 47, 319-370.
- HIYAGON, H. & KENNEDY, B. M. 1992. Noble gases in CH<sub>4</sub>-rich gas fields, Alberta, Canada. *Geochimica et Cosmochimica Acta*, 56, 1569-1589.
- HOLLAND, G. & BALLENTINE, C. J. 2006. Seawater subduction controls the heavy noble gas composition of the mantle. *Nature*, 441, 186-91.
- HUANG, J. 2009. Exploration prospect of shale gas and coal-bed methane in Sichuan Basin. *Lithologic Reservoirs*, 21, 116-120.
- HUGHES, W. B., HOLBA, A. G. & DZOU, L. I. P. 1995. The ratios of dibenzothiophene to phenanthrene and pristane to phytane as indicators of depositional environment and lithology of petroleum source rocks. *Geochimica et Cosmochimica Acta*, 59, 3581-3598.
- HUNT, A. G., DARRAH, T. H. & POREDA, R. J. 2012. Determining the source and genetic fingerprint of natural gases using noble gas geochemistry: A northern Appalachian Basin case study. *Aapg Bulletin*, 96, 1785-1811.
- HURWITZ, S., KIPP, K. L., INGEBRITSEN, S. E. & REID, M. E. 2003. Groundwater flow, heat transport, and water table position within volcanic edifices: Implications for volcanic processes in the Cascade Range. *Journal of Geophysical Research B: Solid Earth*, 108.
- ITALIANO, F., MARTINELLI, G. & NUCCIO, P. M. 2001. Anomalies of mantle-derived helium during the 1997–1998 seismic swarm of Umbria-Marche, Italy. *Geophysical Research Letters*, 28, 839-842.
- J. MATSUDA, T. M., H. SUMINO, K. NAGAO, J. YAMAMOTO, Y. MIURA, 2002. The <sup>3</sup>He/<sup>4</sup>He ratio of the new internal He Standard of Japan (HESJ). *Geochemical Journal*, 36, 191-195.
- JÄHNE, B., HEINZ, G. & DIETRICH, W. 1987. Measurement of the diffusion coefficients of sparingly soluble gases in water. *Journal of Geophysical Research: Oceans*, 92, 10767-10776.
- JANIS Closed cycle cryogenic cold trap system manual. *Janis Research Company*.
- JASON C. POOLE, G. W. M. 1997. Analysis of noble gases in water using a quadrupole mass spectrometer in static mode. *Applied Geochemistry*, 12, 707-714.
- JENDEN, P. D., DRAZAN, D. J. & KAPLAN, I. R. 1993. Mixing of thermogenic natural gases in northern Appalachian Basin. *AAPG Bulletin*, 77, 980–998.
- JENKINS, W. J. & CLARKE, W. B. 1976. The distribution of <sup>3</sup>He in the western Atlantic ocean. *Deep Sea Research and Oceanographic Abstracts*, 23, 481-494.
- KANEOKA, I. & TAKAOKA, N. 1980. Rare Gas Isotopes in Hawaiian Ultramafic Nodules and Volcanic Rocks: Constraint on Genetic Relationships. *Science*, 208, 1366.
- KENNEDY, B. M., HIYAGON, H. & REYNOLDS, J. H. 1990. Crustal Neon - a Striking Uniformity. *Earth and Planetary Science Letters*, 98, 277-286.
- KENNEDY, B. M., LYNCH, M. A., REYNOLDS, J. H. & SMITH, S. P. 1985. Intensive sampling of noble gases in fluids at Yellowstone: I. Early overview of the data; regional patterns. *Geochimica et Cosmochimica Acta*, 49, 1251-1261.
- KENNEDY, B. M., REYNOLDS, J. H. & SMITH, S. P. 1988. Noble gas geochemistry in thermal springs. *Geochimica et Cosmochimica Acta*, 52, 1919-1928.
- KENNEDY, B. M., TORGERSEN, T. & VAN SOEST, M. C. 2002. Multiple atmospheric noble gas components in hydrocarbon reservoirs: a study of the Northwest Shelf, Delaware Basin, SE New Mexico. *Geochimica et Cosmochimica Acta*, 66, 2807-2822.
- KENNEDY, B. M. & VAN SOEST, M. C. 2006. A helium isotope perspective on the Dixie Valley, Nevada, hydrothermal system. *Geothermics*, 35, 26-43.
- KHARAKA, Y. K. & SPECHT, D. J. 1988. The solubility of noble gases in crude oil at 25–100°C. *Applied Geochemistry*, 3, 137-144.
- KIPFER, R., AESCHBACH-HERTIG, W., PEETERS, F. & STUTE, M. 2002. Noble Gases in Lakes and Ground Waters. *Reviews in Mineralogy and Geochemistry*, 47, 615-700.
- KURZ, M. D., JENKINS, W. J. & HART, S. R. 1982. Helium isotopic systematics of oceanic islands and mantle heterogeneity. *Nature*, 297, 43.
- LAPLAIGE, P., LEMALE, J., DECOTTEGNE, S., DESPLAN, A., GOYENECHÉ, O. & DELOBELLE, G. 2005. Geothermal Resources in France - Current Situation and Prospects. *Proc. World Geother. Congress 2005, Antalya, Turkey*.

- LI, J., XIE, Z. Y., DAI, J. X., ZHANG, S. C., ZHU, G. Y. & LIU, Z. L. 2005. Geochemistry and origin of sour gas accumulations in the northeastern Sichuan Basin, SW China. *Organic Geochemistry*, 36, 1703-1716.
- LI, P. P., HAO, F., GUO, X. S., ZOU, H. Y., YU, X. Y. & WANG, G. W. 2015. Processes involved in the origin and accumulation of hydrocarbon gases in the Yuanba gas field, Sichuan Basin, southwest China. *Marine and Petroleum Geology*, 59, 150-165.
- LI, Y. J., FENG, Y. Y., LIU, H., ZHANG, L. H. & ZHAO, S. X. 2013. Geological characteristics and resource potential of lacustrine shale gas in the Sichuan Basin, SW China. *Petroleum Exploration and Development*, 40, 454-460.
- LIANG, C., JIANG, Z. X., ZHANG, C. M., GUO, L., YANG, Y. T. & LI, J. 2014. The shale characteristics and shale gas exploration prospects of the Lower Silurian Longmaxi shale, Sichuan Basin, South China. *Journal of Natural Gas Science and Engineering*, 21, 636-648.
- LIN, M., CLARA, C. M. & M., H. C. 2009. Crustal noble gases in deep brines as natural tracers of vertical transport processes in the Michigan Basin. *Geochemistry, Geophysics, Geosystems*, 10.
- LIPPMANN, J., STUTE, M., TORGERSEN, T., MOSER, D. P., HALL, J. A., LIN, L., BORCSIK, M., BELLAMY, R. E. S. & ONSTOTT, T. C. 2003. Dating ultra-deep mine waters with noble gases and  $^{36}\text{Cl}$ , Witwatersrand Basin, South Africa. *Geochimica et Cosmochimica Acta*, 67, 4597-4619.
- LOLLAR, B. S., O'NIONS, R. K. & BALLENTINE, C. J. 1994. Helium and neon isotope systematics in carbon dioxide-rich and hydrocarbon-rich gas reservoirs. *Geochimica et Cosmochimica Acta*, 58, 5279-5290.
- LOWENSTERN, J. B. & HURWITZ, S. 2008. Monitoring a supervolcano in repose: Heat and volatile flux at the Yellowstone caldera. *Elements*, 4, 35-40.
- LUPTON, J. E. & CRAIG, H. 1975. Excess  $^3\text{He}$  in oceanic basalts: Evidence for terrestrial primordial helium. *Earth and Planetary Science Letters*, 26, 133-139.
- MA, L., CASTRO, M. C. & HALL, C. M. 2009. Atmospheric noble gas signatures in deep Michigan Basin brines as indicators of a past thermal event. *Earth and Planetary Science Letters*, 277, 137-147.
- MA, Y. S., ZHANG, S. C., GUO, T. L., ZHU, G. Y., CAI, X. Y. & LI, M. W. 2008. Petroleum geology of the Puguang sour gas field in the Sichuan Basin, SW China. *Marine and Petroleum Geology*, 25, 357-370.
- MAGRO, G., GHERARDI, F. & BAYON, F. E. B. 2013. Noble and reactive gases of Palinpinon geothermal field (Philippines): Origin, reservoir processes and geodynamic implications. *Chemical Geology*, 339, 4-15.
- MAMYRIN, B. A., ANUFRIEV, G. S., KAMENSKII, I. L. & TOLSTIKHIN, I. N. 1970. DETERMINATION OF THE ISOTOPIC COMPOSITION OF ATMOSPHERIC HELIUM.
- MAMYRIN, B. A. & TOLSTIKHIN, I. N. 1984. Helium isotopes in nature. *Elsevier*, Amsterdam, 273p.
- MARROCCHI, Y., BURNARD, P. G., HAMILTON, D., COLIN, A., PUJOL, M., ZIMMERMANN, L. & MARTY, B. 2009. Neon isotopic measurements using high-resolution, multicollector noble gas mass spectrometer: HELIX-MC. *Geochemistry Geophysics Geosystems*, 10.
- MARTY, B. 1984. On the noble gas, isotopic fractionation in naturally occurring gases. *Geochemical Journal*, 18, 157-162.
- MARTY, B., JAMBON, A. & SANO, Y. 1989. Helium isotopes and  $\text{CO}_2$  in volcanic gases of Japan. *Chemical Geology*, 76, 25-40.
- MAZOR, E. 1972. Paleotemperatures and other hydrological parameters deduced from noble gases dissolved in groundwaters; Jordan Rift Valley, Israel. *Geochimica et Cosmochimica Acta*, 36, 1321-1336.
- MAZOR, E. & BOSCH, A. 1987. Noble gases in formation fluids from deep sedimentary basins: a review. *Applied Geochemistry*, 2, 621-627.
- MAZOR, E. & BOSCH, A. 1992. Physical processes in geothermal systems derived by noble gases. *Isotopes of Noble Gases as Tracers in Environmental Studies*, IAEA, Vienna, 203-218.
- MAZOR, E. & TRUESDELL, A. H. 1984. Dynamics of a geothermal field traced by noble gases: Cerro Prieto, Mexico. *Geothermics*, 13, 91-102.

- MKS MKS Type PDR 2000 Dual Capacitance Diaphragm Gauge Controller
- NAGAO, K., TAKAOKA, N. & MATSUBAYASHI, O. 1981. Rare gas isotopic compositions in natural gases of Japan. *Earth and Planetary Science Letters*, 53, 175-188.
- NI, Y. Y., DAI, J. X., TAO, S. Z., WU, X. Q., LIAO, F. R., WU, W. & ZHANG, D. J. 2014. Helium signatures of gases from the Sichuan Basin, China. *Organic Geochemistry*, 74, 33-43.
- O'NIONS, R. K. & OXBURGH, E. R. 1988. Helium, volatile fluxes and the development of continental crust. *Earth and Planetary Science Letters*, 90, 331-347.
- ÓSKARSSON, N., SIGVALDASON, G. E. & STEINTHÓRSSON, S. 1982. A Dynamic Model of Rift Zone Petrogenesis and the Regional Petrology of Iceland. *Journal of Petrology*, 23, 28-74.
- ÖZGÜR, N. 2002. Geochemical Signature of the Kizildere Geothermal Field, Western Anatolia, Turkey. *International Geology Review*, 44, 153-163.
- OZIMA, M. & PODOSEK, F. A. 1983. Noble Gas Geochemistry. *Cambridge University Press, Cambridge*.
- OZIMA, M. & PODOSEK, F. A. 2002. Noble gas geochemistry. *Cambridge University Press, Cambridge*.
- PHILP, R. P. 1993. Oil-Oil and Oil-Source Rock Correlations: Techniques. In: ENGEL, M. H. & MACKO, S. A. (eds.) *Organic Geochemistry: Principles and Applications*. Boston, MA: Springer US.
- PINTI, D. L., CASTRO, M. C., HALL, C. M., LOPEZ-HERNANDEZ, A. & SHOUAKAR-STASH, O. 2017a. Noble gas isotopes applied to geothermal resources. Canadian Mineralogical Association.
- PINTI, D. L., CASTRO, M. C., LOPEZ-HERNANDEZ, A., HAN, G., SHOUAKAR-STASH, O., HALL, C. M. & RAMÍREZ-MONTES, M. 2017b. Fluid circulation and reservoir conditions of the Los Humeros Geothermal Field (LHGF), Mexico, as revealed by a noble gas survey. *Journal of Volcanology and Geothermal Research*, 333-334, 104-115.
- PINTI, D. L., CASTRO, M. C., SHOUAKAR-STASH, O., TREMBLAY, A., GARDUÑO, V. H., HALL, C. M., HÉLIE, J. F. & GHALEB, B. 2013. Evolution of the geothermal fluids at Los Azufres, Mexico, as traced by noble gas isotopes,  $\delta^{18}\text{O}$ ,  $\delta\text{D}$ ,  $\delta^{13}\text{C}$  and  $87\text{Sr}/86\text{Sr}$ . *Journal of Volcanology and Geothermal Research*, 249, 1-11.
- PINTI, D. L. & MARTY, B. 1995. Noble gases in crude oils from the Paris Basin, France: Implications for the origin of fluids and constraints on oil-water-gas interactions. *Geochimica et Cosmochimica Acta*, 59, 3389-3404.
- PINTI, D. L., MARTY, B. & ANDREWS, J. N. 1997. Atmosphere-derived noble gas evidence for the preservation of ancient waters in sedimentary basins. *Geology*, 25, 111-114.
- PODOSEK, F. A., BERNATOWICZ, T. J. & KRAMER, F. E. 1981. Adsorption of xenon and krypton on shales. *Geochimica et Cosmochimica Acta*, 45, 2401-2415.
- POPE, E. C., BIRD, D. K., ARNORSSON, S. & GIROUD, N. 2016. Hydrogeology of the Krafla geothermal system, northeast Iceland. *Geofluids*, 16, 175-197.
- PORCELLI, D., BALLENTINE, C. J. & WIELER, R. 2002. An Overview of Noble Gas Geochemistry and Cosmochemistry. *Reviews in Mineralogy and Geochemistry*, 47, 1-19.
- POREDA, R. J., CRAIG, H., ARNÓRSSON, S. & WELHAN, J. A. 1992. Helium isotopes in Icelandic geothermal systems: I.  $^3\text{He}$ , gas chemistry, and  $^{13}\text{C}$  relations. *Geochimica et Cosmochimica Acta*, 56, 4221-4228.
- PRINZHOFER, A. 2003. Gas Isotopes Tracing: an Important Tool for Hydrocarbons Exploration. *Oil Gas Science and Technology*, 58, 299-311.
- PRINZHOFER, A. 2013. Noble Gases in Oil and Gas Accumulations. In: BURNARD, P. (ed.) *The Noble Gases as Geochemical Tracers*. Berlin, Heidelberg: Springer Berlin Heidelberg.
- PRINZHOFER, A., DOS SANTOS NETO, E. V. & BATTANI, A. 2010. Coupled use of carbon isotopes and noble gas isotopes in the Potiguar basin (Brazil): Fluids migration and mantle influence. *Marine and Petroleum Geology*, 27, 1273-1284.
- QIN, S., LI, F., LI, W., ZHOU, Z. & ZHOU, G. 2017a. Formation mechanism of tight coal-derived-gas reservoirs with medium-low abundance in Xujiahe Formation, central Sichuan Basin, China. *Marine and Petroleum Geology*.

- QIN, S., LI, F., ZHOU, Z. & ZHOU, G. 2017b. Geochemical characteristics of water-dissolved gases and implications on gas origin of Sinian to Cambrian reservoirs of Anyue gas field in Sichuan Basin, China. *Marine and Petroleum Geology*.
- REBOUR, V., BILLIOTTE, J., DEVEUGHELE, M., JAMBON, A. & LE GUEN, C. 1997. Molecular diffusion in water-saturated rocks: A new experimental method. *Journal of Contaminant Hydrology*, 28, 71-93.
- REID, R. C., PRAUNSNITZ, J. M. & SHERWOOD, T. K. 1977. The properties of gases and liquids. *McGraw-Hill Ed.*, 688p.
- REYNOLDS, J., JEFFERY, P., MCCRORY, G. & VARGA, P. 1978. Improved charcoal trap for rare gas mass spectrometry. *Review of Scientific Instruments*, 49, 547-548.
- REYNOLDS, J. H. 1956. High sensitivity mass spectrometer for noble gas analysis. *Review of Scientific Instruments*, 27, 928-934.
- RISON, W. & CRAIG, H. 1983. Helium isotopes and mantle volatiles in Loihi Seamount and Hawaiian Island basalts and xenoliths. *Earth and Planetary Science Letters*, 66, 407-426.
- ROULLEAU, E., TARDANI, D., SANO, Y., TAKAHATA, N., VINET, N., BRAVO, F., MUNOZ, C. & SANCHEZ, J. 2016. New insight from noble gas and stable isotopes of geothermal/hydrothermal fluids at Cavihue-Copahue Volcanic Complex: Boiling steam separation and water-rock interaction at shallow depth. *Journal of Volcanology and Geothermal Research*, 328, 70-83.
- RUDNICK, R. L. & FOUNTAIN, D. M. 1995. Nature and composition of the continental crust: A lower crustal perspective. *Reviews of Geophysics*, 33, 267-309.
- SÆMUNDSSON, K. 1978. Fissure swarms and central volcanoes of the neovolcanic zones of Iceland. *Geol J Spec*, 415-432.
- SANO, Y. & FISCHER, T. P. 2013. The Analysis and Interpretation of Noble Gases in Modern Hydrothermal Systems. In: BURNARD, P. (ed.) *The Noble Gases as Geochemical Tracers*. Berlin, Heidelberg: Springer Berlin Heidelberg.
- SANO, Y. & MARTY, B. 1995. Origin of carbon in fumarolic gas from island arcs. *Chemical Geology*, 119, 265-274.
- SANO, Y., NISHIO, Y., SASAKI, S., GAMO, T. & NAGAO, K. 1998. Helium and carbon isotope systematics at Ontake volcano, Japan. *Journal of Geophysical Research: Solid Earth*, 103, 23863-23873.
- SANO, Y., TAKAHATA, N. & SENO, T. 2006. Geographical Distribution of  $^3\text{He}/^4\text{He}$  Ratios in the Chugoku District, Southwestern Japan. *Pure and Applied Geophysics*, 163, 745-757.
- SANO, Y., URABE, A., WAKITA, H., CHIBA, H. & SAKAI, H. 1985. Chemical and isotopic compositions of gases in geothermal fluids in Iceland. *Geochemical Journal*, 19, 135-148.
- SANO, Y. & WAKITA, H. 1985. Geographical distribution of  $^3\text{He}/^4\text{He}$  ratios in Japan: Implications for arc tectonics and incipient magmatism. *Journal of Geophysical Research: Solid Earth*, 90, 8729-8741.
- SCHLEGEL, M. E., ZHOU, Z., MCINTOSH, J. C., BALLENTINE, C. J. & PERSON, M. A. 2011. Constraining the timing of microbial methane generation in an organic-rich shale using noble gases, Illinois Basin, USA. *Chemical Geology*, 287, 27-40.
- SCHOELL, M. 1980. The hydrogen and carbon isotopic composition of methane from natural gases of various origins. *Geochimica et Cosmochimica Acta*, 44, 649-661.
- SCHOELL, M. 1983. Genetic characterization of natural gases. *American Association of Petroleum Geologists Bulletin*, 67, 2225-2238.
- SCHOELL, M. 1984. Recent advances in petroleum isotope geochemistry. *Organic Geochemistry*, 6, 645-663.
- SCHOELL, M. 1988. Multiple origins of methane in the Earth. *Chemical Geology*, 71, 1-10.
- SHERWOOD LOLLAR, B., BALLENTINE, C. J. & ONIONS, R. K. 1997. The fate of mantle-derived carbon in a continental sedimentary basin: Integration of CHe relationships and stable isotope signatures. *Geochimica et Cosmochimica Acta*, 61, 2295-2307.
- SMITH, A., WYNN, P., BARKER, P., LENG, M., NOBLE, S. & STOTT, A. 2016. Cave monitoring and the potential for palaeoclimate reconstruction from Cueva de Asiul, Cantabria (N. Spain). *International Journal of Speleology*, 45, 1-9.

- SMITH, S. 1985. Noble gas solubility in water at high temperature. *EOS, Trans Am Geophys Union* 66:397.
- SMITH, S. P. & KENNEDY, B. M. 1983. the solubility of noble gases in water and in NaCl brine.
- STAHL, W. J. 1978. Source rock-crude oil correlation by isotopic type-curves. *Geochimica et Cosmochimica Acta*, 42, 1573-1577.
- STANLEY, R. H. R., BASCHEK, B., LOTT, D. E. & JENKINS, W. J. 2009. A new automated method for measuring noble gases and their isotopic ratios in water samples. *Geochemistry, Geophysics, Geosystems*, 10, n/a-n/a.
- STEFANSSON, V. 1981. The Krafla geothermal field, Northeast Iceland, chapter 10. In: Rybach L, Muffler LJP (eds) Geothermal systems: principles and case histories. *John Wiley and Son Ltd., New York*, 273-294.
- STUTE, M., CLARK, J. F., SCHLOSSER, P., BROECKER, W. S. & BONANI, G. 1995. A 30,000 yr Continental Paleotemperature Record Derived from Noble Gases Dissolved in Groundwater from the San Juan Basin, New Mexico. *Quaternary Research*, 43, 209-220.
- STUTE, M., SCHLOSSER, P., CLARK, J. F. & BROECKER, W. S. 1992. Paleotemperatures in the Southwestern United States Derived from Noble Gases in Ground Water. *Science*, 256, 1000-1003.
- TEDESCO, D., NAGAO, K. & SCARSI, P. 1998. Noble gas isotopic ratios from historical lavas and fumaroles at Mount Vesuvius (southern Italy): constraints for current and future volcanic activity. *Earth and Planetary Science Letters*, 164, 61-78.
- TIAN, H., XIAO, X., WILKINS, R. W. T. & TANG, Y. 2012. An experimental comparison of gas generation from three oil fractions: Implications for the chemical and stable carbon isotopic signatures of oil cracking gas. *Organic Geochemistry*, 46, 96-112.
- TIAN, H., XIAO, X., YANG, L., XIAO, Z., GUO, L., SHEN, J. & LU, Y. 2009. Pyrolysis of oil at high temperatures: Gas potentials, chemical and carbon isotopic signatures. *Chinese Science Bulletin*, 54, 1217-1224.
- TISSOT, B. P. & WELTE, D. H. 1984. Petroleum formation and occurrence: Berlin. *Springer-Verlag*, 49-215.
- TONG, C. G. 1992. Structure Evolution and Petroleum Accumulation of Sichuan Basin. *Geology Press, Beijing*, 21-24.
- TORGERSEN, T. & CLARKE, W. B. 1985. Helium accumulation in groundwater, I: An evaluation of sources and the continental flux of crustal  $^4\text{He}$  in the Great Artesian Basin, Australia. *Geochimica et Cosmochimica Acta*, 49, 1211-1218.
- TORGERSEN, T. & JENKINS, W. J. 1982. Helium isotopes in geothermal systems: Iceland, The Geysers, Raft River and Steamboat Springs. *Geochimica et Cosmochimica Acta*, 46, 739-748.
- TORGERSEN, T. & KENNEDY, B. M. 1999. Air-Xe enrichments in Elk Hills oil field gases: role of water in migration and storage. *Earth and Planetary Science Letters*, 167, 239-253.
- TORGERSEN, T., KENNEDY, B. M., HIYAGON, H., CHIOU, K. Y., REYNOLDS, J. H. & CLARKE, W. B. 1989. Argon accumulation and the crustal degassing flux of  $^{40}\text{Ar}$  in the Great Artesian Basin, Australia. *Earth and Planetary Science Letters*, 92, 43-56.
- VINOGRADOV, A. P. 1988. Regularities in distributions of chemical elements inside Earth's crust. *Selected Papers: Problems in Geochemistry and Cosmochemistry* 1(1).
- WANG, Y. P., ZHAO, C. Y., WANG, H. J., WANG, Z. Y. & WANG, Z. C. 2013. Origins of natural gases from marine strata in Northeastern Sichuan Basin (China) from carbon molecular moieties and isotopic data. *Journal of Asian Earth Sciences*, 65, 13-20.
- WARR, O., SHERWOOD LOLLAR, B., FELLOWES, J., SUTCLIFFE, C. N., MCDERMOTT, J. M., HOLLAND, G., MABRY, J. C. & BALLENTINE, C. J. 2018. Tracing ancient hydrogeological fracture network age and compartmentalisation using noble gases. *Geochimica et Cosmochimica Acta*, 222, 340-362.
- WEBB, M., BARKER, P. A., WYNN, P. M., HEIRI, O., VAN HARDENBROEK, M., PICK, F., RUSSELL, J. M., STOTT, A. W. & LENG, M. J. 2016. Interpretation and application of carbon isotope ratios in freshwater diatom silica. *J Quat Sci*, 31, 300-309.
- WEI, G. Q., CHEN, G. S., DU, S. M., ZHANG, L. & YANG, W. 2008. Petroleum systems of the oldest gas field in China: Neoproterozoic gas pools in the Weiyuan gas field, Sichuan Basin. *Marine and Petroleum Geology*, 25, 371-386.

- WEI, G. Q., WANG, D. L., WANG, X. B., LI, J., LI, Z. S., XIE, Z. Y., CUI, H. Y. & WANG, Z. H. 2014. Characteristics of noble gases in the large Gaoshiti-Moxi gas field in Sichuan Basin, SW China. *Petroleum Exploration and Development*, 41, 585-590.
- WEN, T. 2017. Development of Noble Gas Techniques to Fingerprint Shale Gas and to Trace Sources of Hydrocarbons in Groundwater. *University of Michigan*.
- WEN, T., CASTRO, M. C., ELLIS, B. R., HALL, C. M. & LOHMANN, K. C. 2015. Assessing compositional variability and migration of natural gas in the Antrim Shale in the Michigan Basin using noble gas geochemistry. *Chemical Geology*, 417, 356-370.
- WEN, T., CASTRO, M. C., NICOT, J. P., HALL, C. M., PINTI, D. L., MICKLER, P., DARVARI, R. & LARSON, T. 2017. Characterizing the Noble Gas Isotopic Composition of the Barnett Shale and Strawn Group and Constraining the Source of Stray Gas in the Trinity Aquifer, North-Central Texas. *Environ Sci Technol*, 51, 6533-6541.
- WEN, T., PINTI, D. L., CASTRO, M. C., LÓPEZ-HERNÁNDEZ, A., HALL, C. M., SHOUAKAR-STASH, O. & SANDOVAL-MEDINA, F. 2018. A noble gas and  $87\text{Sr}/86\text{Sr}$  study in fluids of the Los Azufres geothermal field, Mexico – Assessing impact of exploitation and constraining heat sources. *Chemical Geology*, 483, 426-441.
- WETHERILL, G. W. 1954. Variations in the Isotopic Abundances of Neon and Argon Extracted from Radioactive Minerals. *Physical Review*, 96, 679-683.
- WHITICAR, M. J., FABER, E. & SCHOELL, M. 1986. Biogenic methane formation in marine and freshwater environments:  $\text{CO}_2$  reduction vs. acetate fermentation—Isotope evidence. *Geochimica et Cosmochimica Acta*, 50, 693-709.
- WIERSBERG, T., SUER, S., GULEC, N., ERZINGER, J. & PARLAKTUNA, M. 2011. Noble gas isotopes and the chemical composition of geothermal gases from the eastern part of the Buyuk Menderes Graben (Turkey). *Journal of Volcanology and Geothermal Research*, 208, 112-121.
- WINCKLER, G., KIPFER, R., AESCHBACH–HERTIG, W., BOTZ, R., SCHMIDT, M., SCHULER, S. & BAYER, R. 2000. Sub sea floor boiling of Red Sea brines: new indication from noble gas data. *Geochimica et Cosmochimica Acta*, 64, 1567-1575.
- XIAO, Z., XIE, Z., LI, Z. & MA, C. 2008. Isotopic characteristics of natural gas of Xujiahe Formation in southern and middle of Sichuan basin. *Geochimica* 37, 245-250(in Chinese).
- YANG, C., NI, Z., WANG, T., CHEN, Z., HONG, H., WEN, L., LUO, B. & WANG, W. 2018. A new genetic mechanism of natural gas accumulation. *Sci Rep*, 8, 8336.
- YANG, W., XIE, Z. & JIN, H. 2010. Reservoir evaluation and pooling mechanism of the Xujiahe Formation in the Sichuan Basin. *Natural Gas Industry*, 30, 10-15.
- YUAN, H. F., LIANG, J. J., GONG, D. Y., XU, G. S., LIU, S. G. & WANG, G. Z. 2012. Formation and evolution of Sinian oil and gas pools in typical structures, Sichuan Basin, China. *Petroleum Science*, 9, 129-140.
- ZARTMAN, R. E., WASSERBURG, G. J. & REYNOLDS, J. H. 1961. Helium, argon, and carbon in some natural gases. *Journal of Geophysical Research*, 66, 277-306.
- ZHAI, G. M. 1989a. Petroleum Geology of China. *Petroleum Industry Press, Beijing*, 10, 28-150.
- ZHAI, G. M. 1989b. Petroleum Geology of China. *Petroleum Industry Press, Beijing*, 10.
- ZHENG, H., GAO, B., PENG, Y., NIE, H. & YANG, F. 2013. Sedimentary evolution and shale gas exploration direction of the Lower Silurian in Middle-Upper Yangtze area. *Journal of Palaeogeography*, 15, 645-656.
- ZHOU, J., XU, C., YAO, G., YANG, G., ZHANG, J., HAO, Y., WANG, F., PAN, L., GU, M. & LI, W. 2015. Genesis and evolution of Lower Cambrian Longwangmiao Formation reservoirs, Sichuan Basin, SW China. *Petroleum Exploration and Development*, 42, 175-184.
- ZHOU, Q., XIAO, X. M., TIAN, H. & PAN, L. 2014. Modeling free gas content of the Lower Paleozoic shales in the Weiyuan area of the Sichuan Basin, China. *Marine and Petroleum Geology*, 56, 87-96.
- ZHOU, Z. & BALLENTINE, C. J. 2006.  $4\text{He}$  dating of groundwater associated with hydrocarbon reservoirs. *Chemical Geology*, 226, 309-327.
- ZHOU, Z., BALLENTINE, C. J., KIPFER, R., SCHOELL, M. & THIBODEAUX, S. 2005. Noble gas tracing of groundwater/coalbed methane interaction in the San Juan Basin, USA. *Geochimica et Cosmochimica Acta*, 69, 5413-5428.

- ZHOU, Z., BALLENTINE, C. J., SCHOELL, M. & STEVENS, S. H. 2012. Identifying and quantifying natural CO<sub>2</sub> sequestration processes over geological timescales: The Jackson Dome CO<sub>2</sub> Deposit, USA. *Geochimica et Cosmochimica Acta*, 86, 257-275.
- ZHU, Y. M., HAO, F., ZOU, H. Y., CAI, X. Y. & LUO, Y. 2007. Jurassic oils in the central Sichuan basin, southwest China: Unusual biomarker distribution and possible origin. *Organic Geochemistry*, 38, 1884-1896.
- ZOU, C., DU, J., XU, C., WANG, Z., ZHANG, B., WEI, G., WANG, T., YAO, G., DENG, S., LIU, J., ZHOU, H., XU, A., YANG, Z., JIANG, H. & GU, Z. 2014. Formation, distribution, resource potential, and discovery of Sinian–Cambrian giant gas field, Sichuan Basin, SW China. *Petroleum Exploration and Development*, 41, 306-325.
- ZOU, C. N. 2013. Unconventional Petroleum Geology, second ed. *Geology Press, Beijing*, 127-167.